ORIGIN AND EVOLUTION OF HIGH ALUMINOUS ROCKS FROM PARTS OF THE PRECAMBRIAN NORTH SINGHBHUM FOLD BELT, EAST INDIAN SHIELD

Thesis submitted to Jadavpur University
for the degree of
Doctor of Philosophy (Science)

By

MAITRAYEE CHAKRABORTY

Department of Geological Sciences
Jadavpur University
2023

যাদবপুর বিশ্ববিদ্যালয়
কলকাতা - ৭০০০৩২, ভারত

JADAVPUR UNIVERSITY
KOLKATA -700 032, INDIA

FACULTY OF SCIENCE : DEPARTMENT OF GEOLOGICAL SCIENCES

CERTIFICATE FROM THE SUPERVISOR(S)

This is to certify that the thesis titled "**ORIGIN AND EVOLUTION OF HIGH ALUMINOUS ROCKS FROM PARTS OF THE PRECAMBRIAN NORTH SINGHBHUM FOLD BELT, EAST INDIAN SHIELD**" submitted by **Smt. Maitrayee Chakraborty** who got her name registered on 17.06.2013 for award of **Ph.D (Science)** degree of Jadavpur University, is absolutely based upon her own work under the supervision of **Prof. Pulak Sengupta** and **Prof. Sanjoy Sanyal** and that neither this thesis nor any part of it has been submitted for either any degree/ diploma or any other academic award anywhere before.

(Signature of Supervisors)

Pulak Sengupta
11/1/23

Prof. Pulak Sengupta
Department of Geological Sciences
Jadavpur University
Kolkata-700032

Dr. Pulak Sengupta
Professor
Department of Geological Sciences
Jadavpur University, Kolkata-700032

Sanjoy Sanyal 11.1.2023

Prof. Sanjoy Sanyal
Department of Geological Sciences
Jadavpur University
Kolkata-700032

Dr. Sanjoy Sanyal
Professor
Department of Geological Sciences
Jadavpur University
Kolkata: 700032, India

দূরভাষ : ২৪১৪-৬৬৬৬/প্রসারণ : ২২৬৮
Website : www.jadavpur.edu
E-mail : hod_geological@jdvu.ac.in
Phone : 2414 6666/Extn. 2268

“It seems to me that the natural world is the greatest source of excitement; the greatest source of visual beauty; the greatest source of intellectual interest. It is the greatest source of so much in life that makes life worth living.”

-David Attenborough

Dedicated to Didun, Dadu and Thamma

who made me a better human being

with their unconditional love and kindness

ACKNOWLEDGEMENT

The journey of scholars is often said to be solitary. The truth, however, is that scholars are never alone. They are the sum total of all the scholarship that has come before them, the hands that have guided their learning, and the quiet solidarity of friends and community who have made space for the rigours of work and study. This PhD could not have been possible without the guidance, contribution and support of many people who have directed me when I felt lost, supported me and encouraged me when I felt overwhelmed. I would like to extend my heartfelt gratitude and appreciation to those people for helping me bring this work finally into reality.

I would firstly like to sincerely thank my PhD supervisors Prof. Pulak Sengupta and Prof. Sanjoy Sanyal for their support and guidance. They guided and steered me every step of this journey and their insightful comments in critical stages opened my mind to new approaches and ways of thinking. I would also like to extend my regards to them for their patience, motivation and immense knowledge that not only helped me overcome academic hurdles but also informed my broader outlook on life and academic rigour, an invaluable gift I will always cherish.

I would like to thank CSIR for providing me financial assistance in terms of fellowships during the initial period of my work. I am thankful Jadavpur University for providing me the logistical support for my work.

I extend my heartfelt thanks to all the faculty members, researchers and staff of the department of Geological Sciences, Jadavpur University for their help and support. The university has been more than an educational institute for me, it has been my home where I have returned for comfort and solace innumerable times, and I am thankful for all the experiences and learnings I have received here.

. I am thankful to Geological Survey of India (GSI) for giving me the permission to carry on with my doctoral research and providing required help during my work. I would like to extend my gratitude to Shri Partha Dutta, Deputy Director General (DDG), GSI, for supporting and helping me whenever necessary. I am grateful to Shri S.N.Mahapatro, DDG, GSI for enriching me with his knowledge and guidance on various technical matters. I am grateful to Shri Dinesh Thawait, Director (G), GSI, for his help in various matters. I am grateful to Shri Abhishek Ghosh, Geologist, Shri Sameer Debnath, Geologist and Shri Manas

Pratim Baruah, Geologist for their continuous support and guidance in various technical matters. A special shout out to Ms. Priyadarsani Mallik, Geologist, for her unflinching support during the last few months.

I am thankful to Dr. Sandip Nandy, Director, GSI, Shri Sujit Tripathy, Director, GSI and Dr. Upama Dutta, Asst. Prof., ISM, Dhanbad for their help during EPMA analysis. I am indebted to Prof. Andreas Pack, University of Gottingen and Dr. Sukanya Sengupta for their help in oxygen isotope analysis.

I am thankful to all the members of metamorphic petrology research group for being wonderful co-workers who extended their help in both academic as well as personal speheres of life whenever I needed. I want to extend my gratitude to Dr.Moumita Talukdar, Dr.Sayan Ray, Dr.Shreya Karmakar, Dr.Subham Mukherjee, Dr.Anindita Dey, Dr.Enakshi Das, Dr.Satabdi Das, Ms.Sirina Roy Chowdhury, Ms.Arimita Chakrabarty, Shri Somdipto Chatterjee, Ms.Shreyasi Das, Shri Sourav Mitra and Shri Nilanjan Bhowmick for their support. I am lucky to have known Shri Shyamal Sengupta who was a constant source of inspiration and motivation to me. I am specially grateful to Shri Sayan Biswas (Asst. Prof., Presidency University) for helping me out in several matters and taking care of administrative matters related to my PhD in my absence.

I am thankful to Dr. Abhinaba Roy, Dr. Anupendu Gupta, Prof. Alfonso Pesquera, Dr. Encarnacion Roda-Robles, Prof. Subrata Karmakar and Dr. Nandini Sengupta for sharing their knowledge and lending their guidance during various field trips. I am thankful to Moumita di, Sayan (Ray) da, Sayan (Biswas) da and Priyadarshi for accompanying and helping me on my field trips. I am thankful to Dr. Nandini Chattopadhyay for being a wonderful friend and senior. Juniors (now friends) like Monai Mehul Hassan, Sourav Das, Koushik Das, Pritam Karmakar and Prantick Santra made things fun at fieldwork. I am grateful to Dr. Sadhana Mahato (Asst. Prof., Jadavpur University) for her help and guidance whenever required.

I am lucky to have friends like Smt. Sustava Bhattacharya and Shri Prithwiraj Maiti who were there whenever I needed them. I am immensely blessed to have Dr.Priyadarshi Chowdhury, Dr.Anirban Chatterjee and Dr.Sukanya Sengupta as my friends who have tolerated my unending questionares, requests and stood by me through thick and thin. I am grateful to have Dr.Jayati Mukherjee, Ms.Rituparna Sengupta and Ms.Sharmistha Bhowmik as my pillars of support. Frankly I don’t know what I would do without them.

I take the opportunity to express my profound appreciation to my husband, Shri Saswata Biswas, for his unflinching support and sensitivity to give me the space that I needed. And finally, but most importantly, I am thankful to my parents who have always put faith in my abilities, and encouraged me to aim high. My father always supported me regardless of the situation. My mother has beem a source of inspiration for me and instrumental in instilling confidence. I always have my parents to count on when times are rough. Without them, this PhD would not have been possible.

MAITRAYEE CHAKRABORTY

CONTENTS

List of mineral abbreviations

The most frequently occuring mineral abbreviations in the text are mostly after Whitney and Evans (2010). For convenience of the reader a list of mineral abbreviations used has been given below.

Ab- Albite

Alm- Almandine

Bt- Biotite

Chl- Chlorite

Cld- Chloritoid

Crn- Corundum

Dsp- Diaspore

Fcld- Fe-chloritoid

Fst- Fe-staurolite

Grt- Garnet

Ilm-Ilmenite

Kln- Kaolinite

Ky- Kyanite

Kfs- K-feldspar

Mag- Magnetite

Ms- Muscovite

Pa- Paragonite

Prl- Pyrophyllite

Qz- Quartz

Rt- Rutile

Sa- Sanidne

St- Staurolite

Xtm- Xenotime

Other mineral abbreviations

Aug- Augelite

Fl- Florencite

Laz- Lazulite

ABSTRACT

Origin and evolution of the highly aluminous kyanite quartzite, reported only from a few metamorphic fold belts of world, are not properly understood. In the arcuate Palaeoproterozoic North Singhbhum Fold belt (NSFB) of the East Indian shield, the Singhbhum Shear Zone (SSZ) with its rich Fe-Cu –U –phosphate deposits separate the metavolcano-sedimentary sequence of Lower and Upper Dhanjori Fm. from the metasedimentary sequence of Chaibasa Fm. The kyanite quartzite occurs as isolated pods all along the hanging wall side of the SSZ at the immediate contact with the Chaibasa Fm. Both banded (defined by centimetre to decimetre thick alternate layers rich in kyanite and quartz) and massive (without any compositional banding) variety of kyanite quartzite are noted. The rock shows wide variation in terms of kyanite/quartz ration, shape and mode of occurrence of kyanite grains. The kyanite quartzite is intensely deformed and commonly replaced by muscovite. Both kyanite and quartz show crystaloplastic deformation. The stretched grains of kyanite and quartz define a planar fabric that conform the shear fabric in the SSZ. Fabric parallel growth of muscovite after deformed kyanite produce alternate muscovite-and kyanite quartz rich bands. The planar fabric swerves around least deformed lenses showing randomly oriented kyanite grains. In places, kyanite-quartz veins with kyanite grains at nearly perpendicular to the vein wall cuts across the regional planar fabric. The vein itself shows deformation suggesting that these veins were formed during the deformation in the SSZ. These veins are interpreted as fluid conduits in which Al and Si precipitated from the fluid. Relative to the Primitive Mantle compositions, the compositions of the studied muscovite poor kyanite quartzite show elevated LILE, HFSE and LREE with a prominent Nb and Pb anomaly. In terms of REE and most of the HFSE concentrations the rock shows remarkable similarity with the metasedimentary rocks of the Chaibasa Fm. Combining the bulk chemical attributes, high alteration indices (CIA~98, CIW~99, PIA~99, AAAI~94) and the narrow $\delta^{18}O$ values (7-7.7 per mil relative to SMOW) of the kyanite, it is proposed that the advanced argillic alteration of the pelitic rocks of the Chaibasa Fm. This alteration process predated the ~1.6 Ga old shearing and accompanied metamorphism/metasomatism in the SSZ. Extant geochrolological data suggest that the alteration process was associated with the formation of the protoliths of the hydrothermal Cu-Fe sulphide deposits at ~1.8 Ga in the SSZ. This study, therefore, demonstrates contrasting behavior of Al during fluid-rock alteration. Textural modeling study suggests that muscovite was formed during infiltration of K during the ~1.6 Ga tectonothermal event in the SSZ. Owing to its highly aluminous bulk compositions and

variation of the composition of the infiltrating fluids, the kyanite quartzite develop many exotic minerals during the ~1.6 Ga tectonothermal event in the SSZ. Infiltration of Fe-Mg bearing fluid developed metasomatic chloritoid after kyanite that is hitherto not reported from metamorphic belt. Numerically and thermodynamically computed phase diagrams in the P-T and μ_{FeO} - μ_{SiO2} space (at different P-T conditions) constrain that the metasomatic chloritoid developed at 6 ±1 kbar and ~ 500°C along a geothermal gradient~80°C/kbar. Fe and Mg were likely to be transported in the form of $FeCl_4^{2-}$ or $FeCl_3(H_2O)^-$ complexes. Solid volume change of the metasomatic reactions (during formation of muscovite and chloritoid) helped create secondary porosity driven permeability for the metasomatic fluids. The replacement of kyanite by florencite suggests that LREE and P was transported in REE-Phosphate complex in the metasomatic fluid. Sequential infiltration of P- and Mg-rich fluid in develops augelite and lazulite in the banded kyanite quartzite at P-T conditions at which metasomatic chloritoid and muscovite were formed. A fluid–rock ratio of only 0.38 is sufficient to completely convert kyanite to augelite. The P-T conditions of 6 ±1 kbar and ~ 500°C deviates from recorded thermal perturbation with respect to the steady state geothermal gradient that is estimated for Proterozoic period. The observed thermal perturbation in the SSZ and the adjoining lithologies is explained by burial of the exposed section of the crust beneath a continental thrust sheet of ~25 km at ~1.6 Ga tectonothermal event presumably in a continent-continent collision setting. This event was preceded by a period of extension, presumably at ~1.8 Ga, during which the protolith of the metavolcanics, metasedimentary rocks of the NSFB were formed. In the same extensional event, the protoliths of the Cu-Fe-sulphide ores and accompanying advanced argillic alteration that led to the formation of the protolith of the kyanite quartzite in the SSZ were formed.

CHAPTER 1

Introduction

Regional metamorphic belts, in many places, develop rocks of unusual bulk compositions and consequently develop rare alumino-silicate-phosphate minerals (Allard and Whitney, 1994; Morteani et al., 2001; Larsson, 2001). Kyanite-quartzite (KQ) with its abnormally high Al_2O_3 and low FeO, MgO, CaO and Na_2O have only been reported and studied from a handful of regional metamorphic belts (reviewed in Bijnaar et al., 2016; Table 1). Its' unusual composition qualifies it to be in the category of high aluminous rocks. The formation and evolution of the atypical kyanite quartzite is important for several reasons. These are as follows:

(1) Industrial grade kyanite and nearly pure quartz are exploited from this rock (Ihlen, 2000; Sarkar and Gupta, 2012; Bijnaar et al., 2016). Certain gold deposits and hydrothermal Cu-Fe sulphide deposits are also associated with this rock (Hallberg, 1994; Larsson, 2001; Pal et al., 2011; Sarkar and Gupta 2012; Oliveira et al., 2016)

(2) Owing to its unusually Al_2O_3 rich compositions, the kyanite quartzite gives rise to a number of exotic minerals (e.g. chloritoid, Al-phosphate, Al-REE phosphate and tourmaline and other borosilicates) that serve as fingerprint to unravel the ambient physical conditions, compositions of metasomatic fluid and put constraint on the nature of fluid rock interactions at various crustal depths (Morteani et al., 2001; Nagy et al., 2002, Sengupta et al, 2005, 2011; Chakraborty et al., 2014). This information plays critical role in understanding the style of extant and extinct orogenesis in the contact and regional metamorphic belts (Müller et al., 2007)

(3) The kyanite-quartzite also provide an opportunity to study the behavior of Al, its mobility and immobility in crustal fluids, under different physicochemical conditions (reviewed in Beitter et al. 2008).

1.1 Origin of Kyanite quartzite (KQ) at different localities:

Origin of the kyanite-quartzite that occurs in diverse litho-packets over protracted time is not properly understood. The Palaeoproterozoic kyanite-quartzite in the Scandinavia occurs in association with the volcano-sedimentary sequence. The lithounits including the kyanite-quartzite record greenschist- amphibolites facies metamorphism (Larsson, 2001; Müller et al., 2007). Hydrothermal alteration of granitic protolith has been deemed responsible in this occurrence for leaching of alkalis with residual enrichment of Al_2O_3 (Larsson 2001; Table 1).

The kyanite quartzite is associated with Palaeozoic meta volcano- sedimentary sequences in the Piedmont province of USA (Owens and Pasek, 2007; Table 1). Advanced argillic alteration in which highly sulphidic fluid is considered responsible for extensive leaching of different elements from rocks of the meta volcano-sedimentary unit and formed kaolin and quartz. Subsequent metamorphism led to formation of kyanite quartzite (Owens and Pasek, 2007).

The quartz-kyanite rock occurs as pods within mica schist in Palaeoproterozoic fold belt of New Mexico (Simmons et al., 2011). Hydrothermal leaching of a variety of rocks including meta-acid tuffs, quartz mica schists and meta- conglomerate is considered responsible (Simmons et al., 2011).

Extensive leaching of felsic volcanic rocks by sulphidic fluids at (<2 kbar) that was followed by regional metamorphism (>4 kbar, 500-650°C) is suggested to explain the Palaeoproterozoic kyanite quartzite of Bosland (Suriname, Bijnaar et al. 2016; Table 1).

Implicit in all the different metasomatic processes mentioned above is that the kyanite-quartzite was formed by residual concentrations of Al. This then follows that Al remains virtually immobile during the hydrothermal alteration of rocks at different crustal depths (Lentz and Gregoire, 1995). A number of experimental and theoretical studies have demonstrated that Al can be significantly soluble and hence can be transported in aqueous fluids due to complexation of Al with different elements (Ague, 1995; Manning, 2007, 2006; Beitter et al., 2008). A small decrease in temperature and pH of the fluid can led to deposition of kyanite quartz rock (Beitter et al., 2008). Presence of aluminosilicate–quartz veins (Ague 1995; Widmer and Thompson, 2001; Putlitz et al., 2002; Bucholz and Ague, 2010) and mass balanced calculations with pseudomorph of Al-spinel after corundum and chromite (Chowdhury et al., 2013; Talukdar et al., 2017) also support the enhanced solubility of Al during metamorphic fluid flow. Furthermore, the kaolin + quartz assemblage, the inferred protolith of the kyanite-quartzite (Bijnaar et al. 2016) can also be formed by pedogenic processes (Golani, 1989; Voicu and Bardoux, 2002; De Wall et al., 2012). Regional metamorphism of the kaolin + quartz assemblage, a product of pedogenic process can also form Al_2SiO_5–quartz rock (e.g Golani 1989, De Wall et al. 2012).

1.2 Study area:

The Singhbhum Shear Zone (SSZ) of the east Indian shield separates the dominantly Palaeoproterozoic North Singhbhum Fold Belt (NSFB) into a volcano-sedimentary (now metamorphosed) Dhanjori Gp. to the south and the metasedimentary rocks dominated Chaibasa Fm. to the north (Fig.1). E-W to NNW-SSE trending arc-shaped SSZ that has been the loci of Cu-Fe-U deposits, develop several exotic rocks, namely dumortierite-tourmaline rock, quartz-chlorite schist, chloritoid –biotite schist and kyanite quartzite (Reviewed in Sarkar 1984; Pal et al., 2009; Sarkar and Gupta 2012; Sengupta et al., 2011). The detached outcrops of the kyanite-quartzite occur all along the northern fringe of the SSZ (shown in Chapter 5, Fig. 5.1) and contains variable amount of muscovite, chloritoid, dumortierite, tourmaline, Al-phosphate and rare florencite (reviewed in Sarkar, 1984, Sengupta et al., 2011; Chakraborty et al., 2014, 2013). The kyanite-quartzite show wide variation in morphology, kyanite /quartz ratio and are locally quartz free (Sarkar 1984). Both laminated (defined by alternate kyanite-rich and quartz-rich layers) and massive varieties are observed. Lapsa buru that exposes one of the largest kyanite mine in the world is a part of the kyanite-quartzite (Sarkar 1984). Lenses of the kyanite-quartzite are also found well within the metasedimentary unit of the Chaibasa Fm (Sengupta et al., 2005). Owing to absence of robust geochemical and stable isotope data, origin of the enigmatic kyanite-quartzite of the SSZ remains poorly understood. Based on rudimentary geochemical data and the field features (pre-1984), the kyanite-quartzite of the SSZ was considered as metamorphosed palaeosol horizon (reviewed in Sarkar 1984). This is in gross disagreement with (a)the formation of massive kyanite (±corundum) with little or no quartz, locally with pegmatoidal dimension and (b) formation of kyanite quartzite well within the Chaibasa Fm (reviewed in Sarkar 1984). The proposition that the post kinematic massive

kyanite (±corundum) was formed by hydrothermal mobilization of the metamorphic equivalent of a presumed pedogenic deposit (reviewed in Sarkar 1984) is not substantiated with rigorous studies in the light of modern geochemistry and petrology. It is also not clear which process(es) was responsible for the formation of chloritoid, Al-phosphate and florencite in the kyanite quartzite.

In this study I present the field relations, impress of deformation, mineralogical evolution, whole rock geochemistry and limited stable oxygen isotope compositions of kyanite-quartzite rocks exposed in four areas (namely Ujainpur, Surda, Jaduguda and Kanyaluka) along the northern margin of the SSZ. The localities are chosen in manner that they are spread all along the length of the SSZ from northern part to south-eastern part. The localities for this study were picked so as to capture the maximum variation in field features and mineralogy of KQ rocks. The mineralogical variations including muscovite poor KQ and muscovite rich KQ along with some exotic aluminophosphate minerals (discussed in Chapters 5 and 6) are vividly studied from these localities. The KQ rocks are spatially associated with metasedimentary and metavolcanic rocks of the Singhbhum group and Dhanjori Group.

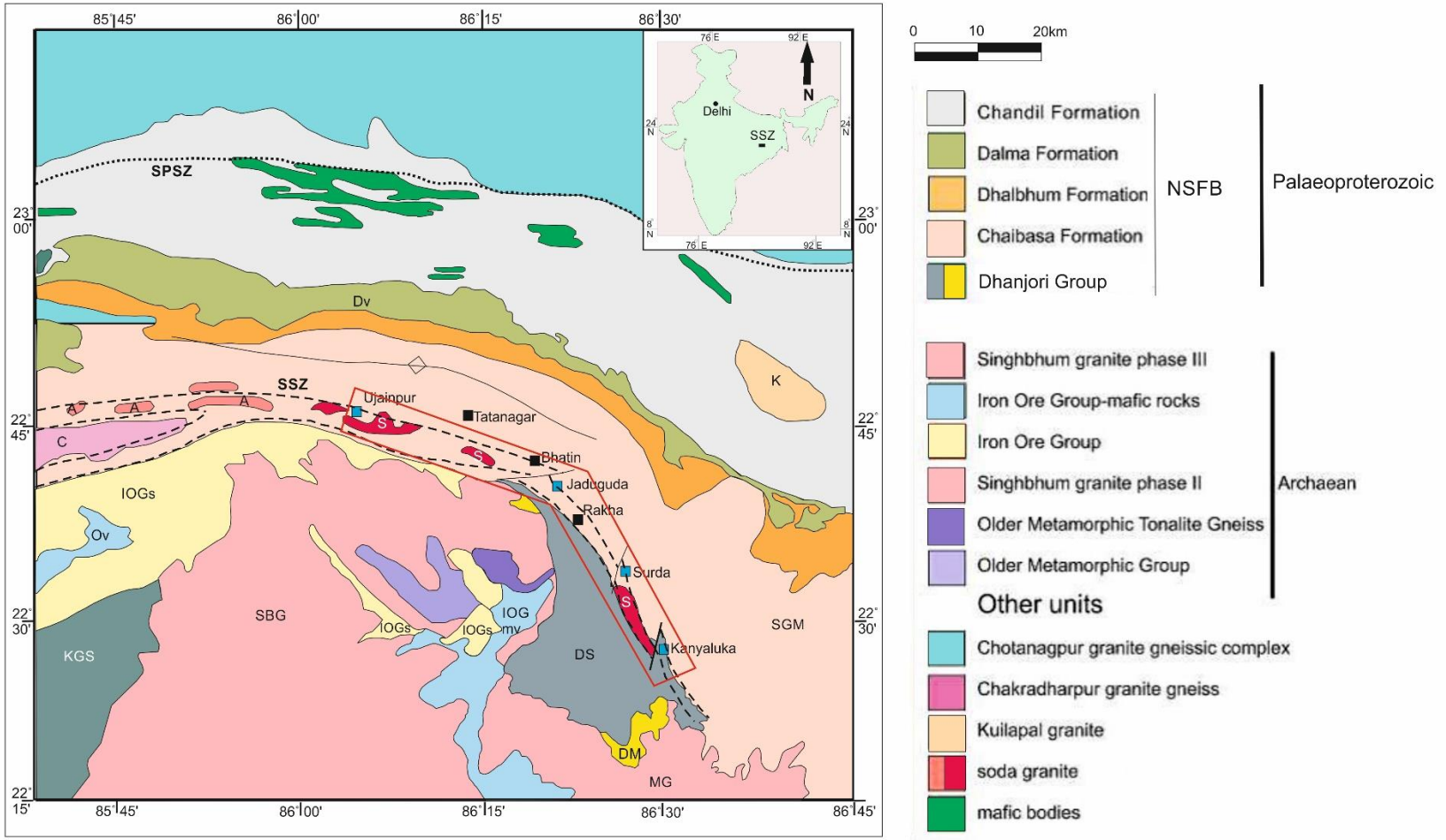

Fig. 1: Geological map of the North Singhbhum Fold Belt (NSFB) and Singhbhum Shear Zone (SSZ) partly after Saha (1994). The arc-shaped SSZ is marked with a broken line. The hollow red box marks the area along SSZ where fieldwork was carried out. The solid blue boxes mark the study areas for the present study. NSFB- North Singhbhum Fold Belt, SSZ- Singhbhum Shear Zone, SPSZ-South Purulia Shear Zone, SGM- Singhbhum Group of Metapelites, DV- Dalma Volcanics, SBG- Singhbhum Granite, A- Arkasani Granite, C- Chakradharpur Granite, S- Soda Granite, MG- Mayurbhanj Granite, K- Kuilapal Granite, IOGs- Iron Ore Group sediments, IOGm- Iron Ore Group meta-volcanics, DS- Dhanjori Sediments, KGS- Kolhan Group of volcanics, DM- Dhanjori Metavolcanism, Ov- Ongarbira metavolcanics.

1.3 Objectives:

The major issues related to the KQ rocks addressed in this study are listed below:

1. What are the mineralogical, textural and microstructural variations in the KQ in the four studied areas along the SSZ?
2. How do the bulk compositions of the KQ compare with the average compositions of the dominant rocks of the upper continental crust?
3. Do the KQs in the SSZ represent metamorphism of unusual sedimentary rocks /weathering profile or produced at depth due to hydrothermal alteration?
4. What is the nature, driving force and products of fluid-rock alteration observed in the KQ? How did different elements behave during the fluid-rock interaction?
5. What are the physical conditions of fluid-rock interactions in the KQ? How do these physical conditions compare with the physical conditions reported from the SSZ and the adjoining parts of the SSZ?
6. What was the tectonic scenario in which the metasomatic minerals assemblages in the KQ were formed along with the other rocks of the SSZ?

1.4 Methodology

Methodologies that have been applied to attain the objectives of this study are:

1. Field work has been carried out to document the field relationship of kyanite quartzites with other litho-members, geological mapping in some parts and collection of bed rock samples
2. Detailed petrographic study for mineral identifications and textural correlation between different existing phases has been done

3. Chemical composition of different minerals in rocks have been analyzed using Electron Micro Probe Analyzer (EPMA).
4. Mineralogical evolution is deciphered from balanced mineral reactions, ternary chemographic projections of phases using C-space integrated with petrological observations
5. Bulk composition study (major and trace elements) of kyanite quartzites and their comparison with available bulk data of other neighbouring litho-members
6. P-T conditions are constrained using conventional thermo-barometry and numerical modelling calculated phase diagrams (using Perple_X software). Fluid character studied with chemical potential diagrams.
7. Oxygen isotope analysis of kyanite grains for determining fluid compositions

Integrated field studies, petrochemical data, stable oxygen isotope of kyanite provide insight about the likely process that led to the formation of the kyanite-quartzite in the SSZ. The driving force for and the mechanism of formation of muscovite, Al-phosphates chloritoid and florencite in the kyanite-quartzite in the studied areas are explored.

1.5 Thesis layout

Chapter 2 deals with the regional geological backdrop of Singhbhum Craton and NSFB

Chapter 3 contains detailed petrological study and textural analysis of kyanite quartzites from different parts of SSZ, their bulk compositional analysis and a geochemical study of these rocks

Chapter 4 deals with the petrological and textural study of chloritoid bearing kyanite quartzites from the study area. Pressure-temperature conditions of formation have been

constrained through P-T pseudosection and conventional thermometry. Fluid composition and mineral stabilities are determined through chemical potential diagrams in Perple_X.

Chapter 5 deals with detailed petrological and textural study of lazulite-augelite bearing kyanite quartzites from Kanyaluka. Pressure-temperature conditions have been constrained using available data in the Al_2O_3-SiO_2-MgO-P_2O_5-H_2O system and stability fields of aluminium silicates, augelite, and lazulite.

Chapter 6 deals with the petrological and textural study of REE bearing aluminophosphates in the kyanite quartzites of Kanyaluka

Chapter 7 encompasses and integrates the findings of chapters 3, 4, 5 and 6. It discusses the evolution of origin and evolution of the KQ rocks from study area, conditions of formation of chloritoid and exotic aluminophosphates in KQ, fluid compositions and conditions of solubility of REE, Mg, P and Al in crustal fluids.

Table 1: Global incidences of kyanite quartzite

Sl.no.	Locality	Age of host rock	Mineral assemblage	Protolith	Process of formation	Authors
1	Minas Gerais, Brazil	Mesoproterozoic	Muscovite- dumortierite-kyanite-quartz	P and B-rich clay-bearing sandstone	Prograde metamorphism (P<440°C and T>3.4kbar)	Morteani et al., 2001
2	Graves Mountain, Lincolnton, Georgia.	Paleozoic	Pyrite-sericite-aluminophosphates -kyanite-quartz	Felsic metapyroclastic lithologies	Hydrothermal alteration	Allard and Whitney, 1994
3	Piedmont Province, Central Virginia	Ordovician	Kyanite, white mica, Cr-muscovite, rutile ± pyrite ± topaz	Mafic and felsic igneous	Hydrothermal alteration	Owens and Pasek, 2007
4	Dabie mountains, China	Mesozoic	Kyanite, talc, epidote, quartz	Aplite	Metamorphism in presence oh high pressure fluids (2.4±0.3 Gpa, 630°C)	Laili et al., 1998
5	Veslehukta, western Spitsbergen	Proterozoic	Kyanite, dolomite, quartz, muscovite, chlorite	dolomitic quartzite	Prograde metamorphism of medium grade	Cheng et al., 1989
6	South Harris, Scotland	Proterozoic (~1.9 Ga)	Orthopyroxene-garnet-kyanite-K-feldspar quartzite	Psammite	Prograde metamorphism (905 ± 25°C, 12.5 ± 0.8 kbar)	Holllis et al., 2006
7	Marowijne greenstone belt, Bosland, Suriname	Palaeoproterozoic	Kyanite-staurolite-quartz	Felsic tuff	Hydrothermal alteration followed by lower amphibolite metamorphism (P>4kbar, 500–650°C)	Bijnaar et al., 2016

Sl.no.	Locality	Age of host rock	Mineral assemblage	Protolith	Process of formation	Authors
8	Sulu terrane, China	Triassic	Kyanite,quartz and topaz, with minor phengite, pyrite, and rutile	n.a.	UHP metamorphism (500–600 °C, 1.0 to 2.5 Gpa)	Zhang et al., 2002
9	Solor area, Norway	Middle to Upper Proterozoic (1.6 to 1.8 Ga)	Kyanite, quartz, muscovite, pyrophyllite, rutile, pyrite	Mafic protolith	Hydrothermal alteration	Muller et al., 2007
10	Sopron-Fertorakos area, E. Alps, W. Hungary		Mg-Chlorite, kyanite, muscovite, quartz ± florencite	Gneiss-micaschist complex	Mg- metasomatism	Demeny et al., 1997, Nagy et al., 2002
11	Hålsjöberg, Diksberg, Hökensås and Västanå, Sweden	Middle to Upper Proterozoic	Kyanite, quartz, Al-phosphates, rutile	Granitoid rocks	Hydrothermal alteration by magmatic fluids(T<400°C, P<2 kbar) followed by regional metamorphism	Larsson 2001
12	Espinhaço Ridge, Bahia State, Brazil		Quartz, dumortierite, kyanite, chromium-bearing muscovite, and lazulite	Sedimentary (contribution of evaporites)	Metamorphism (P ≥ 3.5 kbar, T = 475 - 560°C)	Evangelista and Danderfer, 2012
13	Charlotte Belt of Virginia and Kings Mountain Belt of North Carolina and South Carolina, Appalachian belt, eastern USA	Neoproterozoic-Cambrian	Kyanite, quartz, rutile , muscovite, pyrite, magnetite, diaspore and topaz	felsic tuffs	Sub-seaflcor hydrothermal alteration and associated exhalative processes followed by Metamorphism	Iihlen 2000

References

Ague, J.J., 1995. Mass transfer during Barrovian metamorphism of pelites, south-central Connecticut; II, Channelized fluid flow and the growth of staurolite and kyanite. Am. J. Sci. 294, 1061–1134.

Allard, G.O., Whitney, J.A., 1994. Geology of the Inner Piedmont, Carolina terrane, and Modoc zone in Northeast Georgia. Project Report 20. Georgia Department of Natural Resources. Environ. Prot. Div. Georg. Geol. Surv. Atlanta.

Beitter, T., Wagner, T., Markl, G., 2008. Formation of kyanite-quartz veins of the Alpe Sponda, Central Alps, Switzerland: Implications for Al transport during regional metamorphism. Contrib. to Mineral. Petrol. 156, 689–707. https://doi.org/10.1007/s00410-008-0310-4

Bijnaar, G., Bergen, M.J. Van, Wong, T.E., 2016. The kyanite quartzite of Bosland (Suriname): evidence for a Precambrian metamorphosed alteration system 2016, 447–465. https://doi.org/10.1017/njg.2016.38

Bucholz, C.E., Ague, J.J., 2010. Fluid flow and Al transport during quartz-kyanite vein formation, Unst, Shetland Islands, Scotland. J. Metamorph. Geol. 28, 19–39. https://doi.org/10.1111/j.1525-1314.2009.00851.x

Chakraborty, M., Biswas, S., Sengupta, N., Sengupta, P., 2014a. First report of florencite from the Singhbhum shear zone of the East Indian Craton. Int. J. Mineral. 1–8. https://doi.org/10.1155/2014/978793

Chakraborty, M., Sengupta, N., Biswas, S., Sengupta, P., 2014b. Phosphate minerals as a recorder of P-T-fluid regimes of metamorphic belts: example from the Palaeoproterozoic Singhbhum Shear Zone of the East Indian shield. Int. Geol. Rev. 57, 1619–1632. https://doi.org/10.1080/00206814.2014.982216

Cheng, A., Craddock, C., Zhu, G., 1989. Kyanite in upper Proterozoic quartzite near Veslebukta, Wedel Jarlsberg Land, western Spitsbergen. Polar Res. 7, 147–148. https://doi.org/10.1111/j.1751-8369.1989.tb00365.x

Chowdhury, P., Talukdar, M., Sengupta, P., Sanyal, S., Mukhopadhyay, D., 2013. Controls of PT path and element mobility on the formation of corundum pseudomorphs in Paleoproterozoic high-pressure anorthosite from Sittampundi, Tamil Nadu, India. Am. Mineral. 98, 1725–1737.

De Wall, H., Pandit, M.K., Chauhan, N.K., 2012. Paleosol occurrences along the Archean–Proterozoic contact in the Aravalli craton, NW India. Precambrian Res. 216, 120–131.

Demény, A., Sharp, Z.D., Pfeifer, H.R., 1997. Mg-metasomatism and formation conditions of Mg-chlorite-muscovite-quartzphyllites (leucophyllites) of the Eastern Alps (W. Hungary) and their relations to Alpine whiteschists. Contrib. to Mineral. Petrol. 128, 247–260. https://doi.org/10.1007/s004100050306

Evangelista, H.J., Danderfer, F.A., 2012. Blue quartzite with dumortierite and aluminum

phosphates from the Northern Espinhaço, Bahia: mineralogy and petrogenesis. Rev. Bras. Geociências 42. https://doi.org/10.5327/Z0375-75362012000200011

Golani, P.R., 1989. Sillimanite-corundum deposits of Sonapahar, Meghalaya, India: a metamorphosed Precambrian paleosol. Precambrian Res. 43, 175–189.

Hallberg, A., 1994. The Enåsen gold deposit, central Sweden. Miner. Depos. 29, 150–162.

Hollis, J.A., Harley, S.L., White, R.W., Clarke, G.L., 2006. Preservation of evidence for prograde metamorphism in ultrahigh-temperature, high-pressure kyanite-bearing granulites, South Harris, Scotland. J. Metamorph. Geol. 24, 263–279. https://doi.org/10.1111/j.1525-1314.2006.00636.x

Ihlen, P.M., 2000. Utilisation of sillimanite minerals, their geology, and potential occurrences in Norway-an overview. Norges Geol. Undersokelse Bull. 436, 113–128.

Laili, J., Shutong, X., Yican, L., Weiping, W., Wen, S., 1998. The white schist assemblage in the kyanite quartzite from the ultrahigh-pressure metamorphic belt, eastern Dabie Mountains. Chinese Sci. Bull. 43, 1651–1655.

Larsson, D., 2001. Transition of granite to quartz-kyanite rock at hålsjöberg, southern Sweden: Consequence of acid leaching and later metamorphism. Gff 123, 237–246. https://doi.org/10.1080/11035890101234237

Lentz, D.R., Gregoire, C., 1995. Petrology and mass-balance constraints on major-, trace-, and rare-earth-element mobility in porphyry-greisen alteration associated with the epizonal True Hill granite, southwestern New Brunswick, Canada. J. Geochemical Explor. 52, 303–331.

Manning, C.E., 2007. Solubility of corundum + kyanite in H2O at 700°C and 10 kbar: Evidence for Al-Si complexing at high pressure and temperature. Geofluids 7, 258–269. https://doi.org/10.1111/j.1468-8123.2007.00179.x

Manning, C.E., 2006. Mobilizing aluminum in crustal and mantle fluids. J. Geochemical Explor. 89, 251–253. https://doi.org/10.1016/j.gexplo.2005.12.019

Morteani, G., Ackermand, D., Horn, A.H., 2001. Aluminium-phosphates and borosilicates in muscovite-kyanite metaquartzites near Diamantina (Minas Gerais , Brazil): Petrogenetic implications The rocks studied in this paper are examples of the rather rare cases of sedimentary phosphate-rich rocks of Mi 111–129.

Müller, A., Ihlen, P.M., Wanvik, J.E., Flem, B., 2007. High-purity quartz mineralisation in kyanite quartzites, Norway. Miner. Depos. 42, 523–535. https://doi.org/10.1007/s00126-007-0124-8

Nagy, G., Draganits, E., Demény, A., Pantó, G., Árkai, P., 2002. Genesis and transformations of monazite, florencite and rhabdophane during medium grade metamorphism: Examples from the Sopron Hills, Eastern Alps. Chem. Geol. 191, 25–46. https://doi.org/10.1016/S0009-2541(02)00147-X

Oliveira, C.G. de, Oliveira, F.B. de, Della Giustina, M.E.S., Marques, G.C., Dantas, E.L., Pimentel, M.M., Buhn, B.M., 2016. The Chapada Cu–Au deposit, Mara Rosa magmatic arc, central Brazil: constraints on the metallogenesis of a Neoproterozoic large porphyry-type deposit. Ore Geol. Rev. 72, 1–21.

Owens, B.E., Pasek, M.A., 2007. Kyanite quartzites in the Piedmont Province of Virginia: Evidence for a possible high-sulfidation system. Econ. Geol. 102, 495–509. https://doi.org/10.2113/gsecongeo.102.3.495

Pal, D.C., Barton, M.D., Sarangi, A.K., 2009. Deciphering a multistage history affecting U–Cu (–Fe) mineralization in the Singhbhum Shear Zone, eastern India, using pyrite textures and compositions in the Turamdih U–Cu (–Fe) deposit. Miner. Depos. 44, 61–80.

Pal, D.C., Sarkar, S., Mishra, B., Sarangi, A.K., 2011. Chemical and sulphur isotope compositions of pyrite in the Jaduguda U (-Cu-Fe) deposit, Singhbhum shear zone, eastern India: Implications for sulphide mineralization. J. Earth Syst. Sci. 120, 475–488. https://doi.org/10.1007/s12040-011-0080-7

Putlitz, B., Valley, Æ.J.W., Matthews, Æ.A., 2002. Oxygen isotope thermometry of quartz – Al 2 SiO 5 veins in high-grade metamorphic rocks on Naxos island (Greece). https://doi.org/10.1007/s00410-002-0346-9

Sarkar, S.C., 1984. Geology and ore mineralization of the Singhbhum copper-uranium belt, eastern India, Jadavpur University Press. Jadavpur University.

Sarkar, S.C., Gupta, A., 2012. Crustal evolution and metallogeny in India, Crustal Evolution and Metallogeny in India. Cambridge University Press, New York. https://doi.org/10.1017/CBO9781139196123

Sengupta, N., Mukhopadhyay, D., Sengupta, P., Hoffbauer, R., 2005. Tourmaline-bearing rocks in the Singhbhum shear zone, eastern India: Evidence of boron infiltration during regional metamorphism. Am. Mineral. 90, 1241–1255.

Sengupta, N., Sengupta, P., Sachan, H.K., 2011. Aluminous and alkali-deficient tourmaline from the Singhbhum Shear Zone, East Indian shield: Insight for polyphase boron infiltration during regional metamorphism. Am. Mineral. 96, 752–767. https://doi.org/10.2138/am.2011.3560

Simmons, M.C., Karlstrom, K.E., Williams, M.W., Larson, T.E., Koning, D.J., Kelley, S.A., Lueth, V.W., Aby, S.B., 2011. Quartz-kyanite pods in the Tusas Mountains, northern New Mexico: A sheared and metamorphosed fossil hydrothermal system in the Vadito Group metarhyolite. Geol. Tusas Mt. Ojo Caliente New Mex. Geol. Soc. Guideb. 62, 359–378.

Talukdar, M., Sanyal, S., Sengupta, P., 2017. Metasomatic alteration of chromite from parts of the late Archaean Sittampundi Layered Magmatic Complex (SLC), Tamil Nadu, India. Ore Geol. Rev. 90, 148–165.

Voicu, G., Bardoux, M., 2002. Geochemical behavior under tropical weathering of the Barama–Mazaruni greenstone belt at Omai gold mine, Guiana Shield. Appl.

Geochemistry 17, 321–336.

Widmer, T., Thompson, A.B., 2001. Local origin of high pressure vein material in eclogite facies rocks of the Zermatt-Saas Zone, Switzerland. Am. J. Sci. 301, 627–656.

Zhang, R.Y., Liou, J.G., Shu, J.F., 2002. Hydroxyl-rich topaz in high-pressure and ultrahigh-pressure kyanite quartzites, with retrograde woodhouseite, from the Sulu terrane, Eastern China. Am. Mineral. 87, 445–453. https://doi.org/10.2138/am-2002-0408

CHAPTER 2

General geology

The Eastern Indian Shield preserves an almost uninterrupted record of a complicated geological and tectonic history of geological events spanning from Early Archean to Late Proterozoic. Being one of the oldest cratonic blocks in India, the Singhbhum Craton forms a N-S extending ovoid block encompassing an area of ~39,000 sq km (Mukhopadhyay and Matin, 2020). Conventionally the extension Singhbhum Craton (SC) is bounded by Chhotanagpur Gneissic Complex (CGGC) in the north, Eastern Ghat granulite belt in the south, Mahanadi graben in the west and upto the last exposure of Precambrian rocks in the east (Fig. 2.1). Chatterjee et al. (2010) proposed that a N to NNE trending sinistral deformation zone, known as the Eastern Indian Tectonic Zone (EITZ), bounds the eastern fringe of the Singhbhum Craton. The EITZ defines the eastern boundary of the SC, the NSFB and the CGGC. The Rengali Province (RP) intervening between Eastern Ghats granulites and the SC, is thrusted over the latter (Bose et al., 2015) (Fig. 2.1). The granulite facies lenses found in the gneisses of the RP represent thrusted slices of deeper crustal parts of SC (Bose et al. 2015; Mahapatro et al. 2012). The cratonic nuclei over which the strata of Singhbhum cover sequence was deposited is primarily composed of Paleoarchean Singhbhum suite of granitoids and the Iron Ore Group greenstone belts. The Singhbhum Suite (also known as the Singhbhum Granite or SBG) is a polyphase granitoid complex that forms the felsic core of the craton (3.36-3.24 Ga) (Dey, et al. 2019, Nelson et al. 2014, Upadhyay et al. 2014, Chaudhuri et al. 2018, Upadhyay et al. 2019, Dey et al. 2017, Mitra et al. 2019) (Fig. 2.1). Around this felsic core lies the deformed and low-grade volcano-sedimentary sequences of Iron Ore Group (IOG) (Fig. 2.1). The craton also hosts older granitoids and supracrustals namely the Champua Suite (also known as Older metamorphic tonalitic gneisses or OMTG) and the Older Metamorphic Group (OMG). The Precambrian crust of eastern India grew by

accretion of younger (Proterozoic Supracrustals) terraines around this nucleus (Archean nucleus of the Singhbhum Craton). Other granitoids like the Bonai Granite, Mayurbhanj granite, Kaptipada (Nilgiri) granite, Chakradharpur granite and Kuilapal granite and belts of younger supracrustal rocks are also considered part of the SC. The Palaeo- to Meso Proterozoic (ca.1.5-1.8 Ga) poly-deformed and poly-metamorphosed volcano sedimentary pile (reviewed by Sengupta et al., 2000; Vapnik et al., 2007) known as the North Singhbhum Fold Belt (NSFB) is sandwiched between the Mesoarchean (ca. 3.4 – 3.0 Ga, Sharma et al., 1994) cratonic batholith of 'Singhbhum Granite' towards the south and the Meso-Neo Proterozoic Chotanagpur Granite Gneissic Complex (CGGC) in the north (Mukhopadhyay et al., 1990; Saha, 1994; Gupta and Basu, 2000; Sarkar, 2000) (Fig. 2.1). The northern margin of the Singhbhum craton with North Singhbhum Fold Belt is marked by a prominent ductile shear zone, known as Copper Belt Thrust (Dunn and Dey, 1942) or Singhbhum Shear Zone (SSZ) (Sarkar and Saha, 1962) (Fig. 2.1).

The main litho-stratigraphical provinces that are present in the Eastern Indian Craton are

1. The Singhbhum Craton: An Archean Cratonic block comprising of the Singhbhum Suite with enclaves of OMG and Champua Gneiss (or OMTG)
2. The volcano-sedimentary sequences of IOG occurring along the eastern, western and southern peripheries of the cratonic nucleus
3. The North Singhbhum Fold Belt (NSFB) comprising of the Singhbhum Group, Dhajori Group, Dalma, Ongarbira Group and their equivalents
4. The CGGC with metasedimentary, meta-ultramafic enclaves and granulite components

The stratigraphical succession is based on field relations and tectono-metamorphic status of different rock units is given below:

Table 2.1: Precambrian stratigraphic units of the Singhbhum Craton (after Saha 1994)

Group/Formation	Lithology	Age
South Purulia Shear Zone		0.97 Ga[21]
Kolhan group	Conglomerate, sandstone, shale and limestone	1.16-1.0 Ga[20]
Metamorphism and deformation along SSZ and NSMB		*1.6-1.0 Ga*[19]
Singhbhum Shear Zone		2.0-1.6 Ga[18]
Newer Dolerite dyke swarm	Dolerite	2.76 - <1.76 Ga[17]
Mobile belt rocks		
Chandil Formation	Mica schist, carbon-phyllite, quartzite, mafic-volcanic, acid volcanic and volcani-clastic rocks	c. 1.6 Ga[16]
Dalma Formation	Mafics, ultramafics, agglomerate	c. 1.7-1.6 Ga[16]
Singhbhum Group		c. 2.4-2.3 Ga, >2.2-1.7 Ga[15]
Jagannathpur/Malangtoli/Dhanjori/ Simlipal Group		c. 2.8, 2.7-2.1 Ga[14]
Pallahara gneiss	Granodiorite to granite	2.7-2.8 Ga[13]
Metamorphism of SBG, OMG and OMTG		3.02-2.96, 2.52, 1.06 Ga[12]
Mayurbhanj granite	Granite	3.09-3.08 Ga[11]
Singhbhum granite (SBG-B) Phase III	Granodiorite to granite	c. 3.12 Ga[10]
Metamorphism of Bonai granite, SBG-A, OMG and OMTG		3.19-3.03 Ga[9]
IOG (W)	BIF, chert, breccias, metabasalt, shale, phyllites	c. 3.39, 3.33, 3.05 Ga[8]
Metamorphism of SBG-A, OMG and OMTG		3.24Ga[7]
Bonai granite	Granite, granodiorite	3.37 Ga[6]
Singhbhum Granite(SBG-A) Phase I & II	Granite / Granitic Gneiss	c. 3.44 Ga, 3.35Ga[5]
IOG (IOG-S and E)	BIF, chert, phyllite, tuff, mafic-ultramafic volcanic and plutonic rocks	c. 3.51 -3.1 Ga[4]
Metamorphism of OMG and OMTG		3.40 Ga[3]
Older Metamorphic Group (OMG)	Pelitic Schist, quartzite, para and ortho amphibolite	c. 3.55 Ga, 3.37 Ga[2]
Older Metamorphic Tonalite Gneiss (OMTG)	Tonalite Gneiss, granodiorite	c. 4.24 - 3.5 Ga[1]

[1]Chaudhuri et al. 2018, Upadhyay et al. 2014, Acharyya et al. 2010 [2,3,7,11]Mishra et al. 1999 [4]Jodder et al. 2021, Mukhopadhyay et al. 2008, Auge et al. 2003 [5,9,12]Upadhyay et al. 2014 [6,9]Chakraborty et al. 2019 [8]Adhikari and Vadlamani 2022, Basu et al. 2008 [10]Ghosh et al. 1996 [13]Topno et al. 2018 [14]Adhikari et al. 2021, Misra and Johnson 2005, Roy et al. 2002 [15]Sarkar et al. 1986 [15,16]Reddy et al. 2009 [17]Kumar et al.2017, Shankar et al. 2014 [18]Pal and Rhede 2013 [19]Pal et al.2021 [20]Mukhopadhyay et al. 2021 [21]Dwivedi et al. 2011

1. Singhbhum Craton:

The Singhbhum cratonic nucleus is a N-S extending ovoid body (~150x50 km) comprising of Singhbhum Suite of granitoids including Singhbhum Granite phase I,II and III and enclaves of OMG, trondhjemite grading into tonalities (Champua Gneiss) and other unclassified bodies comparable to components of typical Archean greenstones. The Singhbhum Suite or the SBG makes up to one-third of the SC ranging in composition from tonalite to granite and emplaced in several pulses which have now been categorized into three main phases.

The Champua Suite (or OMTG) occurring as enclaves within the Singhbhum Suite granitoids represent the oldest felsic magmatism in the craton (Table 2.1). They are exposed near Champua (type area), Seraikela, Onlajori, Bahalda, Rairangpur and Thakurmunda. They are composed of high-grade (amphibolite facies to migmatised at places), polydeformed felsic orthogneisses which were emplaced during 3.53-3.36 Ga (Olierook, et al. 2019, Dey et al. 2019). Studies show that they were derived from juvenile, mafic source rocks, with minor contribution from pre-existing, mafic dominated crust (Chaudhuri et al. 2018, Dey et al. 2017, Mitra et al. 2019, Bauer et al 2020, Ranjan et al. 2020). Some older crust, comprising of felsic rocks, also contributed to the formation of this suite as confirmed by Hadean to Eoarchean xenocrystic zircons (~3.7 Ga) reported from granitoids of this suite (Chaudhuri et al. 2018). The zircon grains in Champua Suite show negative $\varepsilon_{Hf(t)}$ values of -4.7±1.4 to -6.6±1.1 (for Eoarchean samples) and -0.4±1.2 to -3.7±1.8 (Paleoarchean samples) (Chaudhuri et al. 2018). A model of tonalite derivation by fluid absent partial melting of lower crustal with retained restitic feldspar after melt extraction was proposed by Nelson et al. (2014). The OMG is composed of mica schists, micaceous quartzites and banded amphibolites which lie as inliers and enclaves in younger plutons of the Singhbhum Suite (Hofmann and Mazumder

2015). Often they are also associated with ortho-amphibolites indicating igneous parentage. Earlier views that OMTG intruded the OMG (Saha et al. 1988) were discarded by later workers as unambiguous evidences of intrusive relationship are lacking (Prabhakar and Bhattacharya 2013). The age of formation of this igneous-supracrustal package is pinned at 3.37 Ga indicating they are younger than the Champua Suite (Nelson et al 2014) (Table 2.1). Hence the OMG is predicted to a remnant of the IOG, a part or equivalent to 3.53-3.29 Ga, due to its age and association with mafic igneous rocks (Hofmann and Mazumder 2015). However the Champua Suite and OMG show coeval deformation and metamorphism at 3.32-3.28 Ga (Nelson et al. 2014, Upadhyay et al. 2014, Prabhakar and Bhattacharya 2019).

The Singhbhum Suite (or SBG) comprises of granitoids ranging in composition from tonalite to granite emplaced in different pulses. Twelve separate bodies identified by their structural and intrusive relationships (Saha, 1972, 1994; Saha and Ray, 1984) were grouped into three phases that were emplaced successively. Phase I being the earliest phase to be emplaced is K-poor, granodiorite to trondhjemite in composition. Phase II and II were emplaced successively and are granodiorite to monzogranite or granite in composition (Saha 1994) (Table 2.1). There are overlapping compositions of SBG and OMTG but the latter are exclusively TTGs while the SBGs are granite, monzogranite, granodiorite and trondhjemite. The magma temperature (minimum) obtained from zircon saturation temperature for porphyritic granite of Phase II pluton is 800°±30°C while for non-porphyritic granite of the Phase III pluton it was 754°±13°C (Pandey et al. 2019). Mostly the pluton preserves low temperature deformation signatures implying rocks cooled before deformation except along western margin of the pluton where high temperature deformation textures are present. Between 3.34-3.62 Ga a high grade metamorphic event is recorded which are coeval with magmatic episodes of SBG and

OMTG. Younger metamorphic resettings are recorded in OMTG and SBG at 3.16-3.11 Ga and 3.0-2.8 Ga. Geochronological data from various parts of SC show that there is no systematic age difference between the OMTG and phases of SBG (Table 2.1). There are different pulses of granitic magma and xenocrysts from older pulses are found in younger ones. As compiled from several studies, the total period of granitic intrusion lasted from 3.52 to 3.28 Ga (Mukhopadhyay and Matin 2020). Younger ages have been recorded in granites from OMTG but they are often not considered part of OMTG by several workers. The mean $\varepsilon_{Hf(t)}$ values for 3.47, 3.35 and 3.30 Ga granitoids from SBG are +2.1±2.8 to +4.8±2.8, +1.8±3.0 to +4.0±3.6, and +0.8±2.8 to +3.7±2.8 respectively (Dey et al. 2017). These values suggest derivation of SBG from melting of mainly tonalite rich source and minor mafic source. Pandey et al. (2019) have observed lower mean $\varepsilon_{Hf(t)}$ values for SBG which suggest a primitive mantle source. Recent studies through time integrated petrogenetic modelling show that the SC became subaerial at ~3.3 to 3.2 Ga due to progressive crustal maturation and thickening of crust by voluminous granitoid magmatism within a plateau-like setting (Chowdhury et al. 2021).

2. Iron Ore Group (IOG)

The felsic core of the SBG is surrounded by the low-grade (greenschist facies) deformed volcano-sedimentary supracrustals of the Iron Ore Group (IOG) which occur as basins at the boundary of the SBG batholith or as keels inside it. They are comprised of volcanics like basalts with minor komatiites and felsic volcanics and sedimentary rocks viz. conglomerates, sandstones, shales, minor carbonates and thick deposits of banded iron formations (BIF) (Olierook et al.2019, Mazumder et al. 2012, Mukhopadhyay et al. 2012, Mazumder et al. 2019, Ghosh and Baidya 2017). These rocks are exposed in three discrete belts occurring as synformal keels—the Gorumahisani-Badampaharbelt to the east, Tomka-Daitari belt to the south, and the Jamda-Koira belt to the west which are also

known as Eastern(E)-IOG, the Southern (S)-IOG, and the western(W)-IOG. The eastern-IOG belt comprises of chert, BIF and phyllites overlying mafic-ultramafic and acid-intermediate volcanic units (Mukhopadhyay et al. 2008a,b). From base to top the western-IOG comprises successively of metabasalt, chert breccias, phyllitic ferruginous shale-carbonates-manganiferous units, BIF and upper phyllitic shale. BIF of the eastern-IOG are richer in magnetite compared to southern or western IOG and the eastern IOG also contain komatiites (Sahu and Mukherjee 2001, Bose 2009). Many workers opine that southern, eastern and western IOGs are of different ages and have noted some differences in their mineralogy, geochemistry and lithological associations (Acharya 1984, Saha 1994, Mukhopadhyay 2001, Bose 2009). Sea-floor hydrothermal leaching and exhalation supplied the iron for the ore deposits (Klein 2005, Nadoll, et al. 2014) while microbial activity caused the oxidation and precipitation of these deposits (Beukes 2004, Kappler et al. 2005, Bekker 2010).

Some enclaves of IOG (BIF, chert and associated mafic rocks in SBG) have evidence of older age than SBG (Saha 1994, Sengupta et al., 1996, Jena and Behera 2000) (Table 2.1). Phase III of SBG is younger than IOG rocks as suggested by its intrusive relationship but phases I and II of the SBG are older. Granite intruding the IOG has been dated to ~3.38 Ga (Nelson et al., 2014). The zircon dates obtained from felsic tuffs below BIF layers of western IOG (~3.39 Ga) and from granitoids that intruded southern IOG suggest an age of formation between 3.51 to 3.29 Ga (Basu et al. 2008, Mukhopadhyay et al. 2008c, 2012, Olierook et al.2019, Dey et al. 2019, Nelson et al. 2014, Mazumder et al. 2019, Sreenivas et al. 2019).

3. North Singhbhum Fold Belt (NSFB):

The NSFB occupies the region between the SC and associated rocks in the south and the CGGC in the north. It is about 50 km wide and 200 km long and has an average

E-W trend with a convexity towards north. It co-extends with CGGC in the east and terminates at the western margin of Dalma suite of rocks which forms the spine of the belt (Sarkar et al. 1992, Saha, 1994, Gupta and Basu 2000) (Fig. 2.2). The Palaeoproterozoic succession of Singhbhum supracrustal rocks (i.e. the Dhanjori, Chaibasa, Dhalbhum and Dalma formations) with a deformation distinctly different from the Archean nucleus and metamorphosed upto greenschist-amphibolite grade constitutes the North Singhbhum Fold Belt (Gupta and Basu 2000; Dasgupta 2004, Sengupta and Chattopadhyay 2004) (Fig. 2.2, Table 2.1, 2.2). It comprises of thick volcano-sedimentary sequences of pelites, psammopelites, mafic-ultramafic and acid lavas which can be delineated into five broad lithostraigraphic domains (Sarkar et al. 1992, Gupta and Basu 2000, Sengupta & Chattopadhyay 2004, Sarkar and Gupta, 2012).

Table 2.1: Lithology and ages of formations of the North Singhbhum Fold Belt (NSFB)

Unit	Lithology	Metamorphism	Age	Refernce
Chandil formation	Rhyolite, tuff, agglomerates, shale, carb shale	Greenschist (Phyllite)	Thermal event: 1.5 Ga	Sengupta et al. 2000
			Rhyolite emplacement: ~1.63 Ga	Reddy et al. 2009
Dalma formation	Basic lava and volcaniclastic sediments of continental affinity	Greenschist	Metamorphism (?): 1.6 Ga	Roy et al. 2002b
Dhalbhum formation	Sandstone, siltstone, orthoquartzite, shale, tuff of continental affinity	Greenschist	Unknown	
SSZ melange	Chlorite, quartz schist, talc/actinolite schist, magnetite-apatite rock, Cu-U ores, tourmalinite, kyanite-bearing quartzite, chloritoid schist,	Greenschist to amphibolite	Shearing and hydrothermal alteration: 1.66 - 1.60 Ga and ~1.0 Ga	Rao and Rao 1983, Pal and Rhede 2013
	Soda granite		Protolith formation: ~1.9 -1.8 Ga Emplacement of granitoid: 2.2 Ga	Pal and Rhede 2013 Sarkar et al. 1985
Chaibasa formation	Shake, sandstone and orthoquartzite with minor basic to ultrabasic rocks	Greenschist to amphibolite	Metamorphism: ~1.6 - 1.3 Ga	Mahato et al. 2008
Lower and Upper Dhanjori formation	Basic and dacitic lava, quartzite, shale and basal conglomerate		Lava flow: ~2.1 Ga	Roy et al. 2002a
Archean basement	Metasedimentary rocks, tonalite, trondjhemite and granitoid intrusions		~2.8 - >3.5 Ga	Mazumder et al. 2012 (review)

Domain I: The oldest Proterozoic cover sediments of the NSFB i.e. the metasedimentary belt and intracratonic sub-basins containing volcanosedimentary suites of Dhanjori - Simlipal and Ongarbira in the eastern and western parts of NSFB, fall in this domain. Dhanjori Group comprises of volcanic, volcaniclastic and siliciclastuc sediments unconformably overlying the granitoids of SBG. Polymictic conglomerate-arkose-wacke in contact with the basement are overlain by grey and purple low-grade metapelites, banded magnetite quartzite, variable contents of tuffaceous rocks and mafic-ultramafic intrusives. The most prominent basal conglomerate horizon is developed near Bisrampur and Jaikan which are described as submarine debris flow deposited at the base of a rifted basin (Bose and Ghosh 1996). Simlipal volcanics in the eastern part of the SC is considered time equivalent of Dhanjori volcanics. Dhanjori Group is divided into two formations viz. the Upper and Lower Dhanjori formations (Gupta et al. 1985, Sarkar et al. 1992, Mazumder and Sarkar 2004, De et al. 2015). The Lower Dhanjori formation is composed of phyllite, gritty and pebbly shale with quartzite, arkose, grit and conglomerate along with mafic-ultramafic intrusives. Acid volcanics and quartz-pebble conglomerates of Lower Dhanjori have reported incidences of uranium and gold (Gupta and Basu 2000). The Upper Dhanjori sequence is volcanic in character and comprises of high-Mg volcaniclastics, alkali olivine basalt, basaltic and peridotitic komatiite and low-K tholeiites. The volcano-sedimentary succession of Dhanjori Group was deposited under terrestrial environment in an intracontinental rift basin (Mazumder and Sarkar 2004). Sm-Nd isotopic data indicates poorly mixed provenance of felsc and mafic rocks (De et al. 2015). The Upper Dhanjori mafic-ultramafic rocks show LREE enrichment and low HREE fractionation (Roy et al. 2002b, Mazumder and Arima 2009). Trace and REE data also suggest an enriched mantle plume as source for the Dhanjori Volcanics (Roy et al. 2002b). Two Sm-Nd isochron ages have been determined i) ~2.07 Ga (Roy et al. 2002b)

ii) ~2.78 Ga (Misra and Johnson 2005) but they isotopic signatures seem to have been disturbed by Proterozoic tectonics. Basal part of the Dhanjori Group intruded by Mayurbhanj Granite has given age of ~3.1 Ga which determines that the lowermost deposits of Dhanjori Group is atleast >3.1 Ga (Table 2.2, 2.3).

Domain II: The arcuate, narrow zone running along the northern boundary of the SC and Domain I for ~120km is known as the Singhbhum Shear Zone (SSZ) and comprises Domain II. It is a high strain zone characterized by multiphase deformation, intense ductile shearing, sodic magmatism, multiple metasomatic features and polymetallic mineralization. It has been discussed in detail later in this chapter.

Domain III: The metasedimentary belt lying north of the SSZ and south of the Dalma volcanics, essentially comprising of thick metapelitic sequences with numerous bands of amphibolite, hornblende schists and quartzite comprises Domain III. The belt comprises the schistose high grade metamorphic (upper greenschist amphibolite facies) sequences of Chaibasa and Dhalbhum formations. The Chaibasa Formation is a marine sequence comprising of sandstones and shales formed in subtidal and shelf setting relatively (Bhattacharya 1991; Bose et al. 1997; Bhattacharya and Bandyopadhyay 1998, Mazumder 2005; Mazumder et al. 2009). The Chaibasa rocks are metamorphosed to garnetiferous muscovite-quartz schists. Chloritoid, biotite, garnet, kyanite, staurolite and sillimanite occur progressively depicting a Barrovian type metamorphism (Naha 1965, Lal and Singh 1978). The SSZ has affected both the Dhanjori and Chaibasa formations (Sengupta & Mukhopadhyay 2000; Sengupta & Chattopadhyay 2004). Kyanite-quartzites also occur as thin units towards southern part of this domain. Rhythmic layers of ultrafine massive kyanite, alternating with tourmaline, occur within mica schist with local pockets of post-tectonic kyanite. The Chaibasa formation has been dated to be of Palaeoproterozoic age ~2.2 Ga (Acharya et al. 2010b) (Table 2.2, 2.3). The Dhalbhum

formation comprises of ferruginous chloritic schists and phyllites, sericite phyllite, minor carbon phyllites, hematite phyllites and quartzite. The phyllites contain large porphyroblasts of andalusite and staurolite. The Dhalbhum Formation consists of terrestrial deposits and unconformably overlies the Chaibasa (Posamantier & Vail 1988, Mazumder et al. 2012).

Domain IV: The Dalma volcano-sedimentary belt, of lowly metamorphosed predominantly basic and ultrabasic volcanics covering the Dalma Range and its extensions to the east and west comprises this domain (Chakraborti and Bose 1985, Bose 1994, Gupta & Basu 2000, Mazumder 2005). It is an arcuate ridge occurring almost along the middle of the North Singhbhum Fold Belt. This arcuate ridge is composed of a greenstone assemblage, which consists of shale/ phyllite, carbonaceous phyllite/ tuff with interlayered basic volcanics. These are overlain by high-Mg volcaniclastics, co-magmatic flows of komatiitic composition and pillowed low-K tholeiites (Gupta and Basu 1991, Gupta et al. 1982). The agglomerates contain basaltic fragments and are interlayered with basalts (Gupta et al. 1980). The models for Dalma volcanism are varied but the latest ones propose a plume model (Roy et al. 2002a, Mazumder 2005). U-Pb zircon age of Dalma volcanics have been pinned at 1750-1600 Ma by Reddy et al. (2009).

Domain V: This domain comprises of pelitic and tuffaceous metasediments bound by Dalma Belt in the south and CGGC in the north. It contains abundant chert and black shale-chert rhythmites, larger mafic-ultramafic bodies, acid volcanics and syenitic rocks which makes it lithologically different from the rocks of domain III (Bose 1994, Ray et al. 1996, Mazumder 2005). The northern contact with CGGC is characterised by prominent phosphorite-bearing carbonatite body and some sporadic sulphide occurences. This metamorphosed volcano-sedimentary succession is known as the Chandil Formation (Ray et al., 1996; Mazumder, 2005). West of Chandil the pelites comprise of tuffaceous

material and sediements are least metamorphosed while in the eastern parts the same belt has garnet and staurolite bearing mica schists. In the eastern and central parts of the belt, the grade of metamorphism increases from low greenschist to greenschist-amphibolite transition towards the north. Rhyolite from this domain has been dated by Nelson et al. (2007) to be of 1631±6 Ma age (zircon/Pb-Pb SHRIMP) (Table 2.2, 2.3).

The stabilization of the Singhbhum craton had occurred around 3.1 – 3.0 Ga which facilitated the deposition of Keonjhar and Mahagiri quartzites. Mayurbhanj Granite, Temperkola Granite and Pallahara Gneiss were the last major granite magmatisms (~3.1 - 2.8 Ga) in the craton (Table 2.2). The deposition in the NSFB likely took place in an intracontinental rift in a rapidly changing tectonic environment (Mazumder and Sarkar, 2004; Mazumder, 2005). The Newer Dolerite dyke swarms mark the end of Archean tensional regime in the craton (~2.76 to <1.77 Ga) which may be related to pre-orogenic basin development of NSFB (Mukhopadhyay and Matin 2019). The Dhanjori Group was deposited in an alluvial to fluavial and partly lacustrine environment (Mazumder and Sarkar, 2004). The Dhanjori Group is conformably overlain by Chaibasa formation of the Singhbhum Group (Mazumder, 2004, 2005; De et al 2015, 2016). A major marine transgression took place marking the major period of sedimentation and basin development in the NSFB. The Singhbhum Group is inferred to have been deposited in a shallow to deep marine environment (Chaibasa formation) with later transition to mostly terrestrial (fluvial-aeolian) or shallow marine environment (Dhalbhum formation). This was followed by Dalma volcanism which took place under terrestrial conditions (largely subaerial) and some subaqueous eruption indicated by pillowed basalt, which constitute a minor (basal) component (Mazumder and Van Loon, 2012). The felsic volcanism of Chandil formation took place in terrestrial (fluvial-aeolian) setting while the fine grained sandstones occurring at top of the Chandil succession are of

shallow marine origin(Chatterjee et al. 2013). The SSZ cuts across rocks of IOG, Dhanjori and the Singhbhum Group. Three phases of deformation are imprinted on the NSFB rocks. Detailed studies by Ghosh and Sengupta (1987), Mukhopadhyay and Deb (1995) and Bandyopadhyay (2003) have shown that regional schistosity in the NSFB is a second generation deformation fabric and peaks of metamorphism outlasted the first and second deformation episodes.

***Singhbhum Shear Zone*:**

The Singhbhum Shear Zone (SSZ) comprises of an amalgamation of metasedimentary, metabasic, metaultramafic rocks belonging to Singhbhum Group (Chaibasa Formation), Dhanjori Group and granitic rocks which separates the SC in the south from the NSFB in the north. The E–W (in the west) to NNW–SSE (in the east) trending, arc shaped, ~200-km-long and 1-5 km wide intensely polydeformed Singhbhum Shear Zone (SSZ) occurs in between Singhbhum craton in south and NSFB in north (Fig. 2.1, reviewed in Dunn and Dey 1942; Mahato et al. 2008; Pal et al. 2010; Sengupta et al. 2011; Sarkar and Gupta 2012). The detailed geology of the Archaean Singhbhum nucleus and the fringing NSFB is discussed earlier. The typical rocks in the SSZ are kyanite-quartzite, apatite-magnetite rock, kyanite-mica schist, quartz-chlorite schist, amphibole-chlorite schist, quartz–sericite schist, talc schist, biotite-muscovite schist, conglomerate, tourmalinite, soda granite/feldspathic schist and mylonitized granite, all of which are highly deformed (Sarkar 1984; Saha 1994; Mukhopadhyay and Deb 1995). The Singhbhum brittle-ductile shear zone (SSZ), cuts across rocks of Iron Ore Group, Dhanjori Group and the Singhbhum Group (Fig. 2.1).

The SSZ is north to north-easterly dipping shear zone with southerly thrust movement (Ghosh and Sengupta 1987). East-west trending regional folds with strong axial planar fabric (second generation) dominate the region (Sengupta and Chattopadhyay

2004). Along the Singhbhum Shear Zone (SSZ), extensive occurrences of mylonites and phyllonites which are developed close to the contact between the fold belt and the Archaean nucleus (Sarkar and Saha 1977). The mylonitic foliation shows down-dip stretching lineation. The asymmetrical folds and other shear-sense criteria, like mica fish, asymmetric tails of pressure shadows, and shear bands, indicate thrust-type movement (Ghosh and Sengupta 1987; Mukhopadhyay and Deb 1995). All shear sense indicators demonstrate an upwards movement of the northern rocks relative to south (Sengupta and Chattopadhyay 2004).

The shear zone rocks underwent two different phases of metamorphism (Sarkar 1984; Sengupta et al. 2005). In SSZ there is evidence of K, Na, and B-metasomatism (Dunn and Dey, 1942; Banerji and Talapatra 1966; Talapatra, 1968; Ghosh, 1972; Banerjee, 1982; Sarkar, 1984, Bhattacharya et al., 1992; Sengupta et al., 2005, Pal et al., 2009) which formed different types of rocks like feldspathic schist/soda granite, biotite schist, chlorite schist and tourmalinite but origin of these hydrothermal deposits and the source of the hydrothermal deposits is still debatable. There are many theories like include magmatic fluid, evaporite-derived/basinal brine and seawater (Dunn and Dey, 1942; Sarkar, 1984; Mishra and Singh, 2003; Mishra et al., 2003) for the source of the fluids. The apatite-magnetite deposits in SSZ contain hydrothermal magnetite (Adak et al. 2021) which ascertains that the apatite was also deposit by hydrothermal fluids carrying iron and phosphate. Apatite-magnetite veins also occur intricately with secondary uraninite deposits with inclusions of uraninite in apatite grains (Rao and Rao 1983). Hydrothermal fluids have deposited Fe, Cu, U, P and REE minerals in SSZ through multiple events, overprinted former alterations of ore deposits and also redistributed them (Pal et al. 2011, Pal and Rhede 2013, Chowdhury and Lentz 2017, Chowdhury et al. 2020). Apatite deposits are also found in the NSFB (South Purulia Shear Zone) at Beldih-

Kutni where petrological evidences show that apatite was deposited during ongoing intense plastic and brittle shearing at epidote-amphibolite facies metamorphism. The host rocks were subjected to soda metasomatism followed by carbonatization (Vapnik et al. 2007). These phosphate deposits of hydrothermal origin were deposited by halite rich and CO_2 rich fluids (Vapnik et al. 2007).

The age of thrusting along the SSZ determined from Rb-Sr whole rock age is ~1.6 Ga (Sarkar et al. 1986) and continued upto ~1.5 Ga post consolidation of Dalma-Chandil volcano-sedimentary units (Sengupta and Mukhopadhyay 2000) (Table 2.3). The SSZ is also the locale of economic deposits of apatite-magnetite, Fe-Cu-P-U ores (Sarkar 1984, 2000). According to Rao and Rao 1983 hydrothermal alteration occurred 1.4 Ga (yielded date from soda granite). Sulfide and uraninite occurring in the SSZ yield dates of ~1.8 Ga (Johnson et al. 1993) and ~1.5–1.6 Ga (Rao et al. 1979), respectively.

Table 2.3: Geochronological information of tectonothermal events in NSMB

Age (Ga)	Mineral / Lithology	Dating method	Type of age	Event	Reference
0.970 ± 0.008	Mica schist (muscovite) of SSZ	$^{40}Ar/^{39}Ar$	Metamorphic	Final major reactivation along SSZ	Olierook et al. 2019
0.959 ± 0.083	Florencite from SSZ	U-Pb	Metasomatic	LREE metasomatism-III	Pal et al. 2021
0.955 ± 0.007	Monazite from SSZ	U-Pb		LREE metasomatism-III	
1.63 ± 0.011	Allanite from SSZ	U-Pb		LREE metasomatism-II	
1.80 ± 0.009	Monazite from SSZ	U-Pb		LREE metasomatism-I	
1.88 ± 0.014	Allanite from SSZ	U-Pb		LREE metasomatism-I	
1.64-1.59	Molybdenite from U-ores of SSZ	Re–Os	Mineralization age	Shear deformation of SSZ	Pal et al. 2022
~1.0	Uraninite from SSZ	U-Pb	Metasomatic	hydrothermal event	Pal and Rhede 2013, Pal et al. 2011a
~1.66	Uraninite from SSZ	U-Pb		HREE metasomatism	
1.80 to 1.90	Uraninite from SSZ	U-Pb		U mineralisation in SSZ	
c. 1.58	Uraninite from SSZ (Narwapahar)	$^{207}Pb/^{206}Pb$	Metasomatic	Primary uraninite mineralization	Krishna Rao et al. 1979
1.6 ± 0.008	Uraninite from SSZ	$^{207}Pb/^{206}Pb$		Uranium mineralization and metasomatic ore mineralization in SSZ	Vinogradov et al., 1964
~1.6	Soda granites, Arkasani granophyre	Rb–Sr	Magmatic	Age of metamorphism of the sediments and of thrusting along the SSZ	Krishna Rao et al.,1979; Sarkar et al., 1986; Sengupta and Mukhopadhaya,2000; Mazumder and Sarkar, 2004
1.62 ± 0.004	Rhyolite of Chandil formation	U–Pb SHRIMP	Magmatic	Crystallization of rhyolite	Reddy et al. 2009
1.67 ± 0.011		$^{207}Pb/^{206}Pb$ age	Magmatic		Sarkar et al. 1986
1.61 ± 0.038	Gabbro–pyroxenite intrusives of Dalma	Rb–Sr	Magmatic	Dalma volcanic rocks were metamorphosed and intruded by ultramafic-mafic rocks	Roy et al. 2002a, Acharyya, 2003
1.62 ± 0.006	Rhyolite of Lower Chandil Formation (Igneous zircon)	U–Pb SHRIMP	Magmatic	Crystallization of rhyolite	Olierook et al. 2019
1.63 ± 0.006	Rhyolite at contact of Chandil and Dalma (Igneous zircon)	U–Pb SHRIMP	Magmatic	Crystallization of rhyolite	Nelson et al., 2007;

Age (Ga)	Event	Dating method	Type of age	Event	Reference
1.63 ± 0.006	Rhyolite of basal Dalma volcanics (Igneous zircon)	U–Pb SHRIMP	Magmatic	Crystallization of rhyolite	Bhattacharya et al., 2015
≤1.76 ± 0.01	Volcaniclastic sandstone of Upper Dhalbhum Formation (Detrital Zircon)	U–Pb SHRIMP	Older thermal events	Provenance age	Olierook et al. 2019
1.86 ±0.006	Arkasani Granophyre	U–Pb SHRIMP	Magmatic	Marks closure of the Chaibasa and Dhanjori sub-basins	Bhattacharya et al. 2015
2.07 ± 0.10	Metavolcanics of Upper Dhanjori	WR Sm-Nd TIMS	Magmatic	Crystallization	Roy et al., 2002b
2.2	Chaibasa clastics	Nd model age		Average crustal residence times	De et al 2015
2.5	Dhanjori phyllite	Nd model ages		Average depositional age	Acharyya et al., 2010b
2.78±0.27	Metavolcanics of Lower Dhanjori	WR Sm-Nd		Age of separation of the mafic rocks from the mantle	Misra and Johnson, 2005
2.79±0.21	Metavolcanics of Lower Dhanjori	WR Pb-Pb		Age of separation of the mafic rocks from the mantle	
2.8 Ga	Temperkola Granite; Main phase of Mayurbhanj Granite	$^{207}Pb/^{206}Pb$	Magmatic	Thermal events	Bandyopadhyay et al. 2001
~3.04 to ~3.09	Basal conglomerate of Dhanjori (detrital Zircon)	U-Th-Pb	Chemical age	Mineralization	Sunilkumar et al., 1996
3.33 ± 0.58	Basal acid tuff of Dhanjori(Zircon)	U-Pb	Magmatic	Possibly inherited from ~3.3 Ga old SBG-A and OMTG rocks	Acharyya et al. 2010
3.36 ± 0.11	Basal acid tuff of Dhanjori (Zircon)	U–Pb			

4. Chotonagpur Granitic Gneissic Complex (CGGC):

The granite and granite gneiss with patches of high grade supracrustals commonly known as Chhotanagpur Granitic Gneissic Complex (CGC), lying to the north of the NSFB, is an east–west-trending sub-arcuate belt of the East Indian Shield that covers approximately 100,000 km^2 (c. 500 km long in the east–west direction and 200 km in width) across the states of Chhattisgarh, Jharkhand, Bihar and West Bengal (reviewed in Mahadevan, 1992; Acharyya 2003; Sharma 2009). An east–west- to ENE–WSW-trending crustal-scale brittle–ductile shear zone, known as the Tamar–Porapahar–Khatra Fault Zone (TPKF: Mahadevan, 2002), the Northern Shear Zone (NSZ: Kumar et al., 1978) or the South Purulia Shear Zone (SPSZ: Mazumdar, 1988) marks the southern margin of the CGGC. This shear/fault zone separates the CGGC from the Palaeo- to Mesoproterozoic North Singhbhum Fold Belt (NSFB). The Gangetic alluvium in the north and the Mesozoic Rajmahal trap basalt in the east covers parts of the CGGC. In the west the CGGC is covered by Gondwana deposits of the Son-Mahanadi Valley, and supracrustal rocks and granitoids of the Palaeoproterozoic Mahakoshal Group of the Central Indian Tectonic Zone (CITZ). CGGC represents granulite-gneiss terrain largely composed of granitic rocks with numerous enclaves of meta-pelites of varying composition and metamorphic grade, calc silicates, marble, quartzites, amphibolites, gabbro-norites, alkaline rocks, ultramafics, anorhosites, carnockite, pyroxene granulite and skarn rocks. The granitic rocks vary in composition from granite through grannodiorite to tonalite. The gneissic rocks vary widely from fine to coarse grained to porphyritic types and have a diverse chemical composition (Ghose, 1983; Ghose et al., 1990; Bhattacharyya and Chatterjee, 1990; Singh and De, 1990). A large part of the CGC is occupied by migmatites (Mazumder, 1988) and different variant of migmatites are present corresponding to the nature of parent rocks. CGC also contains enclaves and patches of

supracrustals like amphibolites, calcsilicate rock, quartzite and mica schist. Generally, these rocks show high amphibolite facies to granulite facies Metamorphism (Bhattacharya, 1976, 1982, Ghose, 1983). It is commonly believed that metamorphic grade decreases from north towards south in the CGGC (Banerji., 1991). Typical granulite facies rocks like khondalite, leptynite and charnockite along with porphyritic and augen type granites are found in the northern part of the CGC (Sen, 1947; Sen and Manna, 1976). A massif type anorthosite occurs within the granulite facies milieu near Bankura in the eastern part of the CGC, known as "Bengal Anorthosite" covering 250 km^2 in parts of Purulia and Bankura districts, West Bengal (Chatterjee, 1936; Roy, 1977). The stratigraphic status of the CGC is not yet clear due to lack of radiometric age data. Existing age data suggest geological evolution of CGC is spanning from 1700 to 800 Ma. From the latest geochronological and petrological published data to date indicates the presence of three major phases of deformation-metamorphism experienced by the CGGC, of which the first two are the most intense and penetrative and are also more or less coaxial (Chatterjee *et al.*, 2010; Ghosh and Sengupta, 1999; Maji *et al.*, 2008; Mukherjee *et al.*, 2017; Sanyal and Sengupta, 2012). Metapelitic enclaves within the granitiods record the oldest metamorphic event (ultra-high temperature metamorphism at moderate pressure) (Sanyal and Sengupta, 2012), yield an age of ~1650 Ma (Dey *et al.*, 2017). Intrusion of the porphyritic granite in the western and northern part of the terrane is constrained between 1750-1660 Ma (Chatterjee and Ghose, 2011; Saikia *et al.*, 2017). Emplacement age of the massif anorthosite in the south-eastern part gave an age of 1550±12(U-Pb zircon data). Intrusion of syenitic body in the eastern part of the terrane near Dumka yield an age of 1457±63 Ma (Rb- Sr isochorn) Ray Barman and Bishui, 1994). However much younger age 870-780 Ma was reported due to subsequent intrusion

of mafic dykes and followed by an amphibolite grade metamorphic event (Chatterjee *et al.*, 2010; Sanyal and Sengupta, 2012).

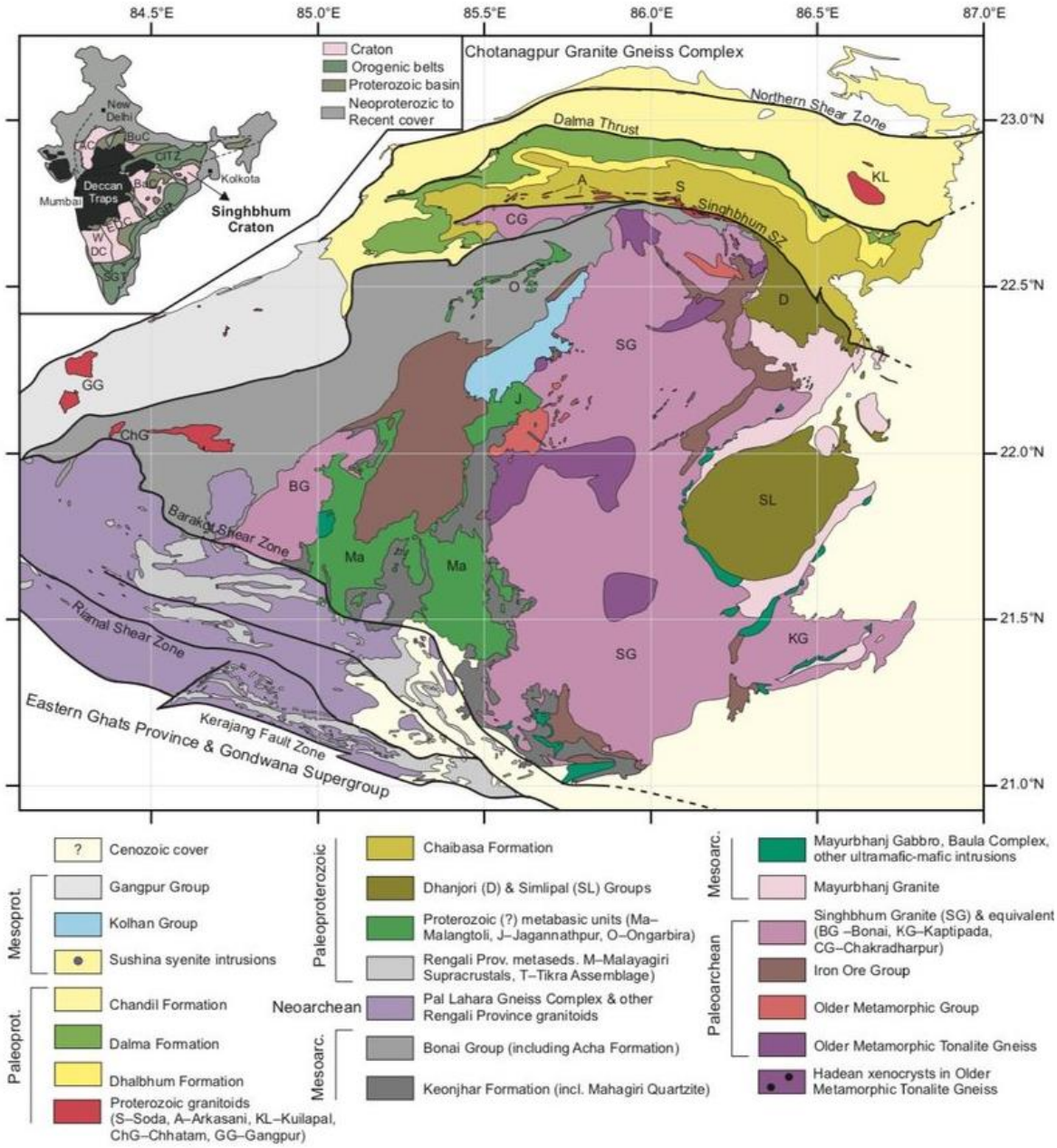

Fig 2.1: Generalised geological map of the Singhbhum craton and supracrustal provinces showing different tectonographic components (after Oleirook et al 2019; compiled from maps of Geological Survey of India, after Saha 1994, Sengupta et al. 1997, Mukhopadhyay 2001, Misra, 2006, Mukhopadhyay et al., 2014, Ghosh et al., 2015). Inset map shows generalized geology of the Indian shield with location of Singhbhum craton modified after Upadhyay et al 2014.

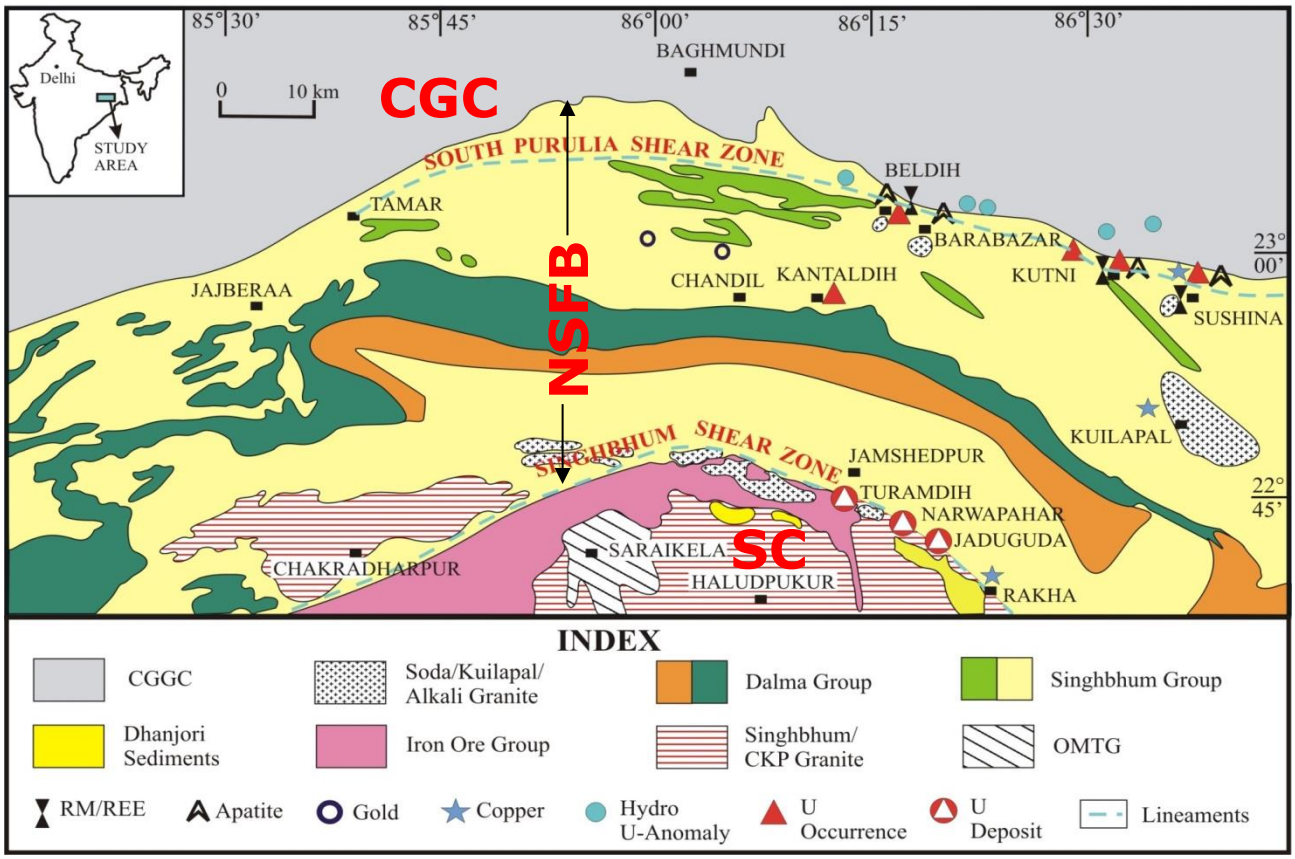

Fig 2.2: Geological map of the North Singhbhum Fold Belt (after Dunn and Dey, 1942 and Saha, 1994, Jena and Behera 2000, Sarkar and Gupta 2011)

References

Acharya, S., 1984. Stratigraphy and structural evolution of the rocks of the iron ore basin in Singhbhum–Orissa Iron Ore Province. In Proc. Sem. on Crustal evolution of the Indian shield and its bearing on metallogeny. Ind. J. Earth Sci., 19–28.

Acharyya, S.K., 2003. The nature of Mesoproterozoic Central Indian Tectonic Zone with exhumed and reworked older granulites. Gondwana Res. 6, 197–214.

Acharyya, S. K., Gupta, A., Orihashi, Y., 2010b. Neoarchaean–Palaeoproterozoic stratigraphy of the Dhanjori basin, Singhbhum Craton, Eastern India: and recording of a few U–Pb zircon dates from its basal part. J. of Asian Earth Sci., 39, 527–536. doi:10.1016/j.jseaes.2010.04.023.

Adak, S., Pal, D., Mondal, R., 2021. Geochemistry of magnetite in magnetite-apatite veins and magnetite-ilmenite pods in the Singhbhum Shear Zone, eastern India and it's implications in ore-forming processes, AGU Fall Meeting Abstracts, dec. 2021, V41B-07.

Bandyopadhyay, N., 2003. Metamorphic histoy of the rocks in the southern part of the Bailadila Range, district Bastar (MP). Unpub. PhD. Thesis, University of Calcutta, 256.

Bandyopadhyay, P.K., Chakrabarti, A.K., Deomurari, M.P., Misra, S., 2001. 2.8 Ga old anorogenic granite-acid volcanics association from western margin of the Singhbhum-Orissa Craton, eastern India. Gondwana Res. 4, 465–475.

Basu, A., Bandyopadhyay, P., Chakrabarti, R., Zou, H., 2008. Large 3.4 ga algoma-type BIF in the Eastern Indian Craton. Geochim. Cosmochim. Acta Suppl., 72, A59.

Bauer, A. M., 2020. Hafnium isotopes in zircons document the gradual onset of mobile-lid tectonics. Geochem. Perspect. Lett., 14, 1–6.

Bekker, A., Slack, J.F., Planavsky, N., Krapez, B., Hofmann, A., Konhauser, K.O., Rouxel, O.J., 2010. Iron formation: the sedimentary product of a complex interplay among mantle, tectonic, oceanic, and biospheric processes. Eco. Geol., 105, 467-508.

Beukes, N., 2004. Biogeochemistry: Early options in photosynthesis. Nature, 431, 522.

Bhattacharya, H. N. 1991. A reappraisal of the depositional environment of the Precambrian metasediments around Ghatshila-Galudih, eastern Singhbhum. J. of the Geol. Soc. of Ind., 37, 47–54.

Bhattacharya, H.N., Bandyopadhyay, S. 1998. Seismites in a Proterozoic tidal succession, Singhbhum, Bihar, India. Sedi. Geol., 119, 239–252.

Bhattacharya, H.N., Nelson, D.R., Thern, E.R., Altermann, W., 2015. Petrogenesis and geochronology of the Arkasani Granophyre and felsic Dalma volcanic rocks: implications for the evolution of the Proterozoic North Singhbhum Mobile Belt, east India. Geol. Mag. 152, 492–503.

Bose, M. K. 1994. Sedimentation pattern and tectonic evolution of the Proterozoic Singhbhum basin in the eastern Indian shield. Tectonophysics, 231, 325–346.

Bose, M.K., Ghosh, A., 1996. Redeposited conglomerate on an Archean basement: debris flow in Proterozoic Singhbhum basin, Eastern India, Ind. Min., 50(3), 123-138

Bose, M.K., 2009. Precambrian mafic magmatism in the Singhbhum craton, eastern India. J. of the Geol. Soc. of Ind., 73, 13-35.

Bose, P. K., Mazumder, R., Sarkar, S., 1997. Tidal sandwaves and related storm deposits in the transgressive Protoproterozoic Chaibasa Formation, India. Precamb. Res., 84, 63–81.

Bose, S., Guha, S., Ghosh, G., Das, K., Mukhopadhyay, J., 2015. Tectonic juxtaposition of crust and continental growth during orogenesis: example from the Rengali Province, eastern India. Geosci. Front., 6, 537–555.

Chakraborti, M. K. & Bose, M. K., 1985. Evaluation of the tectonic setting of Precambrian Dalma volcanic belt, eastern India using trace element data. Precamb. Res., 28, 253–268.

Chatterjee, N., Banerjee, M., Bhattacharya, A., Maji, A., 2010. Monazite chronology, metamorphism–anatexis and tectonic relevance of the mid-Neoproterozoic Eastern Indian Tectonic Zone. Precamb. Res., 179, 99-120.

Chatterjee, P., De, S., Ranaivoson, M., Mazumder, R., Arima, M., 2013. A review of the ~1600 Ma sedimentation, volcanism, and tectono-thermal events in the Singhbhum craton, Eastern India. Geosci. Front., 4 (3). https://doi.org/10.1016/j.gsf.2012.11.006

Chaudhuri, T., Wan, Y., Mazumder, R., Ma, M., Liu, D., 2018. Evidence of Enriched, Hadean Mantle Reservoir from 4.2-4.0 Ga zircon xenocrysts from Paleoarchean TTGs of the Singhbhum Craton, Eastern India. Scientific reports, 8, 7069. doi:10.1038/s41598-018-25494-6.

Chowdhury, S., Lentz, D.R., 2017. Minor- and trace-element characteristics of different pyrite types and their S-isotope geochemistry from the Proterozoic Rakha Copper deposit, Singhbhum Shear Zone, India. Neues Jahrbuch für Mineralogie - Abhandlungen 194, 251–277. https://doi.org/10.1127/njma/2017/0006.

Chowdhury, S., Pal, D.C., Papineau, D., Lentz, D.R., 2020. Major and trace element and multiple sulfur isotope composition of sulfides from the Paleoproterozoic Surda copper deposit, Singhbhum shear Zone, India: Implications for the mineralization processes. Ore Geol. Rev. 120, 103396 https://doi.org/10.1016/j.oregeorev.2020.103396.

Dasgupta, S. 2004. Modelling ancient orogens – an example from North Singhbhum Mobile Belt. In: Proceedings of the Workshop on (IGCP-453): Uniformitarianism Revised Edition on Orogens of India. Geol. Surv. of Ind., Spec. Publ., 84, 33–42.

De, S., Mazumder, R., Ohta, T., Hegner, E., Yamada, K., Bhattacharyya, T., Chiarenzelli, J., Altermann, W., Arima, M., 2015. Geochemical and Sm–Nd isotopic characteristics of the Late Archaean-Palaeoproterozoic Dhanjori and Chaibasa metasedimentary

rocks, Singhbhum craton, E. India: Implications for provenance, and contemporary basin tectonics. Precamb. Res., 256, 62-78.

Dey, S., Mitra, A., Nandy, J., Mondal, S., Topno, A., Liu, Y., Zong, K., 2019. "Early crustal evolution as recorded in the granitoids of the Singhbhum and Western Dharwar Cratons" in Earth's Oldest Rocks, M. J. Van Kranendonk, V. C. Bennett, J. E. Hoffmann, Eds. (Elsevier), 741–792.

Dey, S., Topno, A., Liu, Y., Zong, K., 2017. Generation and evolution of Palaeoarchaean continental crust in the central part of the Singhbhum craton, eastern India. Precamb. Res., 298, 268-291.

Dunn, J.A., Dey, A.K., 1942. The geology and petrology of eastern Singhbhum and surrounding areas. Memoir Geol. Surv. of Ind., 69, 281-450.

Ghosh, G., Ghosh, B., Mukhopadhyay, J., 2015. Chapter 9 Palaeoarchaean–Mesoproterozoic sedimentation and tectonics along the westnorthwestern margin of the Singhbhum Granite body, eastern India: a synthesis. Geol. Soc. Lond. 43 (1), 121–138.

Ghosh, S.K. & Sengupta, S., 1987. Progressive development of structures in a ductile shear zone. J. of Struc. Geol., 9, 277–287.

Gupta,A., Basu, A., 2000. North Singhbhum Proterozoic mobile belt Eastern India—a review. In: National Seminar Commemorating Dr M. S. Krishnan's Birth centenary (Proceedings Volume). Geol. Surv. of Ind., Spec. Publ., 55, 195–226.

Hofmann, A., Mazumder, R., 2015. A review of the current status of the Older Metamorphic Group and Older Metamorphic Tonalite Gneiss: insights into the Palaeoarchaean history of the Singhbhum craton, India. Memoirs of Geol. Soc., London, 43, 103-107.

Jena, B.K., Behera, U.K., 2000. The oldest supracrustal belt from Singhbhum craton and its possible correlation; Geol. Surv. of Ind. Spec. Publ., 57, 106-121.

Kappler, A., Pasquero, C., Konhauser, K.O., Newman, D.K., 2005. Deposition of banded iron formations by anoxygenic phototrophic Fe (II)-oxidizing bacteria. Geol., 33, 865-868.

Klein, C., 2005. Some Precambrian banded iron-formations (BIFs) from around the world: Their age, geologic setting, mineralogy, metamorphism, geochemistry, and origins. Am. Min., 90, 1473-1499.

Krishna Rao, N., Aggarwal, S. K., Rao, G. V. U., 1979. Lead Isotopic Ratios of Uraninites and the Age of Uranium Mineralization in Singhbhum Shear Zone, Bihar. Geol. Soc. Ind., [S.l.], 124-127.

Lal, R.K., Singh, J.B., 1978. Prograde polyphase regional metamorphism and metamorphic reactions in politic schists in Sini, district Singhbhum, India. Neues. Jahrb. Miner. Abh., 131, 304-333.

Mahapatro, S., Pant, N., Bhowmik, S., Tripathy, A., Nanda, J., 2012. Archaean granulite facies metamorphism at the Singhbhum Craton–Eastern Ghats Mobile Belt interface: implication for the Ur supercontinent assembly. Geol. J., 47, 312-333.

Mahato, S., Goon, S., Bhattacharya, A., Mishra, B., Bernhardt, H.J., 2008. Thermotectonic evolution of the North Singhbhum Mobile Belt (eastern India): A view from the western part of the belt. Precambr. Res. 162, 102–127. https://doi.org/10.1016/j.precamres.2007.07.015.

Mazumder, R. 2005. Proterozoic sedimentation and volcanism in the Singhbhum crustal province, India and their implications. Sedi. Geol., 176, 167–193.

Mazumder, R., Sarkar, S., 2004. Sedimentation history of the Palaeoproterozoic Dhanjori Formation, Singhbhum, eastern India. Precamb. Res., 130, 267-287.

Mazumder, R., Arima, M., 2009. Implication of mafic magmatism in an intracontinental rift setting: a case study from the Paleoproterozoic Dhanjori formation, Singhbhum crustal province, India. The J. of Geol., 117, 455-466.

Mazumder, R., Chaudhuri, T., Biswas, S., 2019. Palaeoarchaean sedimentation and magmatic processes in the eastern Iron Ore Group, eastern India: A commentary. Geol. J. 54,3078–3087.

Mazumder, R., Eriksson, P. G., De, S., Bumby, A. J. & Lenhardt, N. 2012. Palaeoproterozoic sedimentation on the Singhbhum Craton: global context and comparison with Kaapvaal. In: Mazumder, R. & Saha, D. (eds) Palaeoproterozoic of India. Geol. Soc., Lond., Spec. Publ., 365, 49–74, http://dx.doi.org/10.1144/SP365.4.

Mazumder, R., Rodriguez-Lopez, J. A., Arima, M. & van Loon, A. J. 2009. Palaeoproterozoic seismites (fine-grained facies of the Chaibasa Fm., E. India) and their soft-sediment deformation structures. In: Reddy, S. M., Mazumder, R., Evans, D. A. & Collins, A. S. (eds) Palaeoproterozoic Supercontinent and its Global Evolution. Geol. Soc., Lond., Spec. Publ. 323, 301–318.

Mazumder, R., Van Loon, A.J., Mallik, L., Reddy, S.M., Arima, M., Altermann, W., Eriksson, P.G. and De, S., 2012b. Mesoarchaean-Palaeoproterozoic Stratigraphic Record of the Singhbhum Crustal Province, Eastern India: a synthesis. In: Mazumder, R., Saha, D. (Eds.), Palaeoproterozoic of India. Geol. Soc., Lond., Spec. Publ. 365, 31–49, http://dx.doi.org/10.1144/SP365.3.

Misra, S., 2006. Precambrian chronostratigraphic growth of Singhbhum-Orissa craton, Eastern Indian shield: an alternative model. J. Geol. Soc. India 67 (3), 356.

Misra, S., Johnson, P.T., 2005. Geochronological constraints on evolution of Singhbhum mobile belt and associated basic volcanics of eastern Indian shield. Gond. Res., 8, 129-142.

Mitra, A., Dey, S., Zong, K., Liu, Y., Mitra, A., 2019. Building the core of a Paleoarchean continent: Evidence from granitoids of Singhbhum Craton, eastern India. Precamb. Res. 335, 105436.

Mukhopadhyay, D., Deb, G. K., 1995. Structural and textural development in Singhbhum shear zone, eastern India. Proc. of Ind. Aca. of Sci.(Earth and Planetary Scinces). 104, 385-405.

Mukhopadhyay, D., Matin, A., 2020. The architecture and evolution of the Singhbhum Craton, IUGS. 19-49, https://doi.org/10.18814/epiiugs/2020/020002

Mukhopadhyay, D., 2001. The Archaean nucleus of Singhbhum: the present state of knowledge. Gond. Res.. 4, 307-318.

Mukhopadhyay, D., Bhattacharya, T., Chakraborty, T., Dey, A.K., 1990. Structural pattern in the Precambrian rocks of Sonua- Lotapahar region, North Singhbhum, eastern India. Proc. of Ind. Aca. of Sci.- Ear. and Plan. Sci., 99, 249-268.

Mukhopadhyay, J., Beukes, N. J., Armstrong, R. A., Zimmermann, U., Ghosh, G. & Medda, R. A. 2008. Dating the oldest Greenstone in India: a 3.51 Ga precise U–Pb SHRIMP Zircon Age for Dacitic Lava of the Southern Iron Ore Group, Singhbhum Craton. J. of Geol., 116, 449–461.

Mukhopadhyay, J., Crowley, Q.G., Ghosh, S., Ghosh, G., Chakrabarti, K., Misra, B., Heron, K., Bose, S., 2014. Oxygenation of the Archean atmosphere: New paleosol constraints from eastern India. Geology 42 (10), 923–926.

Mukhopadhyay, J., Ghosh, G., Zimmermann, U., Guha, S., Mukherjee, T., 2012. A 3.51 Ga bimodal volcanics-BIF-ultramafic succession from Singhbhum Craton: implications for Palaeoarchaean geodynamic processes from the oldest greenstone succession of the Indian subcontinent. Geol. J., 47, 284-311.

Mukhopadhyay, J., Gutzmer, J., Beukes N. J., Hayashi, K..I., 2008b. Stratabound magnetite deposits from the eastern outcrop belt of the Archean Iron Ore Group, Singhbhum craton, India. App. Ear. Sci.(Trans. Inst. Min. Metall. B), 117, 175-186. doi 10.1179/174327508X387492.

Mukhopadhyay, J., Gutzmer, J., Beukes, N.J., Bhattacharya, H.N., 2008a. Geology and genesis of banded iron formation-hosted high-grade iron ore deposits of India. Soc. of Eco. Geol. Rev., 15, 291-316.

Nadoll, P., Angerer, T., Mauk, J.L., French, D., Walshe, J., 2014. The chemistry of hydrothermal magnetite: a review. Ore Geol. Rev., 61, 1-32.

Naha, K. 1965. Metamorphism in relation to stratigraphy, structure and movements in parts of east Singhbhum, Eastern India. Quarterly Journal of the Geological, Mineralogical, Metal. Soc. of Ind., 37, 41–88.

Nelson, D. R., Bhattacharya, H. N., Misra, S., Dasgupta, N. & Altermann, W. 2007. New SHRIMP U–Pb zircon dates from the Singhbhum craton, Jharkhand–Orissa region, India. Abstract. In: Banerjee, S. (ed.) International Conference on Precambrian Sedimentation & Tectonics & the Second GPSS Meeting. Indian Institute of Technology, Bombay.

Nelson, D. R., Bhattacharya, H., Thern, E. R., Altermann, W., 2014. Geochemical and ion-microprobe U–Pb zircon constraints on the Archaean evolution of Singhbhum Craton, eastern India. Precamb. Res., 255, 412-432.

Olierook, H. K. H., Clark, C., Reddy, S. M., Mazumder, R., Jourdan, F., Evans, N. J., 2019. Evolution of the Singhbhum Craton and supracrustal provinces from age, isotopic and chemical constraints. Ear. Sci. Rev., https://doi.org/10.1016/j.earscirev.2019.04.020.

Pal, D.C., Chaudhuri, T., McFarlane, C., Mukherjee, A., Sarangi, A.K., 2011a. Mineral chemistry and in situ dating of allanite, and geochemistry of its host rocks in the Bagjata uranium mine, Singhbhum shear zone, India-implications for the chemical evolution of REE mineralization and mobilization. Econ. Geol. 106, 1155–1171. https://doi.org/10.2113/econgeo.106.7.1155.

Pal, D., Selby, D., & Sarangi, A., 2022. Timing of shear deformation in the Singhbhum Shear Zone, India: Implications for shear zone-hosted polymetallic mineralization. Geol. Mag., 1-7. doi:10.1017/S0016756822001091

Pal, D.C., Rhede, D., 2013. Geochemistry and chemical dating of uraninite in the Jaduguda uranium deposit, Singhbhum shear zone, India-implications for uranium mineralization and geochemical evolution of uraninite. Econ. Geol. 108, 1499–1515. https://doi.org/10.2113/econgeo.108.6.1499.

Pal, D.C., Trumbull, R.B., Wiedenbeck, M., 2010. Chemical and boron isotope compositions of tourmaline from the Jaduguda U (-Cu-Fe) deposit, Singhbhum shear zone, India: Implications for the sources and evolution of mineralizing fluids. Chem. Geol., 277, 245–260. https://doi.org/10.1016/j.chemgeo.2010.08.008.

Pal, D.C., Banerjee, A., Dutta, A., Sarangi, A.K., 2022. Hydrothermal alterations and U-REE mineralisation in the Narwapahar uranium deposit, Singhbhum shear zone, India. J. Earth Syst. Sci. 131. https://doi.org/10.1007/s12040-021-01782-0

Posamantier, H. W. & Vail, P. R. 1988. Eustatic controls on clastic deposition 1. Sequence and systems tract models. In: Wilgus, C. K., Ross, C. A. & Posamentier, H. (eds) Sea Level Changes: An Integrated Approach. SEPM, Spec. Publ., 42, 109–124.

Prabhakar, N., Bhattacharya, A., 2013. Paleoarchean partial convective overturn in the Singhbhum Craton, Eastern India. Precamb. Res., 231, 106-121.

Ranjan, S., Upadhyay, D., Pruseth, K. L., Nanda, J. K., 2020. Detrital zircon evidence for change in geodynamic regime of continental crust formation 3.7–3.6 billion years ago. Ear. Plan Sci. Lett., 538, 116206.

Rao, K.N., Rao, G. V. U., 1983. Uranium Mineralization in Singhbhum Shear Zone, Bihar: III. Nature of Occurrence of Uranium in Apatite-Magnetite Rocks. Geol. Soc. Ind., [S.l.], 555-561, nov. 1983. ISSN 0974-6889.

Ray, K. K., Ghosh-Roy, A. K. & Sengupta, S. 1996. Acid volcanic rocks between the Dalma volcanic belt and Chotanagpur gneissic complex, east Singhbhum and Purulia districts of Bihar and West Bengal. Ind. Min., 50, 1–8.

Reddy, S.M., Evans, D. A. D. 2009. Palaeoproterozoic supercontinents and global evolution:correlations from core to atmosphere. In: Reddy, S. M., Mazumder, R., Evans, D. A. D. & Collins, A. (eds) Palaeoproterozoic Supercontinents and Global Evolution. Geol. Soc., Lond., Spec. Publ., 323, 1–26.

Roy, A., Sarkar, S., Jeyakumar, S., Aggrawal, S.K., Ebihara, M., 2002a. Mid-Proterozoic Plume-related thermal event in Eastern Indian Craton: evidence from trace elements, REE geochemistry and Sr–Nd isotope systematics of basic–ultrabasic intrusives from Dalma Volcanic Belt, Gond. Res. 5, 133–146.

Roy, A., Sarkar, A., Jeyakumar, S., Aggarwal, S.K. and Ebihara, M., 2002b. Sm-Nd age and mantle source characteristics of the Dhanjori volcanic rocks, Eastern India, Geochem. J., 36, 503-518.

Saha, A. K. 1994. Crustal Evolution of Singhbhum–North Orissa, eastern India. Mem. of the Geol. Soc. of Ind., 27.

Saha, A. K., Ray, S. L. & Sarkar, S. N. 1988. Early history of the Earth: evidence from the Eastern Indian Shield. In: Mukhopadhyay, D. (ed.) Precambrian of the Eastern Indian Shield. Mem. of the Geol. Soc. of Ind., 8, 13–37.

Saha, A.K., 1994. Crustal evolution of Singhbhum-North Orissa, eastern India. J. of the Geol. Soc. of Ind., Mem., 27, 341

Sahu, N.K., Mukherjee, M.M., 2001. Spinifex textured komatiite from Badampahar-Gorumahisani schist belt, Mayurbhanj District, Orissa. J. of Geol. Soc. Ind., 57, 529-534.

Sarkar, B., 1984, Microfossils in the banded iron formation from the Noamundi basin, eastern India. Quart. J. of Geol. Min. and Metall. Soc. of Ind., 56, 41-46.

Sarkar, G., Bishui, P.K., Chattopadhyay, B., Chaudhury, S., Chaudhury, I., Saha, K.C., Kumar, A., 1992, Geochronology of granites and felsic volcanic rocks of Dehi fold belt. Rec., Geol. Surv. India 125(2), 21-23.

Sarkar, S.C., Gupta, A., 2012, Crustal evolution and metallogeny in India. Cambridge University Press. 840.

Sarkar, S.C., 2000. Crustal evolution and metallogeny in Eastern Inidan Craton. Geol. Surv. India, Spl. Pub., 55(1), 169-194

Sarkar, S.N., Saha, A.K., 1962, A revision of the Precambrian stratigraphy and tectonics of Singhbhum and adjacent regions, Quart. J. of Geol. Min. and Metall. Soc. of Ind., 34, 97-136.

Sengupta, N., Mukhopadhyay, D., Sengupta, P., Hoffbauer, R., 2005. Tourmaline-bearing rocks in the Singhbhum shear zone, eastern India: Evidence of boron infiltration during regional metamorphism. Am. Min. 90, 1241–1255. https://doi.org/10.2138/am.2005.1578.

Sengupta, N., Sengupta, P., Sachan, H. K., 2011. Aluminous and alkali-deficient tourmaline from the Singhbhum Shear Zone, East Indian shield: Insight for polyphase

boron infiltration during regional metamorphism. Am. Min., 96 (5–6), 752–767. https://doi.org/10.2138/am.2011.3560

Sengupta, S., Chattopadhyay, B. 2004. Singhbhum Mobile Belt – How far it fits an Ancient Orogen. In: Proceedings of the Workshop on (IGCP-453): Uniformitarianism Revised Edition on Orogens of India. Geol. Surv. of Ind., Spec. Publ., 84, 24–31.

Sengupta, S., Mukhopadhyay, P. K. 2000. Sequence of Precambrian events in the eastern Indian craton. Geol. Surv. of Ind. Spec. Publ., 57, 49–56.

Sengupta, S., Corfu, F., McNutt, R., Paul, D. K., 1996, Mesoarchaean crustal history of the eastern Indian craton: Sm-Nd and U-Pb isotopic evidence. Precamb. Res., 77, 17-22.

Sengupta, S., Sarkar, G., Ghosh-Roy, A. K., Bhaduri, S. K., Gupta, S.N., Mandal, A. 2000. Geochemistry and Rb–Sr Geochronology of acid tuffs from the northern fringe of the Singhbhum craton and their significance in the Precambrian evolution. Ind. Min., 54, 43–56.

Sharma, M., Basu, A.R., Ray, S.L., 1994. Sm-Nd isotopic and geochemical study of the Archean tonalite-amphibolite association from the eastern Indian Craton. Contrib. to Min. Pet., 117, 45-55.

Sreenivas, B., Dey, S., Rao, Y.B., Kumar, T.V., Babu, E., Williams, I.S., 2019. A new cache of Eoarchaean detrital zircons from the Singhbhum craton, eastern India and constraints on early Earth geodynamics. Geosci. Front., https://doi.org/10.1016/j.gsf.2019.02.001.

Sunilkumar, T.S., Parthasarathy, R., Palrecha, M.M., Shah, V.L., Sinha, K.K., Rao, N.K., 1996. Chemical age of detrital zircons from the basal quartz–pebble conglomerate of Dhanjori Group, Singhbhum craton, Eastern India. Curr. Sci. 482–486.

Upadhyay, D., Chattopadhyay, S., Kooijman, E., Mezger, K., Berndt, J., 2014. Magmatic and metamorphic history of Paleoarchean tonalite–trondhjemite–granodiorite (TTG) suite from the Singhbhum craton, eastern India. Precamb. Res. 252, 180–190.

Vapnik, Y., Bushmin, S., Chattopadhyay, A., Dobrovolsky, D.D., 2007. Fluid inclusion and mineralogical study of vein-type apatite ores in shear zones from the Singhbhum metallogenetic province, West Bengal, India. Ore Geol. Rev., 32, 1–2, 412-430, https://doi.org/10.1016/j.oregeorev.2006.11.002.

Vinogradoy, A., Lugarinoy, A., Zhykoy, C., Stapnikoya, N., Ribikoya, E., Krerre, K, 1964. Geochronology of Indian Precambrian. Rep. 22nd 1GC, New Delhi, Pet. J, 353-567.

CHAPTER 3

The high aluminous rocks of the study area: Kyanite quartzite

The kyanite-rich rocks that show highly variable proportions of kyanite, quartz and muscovite form a marker horizon along the hanging wall of the arcuate SSZ (Fig. 1). Vestiges of this rock are also found well within the pelitic rocks of the Chaibasa Formation (Sengupta et al., 2005; Ghosh et al., 2006). The different components of the rocks are collectively referred to as kyanite quartzite (KQ) though in many places, the rock is quartz or muscovite rich with very minor kyanite. The KQ rocks are associated with metasedimentary and metabasic rocks of the Singhbhum group and Dhanjori Group. Within the scope of this study, KQ is studied from Ujainpur, Jaduguda, Surda and Kanyaluka (Fig. 1). In the following sections, major varieties of the KQ are described.

3.1 Field relations

3.1.1 Field features of kyanite quartzite rock

Kyanite quartzite bodies occur along the SSZ as isolated patches and lenses. At Surda they are exposed as massive isolated mounds (Fig. 3.1a) which display knot-like aggregates of kyanite grains. KQ bodies also display mylonitic foliation (Fig. 3.1b) most likely due to heterogeneous strain distribution in the SSZ. The KQ bodies are associated with chloritoid-muscovite schists, chloritoid-garnet-biotite schists, quartz-chlorite schists, chlorite-muscovite-tourmaline bearing schists, ferruginous quartzites and metamorphosed psammo-pelitic units. Mylonitised soda-granites and meta-rhyolites are also present in near vicinities. The mylonitised KQ has a sheeted appearance with nodules of kyanite standing out on the surface (Fig. 3.1b). Kyanite porphyroclasts are rounded, augen-shaped and often occur as asymmetric ‘tadpole’ shaped bodies in sheared kyanite quartzite (Fig. 3.1b). Muscovite never exceeds more than 10 vol% in the muscovite poor KQ while in muscovite rich KQ one can encounter ~30-40 vol% of muscovite. The muscovite poor KQ grades into

muscovite rich KQ and a gradational contact is observed. In completely altered parts the KQ are converted to white mica schists. Near Surda, chloritoid bearing white mica schists are observed at the contact of muscovite rich KQ (Fig. 3.1c).

Near Kanyaluka the KQ appears laminated with millimetre to decimetre thick alternate layers rich in kyanite (~50 vol%) and quartz (with < 15 vol% kyanite) (Fig. 3.1d). At places some quartz-rich layers contain up to 90 vol% quartz (<10 vol% kyanite) and kyanite-rich layers contain up to 60 vol% kyanite (Fig. 3.1d). In places, the boundary of the kyanite- and quartz–rich layers are wavy (Fig. 3.1c). This feature along with lateral persistence of laminations up to several meters simulates the primary sedimentary structures (laminations of quartzite and shale (now mica schist), flame, load and flute cast structures) that are preserved in the psammopelites of the Chaibasa Formation (Fig. 3.1e). In places, the silica-rich layers are very fine grained and resemble chert (Fig. 3.1f). The KQ observed here is practically devoid of any muscovite. Stretched and deformed grains of quartz and deformed kyanite grains attest to the fact that the KQ has undergone shearing (evident in petrographic study discussed later, section 3.2). The KQ rocks are intimately associated with highly iron-rich chloritoid-garnet-biotite schists, garnet-muscovite-biotite schists and tourmalinite (Fig.5.1; Sengupta 2012).

Near Ujainpur isolated bodies of mylonitised KQ are observed. The KQ observed here are mostly muscovite rich. Asymmetrical stretched lenses of KQ, signifying intense shearing, are observed within the mica rich layers (Fig. 3.1f). The fringes of the pods are rich in muscovite. Stretched grains of kyanite, quartz and minor white mica define the regional shear foliation of the kyanite quartzite (S_2).

At Jaduguda, laminated KQ somewhat similar to that exposed at Kanyaluka, is observed. Layer parallel stretching of the laminated KQ produced lateral variation of the thickness of

the mineralogical layering or development of pinch-and-swell structure or boudins of the laminated unit (Fig. 3.1h). Chloritoid is observed developing at boudin necks (discussed later in Chapter 4). This muscovite rich KQ grades to completely muscovite rich schist at the borders (Fig. 3.1i).

3.1.2 Quartz veins: The muscovite poor KQ, muscovite rich KQ and associated rocks in near vicinities are intruded by quartz veins. These veins comprise of milky white quartz and sometimes contain chloritoid or amphibole. The quartz veins have been identified to be of at least three generations from their different shapes, deformation patterns, thickness and orientations. The first generation of veins, formed prior to S_1, are thin (~1-2 cm in thickness) and show pinch and swell structure which are parallel to the S_1 foliation near fold limbs. These quartz veins form rootless isoclinal folds that are observed in adjacent feldspathic schists (Fig. 3.1j). The second generation of veins (~2-3 cm in diameter) are parallel to the shear foliation (S_2 which is the regional foliation here; Fig. 3.1k) and make a 50° -70° angle with S_1 foliation. Some second generation veins are thinner (~0.5-1 cm in thickness) and occur as enechelon pattern in muscovite rich KQ. The third generation veins vary from 8-30 cm in thickness and occur haphazardly within KQ, cutting across all foliations (Fig. 3.1l).

3.1.3 Kyanite veins: Late stage kyanite (±quartz) veins cut across shear foliations in all KQ rocks. The veins, comprising of ~70-80 vol% kyanite and 20-30 vol% of quartz, ranging in thickness from 3mm-3cm, cut haphazardly across the KQ (Fig. 3.1m). The kyanite grains display wall-controlled growth in most veins (Fig. 3.1m,n) and some also exhibit kinking and shearing. Kyanite-quartz veins (~80 vol% kyanite and 20 vol% quartz), cutting across laminated KQ observed near Kanyaluka, are also associated with some uncommon aluminophosphate minerals viz. Florencite, Augelite and Lazulite (will be discussed in elaboration in Chapters 5 & 6)

From the field features it is evident that the kyanite quartzite has been affected by the intense shearing in the SSZ. Heterogeneity in shearing left pockets of massive KQ while at other places KQs suffered intense deformation making an extremely hard, massive rock sheeted in appearance. The massive KQ is foliated due to deformation and intense muscovitization is noticed in it. Quartz and kyanite veins cut across the foliated KQ. Later stages of deformation affected the altered rock in ways similar to the neighbouring rocks in the SSZ and deformed the kyanite veins. Muscovitization continued post deformation as evident from muscovite replacing kyanite in veins.

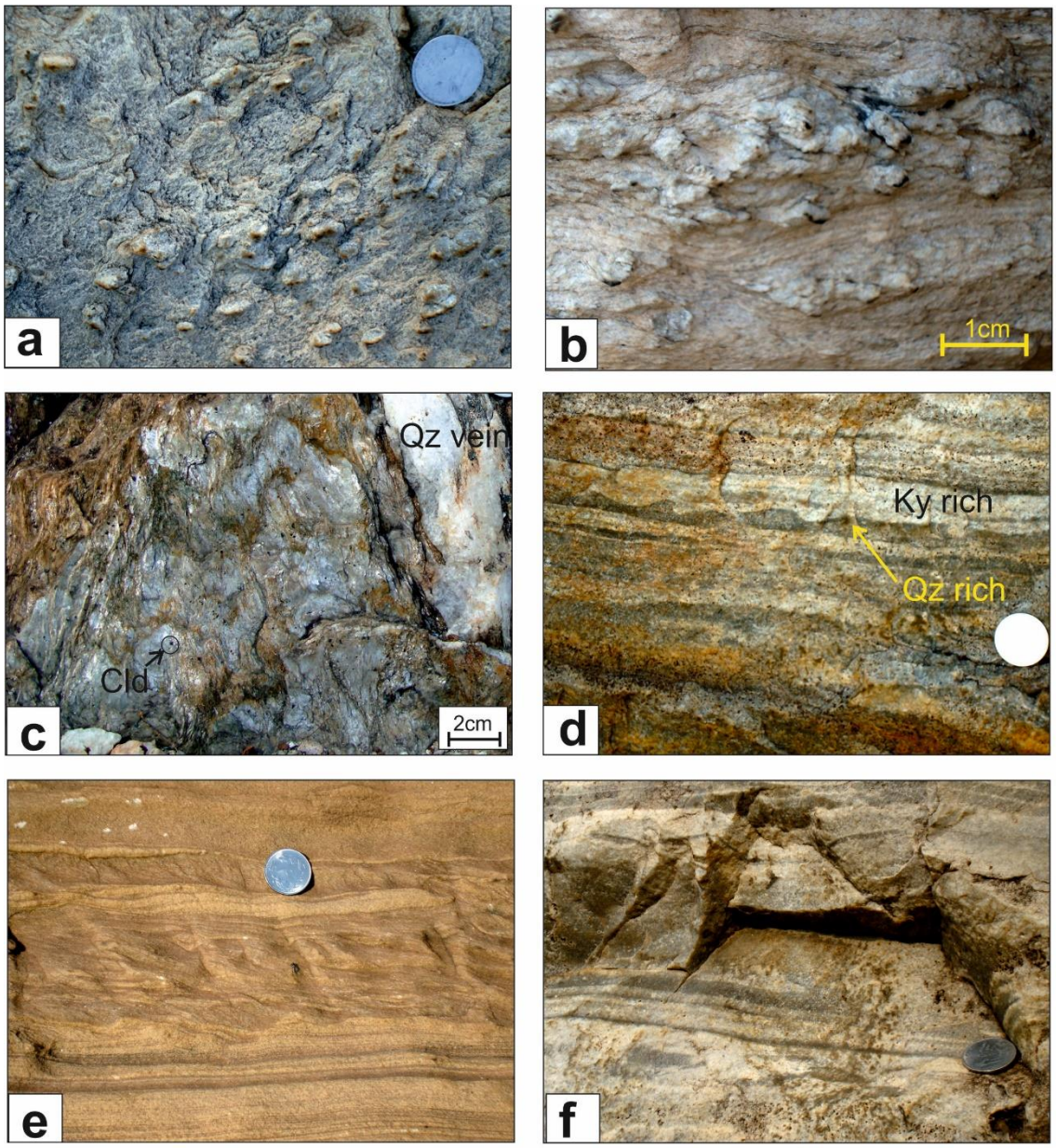

Fig 3.1: a) Knotty appearence of KQ due to kyanite porphyroclasts at Surda b) Kyanite grains of different shapes, e.g. rounded, augen-shaped and asymmetric 'tadpole' shaped porphyroclast in sheared KQ at Surda c) Chloritoid bearing muscovite schist at the contact of muscovite rich KQ near Surda college d) Laminated KQ with alternating kyanite and quartz rich layers at Kanyaluka. Primary sedimentary features preserved in KQ near Kanyaluka are visible in the photo e) Primary sedimentary features in psammopelites of Chaibasa Formation f) Cherty quartzite observed in few parts of laminated KQ at Kanyaluka

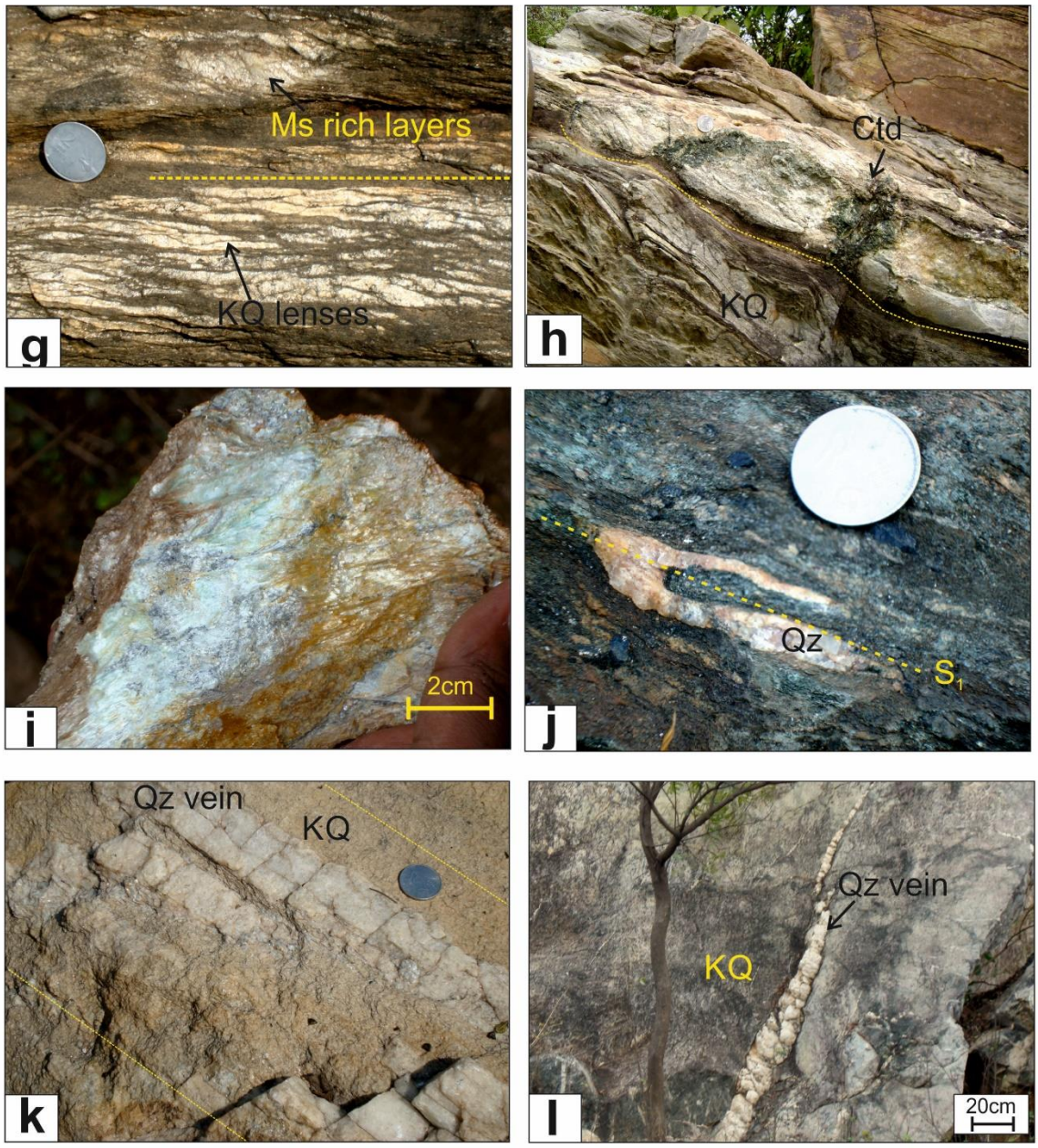

Fig 3.1: g) Fluxion fabric shown by mylonitic foliation in muscovite rich KQ defined by sheared lenses of KQ (white) in mica rich (grey coloured) band near Ujainpur. Yellow dashed line marks the C-plane of shear foliation h) Sheared and boudinaged KQ layers. Chloritoid forms at the neck of the boudins in KQ near Jaduguda i)Muscovite schist in the vicinity of KQ at Jaduguda j) Isoclinal rootless folds in first generation quartz vein observed in schists adjacent to KQ near Surda k) Second generation quartz veins develop parallel to S_2 foliation (shown in yellow dashed lines) in KQ near Surda l) Quartz veins of third generation cut across all foliations in KQ near Ujainpur.

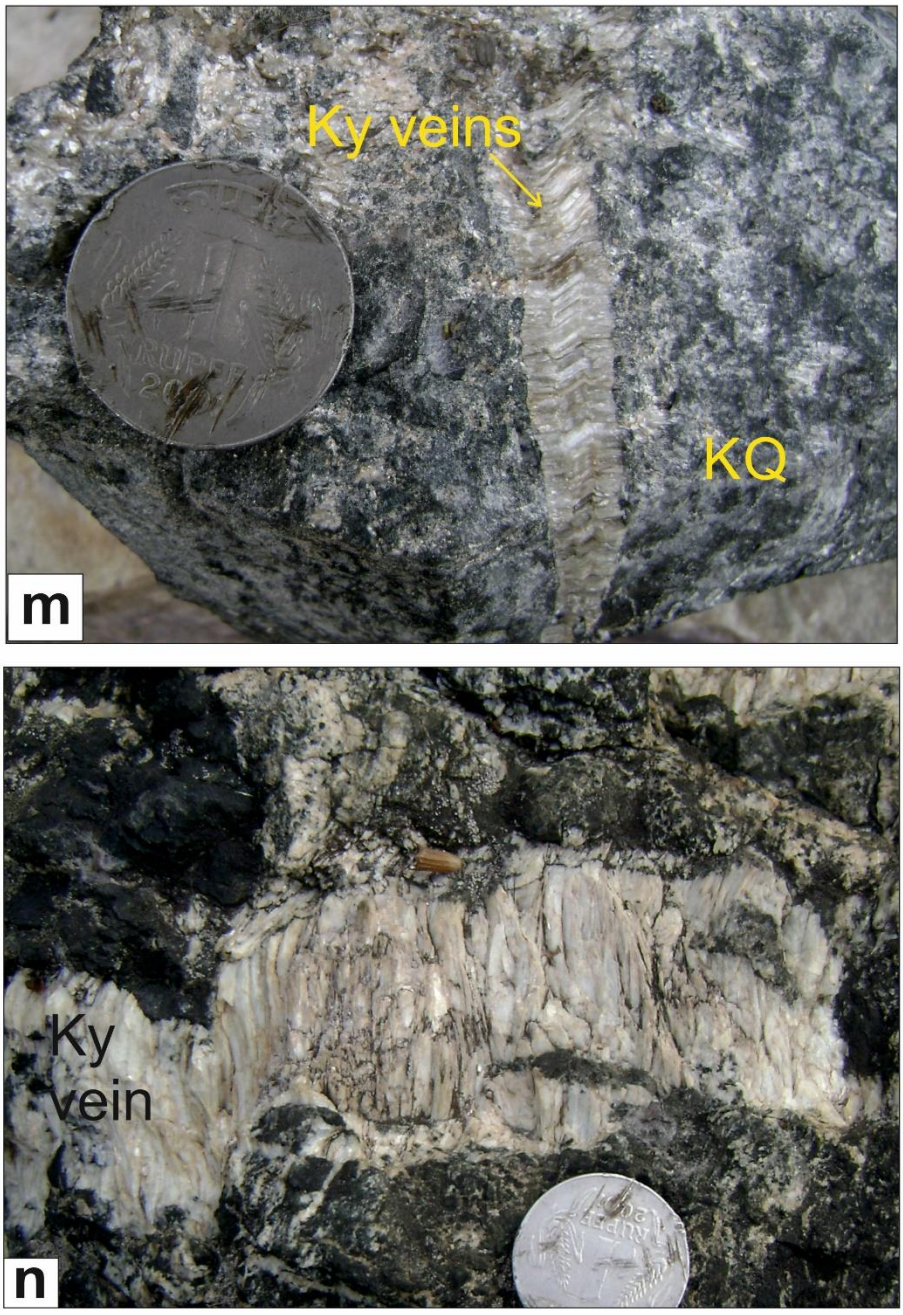

Fig 3.1:m) Deformed kyanite veins cutting across muscovite rich KQ at Ujainpur. Wall controlled growth is observed. Kyanite is also replaced by muscovite in these veins n) Teeth-like wall controlled growth of kyanite in vein at Ujainpur

3.2 Petrography of kyanite bearing quartzite:

Textural relations between different minerals in the KQ rock from different areas in SSZ show that kyanite, quartz and rutile form the earliest recognisable assemblage. In the kyanite rich layers of both muscovite poor and muscovite rich KQ, kyanite occupies more than 80 vol% of the rocks and rutile and quartz occupy the interstitial spaces. The muscovite poor KQ in less deformed parts and in the knots exhibits blades of kyanite in a rosette form and also exhibits twinning at various places (Fig.3.2a,b). In the laminated muscovite poor KQ of Kanyaluka, cluster of kyanite grains form layers alternating with quartz (Fig. 3.2c). In muscovite rich KQ, deformed and broken kyanite grains are replaced by muscovite and pyrophyllite (which has a rarer occurrence than muscovite) (Fig.3.2d). Phyllosilicates develop along shear planes and define schistosity in most places in the muscovite rich KQ (Fig.3.2d,e). Recrystallized kyanite are observed aligned along the schistosity (Fig. 3.2d). Asymmetric deformed kyanite grains along with deformed quartz and rutile define the mylonitic fabric in muscovite rich KQ (Fig. 3.2e). Phyllosilicates replacing kyanite sometimes preserve the shape of kyanite grains (Fig. 3.2f). Sheaf-like muscovite which outlasted deformation develops replacing kyanite (Fig.3.2g). Variable proportion of rutile (5-10 vol%) and quartz (upto 15 vol%) are present in these bands along with kyanite. Primary rutile is found ubiquitously distributed throughout the quartzites. Most of them are coarse amber coloured prisms with resorbed boundaries and/or deformed (Fig.3.2e).

Corundum developing at the expense of kyanite in the muscovite rich KQ, forms small aggregates which lack a definite shape (Fig.3.2h). Islands of kyanite are observed in corundum in backscattered electron images (Fig. 3.2h). Grains of xenotime are observed in corundum (Fig.3.2h). Diaspore develops from the margins of corundum and kyanite replacing corundum in the form of a network. Grains of monazite and apatite are found in

diaspore. Muscovite replaces corundum leaving islands of the latter in the former (Fig. 3.2i).

The petrographic study makes it clear that the kyanite, quartz and rutile form the earliest assemblage in the KQ. Deformation assisted by fluid infiltration led to development of muscovite (±pyrophyllite, chloritoid) by replacing kyanite. Phyllosilicates (mainly muscovite) define the shear foliation. Deformed quartz and kyanite are part of the mylonitic fabric. Kyanite in the veins, formed later than those observed in the KQ (discussed in Chapter 7), is also deformed. Muscovite growth occurs replacing kyanite in KQ and defines the schistosity/shear foliation in KQ. Corundum develops replacing kyanite while diaspore develops replacing both corundum and kyanite in KQ post deformation. Muscovite that develops post deformation develops by replacing kyanite as well, but occurs as bigger grains or as overgrowth on kyanite and also replaces corundum.

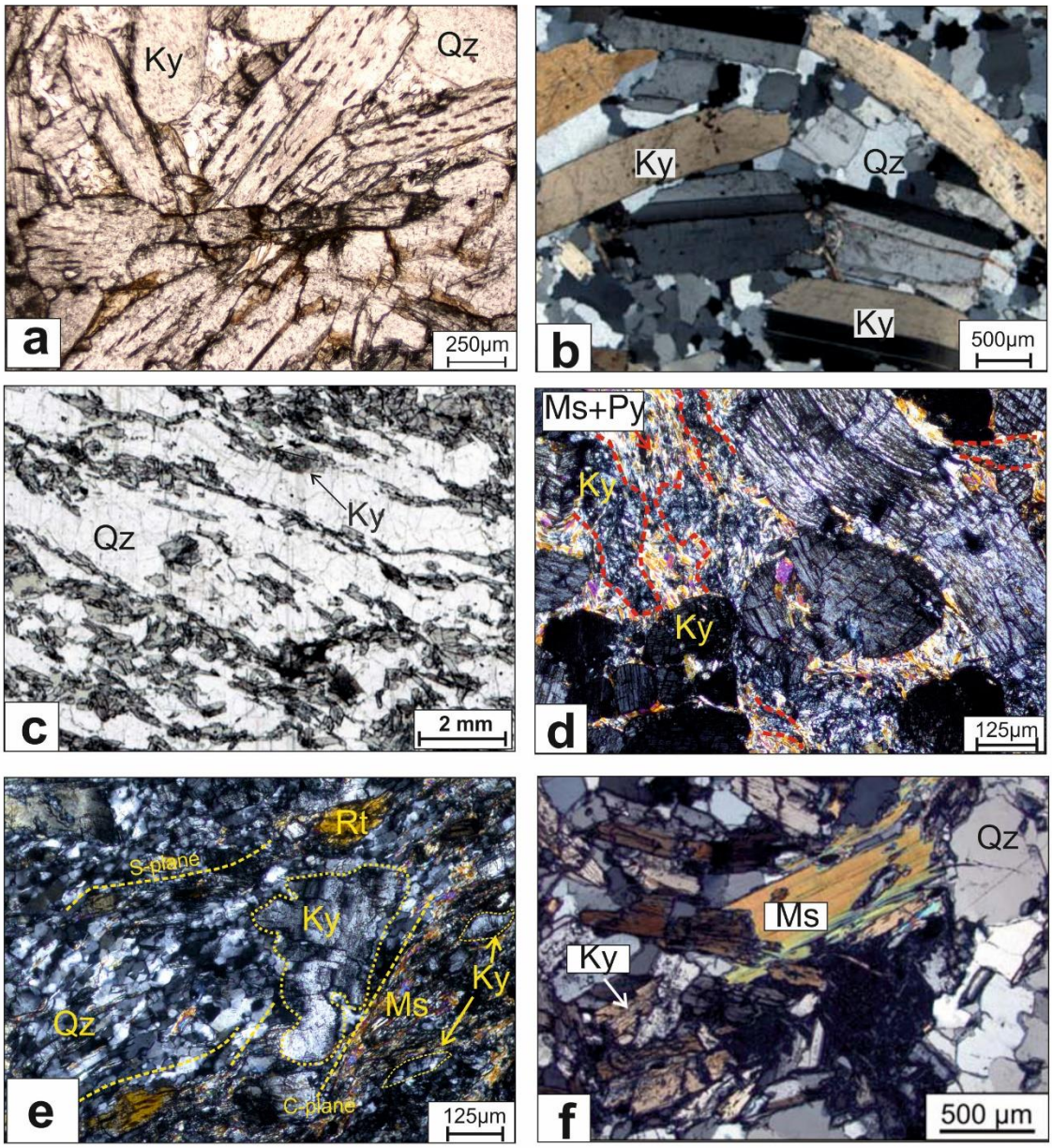

Fig 3.2:a)Kyanite and quartz forming the early assemblage of less deformed muscovite poor KQ of Surda. Kyanite grains exhibit rosette texture b)Kyanite grains exhibit twinning in less deformed zones of muscovite poor KQ of Surda c)Laminated kyanite quartzite from Kanyaluka where quartz rich layers alternate with thin kyanite rich layers d) Muscovite rich KQ from Ujainpur- Deformed and fractured kyanite grains replaced by muscovite and pyrophyllite which defines the foliation. Recrystallised small grains of kyanite are aligned parallel to the foliation (boundaries marked by red dashed lines) e) Muscovite rich KQ from Surda- Chessboard deformation fabric in quartz. Deformed quartz, rutile grains and asymmetric kyanite grains are observed along S-planes. Stubby corroded kyanite grains are also left behind f) Retrograde muscovite overgrowth on kyanite in muscovite rich KQ from Jaduguda. All abbreviations of mineral names are after Whitney and Evans (2010).

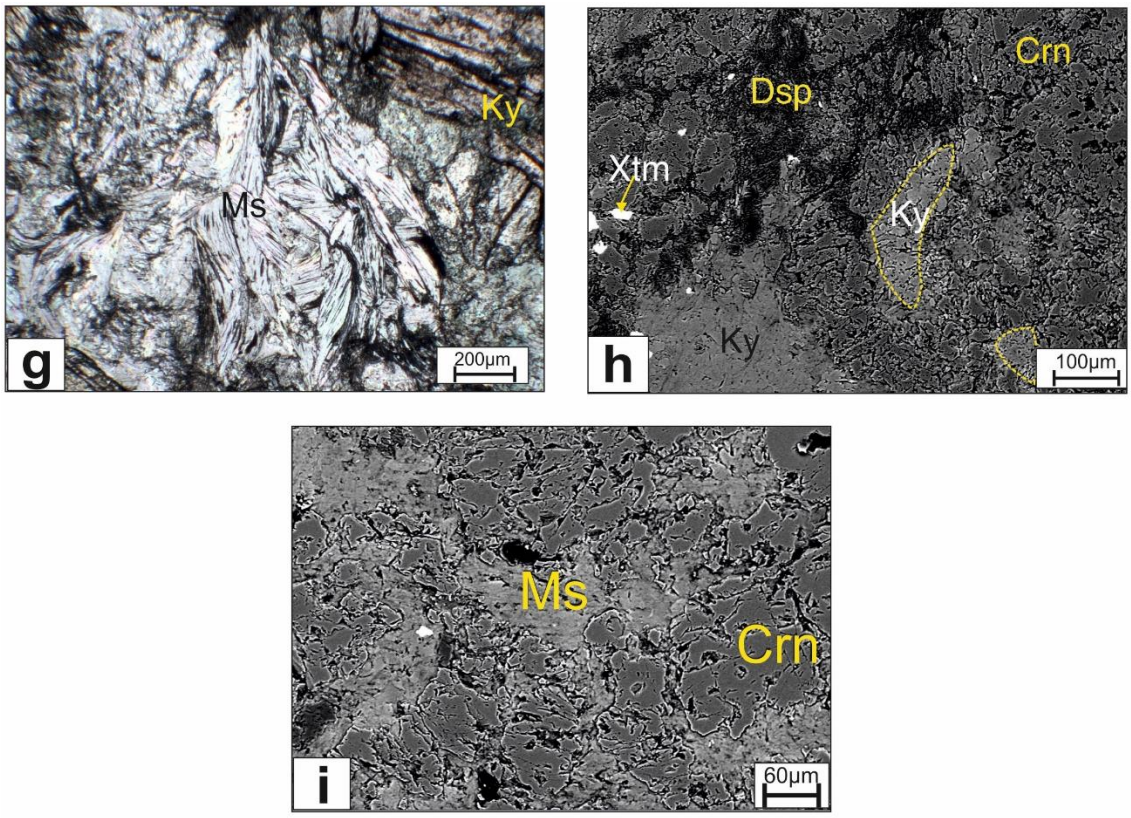

3.2 g) Sheaf -like muscovite replaces deformed kyanite grains in muscovite rich KQ near Ujainpur h) Kyanite grains display corroded margins as they give way to corundum in muscovite rich KQ from Ujainpur. Diaspore occupies the interstitial spaces as it develops from corundum and kyanite (i) Muscovite replacing corundum leaving islands of corundum within itself. Crn-Corundum, Dsp-Diaspore, Xtm-Xenotime, Ms-Muscovite, Ky-Kyanite, Prl-Pyrophyllite, Rt-Rutile, Qz-Quartz. All mineral abbreviations are after Whitney and Evans (2010)

3.3 Microstructural analysis:

Microstructural characteristics of different rock forming minerals have been studied as they can give us an insight into temperature, pressure, shear sense and strain rate. Microstructural analysis of kyanite and quartz are discussed below.

Kyanite: Kyanite forms euhedral prismatic crystals which form fan shaped less deformed aggregates in the relatively stress-free regions (Fig.3.2a). In the kyanite rich layers/regions of both muscovite poor and rich KQ, kyanite grains are often completely recrystallised (Fig.3.3a). Partial dynamic recrystallization of kyanite from the grain margins forming core and mantle structures is also observed in muscovite poor KQ (Fig.3.3b). Kyanite crystals with undulatory extinction, cross fractures and sideways migration of kink band boundaries (Fig.3.3c,d) are also common. One bent kyanite grain in muscovite rich KQ from Ujainpur exceptionally exhibits both sweeping extinction and a kink on the other side of the crystal (Fig.3.3d). Fractured kyanite grains floating in a groundmass of muscovite are also observed (Fig.3.3c,e). Kyanite grains are found intensely folded in the muscovite rich KQs from Ujainpur and Surda (Fig. 3.3f,g). Muscovite replacing folded kyanite at boundaries and along axial planes are observed (Fig.3.3f).

Quartz: The quartz grains show sweeping undulatory extinction, kink bands and moderate to high levels of recrystallization. Subgrain formation in quartz is commonly observed in the KQs (Fig. 3.3h). Ribbon shaped quartz grains, which are relicts of old large quartz grains, with undulose extinction, grade laterally into domains of small, dynamically recrystallized grains (Fig.3.3i). Grain boundary bulging of less deformed quartz grain into more deformed one is observed (Fig.3.3j). Several polycrystalline quartz grains with irregular sutured and lobate grain boundary causes one grain to bulge into another (Fig.3.3i,j).Polycrystalline aggregates of quartz formed by subgrain rotation and

recrystallization gives rise to a chess-board deformation fabric (Fig.3.2e). The deformed quartz grains define the shear foliation. Mica fish and asymmetric kyanite grains are noticed in the rock. Stubby kyanite grains with corroded boundaries are also observed (Fig. 3.2e).

Microstructural analysis of quartz has earlier helped constrain deformation conditions for naturally deformed quartz as it is dependent on the temperature, pressure, strain-rate and fluid pressure (Stipp et al., 2002; Menegon et al., 2008). The deformation features and mechanisms of quartz are well constrained from different studies (Hirth & Tullis, 1992; Sengupta et al., 2005; Passchier & Trouw, 2005). The deformation features of aluminosilicates however have been studied by very less workers (Hirth and Tullis, 1992; Beane & Field, 2007).

Crystal plastic deformation in minerals caused by dislocation creep has two distinct expressions in kyanite- *undulatory* and *kinked* crystal forms (Beane and Field, 2007). Similar deformational features as observed in kyanites from SSZ are also found in kyanite from kyanite-quartz veins studied in the Raft River Mountains, Utah, USA (Whitney & Dilek, 2000; Beitter et al., 2008). Bent and kinked crystals of kyanite and pull-apart fractures in kyanite crystals are quite common (Ryan, 2010). The kyanite grains in all KQ rocks of the SSZ display an array of deformation features i.e. kinks, undulatory extinction, bends, fractures, pull-apart structures, folds, recrystallization etc. Recovery mechanisms in kyanite crystals give rise to undulatory extinction and cross fractures. Thus, kyanite grains display both brittle and plastic crystal deformation. The plastic deformation in kyanite can be achieved by slow strain rates and fluid presence which are both facilitated by shearing.

Ribbon-shaped quartz is typical of dynamic recrystallization (Hirth and Tullis, 1992). The ribbons are surrounded by core mantle structures of quartz grains which confirm that the recrystallization was partial. Local displacement of grain boundaries to reduce

dislocation density in deformed crystals causes bulging of grain boundary of less deformed crystal into more deformed one (Fig.3.3k). Polycrystalline quartz grains with irregular boundaries are non-equilibrium "frozen" mobile boundaries formed by strain-induced grain boundary migration. These are typical low-grade metamorphic deformation features of quartz that form between 300-400°C (Stipp, 2002). Chessboard fabric is a typical fabric for medium metamorphic conditions with temperature range of 400-500°C. Similar quartz microstructures as described by Hirth and Tullis (1992) are found in the kyanite-quartz veins of Raft River mountains, Utah, which also display ribbon shaped grains, deformation lamellae, sweeping extinction and core-mantle structures (Gottardi et al., 2008, Sullivan, 2008, Ryan, 2010). Overall, the quartz microstructures (sweeping/undulatory extinction, core and mantle structures, ribbon-shaped grains) generally resemble those described by Hirth and Tullis (1992) as regime II. The deformation temperature range for regime II microstructures at low strain rates is confirmed by Stipp (2002) and Gottardi (2008) as ~350°C to 480°C. The temperature range derived from deformation features is also similar to P-T conditions derived through thermodynamic modelling in the adjacent rocks.

Fluid flow processes into shear zones though frequently observed in nature are still highly debated. Ductile shear zones are zones of tremendous pressure as compared to their surroundings and fluid flowing/ channeling into a high-pressure zone from a low-pressure zone i.e. the surroundings (Mancktelow, 2006). If the effect of pressure would have been absent then strain rate would be directly proportional to the effective viscosity within the shear zone and then increasing strain would cause strain softening through grain-size reduction, development of CPO or mineral reactions (Carter & Tsenn, 1987). Fault zones/ brittle shear zones for example are lower pressure regimes and channels for fluid flow are easily established. However, in a ductile shear zone developing at mid to lower crustal levels like the SSZ pressure within the shear zone plays a major role in microcracking of

grains to create temporary brittle zones/windows which minimize the pressure locally and allow channelling of fluids and enhance permeability which would otherwise be improbable (Mancktelow, 2006). A repeated interplay of elastic, viscous and plastic mechanisms occur on spatial and temporal scales (Regenauer-Lieb and Yuen, 2003) which lead to mutual overprinting of brittle fracturing and ductile shearing evidences (Kisters et al., 2000; Kolb et al., 2004). The evidence of microfracturing is widely observed in the studied KQs where of stubby fractured kyanite grains floating in a mica-rich matrix are frequently observed. These attest to the brittle precursor of a larger ductile shear zone. Folded and bent kyanite grains are also fractured leading to assertion of numerous cycles of fracturing and subsequent shearing.

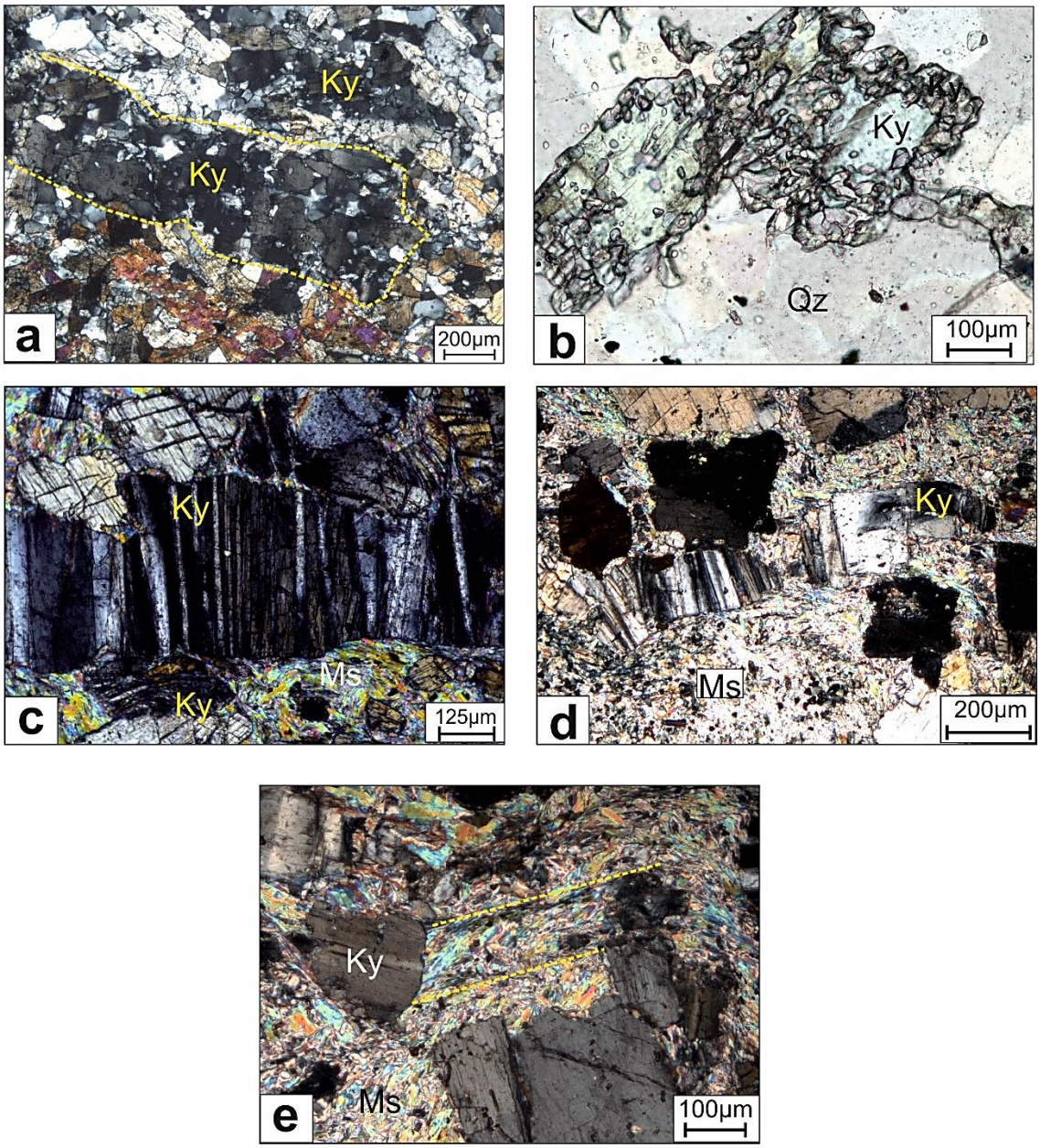

Fig 3.3: a) Kyanite grain entirely recrystallized in kyanite rich zone of muscovite poor KQ near Surda b)Core mantle recrystallization feature in kyanite from muscovite poor KQ near Kanyaluka c) Kyanite grain with pronounced kink bands. Fractured kyanite crystals float in a muscovite rich groundmass in muscovite rich KQ near Surda d) Kyanite grains exhibit sweeping extinction even in bent crystals with kinks on other part of grain (muscovite rich KQ near Ujainpur) e) Fractured kyanite grains with corroded margins floating muscovite. Some shear bands defined by muscovite also observed in muscovite rich KQ from Ujainpur

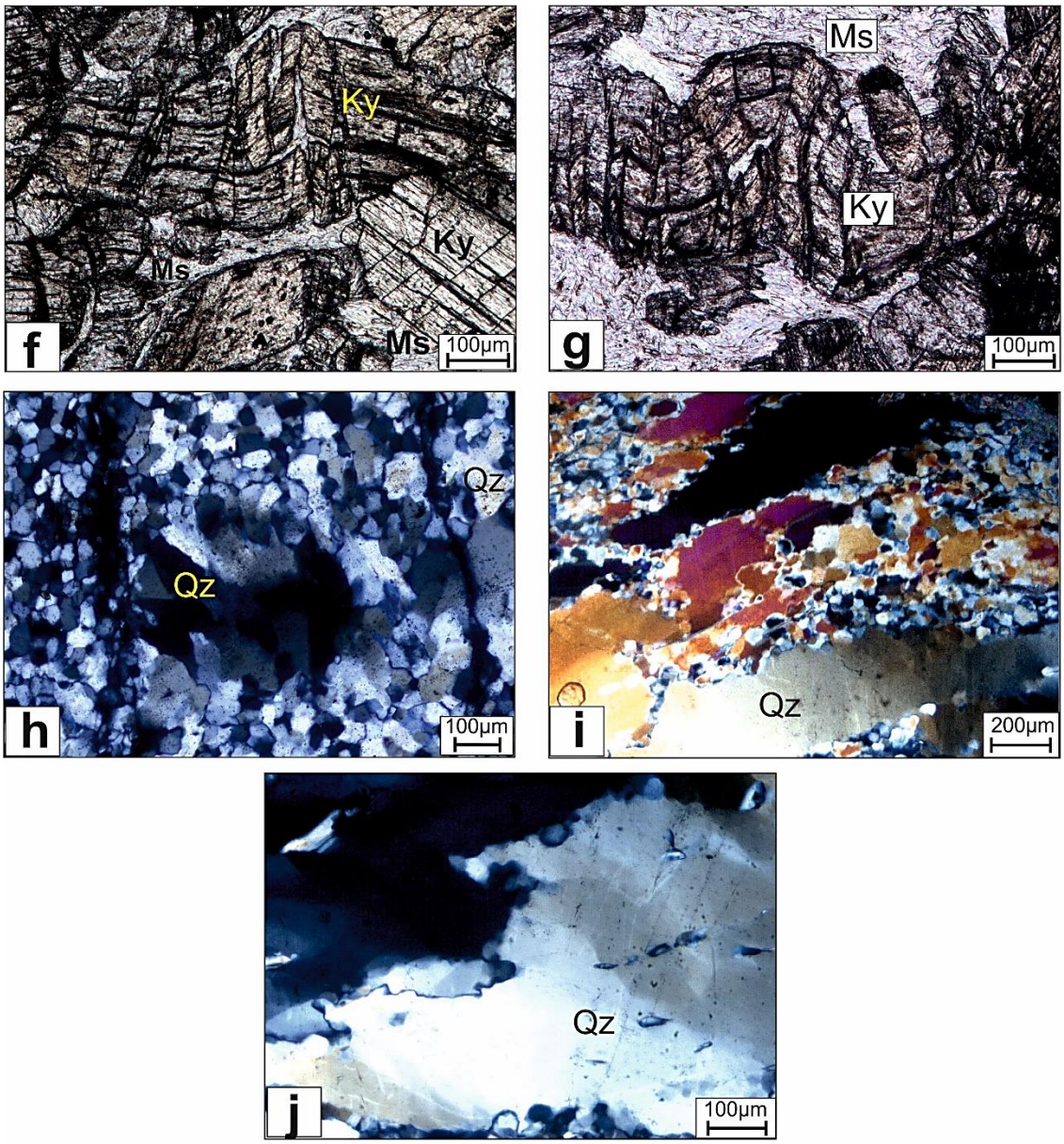

Fig 3.3 f) Fractured kyanite grains which are replaced by muscovite in muscovite rich KQ near Ujainpur g) Folded kyanite crystals in muscovite rich KQ near Ujainpur h) Undulatory extinction in quartz, sub grain formation and recrystallization in quartz from quartz rich layers in muscovite poor KQ from Kanyaluka i) Sweeping undulatory extinction in ribbon quartz from KQ near Surda. Recrystallised smaller quartz crystals are formed from previously bigger size crystals j) Bulging of grain boundaries of one quartz crystal into another observedin muscovite rich KQ near Surda

3.4 Mineral chemistry:

The compositions of the minerals in the KQ are measured with Cameca SX100 Electron Probe Micro Analyzer (EPMA) Central Petrological Laboratory, Geological survey of India, Kolkata. The analytical details are presented in the Appendix III. The representative analyses of the minerals are given in the Tables 3.1-3.3. In the following section, the salient compositional characteristics of the minerals are presented:

Kyanite: The kyanites essentially have an Al_2SiO_5 composition. Besides Al and Si, minor Fe (up to 0.003 a.p.f.u.), Cr (up to 0.003 a.p.f.u.), Ti (<0.002 a.p.f.u.) and Mg (upto 0.002 a.p.f.u.) are present in the mineral (Tab. 3.1).

Rutile: The rutile is essentially pure TiO_2 with small amounts of Fe and Cr.

Pyrophyllite and muscovite: In the pyrophyllite the Si varies from 7.543-7.852 a.p.f.u. and Al varies from 4.115-4.415 a.p.f.u (Tab. 3.2). The muscovites have Al content between 5.470-6.095 a.p.f.u. while Si content is between 6.062-6.350 a.p.f.u (Tab. 3.2). The muscovite in the KQ rocks are basically a mixture of muscovite and pyrophyllite (16-29 mol%). Variable amounts of paragonite (8-20 mol%) is also observed.

Diaspore and corundum: Both the minerals have nearly end-member composition (Al= 1.967 a.p.f.u.) and only minor amounts of Fe and Si could be detected (Tab. 3.3). The Fe_2O_3 content of corundum and diaspore both are very low between 0.01-0.08 wt%.

Xenotime, monazite and apatite present in the rocks have only been analysed qualitatively.

The compositions of kyanite reflect that the kyanite was compositionally homogeneous. It also means that kyanite did not equilibrate with Fe-Ti oxides during its formation. Kyanites from metapelites were studied by Albee and Chodos (1969), Chinner et al. (1969), Rumble (1973), Grambling (1981) and many others. These studies show that most metapelitic

kyanites contain mostly <0.50 wt% Fe_2O_3. Kyanite with higher Fe content (>1 wt%) is found in metabauxites and quartzites but that is clearly not the case here. Fe and Ti content of the host rock has a clear relation with the Fe-Ti content in kyanites. The partial pressure of oxygen controls the substitution of Fe for Al in kyanites (Chinner et al., 1969). In the present study the kyanite bearing rocks contain rutile coexisting with the kyanite but paucity of Fe-Ti in the host rocks may have led to the anomalously low Fe-Ti content in kyanites. Also rutile may have formed earlier than kyanite so that the latter is unbuffered with respect to Ti. Muscovite is the only phase with considerable K^+ suggesting the K^+ has been introduced into deposits through fluids. The poor Fe content of corundum which may be a consequence of the iron-poor composition of the sample.

Table 3.1: Representative oxide analyses and calculated cations of Kyanite

Phases	Kyanite												
	S30A	S30A	S30C	S30C	S30C	S30C	S30C	S30D	S30D	S30D	S30D	S30A	S30D
DataSet/ Point	19 / 1 .	21 / 1 .	2 / 1 .	8 / 1 .	11 / 1 .	16 / 1 .	18 / 1 .	4 / 1 .	9 / 1 .	22 / 1 .	24 / 1 .	11 / 1 .	20 / 1 .
SiO_2	37.26	36.65	37.44	37.27	37.62	37.32	37.75	36.52	37.13	36.73	36.16	37.21	36.84
TiO_2	0.00	0.01	0.00	0.04	0.01	0.02	0.05	0.11	0.01	0.00	0.00	0.00	0.00
Al_2O_3	63.51	62.22	62.98	63.72	63.37	63.41	63.74	62.45	62.50	62.29	61.65	62.76	62.68
Cr_2O_3	0.16	0.00	0.08	0.00	0.00	0.06	0.06	0.06	0.16	0.00	0.01	0.04	0.08
FeO	0.12	0.04	0.13	0.09	0.09	0.10	0.05	0.15	0.12	0.10	0.04	0.00	0.03
MnO	0.00	0.08	0.00	0.00	0.00	0.00	0.06	0.03	0.00	0.00	0.00	0.00	0.04
MgO	0.00	0.03	0.00	0.02	0.02	0.01	0.01	0.01	0.00	0.00	0.06	0.04	0.03
CaO	0.00	0.09	0.00	0.06	0.00	0.01	0.01	0.00	0.02	0.03	0.06	0.04	0.01
Na_2O	0.00	0.03	0.01	0.01	0.02	0.03	0.03	0.00	0.00	0.01	0.04	0.06	0.01
K_2O	0.01	0.02	0.00	0.02	0.01	0.02	0.03	0.01	0.01	0.00	0.01	0.00	0.01
Total	101.06	99.17	100.64	101.22	101.13	100.98	101.79	99.33	99.95	99.16	98.03	100.16	99.72
Si	0.996	0.998	1.004	0.994	1.004	0.998	1.001	0.993	1.003	1.000	0.996	1.003	0.997
Ti	0.000	0.000	0.000	0.001	0.000	0.000	0.001	0.002	0.000	0.000	0.000	0.000	0.000
Al	2.000	1.997	1.991	2.003	1.993	1.998	1.993	2.002	1.990	1.998	2.001	1.993	2.000
Cr	0.003	0.000	0.002	0.000	0.000	0.001	0.001	0.001	0.003	0.000	0.000	0.001	0.002
Fe	0.003	0.001	0.003	0.002	0.002	0.002	0.001	0.003	0.003	0.002	0.001	0.000	0.001
Mn	0.000	0.002	0.000	0.000	0.000	0.000	0.001	0.001	0.000	0.000	0.000	0.000	0.001
Mg	0.000	0.001	0.000	0.001	0.001	0.000	0.000	0.000	0.000	0.000	0.002	0.002	0.001
Ca	0.000	0.003	0.000	0.002	0.000	0.000	0.000	0.000	0.001	0.001	0.002	0.001	0.000
Na	0.000	0.002	0.001	0.001	0.001	0.002	0.002	0.000	0.000	0.001	0.002	0.003	0.000
K	0.000	0.001	0.000	0.001	0.000	0.001	0.001	0.000	0.000	0.000	0.000	0.000	0.000
Σcation	3.003	3.004	3.000	3.004	3.001	3.003	3.002	3.003	3.001	3.002	3.005	3.002	3.002

Table 3.2: Representative oxide analyses and calculated cations of Muscovite and Pyrophyllite

	Muscovite										Pyrophyllite		
Sample no	S 22C	S 22C	S 22C	S 22C	S 22C	S 30A	S 30A	S 30A	S 30C	S 30C	S 30C	S 30C	S 30C
DataSet/ Point	1 / 1 .	8 / 1 .	11 / 1 .	14 / 1 .	21 / 1 .	3 / 1 .	17 / 1 .	20 / 1 .	12 / 1 .	20 / 1 .	2 / 1 .	22 / 1 .	23 / 1 .
SiO_2	48.10	48.44	48.02	47.44	49.70	48.74	49.19	48.57	47.61	47.84	62.88	63.62	62.73
TiO_2	0.25	0.24	0.28	0.27	0.27	0.09	0.12	0.07	0.00	0.02	0	0	0
Al_2O_3	36.17	36.19	35.75	36.55	36.32	40.99	39.88	40.20	39.72	40.81	30.81	28.57	31.63
Cr_2O_3	0.00	0.08	0.00	0.05	0.05	0.07	0.12	0.20	0.06	0.14	b.d.l	b.d.l	b.d.l
FeO	2.50	2.52	2.66	2.71	2.83	0.07	0.46	0.24	0.13	0.09	0.14	0.11	0.17
MnO	0.08	0.00	0.04	0.00	0.00	0.05	0.00	0.00	0.01	0.00	0.04	0.02	0.05
MgO	0.74	0.75	0.81	0.58	0.76	0.09	0.13	0.08	0.05	0.03	0.03	0.03	0.03
CaO	0.02	0.02	0.00	0.02	0.00	0.00	0.01	0.00	0.00	0.02	0.04	0.02	0.01
Na_2O	0.74	0.69	0.72	0.74	0.67	0.87	0.74	0.69	1.60	1.36	0.54	0.6	0.48
K_2O	7.76	7.11	6.27	6.44	6.19	7.73	7.24	7.32	6.56	6.51	0	0	0
Total	96.37	96.03	94.56	94.78	96.80	98.70	97.89	97.36	95.73	96.80	94.48	92.97	95.1
Si	6.244	6.278	6.294	6.215	6.350	6.086	6.179	6.134	6.109	6.062	7.643	7.852	7.543
Ti	0.024	0.023	0.028	0.027	0.026	0.008	0.011	0.007	0.000	0.002	0	0	0
Al	5.534	5.528	5.523	5.644	5.470	6.034	5.904	5.983	6.008	6.095	4.415	4.115	4.517
Cr	0.000	0.008	0.000	0.005	0.005	0.007	0.012	0.020	0.006	0.014	b.d.l	b.d.l	b.d.l
Fe^{2+}	0.272	0.274	0.291	0.297	0.302	0.007	0.049	0.025	0.014	0.010	0.014	0.01	0.019
Mn	0.009	0.000	0.005	0.000	0.000	0.006	0.000	0.000	0.001	0.000	0.004	0.001	0.006
Mg	0.144	0.145	0.159	0.112	0.145	0.017	0.025	0.015	0.010	0.005	0.005	0.005	0.005
Ca	0.003	0.002	0.000	0.002	0.000	0.000	0.001	0.000	0.000	0.003	0.005	0.002	0
Na	0.185	0.173	0.183	0.188	0.166	0.210	0.181	0.168	0.397	0.333	0.127	0.132	0.12
K	1.285	1.176	1.048	1.077	1.009	1.231	1.160	1.179	1.075	1.052	0	0	0
Σcation	13.699	13.606	13.532	13.566	13.474	13.606	13.522	13.531	13.620	13.575	12.214	12.118	12.211
Muscovite	0.59	0.55	0.48	0.51	0.46	0.65	0.61	0.63	0.57	0.58	0.02	0.00	0.02
Pyrophyllite	0.19	0.23	0.27	0.24	0.29	0.16	0.21	0.20	0.16	0.17	0.88	0.92	0.87
Phlogopite-annite	0.11	0.12	0.15	0.15	0.15	0.08	0.08	0.08	0.07	0.09	0.04	0.00	0.05
Paragonite	0.09	0.09	0.09	0.09	0.08	0.11	0.09	0.08	0.20	0.17	0.06	0.07	0.06
Ti- muscovite	0.01	0.01	0.01	0.01	0.01	0.00	0.01	0.00	0.00	0.00	0.00	0.00	0.00

Note: Cation recalculation on 22(O).

Table 3.3: Representative oxide analyses and calculated cations of Corundum, Rutile and Diaspore

	Corundum	Rutile	Diaspore
SiO_2	0.00	0.02	1.00
TiO_2	0.00	100.90	0.17
Al_2O_3	99.96	0.06	83.04
Cr_2O_3	0.00	0.06	0.13
$Fe_2O_3^*$	0.00	0.00	0.00
FeO^*	0.01	0.00	0.02
MnO	0.00	0.10	0.02
MgO	0.00	0.02	0.01
CaO	0.00	0.00	0.02
Na_2O	0.00	0.02	0.01
K_2O	0.00	0.03	0.00
P_2O_5	n.a.	n.a.	n.a.
B_2O_3	n.a.	n.a.	n.a.
H_2O			
Total	99.97	101.02	84.42
Oxygen basis	3	2	3
Si	0.000	0.000	0.020
Ti	0.000	0.998	0.003
Al	2.003	0.001	1.967
Cr	0.000	0.001	0.002
Fe^{3+}	0.000	0.000	0.000
Fe^{2+}	0.000	0.001	0.000
Mn	0.000	0.000	0.000
Mg	0.000	0.000	0.000
Ca	0.000	0.000	0.000
Na	0.000	0.001	0.000
K	0.000	0.000	0.000
P	n.a.	0.000	n.a.
B	n.a.	n.a.	n.a.
OH	n.a.	n.a.	
Total	2.003	1.002	1.993

3.5 Textural modelling

Formation of muscovite rich KQ and white mica schists from kyanite quartzite was an open system process. To understand the formation of various minerals from kyanite textural modelling study was performed integrating inputs from textural studies and measured chemical conditions. The computer program "C-Space" published by Torres-Roldan et. al. (2000), based on the algorithm published by Fisher (1989, 1993), applies the method of SVD to achieve desired results. The details of the computational process is given in the Appendix-I.

Results

Following modelled reactions are consistent with both the textural features and the compositional characteristics of the minerals. Also included in the reactions are the solid volume change of the reactons (given in the parenthesis)

Formation of Muscovite after Kyanite

1 Kyanite + 1.29 SiO_2 + 0.13 Na + 0.34 K + 0.003 Fe + 0.004 Mg + 0.002 Ti+ 0.7 H_2O = 0.53 Muscovite + 0.16 Pyrophyllite ……..(R1)

ΔV_{solid}= *25.31 cc*

Formation of Corundum after Kyanite

1 Kyanite = 0.99 Corundum + 1.004 SiO_2 + 0.0017 Mg + 0.001 Ca + 0.003 Na …(R2)

ΔV_{solid} = *4.99 cc*

Formation of Muscovite after Corundum

2.84 Corundum + 0.14 Mg + 0.002 Ca + 0.27 Fe + 6.45 SiO_2 + 0.18 Na + 2.004 H_2O + 0.22 Rutile + 0.97 K = 1 Muscovite …… (R3)

ΔV_{solid} = *-84.20 cc*

Formation of Diaspore after Corundum and Kyanite

1 Corundum+ 0.02 SiO_2+ 0.0003 Mg + 0.0004 Ca + 0.0003 Fe + 0.0004 Na + 1.01 H_2O = 1.01 Diaspore ……. (R4)

ΔV_{solid} = *-8.10 cc*

1 Kyanite + 0.0005 Fe + 1.01 H_2O = 1.01 Diaspore + 0.0013 Mg + 0.0005 Ca + 0.98 SiO_2 + 0.003 Na……..(R5)

ΔV_{solid} = *-1.03 cc*

Reaction R1 and R2 explains the formation of muscovite and corundum from kyanite while the reactions R3 – R5 explain the growth of muscovite from corundum and diaspore from kyanite and corundum. Corroboration of reaction textures by the modelled chemical reactions justifies the view that SVD technique is a powerful tool in modelling reaction textures in multicomponent natural systems (Lang et al., Sengupta et al., 2009; See Appendix I). The important features that emerge from the balanced chemical reactions are presented below.

1. The assemblage, kyanite + rutile + quartz, represents the earliest assemblage of the KQs which were converted to muscovite and pyrophyllite due to infiltration of H_2O. Corundum was also formed from kyanite in the late stages. Al^{3+} was considered immobile species during the metamorphism.
2. Diaspore and muscovite were formed from corundum (R3 and R4) as evident from textural relations. The negative ΔV in reactions R3, R4, R5 indicate that pore spaces opened up for passage of more fluid and facilitated the reactions even more. Quartz veins deposited during different stages are an indicator.
3. It is evident from the aforesaid analyses that complex metasomatic reactions that involved a number of mobile species were responsible for the development of muscovite, pyrophyllite, corundum and diaspore in the KQ.

3.6 Geochemistry

Major and trace element concentrations in the samples of the studied kyanite quartzite are presented in Table 3.4 (a,b). Details of the analytical procedures are given in the Appendix-III.

3.6.1 Major elements:

The muscovite poor KQ rocks (Table 3.4a) is rich in SiO_2 (62.78-76.95%) and have variable amounts of Al_2O_3 (19.97-43.58%). The rocks are low in MgO (<0.22%), Na_2O (<0.22%), P_2O_5 (<0.19%) and K_2O (0.02-1.36%). The TiO_2 (0.43-1.51%), FeO (0.03-4.57%) and CaO (0.02-0.27%) values are also quite low (Table 3.4a).

Compared to the muscovite poor variety, the muscovite rich kyanite quartzite is distinctly richer in K_2O (3.37-7.10%) and Na_2O with K_2O/Na_2O >1 (Table 3.4b). The composition of the muscovite rich KQ rock comprises of SiO_2 varying between 49.35-70.13% and Al_2O_3 that varies between 13.61-25.76%. Amount of FeO (1.29-19.34%) in muscovite rich KQ is considerably higher than muscovite poor KQ. The aluminophosphate (AP) bearing KQ has higher content of P_2O_5 than all KQ rocks but does not have K_2O or Na_2O content due to absence of muscovite.

Almost all muscovite poor KQ rocks fall along a linear array joining quartz and kaolinite compositions (Fig.3.4a). The slight offsets are due to presence of minor elements besides Si and Al. The low concentration of FeO and TiO_2 in the KQs reflect low abundances of heavy minerals such as ilmenite, titanite and Ti-magnetite.

When compared to average pelitic and granitic compositions of the world, the studied muscovite poor kyanite-quartzite rocks have much higher Al_2O_3 content and much lower CaO, K_2O, Na_2O content (Table-3.5).

3.6.2 Trace elements:

The representative trace elements concentrations in the muscovite poor and muscovite rich KQ are presented in Table-3.4a,b. The trace elements including some REE have been normalised to the trace elemental compositions of the Upper Continental Crust (UCC; Taylor & McLennan, 1995) and Primitive mantle (Sun and McDonough, 1989) and plotted in spider diagrams (Fig.3.4b,c,d,e,f). Two types of spidergrams are constructed and in each of them muscovite poor and muscovite rich KQ are plotted separately. In one type, only the incompatible elements (normalised to UCC and Primitive mantle in separate diagrams) are considered (Fig.3.4b,c,d). The incompatible elements of muscovite poor KQ normalised to UCC are plotted in two spidergrams for clarity (Fig. 3.4b,c). Also included in the UCC normalised diagrams are the trace elemental compositions of (a) the PAAS (Post Archaean Average Shale, Pourmand 2012) and (b) Carbonaceous Chondrite (Sun and McDonough 1995) and (c) trace elements of some well-studied kyanite-quartzite in the world. ~~All the compositions are normalized to UCC.~~ In the other type of diagram, both compatible and incompatible elements (normalised to UCC) are arranged in order of decreasing compatibilities are shown (Fig. 3.4g,h; after Hassan et al., 1999, Ghosh & Sarkar, 2010). The variation of the REE compositions for muscovite poor and muscovite rich KQ (normalized to the UCC- Fig.3.4e,f and Carbonaceous Chondrite- Fig.3.4 i,j) are shown separately. In the following section the salient features of compatible and incompatible trace element compositions of the studied rocks are presented.

Compatible elements: Most samples of muscovite poor KQ are depleted Ni, Co and Cr with Sc and V close to the compositions of UCC. Only a couple of samples show slightly higher Cr and Co relative to UCC (Fig. 3.4g,h). Barring two samples (15,17C), the compatible elements in the muscovite rich KQ are close to the UCC. Sample 17C is rich in

Sc, Cr and are depleted in Co and Ni. The other sample (K2C) show lower concentrations of V and Cr relative to the UCC (Fig. 3.4h).

Incompatible elements:

In the plots where incompatible elements are normalised to UCC, Zr, Hf, Ti and Nb values of the studied rock in both muscovite poor and muscovite rich KQ show near UCC values with a slightly positive anomaly for Ta for some samples (Fig. 3.4b,c,d). The slightly high values of Ta possibly owe its origin to rutile, a sink for Ta (Rollinson, 1993). Nd, Tb, Y, Tm and Yb concentrations are similar to UCC in most KQ samples (muscovite rich or poor) and do not show anomalous pattern (Fig.3.4 b,c,d). Th and U contents are almost close to UCC in most muscovite poor KQ except samples S30, 23A and 23 (Fig. 3.4c). Ce shows slight enrichment in some muscovite poor KQ which may be correlated with Ce bearing minerals in KQ rocks (xenotime, apatite).

All samples of KQ (muscovite rich and poor) are depleted in Sr. Samples of muscovite poor KQ show a strong negative anomaly in K, Rb and Ba compared to UCC (Fig. 3.4b,c). Cs values are almost close to UCC (Fig. 3.4b,c). The strong depletion in K in muscovite poor KQ can be attributed to absence of feldspar or mica in the rocks.

In the muscovite rich KQ, K, Rb and Ba plot close to UCC (Fig.3.4d). Th and U concentrations are mostly close to UCC.

When normalised to primitive mantle the incompatible elements of almost all of the muscovite poor KQ show ~10 to 200 times enrichment excepting K, and Sr (Fig.3.4e). Cs has distinctly higher concentrations (~1000 times enrichment). A few samples also have elevated U and Th (~1000 times enrichment). A prominent positive anomaly for Pb is seen whereas K, Ba, and Rb ~~Ti and P~~ show a strong negative anomaly (Fig. 3.4e). Compared to

the muscovite poor KQ, the trace element concentrations of the muscovite rich KQ show positive values for LILE (Fig. 3.4f). Higher concentrations of LILE can be explained by abundance of muscovite in the rock.

The UCC normalized REE pattern of the muscovite poor KQ are shown in Fig.3.4i. Barring Ce (shows both positive and negative anomaly) and Eu (small positive deviation with Eu/Eu*: 1.22-1.42), all other REE of the muscovite poor KQ show compositions similar to the UCC (Fig. 3.4e,f). Decoupling of Sr (negative anomaly) and Eu (positive anomaly) in the UCC normalized diagrams is intriguing. Positive Eu anomaly of the kyanite quartzite has been also reported by Owens and Pasek (2007). The muscovite rich KQ show slightly depleted values than the UCC in most REE (Fig.3.4j). Only Eu values cause a slight positive deviation in the slope. The muscovite rich REE normalised to UCC show mostly depleted or near UCC values and nearly flat REE patterns (Fig. 3.4j)

In the chondrite normalised (McDonough and Sun 1995) REE patterns, both muscovite poor and muscovite rich KQ show enriched LREE with flat and depleted HREE (Fig. 3.4k,l). Eu shows a small negative anomaly while a couple of samples show no Eu anomaly (Fig. 3.4k,l). The La_N/Yb_N varies from 8.23-25.81 and 1.67-21.21 in muscovite poor and muscovite rich KQ respectively.

3.6.3 Chemical alteration indices:

The unusual bulk compositions of the kyanite quartzite raises the possibility that the secondary process might have had a role to play in the formation of the protolith of the studied rocks. Following chemical alteration indices are obtained to understand the degree of chemical alteration. In view of their secondary nature, the muscovite, chemical alteration indices of the chloritoid and the other Al-phosphates bearing kyanite quartzite are calculated separately (Table 3.4a,b). The deviation of the chemical alteration indices

between the muscovite poor and muscovite (±chloritoid, Al-Phosphate) rich kyanite rich rocks should represent addition/extraction of the chemical species during the metasomatic alteration. Details of alteration indices are given in Appendix II.

Chemical Index of Alteration (CIA):

The average value for CIA for the KQ rocks is 98.31 (± 1.57). The average CIA value for muscovite rich KQ including chloritoid bearing KQ is 76.25 (± 4.80). The aluminophosphate (AP) bearing KQ has CIA of 94.47 as it is low to nil muscovite content (Table 3.4b). Unweathered igneous and sedimentary rocks have values of 50 or below (Nesbitt and Young, 1982). CIA values for unaltered plagioclase and K-feldspars are approximately equal to 50 and values of 100 indicate complete conversion of feldspar to aluminous clay minerals like kaolinite and gibbsite (Fedo et al., 1995).

A-CN-K ternary diagram: The muscovite poor KQ rocks of the study area plot in A-CN-K diagram above the feldspar join just near the Al_2O_3 apex (80-99% Al_2O_3) with a trend parallel to the CN-A arm (Fig.3.4m). The muscovite rich KQ rocks also plot above the feldspar join from 60-75% Al_2O_3 and the trend is parallel to the CN-A line too. The weathering trend of these rocks are obtained by taking the best fit line through their data point, as advocated by Bhat and Ghosh (2001). The weathering trends are near parallel to that of Average Upper Continental Crust (AUCC) which indicates that the quartzites may be derived from highly weathered rocks.

A-CNK-FM ternary diagram: Most of the data points of the studied muscovite poor and muscovite rich KQ rocks lie above the line joining feldspar point on the A-CNK boundary to the FM apex (Fig.3.4n). The muscovite poor KQs plot in a straight line extremely close and parallel to A-CNK line. The muscovite rich KQ rocks are scattered showing no single conclusive trend. However, a mixed source for the quartzites can be predicted.

Chemical Index of Weathering (CIW): The average CIW index for muscovite poor KQ rocks of the study area is 99.21 (±0.55). For the muscovite rich KQ the index average is 93.37 (±5.18). The CIW values for unaltered granitic and sedimentary rocks are ≤50 (Harnois 1988).

ACN ternary diagram or Plagioclase Index of Alteration (PIA): The average PIA values of muscovite poor KQ vary is 99.20 (±0.56) and of the muscovite rich KQ rocks is 91.48 (±6.48). The PIA values of muscovite rich and muscovite poor KQ rocks are plotted in the Al_2O_3-CaO-Na_2O diagram (Fig.3.4o). PIA values ≤50 are those of unweathered granitic and sedimentary rocks while values close to 100 indicate complete conversion into secondary aluminous clay minerals such as kaolinite, illite, and gibbsite (Fedo et al., 1995).

Advanced argillic alteration index (AAAI): The average value for advanced argillic alteration index for muscovite poor KQ varies is 95.77 (±2.29). In muscovite rich KQ the average AAAI value is 71.55 (±9.78) which is mostly due to the presence of mica.

The geochemical attributes of the studied KQ are consistent with the following:

1. The muscovite poor KQ is exceptionally rich in Al_2O_3 and depleted in FeO, MgO, CaO and Na_2O relative to the average compositions of sedimentary rocks and granitoids (and their metamorphic equivalents).
2. Positive values of Nb and positive anomaly of Pb (in Primitive mantle) and the near UCC concentrations of most of the muscovite poor KQ samples suggest its crustal origin.

3. High concentrations and Fractionated LREE and HREE (chondrite normalised La_N/Yb_N = 8.23-25.81) is consistent with the view that the protoliths of the KQs from a felsic /pelitic sources
4. Low concentrations of K in crustally derived protolith of the muscovite poor KQ require removal of K from the protolith in the secondary alteration process.
5. Small or no Eu anomaly (chondrite normalized) with insignificant Sr anomaly (primitive mantle normalized) is consistent with the view that the protolith of the muscovite poor KQ was derived from source rocks that did not contain significant calcic plagioclase.
6. The high CIA values of KQ reflect the removal of labile cations (Ca^{2+}, Na^{+}, K^{+}) relative to the static residual constituents (Al^{3+}) during weathering (Nesbitt and Young, 1982). The CIW index increases with the degree of depletion of sediment in Na and Ca relative to Al. The CIW index, however, avoids problems related to the remobilization of K during diagenesis or metamorphism. Hence CIW index values are higher than CIA values of the muscovite rich KQ, due to exclusion of K_2O from the index. Values of all the alteration indices of muscovite poor KQ rocks of the study area may be interpreted to show intense weathering with near complete alteration of feldspars in the precursor rocks. The muscovite rich KQ have comparatively lower values due presence of muscovite (±chloritoid, AP minerals)

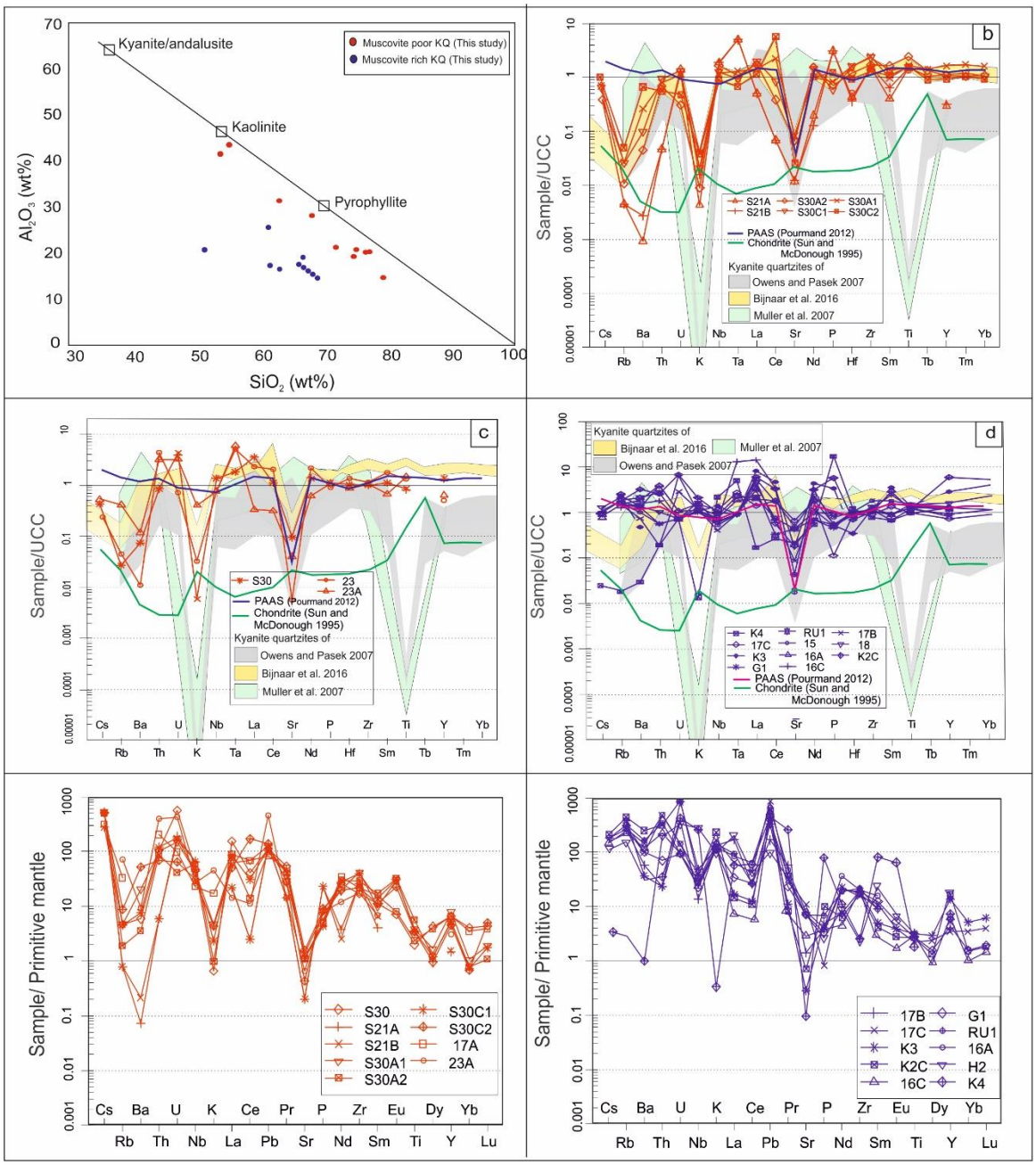

Fig 3.4 a) Plot of SiO_2 vs. Al_2O_3 (wt.%) in whole-rock samples of muscovite rich and muscovite-poor kyanite quartzite rocks of this study. Included for reference are the positions of quartz, pyrophyllite and kaolinite (plotted on an anhydrous basis).b) Trace element plot for muscovite-poor kyanite quartzite rocks from study area normalised against upper continental crust (UCC) from Taylor and McLennan (1995) c) Trace element plot for muscovite-poor kyanite quartzite rocks with slightly enriched La, Th and U from study area normalised against upper continental crust (UCC) from Taylor and McLennan (1995) d) Trace element compositions of muscovite-rich kyanite quartzite rocks from study area normalised against upper continental crust (UCC) from Taylor and McLennan (1995).e) Trace element plot for muscovite-poor kyanite quartzite of study area normalised against primitive mantle (Sun and McDonough 1989) f)Trace earth element plot for muscovite-rich kyanite quartzite of study area normalised against primitive mantle (Sun and McDonough 1989)
Post-Archean Australian shale (PAAS) data from Pourmand et al. 2012; Chondrite data from McDonough and Sun 1995; The shaded grey, green and yellow areas represent kyanite quartzite compositions from Piedmont Province Virginia (Owens and Pasek 2007), Solor, Norway (Muller 2007) and Suriname, Bosland (Bijnaar et al. 2016)

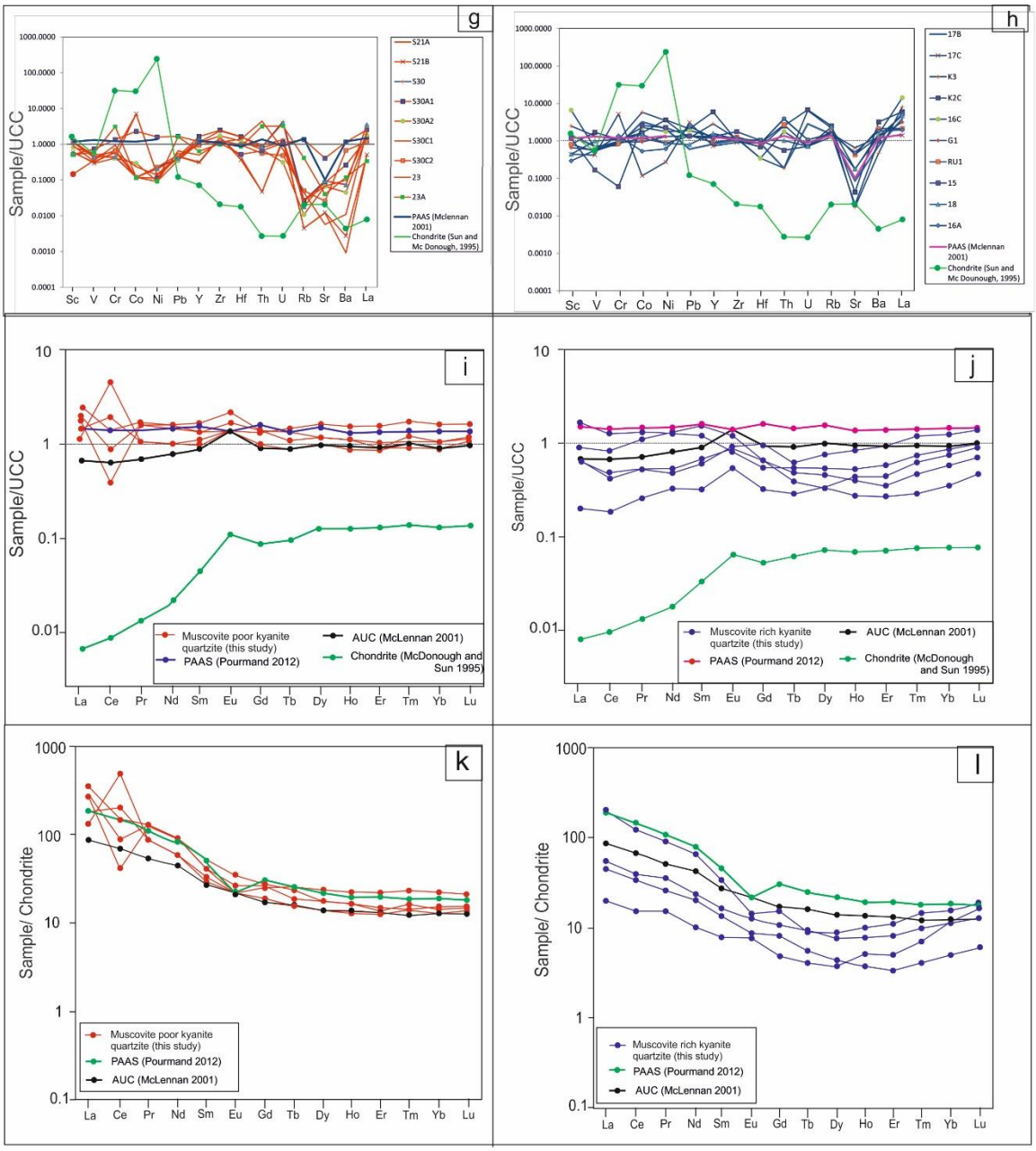

Fig 3.4 g) Spider plot of trace element compositions of muscovite-poor kyanite quartzite rocks from study area normalised against upper continental crust (UCC) from Taylor and McLennan (1995) h) Spider plot of trace element compositions of muscovite-rich kyanite quartzite rocks from study area normalised against upper continental crust (UCC) from Taylor and McLennan (1995) i) Rare earth element plots for muscovite-poor kyanite quartzite rocks of study area normalised against UCC (Taylor and McLennan1995) j) Rare earth element plots for muscovite-rich kyanite quartzite rocks of study area normalised against UCC (Taylor and McLennan 1995) k) Rare earth element plots for muscovite poor kyanite quartzite rocks of study area normalised against chondrite (McDonough and Sun 1995). l) Rare earth element plots for muscovite-rich kyanite quartzite rocks of study area normalised against chondrite (McDonough and Sun 1995)

Post-Archean Australian shale (PAAS) data from Pourmand et al. 2012; Chondrite data from McDonough and Sun 1995; Archean upper crust (AUC) data from McLennan 2001.

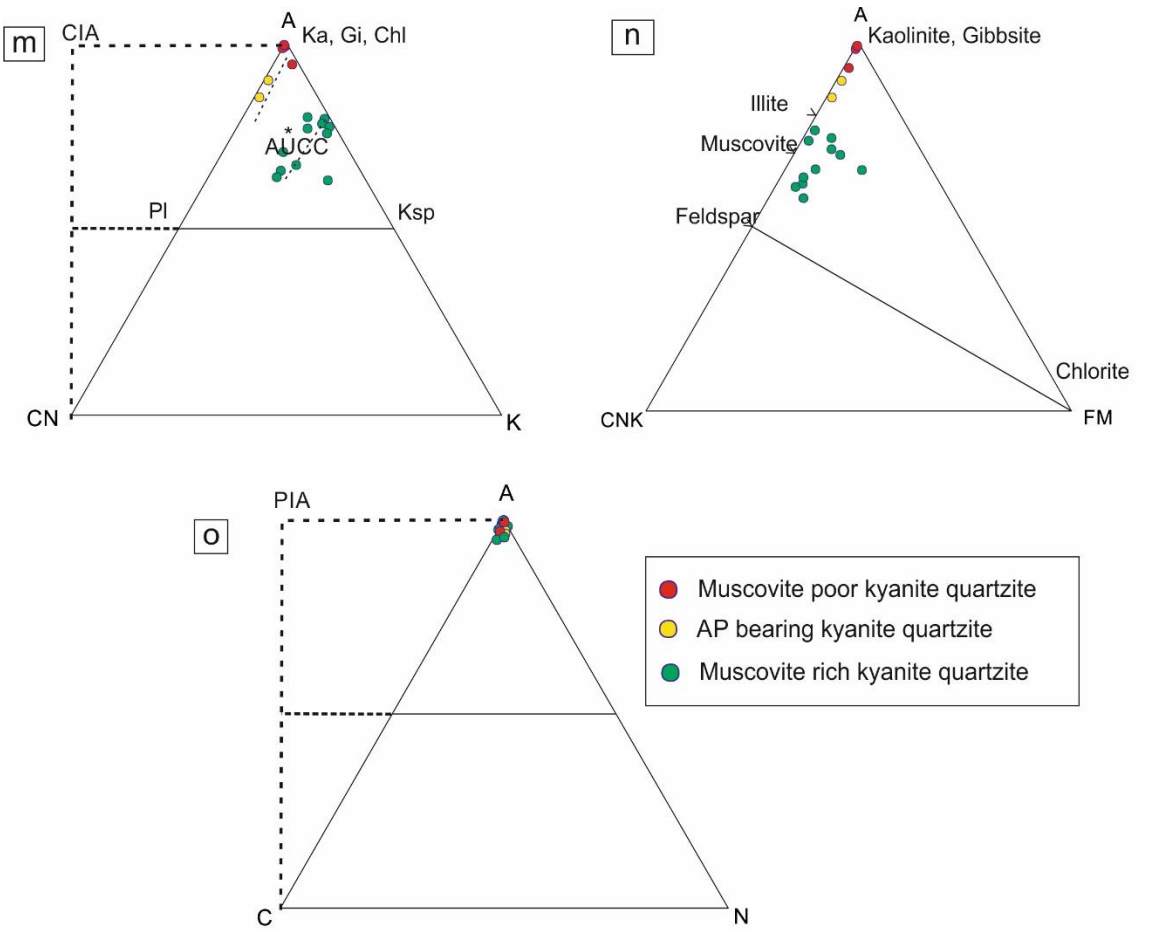

Fig 3.4: m) A-CN-K (in molecular proportion) ternary plot (Nesbitt and Young, 1984) for the muscovite poor and rich KQ, where CaO is the silicate fraction of rocks. CIA=[Al_2O_3/(Al_2O_3+CaO*+Na_2O+K_2O)] x 100. Mineral abbreviations: ka=kaolinite, gi=gibbsite, chl=chlorite, sm=smectite, K-sp=potassium feldspar, pl=plagioclase, AUCC=Average Upper Continental Crust n) A-CNK-FM (in molecular proportion) ternary plot (Nesbitt and Young,1989) for the muscovite poor and rich KQ rocks, where CaO* is the silicate fraction of rocks o) A-C-N (in molecular proportion) ternary plot (Fedo et al., 1995) for muscovite poor and rich KQ rocks. PIA = [(Al_2O_3-K_2O)/(Al_2O_3+CaO+NaO-K_2O)] x 100*

Table 3.4a: Bulk data analysis for rocks for muscovite poor kyanite quartzite from the studied area

	Muscovite poor kyanite quartzite									
Sample no.	S30	S21A	S21B	S30A1	S30A2	S30C1	S30C2	23A	17A	23
Al_2O_3	43.58	19.97	20.21	21.02	19.15	19.09	14.45	31.18	20.53	27.99
Na_2O	0.15	0.00	0.00	0.06	0.04	0.05	0.09	0.02	0.22	0.02
MgO	0.20	0.10	0.10	0.07	0.21	0.08	0.22	0.03	0.10	0.12
SiO_2	54.50	76.21	76.95	71.63	74.49	74.36	79.21	62.78	74.95	67.89
P_2O_5	0.18	0.50	0.50	0.153	0.105	0.095	0.197	0.17	0.11	0.14
SO_3	0.01	0.03	0.06					0.01	n.a.	0.01
K_2O	0.02	0.00	0.00	0.14	0.03	0.07	0.13	1.36	0.52	0.11
CaO	0.23	0.08	0.08	0.02	0.07	0.02	0.21	0.27	0.11	0.10
TiO_2	0.43	0.74	0.75	0.83	1.51	0.76	0.74	0.73	0.51	0.67
FeO	0.03	0.20	0.17	5.9	3.14	3.93	4.57	0.12	0.27	0.03
MnO	0.00	0.00	0.00	0.01	0.02	0.02	0.01	0.00	0.01	0.00
L.O.I	0.00	0.39	0.36	0.66	0.61	2.06	0.39	0.00	n.a.	0.00
Sum	99.33	98.22	99.20	100.46	99.71	100.51	100.71	96.68	97.33	97.09
Sc	16.00	7.80	8.20	n.a.	n.a.	n.a.	n.a.	7.0	13.03	2.0
V	47.00	33.20	31.20	52.00	57.00	35.00	45.00	62.0	84.00	38.0
Cr	36.00	51.20	33.80	n.a.	n.a.	n.a.	n.a.	256.0	423.00	78.0
Co	2.00	118.10	119.10	n.a.	n.a.	n.a.	n.a.	2.0	<5	2.0
Ni	10.00	6.30	6.10	n.a.	n.a.	n.a.	n.a.	4.0	<5.0	4.0
Cu	3.00	0.00	0.50	12.00	4.00	124.00	4.00	3.00	35.31	3.00
Zn	5.00	2.30	2.50	n.a.	n.a.	n.a.	n.a.	3.00	5.48	3.00
Ga	20.00	2.50	2.00	32.20	27.30	28.70	25.20	12.00	10.03	22.00
As	4.00	0.50	0.50	n.a.	n.a.	n.a.	n.a.	4.00	n.a.	4.00
Rb	3.00	0.50	0.50	3.00	1.20	2.90	5.60	46.00	21.03	5.00
Sr	33.00	4.20	4.30	29.30	23.10	23.50	9.00	14.00	23.87	2.00
Y	30.00	6.60	7.00	36.10	23.80	24.60	20.50	14.00	29.92	11.00
Zr	190.00	295.60	300.80	467.00	325.00	448.00	246.00	196.00	247.62	217.00
Nb	34.00	46.70	47.20	29.90	42.20	31.10	22.20	19.00	16.15	19.00
Mo	2.00	0.50	0.50	n.a.	n.a.	n.a.	n.a.	2.00	n.a.	2.00
Sn	7.00	7.00	7.00	3.00	2.00	3.00	2.00	7.00	n.a.	7.00
Ba	41.00	0.50	1.50	144.00	24.80	54.10	368.00	65.00	n.a.	6.00
La	106.00	15.10	15.30	43.20	52.50	60.50	35.70	10.00	n.a.	68.00
Ce	72.00	4.40	4.40	124.00	24.80	54.10	300.00	20.00	n.a.	130.00
Pr	15.00	4.00	4.00	8.92	11.25	10.60	7.65	4.00	n.a.	15.00
Nd	35.00	5.10	3.40	25.60	42.60	38.56	25.80	16.00	n.a.	57.00
Sm	5.00	1.80	2.90	4.35	7.56	6.04	5.98	3.00	n.a.	8.00
Hf	6.00	2.50	2.10	9.49	7.16	8.20	5.30	5.00	n.a.	8.00
Ta	4.00	11.00	11.00	2.93	2.40	2.15	1.50	13.00	n.a.	11.00
W	31.00	1011.50	1020.70	n.a.	n.a.	n.a.	n.a.	21.00	n.a.	11.00
Pb	8.00	9.10	9.00	n.a.	n.a.	n.a.	n.a.	32.00	5.89	13.00
Bi	3.00	3.00	3.00	n.a.	n.a.	n.a.	n.a.	3.00	n.a.	3.00
Th	9.00	0.50	0.50	8.61	7.46	10.20	5.93	34.00	17.37	47.00
U	12.00	4.00	3.50	3.19	0.87	3.71	1.35	9.00	2.07	2.00
Eu	n.a.	n.a.	n.a.	1.23	1.93	1.46	1.23	n.a.	n.a.	n.a.
Gd	n.a.	n.a.	n.a.	4.01	5.12	5.18	3.97	n.a.	n.a.	n.a.
Tb	n.a.	n.a.	n.a.	0.92	0.85	0.68	0.58	n.a.	n.a.	n.a.
Dy	n.a.	n.a.	n.a.	5.76	4.27	4.21	3.38	n.a.	n.a.	n.a.
Ho	n.a.	n.a.	n.a.	1.23	0.89	0.89	0.7	n.a.	n.a.	n.a.
Er	n.a.	n.a.	n.a.	3.55	2.58	2.18	2.02	n.a.	n.a.	n.a.
Tm	n.a.	n.a.	n.a.	0.59	0.35	0.4	0.36	n.a.	n.a.	n.a.
Yb	n.a.	n.a.	n.a.	4.48	2.68	2.32	2.05	n.a.	n.a.	n.a.
Lu	n.a.	n.a.	n.a.	0.52	0.38	0.36	0.34	n.a.	n.a.	n.a.
CIA	99.09	99.60	99.61	98.96	99.27	99.27	97.11	94.97	96.04	99.18
CIW	99.14	99.60	99.61	99.62	99.43	99.63	97.97	99.08	98.41	99.57
PIA	99.14	99.60	99.61	99.62	99.43	99.63	97.95	99.04	98.37	99.57
AAAI	90.38	97.69	97.71	97.95	95.88	98.02	93.84	95.15	94.53	96.59

Major oxides are given in wt%; Trace elements are given in ppm

Table 3.4b: Bulk data analysis for rocks for muscovite rich kyanite quartzite and associated rocks from the studied area

	Muscovite rich kyanite quartzite											AP bearing KQ	Ap bearing schist	Grt-Cld-Bt Schist	Grt-Cld-Bt Schist	Cld Mus Schist	Mylonitized Soda granite	Muscovite schist	Kyanite tourmaline schist	Kyanite tourmaline schist
Sample no.	17B	17C	K3	K2C	16C	G1	RU1	15	18	H2	16A	K4	19C	L5A	K3	L8	L9	N5A	NS7	SG20
Al_2O_3	17.81	25.76	20.29	17.01	16.23	14.97	16.70	13.61	20.60	15.91	16.17	41.35	47.84	17.54	16.96	20.88	15.28	33.96	54.21	20.87
Na_2O	0.12	1.31	0.02	0.12	0.02	1.45	0.43	0.02	0.38	1.19	1.58	0.15	0.85	0.30	0.19	0.67	5.40	0.95	0.28	0.13
MgO	2.39	0.26	2.98	2.13	0.89	1.47	0.88	1.56	0.39	1.66	1.06	0.16	0.14	3.55	3.90	1.29	5.98	0.28	1.24	0.05
SiO_2	65.62	61.15	49.35	60.51	62.59	69.02	66.78	70.13	67.62	68.45	67.98	53.55	42.78	63.39	54.44	60.59	53.32	52.11	24.29	75.38
P_2O_5	0.08	0.02	0.54	0.91	0.08	0.07	0.15	0.12	0.09	0.06	0.09	1.74	2.74	0.18	0.93	0.12	2.11	0.05	0.05	0.05
SO_3	0.01	0.01	0.01	0.01	0.01	0.01	0.01	0.01	0.01	0.01	0.01	0.01	0.01	n.a.	n.a.	n.a.	n.a.	n.a.	n.a.	n.a.
K_2O	4.00	5.14	3.51	7.10	3.72	3.37	4.33	3.51	5.49	2.93	3.73	0.01	0.04	4.14	4.67	3.49	3.22	7.36	0.16	0.48
CaO	0.06	0.05	0.69	1.21	0.27	1.00	1.54	0.10	0.07	0.84	1.40	2.26	3.75	0.25	1.13	0.10	3.04	0.01	0.38	0.01
TiO_2	0.63	0.49	0.70	0.58	0.65	0.59	0.65	0.77	0.74	0.68	0.69	0.40	0.48	0.69	0.80	0.74	0.46	0.59	0.79	0.77
FeO	4.93	0.61	19.34	6.95	11.68	5.12	4.92	7.40	1.29	6.14	4.14	0.03	0.05	7.22	16.68	6.89	8.89	0.78	1.94	0.23
MnO	0.00	0.00	0.02	0.02	0.08	0.03	0.07	0.00	0.00	0.05	0.08	0.00	0.00	0.02	0.02	0.03	0.02	0.01	0.01	0.01
L.O.I	0.00	0.00	0.00	0.00	0.00	0.00	0.00	0.00	0.00	0.00	0.00	0.00	0.00	n.a.	n.a.	n.a.	n.a.	n.a.	n.a.	n.a.
Sum	95.65	94.80	97.46	96.56	96.23	97.11	96.46	97.24	96.68	97.92	96.93	99.66	98.69	97.28	99.72	94.81	97.72	96.10	83.36	97.99
Sc	19.0	6.0	34.0	11.0	90.0	9.0	11.0	16.0	6.0	7.00	4.0	15.00	5.0	17.40	12.21	15.52	15.11	6.71	12.63	9.80
V	77.0	45.0	145.0	182.0	70.0	61.0	57.0	18.0	106.0	79.00	60.0	47.00	245.0	4.00	136.00	97.00	227.00	55.00	167.00	87.00
Cr	63.0	433.0	89.0	93.0	81.0	77.0	71.0	5.0	91.0	111.00	113.0	37.00	97.0	214.00	236.00	96.00	284.00	129.00	327.00	350.00
Co	55.0	2.0	99.0	28.0	39.0	16.0	20.0	44.0	25.0	39.00	9.0	2.00	2.0	39.25	48.68	35.73	33.13	<5	32.44	<5
Ni	93.0	12.0	153.0	160.0	78.0	57.0	38.0	100.0	38.0	70.00	27.0	9.00	4.0	42.90	88.00	24.61	160.94	<5.0	65.21	<5.0
Cu	48.00	3.00	192.00	42.00	739.00	3.00	20.00	60.00	3.00	44.00	4.00	3.00	3.00	80.56	82.37	73.43	313.13	32.76	51.41	35.25
Zn	3.00	3.00	3.00	15.00	55.00	77.00	24.00	3.00	3.00	70.00	66.00	5.00	8.00	7.45	9.80	12.91	5.17	2.46	16.39	6.07
Ga	21.00	16.00	29.00	27.00	19.00	19.00	22.00	23.00	32.00	16.00	23.00	19.00	47.00	14.76	21.13	18.40	20.51	5.54	15.70	3.47
As	4.00	4.00	4.00	4.00	4.00	4.00	4.00	4.00	4.00	4.00	4.00	4.00	4.00	n.a.	n.a.	n.a.	n.a.	n.a.	n.a.	n.a.
Rb	168.00	175.00	246.00	282.00	142.00	197.00	207.00	174.00	261.00	151.00	171.00	2.00	2.00	152.73	178.01	144.99	192.89	225.04	2.77	13.95
Sr	30.00	230.00	6.00	15.00	61.00	151.00	150.00	7.00	62.00	141.00	170.00	33.00	74.00	3.55	3.21	30.89	19.79	27.76	48.67	5.04
Y	18.00	16.00	63.00	131.00	29.00	20.00	26.00	29.00	35.00	26.00	27.00	29.00	26.00	24.66	57.79	23.83	141.85	0.65	19.46	22.82
Zr	199.00	173.00	218.00	193.00	228.00	214.00	242.00	337.00	208.00	201.00	224.00	189.00	146.00	280.00	140.57	187.05	146.93	147.60	207.11	204.38
Nb	10.00	28.00	35.00	25.00	17.00	16.00	21.00	13.00	15.00	8.00	19.00	34.00	54.00	20.07	16.26	16.03	9.79	14.98	20.87	21.37
Mo	7.00	2.00	12.00	10.00	7.00	2.00	2.00	2.00	2.00	2.00	2.00	2.00	11.00	n.a.	n.a.	n.a.	n.a.	n.a.	n.a.	n.a.
Sn	7.00	11.00	7.00	21.00	15.00	7.00	19.00	7.00	7.00	7.00	7.00	7.00	7.00	n.a.	n.a.	n.a.	n.a.	n.a.	n.a.	n.a.
Ba	405.00	698.00	260.00	1763.00	850.00	712.00	1166.00	545.00	742.00	630.00	1004.00	40.00	16.00	n.a.	n.a.	n.a.	n.a.	n.a.	n.a.	n.a.
La	117.00	42.00	246.00	181.00	426.00	95.00	64.00	162.00	142.00	76.00	59.00	106.00	5.00	n.a.	n.a.	n.a.	n.a.	n.a.	n.a.	n.a.
Ce	46.00	116.00	300.00	212.00	222.00	21.00	47.00	109.00	36.00	90.00	114.00	72.00	17.00	n.a.	n.a.	n.a.	n.a.	n.a.	n.a.	n.a.
Pr	16.00	9.00	34.00	25.00	50.00	14.00	10.00	23.00	20.00	12.00	13.00	15.00	3.00	n.a.	n.a.	n.a.	n.a.	n.a.	n.a.	n.a.
Nd	30.00	46.00	112.00	82.00	84.00	18.00	26.00	61.00	18.00	42.00	49.00	36.00	14.00	n.a.	n.a.	n.a.	n.a.	n.a.	n.a.	n.a.
Sm	4.00	6.00	16.00	13.00	11.00	3.00	4.00	8.00	4.00	6.00	7.00	5.00	3.00	n.a.	n.a.	n.a.	n.a.	n.a.	n.a.	n.a.
Hf	5.00	5.00	2.00	4.00	2.00	6.00	5.00	6.00	6.00	3.00	5.00	6.00	7.00	n.a.	n.a.	n.a.	n.a.	n.a.	n.a.	n.a.
Ta	2.00	6.00	2.00	2.00	29.00	2.00	5.00	2.00	2.00	2.00	4.00	4.00	11.00	n.a.	n.a.	n.a.	n.a.	n.a.	n.a.	n.a.
W	11.00	8.00	7.00	27.00	42.00	5.00	11.00	12.00	14.00	3.00	3.00	32.00	75.00	n.a.	n.a.	n.a.	n.a.	n.a.	n.a.	n.a.
Pb	12.00	62.00	24.00	42.00	38.00	28.00	27.00	27.00	16.00	33.00	48.00	8.00	6.00	3.32	7.37	4.29	5.34	3.90	6.39	5.53
Bi	28.00	3.00	18.00	3.00	17.00	3.00	3.00	11.00	9.00	17.00	3.00	3.00	3.00	n.a.	n.a.	n.a.	n.a.	n.a.	n.a.	n.a.
Th	2.00	41.00	2.00	27.00	19.00	6.00	29.00	6.00	11.00	7.00	42.00	9.00	2.00	25.87	14.09	20.61	34.77	5.98	38.56	16.97
U	8.00	3.00	18.00	19.00	2.00	2.00	2.00	2.00	2.00	3.00	3.00	11.00	2.00	3.68	10.25	4.64	10.47	3.84	2.47	2.60
CIA	80.99	79.85	82.78	66.86	80.19	72.01	72.61	78.94	77.62	76.23	70.67	94.47								
CIW	99.00	94.99	96.62	92.75	98.24	85.94	89.45	99.13	97.86	88.68	84.44	94.49								
PIA	98.71	93.81	95.94	88.17	97.73	82.56	86.26	98.83	97.11	86.48	80.67	94.49								
AAAI	71.86	79.06	57.22	63.62	84.14	63.78	70.09	80.67	88.95	64.97	62.72	67.57								

Major oxides are given in wt%; Trace elements are given in ppm

Table 3.5: Bulk data analysis for rocks for kyanite quartzites and associated rocks from the Singhbhum shear zone

	KQ (this study)		Granite*		Pelite**	
Sample	Avg.	σ	Avg.	σ	Avg.	σ
SiO_2	69.50	8.46	72.48	4.09	63.95	2.71
TiO_2	0.70	0.21	0.30	0.11	0.88	0.15
Al_2O_3	24.54	9.55	14.04	0.69	19.43	1.50
FeO	2.14	2.61	4.06	1.51	6.96	0.93
Na_2O	0.17	0.33	3.07	0.27	1.48	0.46
K_2O	0.44	0.87	4.64	0.85	3.92	0.29
CaO	0.36	0.64	1.46	0.48	0.79	0.49
MgO	0.25	0.45	0.19	0.32	2.49	0.45
MnO	0.01	0.02	0.07	0.03	0.09	0.03
P_2O_5	0.33	0.47	0.04	0.01	n.a.	n.a.
SO_3	0.02	0.02	n.a.	n.a.	n.a.	n.a.
L.O.I	0.41	0.61	0.77	0.46	n.a.	n.a.
Sum	98.90		101.11		100.00	

*Average granite composition from Yadav et al. 2016; **Average pelite compositions from Forshaw and Pettison 2022. All iron is shown as FeO_{total} with volatiles (loss-on-ignition [LOI], H_2O, CO_2, and SO_3) removed; σ=standard deviation from samples of a population

Table 3.6: Bulk data analyses of rocks from Chaibasa and Dhalbhum formations from various publications

	Upper Chaibasa Schist		Upper Chaibasa Phyllite	Upper Chaibasa Quartzite		Upper Dhanjori Schist		Upper Dhanjori quartzite			Lower Dhanjori quartzite			Lower Dhanjori phyllite	Dhanjori Tuff		Dhanjori volcanic	
Al_2O_3	12.47	13.96	20.18	4.54	12.96	31.60	28.82	0.53	0.60	2.36	2.28	11.80	15.25	19.68	13.60	13.85	8.22	6.30
Na_2O	1.87	2.26	1.30	0.61	2.37	0.79	0.73	0.04	0.04	0.04	0.02	3.51	3.66	0.09	2.56	2.26	2.93	1.92
MgO	0.91	0.87	1.24	0.13	1.24	0.74	0.44	0.02	0.11	0.61	0.09	0.52	0.76	1.95	8.43	9.07	9.51	10.70
SiO_2	73.67	71.50	59.97	57.00	89.32	73.08	50.50	56.16	95.30	94.18	89.29	95.21	79.75	73.10	61.09	49.83	48.98	56.08	54.34
P_2O_5	0.05	0.07	0.08	0.09	0.03	0.04	0.07	0.10	0.01	0.03	0.10	0.02	0.03	0.04	0.07	0.13	0.12	0.09	0.07
K_2O	2.07	2.18	5.04	5.28	1.92	2.12	9.10	7.89	0.15	0.15	0.27	0.78	1.75	2.85	7.66	0.29	0.13	0.41	0.19
CaO	1.07	1.46	0.64	0.51	0.15	1.09	0.17	0.10	0.01	0.02	0.02	b.d.	0.12	0.18	0.07	11.03	11.69	9.13	10.56
TiO_2	0.48	0.58	0.90	0.96	0.12	0.50	0.56	0.36	0.83	0.03	0.09	0.06	0.13	0.11	0.61	0.80	0.71	0.77	0.64
Fe_2O_3	4.57	3.81	6.15	7.78	1.01	4.54	2.22	1.37	2.59	4.43	5.12	0.16	0.85	1.92	4.62	13.23	11.73	13.28	14.85
MnO	0.07	0.07	0.07	0.17	0.01	0.06	b.d.	b.d.	b.d.	0.01	b.d.	b.d.	0.02	0.04	0.05	0.16	0.15	0.16	0.20
L.O.I	2.40	2.80	4.10	4.20	1.60	1.80	4.10	3.90	0.30	0.30	1.80	1.20	1.40	1.90	3.90	1.83	2.11	–	–
Sum	99.63	99.56	99.67	99.63	99.44	99.79	99.85	99.87	99.78	99.85	99.70	99.82	99.88	99.81	99.79	101.00	101.00	100.58	99.70
Sc	10	10	20	21	3	8	34	16	6	1	3	2	2	1	12	32	26		
V	61	57	113	130	17	72	222	102	6	10	43	10	16	12	52	353	160	127	140
Cr	68	62	103	123	b.d.	55	198	164	27	136	89	34	21	b.d.	55	296	102	1270	962
Co																53	46	69	61
Ni	28.9	23	37.1	48.2	2.9	41.9	0.7	1.9	4	23	76	2.3	9.4	6.3	15	107	41	290	257
Cu	39	37	28	28	9.8	55	4.3	7.8	7.1	175	1055	3.9	1.6	1.9	0.9	49	194	135	72
Zn																55	54	81	71
Ga																		11	14
Rb	103	1158	219	221	60	114	354	242	6.5	4.9	11.6	36.4	69	103	279	7	2	3	17
Sr	142	188	114	88.5	39.7	153	51.7	35.7	2.2	32.6	12.5	6.6	82.6	105	15.1	129	76	38	89
Y	24.4	20.7	23.4	22.9	11.3	14.5	39	14.1	13.2	4.7	22.7	6.8	5.5	2.9	19.2	17.1	15	17.8	23.9
Zr	194	211	206	200	98.3	266	222	147	258	44.9	77	48.2	84.9	112	218	44	42	85	128
Nb	9	12.1	18.9	18.1	2.9	9	12.8	9.7	16.5	0.8	2	2	3.7	3.9	16.4	3.3	2	4	5.5
La	30.4	30	41.4	31.1	17.8	21.9	2	16.1	2	4.1	16.4	4.9	18.3	51.7	33.9	4.53	1.67	9.07	19.6
Ce	66.4	47.9	81.4	82.8	32.6	57	4	33.6	4	8.6	36.2	9.7	37.8	119.3	84.1	9.96	3.78	21.6	42.8
Pr	7.54	7.28	9.68	7.17	4.08	5.6	0.53	4.42	0.45	1.04	4.11	1.15	3.7	8.97	9.18	nd	nd	2.19	4.62
Nd	27.7	26.7	36.1	27.3	15.1	21.7	2.1	19.5	1.5	3.7	16	4.6	12.8	27.9	33	7.14	4.44	9.44	18.5
Sm	5	4.8	6.7	5.1	2.8	3.9	0.9	4.4	0.3	0.8	3.3	0.9	1.8	3	5.8	2.17	1.51	2.69	4.58
Hf	5.2	6.2	6.2	6	3	7.8	6.6	4.4	7.2	1.2	2.2	1.3	2.3	3.1	6.8	1.13	1.08	2.3	3.3
Pb	44	7.4	4.3	3.7	3.6	4.2	1.5	2.4	1.3	1.1	0.6	0.5	1.4	2.1	2.2				
Th	12.8	17.7	23.5	22.9	5.7	12	17.2	72	6.3	1.1	3.6	2.2	5.6	13.8	23.3	2	2	2.33	3.17
U	2.8	3.6	3.1	2.2	1.1	1.7	3.5	3.7	3.6	0.8	11	1.1	0.7	0.9	4.4	2	2	0.41	0.47
Ba	465	495	1216	1092	414	447	472	301	28	39	41	78	173	280	735			7	23
Eu	0.97	0.9	1.33	1.01	0.59	0.78	0.36	0.9	0.14	0.14	0.34	0.19	0.46	0.5	1.27	0.92	0.59	1.07	1.33
Gd	3.79	3.68	5.21	3.72	2.4	2.96	1.97	3.03	0.7	0.55	3.4	0.97	1.16	1.06	3.68	2.7	2.45	2.99	4.43
Tb	0.66	0.62	0.87	0.68	0.39	0.44	0.57	0.43	0.23	0.15	0.7	0.17	0.18	0.15	0.67	0.48	0.32	0.56	0.77
Dy	4.07	3.92	4.75	4.1	2.14	2.43	4.53	2.08	1.92	0.86	4.2	1.05	0.85	0.56	3.87	3.2	2.47	3.45	4.33
Ho	0.83	0.77	0.86	0.88	0.43	0.47	1.13	0.45	0.49	0.18	0.89	0.22	0.19	0.09	0.78	0.68	0.41	0.67	0.84
Er	2.46	2.49	2.75	2.59	1.23	1.48	3.66	1.38	1.52	0.49	2.63	0.64	0.55	0.31	2.58	1.86	1.4	1.94	2.53
Tm	0.35	0.38	0.43	0.4	0.17	0.24	0.63	0.23	0.31	0.09	0.39	0.11	0.09	0.05	0.42	nd	0.27	0.263	0.362
Yb	2.33	2.48	2.89	2.6	1.19	1.59	3.81	1.65	2.3	0.58	2.37	0.66	0.54	0.33	3.04	1.81	1.41	1.5	2.11
Lu	0.35	0.38	0.46	0.41	0.18	0.26	0.58	0.28	0.32	0.08	0.33	0.1	0.09	0.06	0.44	0.33	0.19	0.196	0.297

Sources: Roy et al 2002, Mazumder and Arima 2009, De et al 2015, Singh et al 2018; Trace element data in ppm, Oxide data in wt%

3.7 Physical conditions of metamorphism

Mineral assemblage of the studied rocks are not suitable for application of the conventional geothermobarometry. For this reason, pseudosection for an appropriate muscovite rich KQ has been constructed using the the computer program PERPLE_X version 6.9 (Connolly, 2009, 2005) with the thermodynamic dataset of Holland and Powell (1998) and solution model used for white mica was (Holland and Powell, 1998). In view of the mineral compositions TiKASH (TiO_2-K_2O-Al_2O_3-SiO_2-H_2O) system has been chosen. Na_2O is excluded owing to its low concentrations in the chosen bulk. H_2O is considered as a saturated fluid with activity of H_2O=1. Fig. 3.5.1 represents the P-T pseudsection. The studied rock develops the assemblage kyanite + rutile + quartz + muscovite. The stability field of this studied assemblage determines the peak metamorphic field (marked in green) in P-T space. The pseudosection constrain a large temperature range (400°C-650°C) in the pressure range between 6-7 kbar (Fig. 3.5.1). Owing to temperature sensitive reactions and presence of only kyanite (no sillimanite or andalusite), precise estimation of pressure cannot be inferred from the pseudosection. Nevertheless, a pressure more than 4 kbar can be inferred in the temperature is at or more than the P-T conditions where three Al_2SiO_5 are stable.

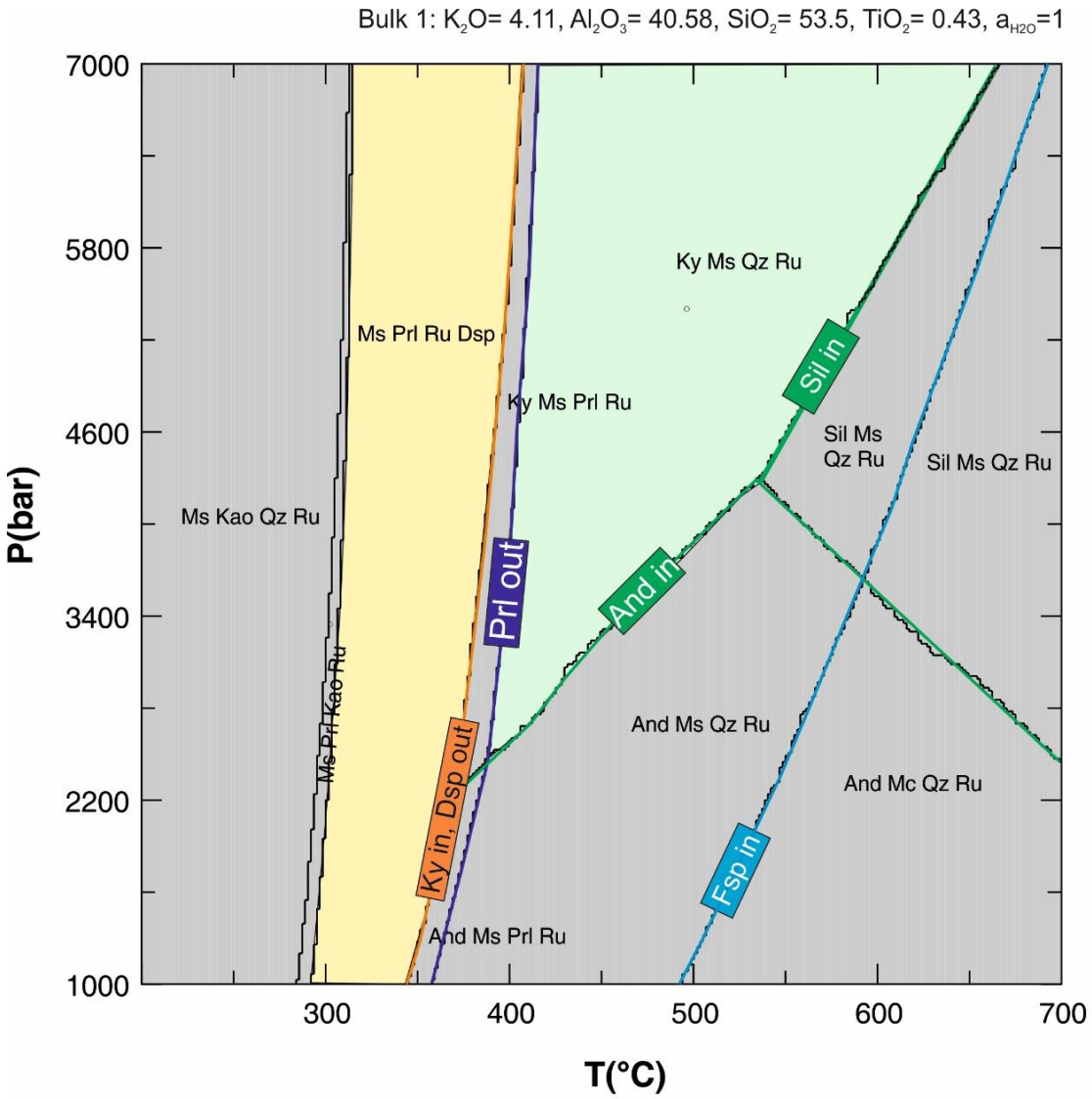

Fig 3.5.1 P-T pseudosection calculated for kyanite quartzite of Ujainpur in TiKASH model system with bulk 1. The bulk composition is given as wt% of the oxides. Field marked in green colour in the diagram represents the peak assemblage of the rock. The area marked in yellow colour in the diagram represents the retrograde assemblage in the rock. All abbreviations are after Whitney and Evans (2010)

.

3.8 Stability of different mineral assemblages in the muscovite poor and muscovite rich KQ rocks in compositional space: the isothermal-isobaric chemical potential diagram (μ_{K2O}-μ_{SiO2})

The 'frozen in' textures in the muscovite poor KQ and muscovite rich KQ suggest formation of muscovite and corundum after kyanite (section3.2). Textural modelling of these reactions (section 3.5), suggest infiltration of aqueous fluid loaded with alkali into the KQ developed muscovite (Fig.3.2c,d) and corundum(Fig.3.2e) after kyanite. In order to understand the fluid rock interaction during the infiltration driven metamorphism two sets of μSiO_2-μK_2O diagrams were constructed in the K_2O-Al_2O_3-SiO_2-H_2O (KASH) system. The computer program PERPLE_X (version 6.8.6) was used together with the thermodynamic data of Holland and Powell (2002). The activity of H_2O is considered as 1, an assumption that is considered reasonable for low grade metamorphic rocks. Also included in the chemical potential diagram is the minimum silica activity at which quartz is stable (the Qz sat line).

In the first set of diagrams pressure was held constant and the temperature varied from 450^{o}C to 600^{o}C (Fig. 3.5.2 a-d). In the other set, pressure varied in the range of 6-8 kbar at the constant temperature of 500^{o}C (Fig. 3.5.3 a-d). The variations of temperature at constant pressure (or pressure at constant temperature) help visualize the change of the stability fields of the mineral assemblages relevant to the present study at different geothermal gradients (~63-100^{o}C/km).

Results:

The constructed chemical potential diagrams have the following features:

1. Corundum forms after kyanite and muscovite with decreasing chemical potential of μSiO_2 below the saturation of quartz**.** A reduction of μK_2O can directly convert

muscovite to corundum. The constructed chemical potential diagrams suggest that quartz and corundum are unstable in the chosen range of P-T conditions.

2. With increasing μK_2O both corundum and kyanite transforms to muscovite to K-feldspar. K-feldspar is stable at higher μK_2O and μSiO_2 relative to all other phases.
3. Temperature has stronger effect than the pressure on the stability of the different mineral assemblages in the chemical potential diagrams. At constant pressure, increasing temperature (i.e. hotter geothermal gradient) increases the stability field of corundum significantly and K-feldspar is completely eliminated at temperature beyond 550^{o}C. In the temperature range of 550-600^{o}C, kyanite to muscovite transformation is possible only at μSiO_2 close to quartz saturation (Fig. 3.5.2 c,d).
4. Kyanite can form from muscovite only by reduction of μK_2O irrespective of the abeyant P-T condition.

In view of these general observations, the mineral transformation in the studied rocks can be attempted. The textural features show that muscovite and corundum form in isolated domains that are separated by kyanite (±quartz) aggregates. Formation of muscovite in layers and pods in the kyanite rich rocks (even in a single thin section) can only be explained by an increase in μK_2O during infiltration of the aqueous fluid at constant pressure and temperature condition (shown by white arrow, Figs.3.5.2, 3.5.3) Similarly, corundum formed after kyanite only when the μSiO_2 of the fluid dropped at or below the kyanite-corundum line (shown by red arrow in Figs. 3.5.2, 3.5.3). Since kyanite-muscovite transformation is more common than kyanite-corundum transformation the temperature during the infiltration driven process is likely to be around 500^{o}C at pressure between 5-7 kbar. The kyanite-muscovite has a negative slope in the μSiO_2-μK_2O diagram, whereas kyanite-corundum line is insensitive to μK_2O (Figs. 3.5.2, 3.5.3). This follows then that muscovitization and formation of corundum

after kyanite are likely to have formed by two different fluids. Since corundum and quartz are not stable, corundum after kyanite occurred in quartz absent domains.

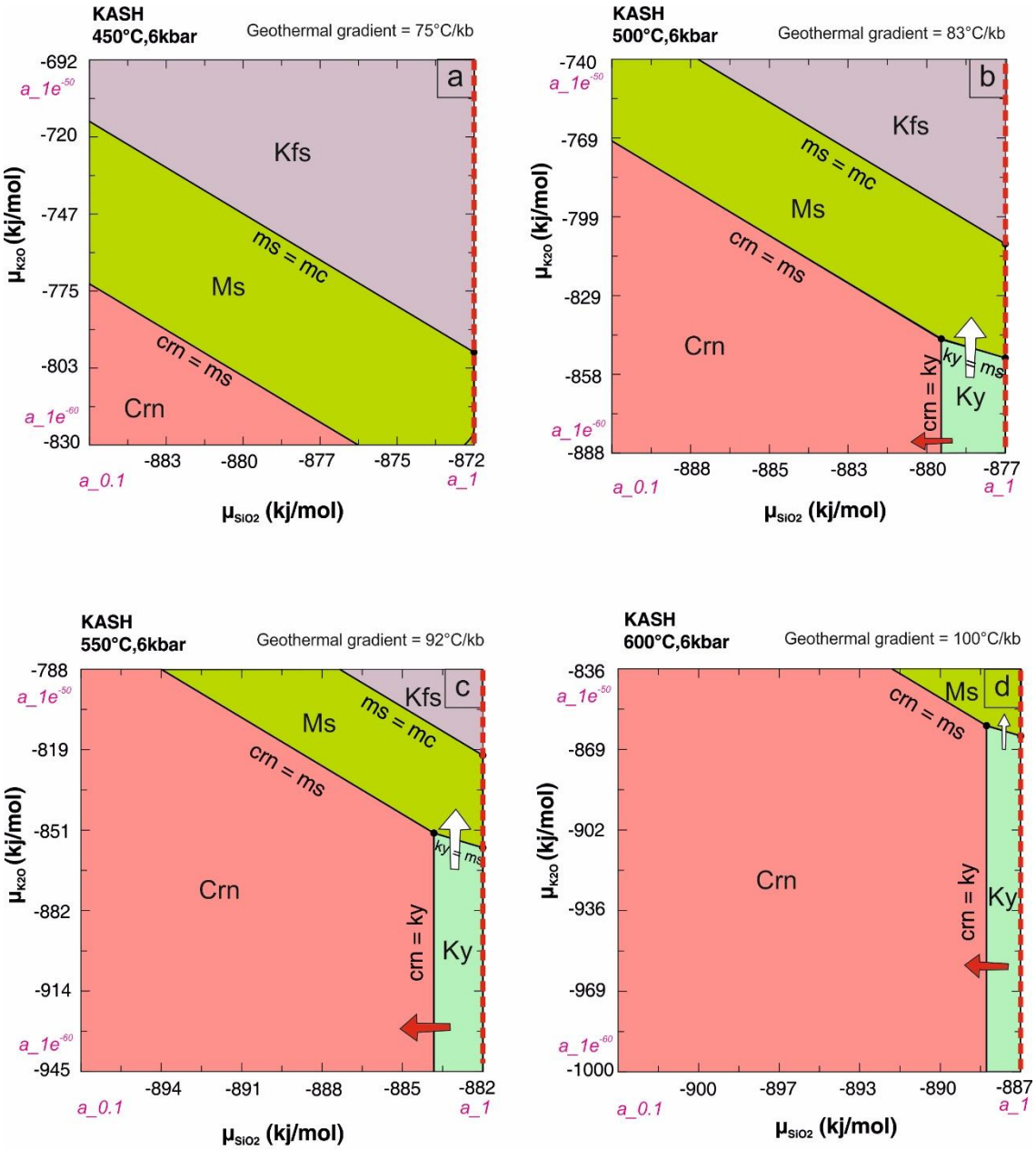

Fig 3.5.2: μK2O-μ SiO2 diagram computed at 6kb and a) 450°C b) 500°C c) 550°C and d) 600°C in a KASH (K_2O-Al_2O_3-SiO_2-H_2O) system. The thick white arrow indicates formation of muscovite from kyanite. The red arrow shows formation of kyanite from corundum. The red dotted line marks the quartz saturation line. Mineral abbreviations are after Whitney and Evans (2010)

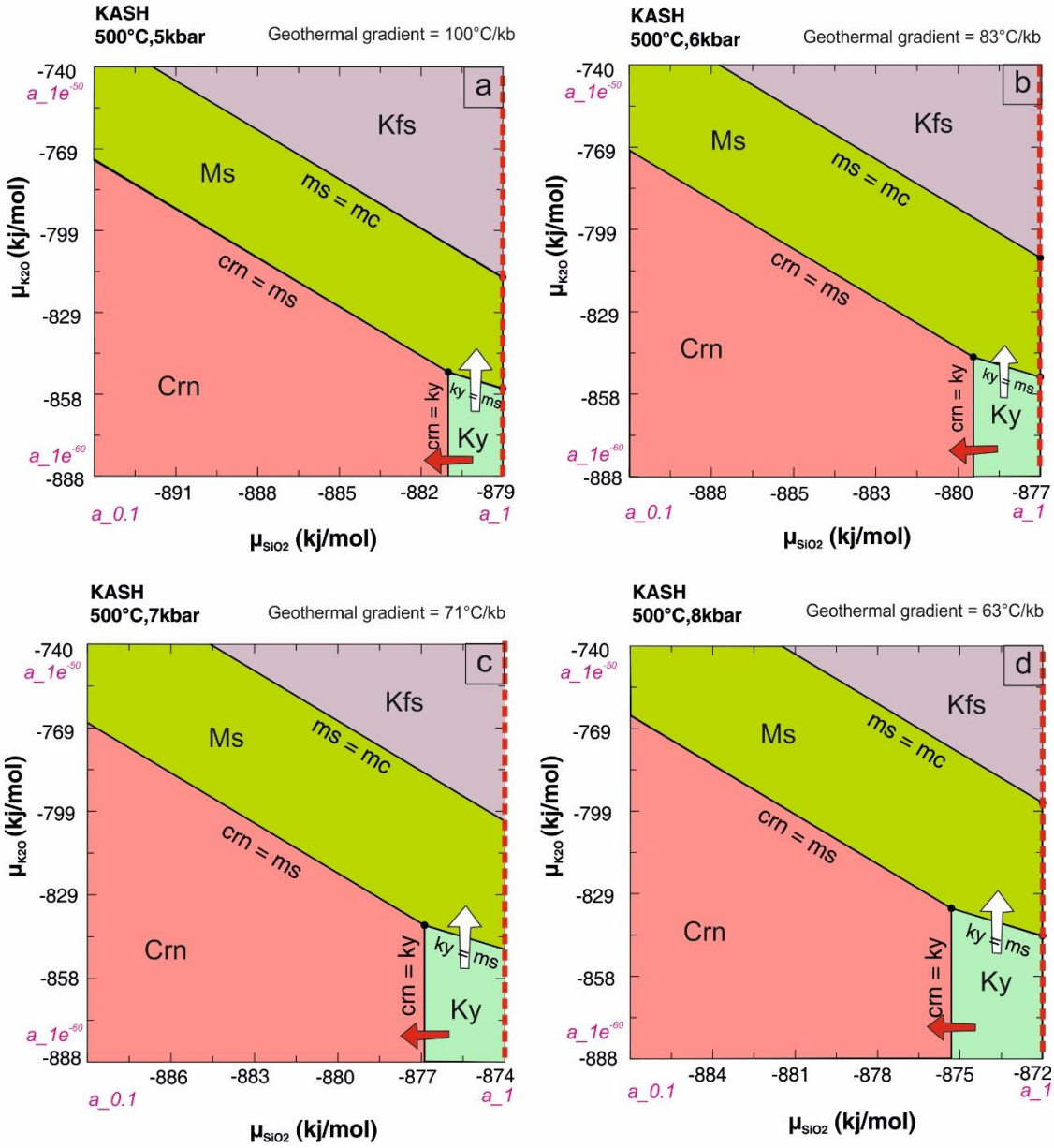

Fig 3.5.3: μK_2O-μSiO_2 diagram computed at 500°C and a) 5kb b) 6kb c) 7kb and d) 8kb in a KASH (K_2O-Al_2O_3-SiO_2-H_2O) system. The thick white arrow indicates formation of muscovite from kyanite. The red arrow shows formation of kyanite fromcorundum. The red dotted line marks the quartz saturation line. Mineral abbreviations are after Whitney and Evans (2010)

3.9 Stable isotope composition

The stable oxygen isotope values of kyanite from nearly muscovite free KQ are presented in Table-3.7a. δ^{18}Ovalues of these samples are calculated using the VSMOW standard. The analyses of stable isotope of kyanite have been conducted at Stable isotope laboratory, University of Gottingen, Germany. The detail of the analytical process is presented in the Appendix-III.

Result:

Irrespective of places and domain of analyses the δ^{18}O values of kyanite cluster in narrow range 7.04-7.67 per mil (Table-3.7a). The range of δ^{18}O of the kyanite in the studied KQ overlaps with the δ^{18}O values of kyanite that are reported from the kyanite-bearing hydrothermal veins (6.62-7.9 per mil, Table-3.7b). The range of δ^{18}O values of kyanite of this study is similar to the δ^{18}O of the average continental crust (δ^{18}O = 6.97, Sharp et al., 2018). The average δ^{18}O values of the unaltered granitoids, however, is distinctly higher (8.5 per mil) than the δ^{18}O values reported from this study and from the kyanite in hydrothermal veins (Table 3.7b).

Tab 3.7a: Oxygen isotope data ($\delta^{18}O_{VSMOW}$) of kyanite from kyanite quartzite rocks of of the study area corrected to VSMOW

Sl.no.	Sample name	$\delta^{18}O$ (per mil)
1	S30a	7.042
2	S21_2	7.380
3	S21_1	7.621
4	S30d	7.672

Tab 3.7b: $\delta^{18}O_{VSMOW}$ values of kyanites from kyanite-quartz veins and kyanite-quartzites from other localities

Sl. No.	Lithology/mineral	$\delta^{18}O$ (per mil)	Locality	Reference
1	Kyanite in kyanite quartzite	7.04-7.67	Singhbhum shear zone, India	This study
2	Kyanite from aluminosilicate bearing albite-quartz veins	6.62-8.92	Simano nappe, Central Alps, Switzerland	Allaz et al. 2005
3	Kyanite from quartz-kyanite veins	6.9-7.9	Alpe Sponda, Central Alps	Beitter et al. 2008
4	Quartz (hydrothermal origin) in kyanite-quartzite	6.5	Madisonville and Baker Mountain,Piedmont Province of Virginia	Owen and Pasek 2007

3.10 Nature of source from trace elements:

The muscovite poor KQ rocks bear signatures of different types of provenances. They are mostly enriched in incompatible elements and depleted in Co and Ni with respect to UCC which strongly suggest felsic sources. However, some samples are slightly enriched in Cr or Co. One sample of KQ shows mixed signature of felsic and mafic as it has slight enrichment of incompatible elements as well as Cr, Co and Ni. Presence of cobalt in samples may be caused by detrital pyrites where Co replaced ferrous ion. Variable concentrations of La, Th and U and compatible elements in quartzites point to a mixed source terrain of felsic and mafic rocks. The Cr/Th and Sc/Th values in volcano-sedimentary successions show a sharp decrease at the Archean-Proterozoic boundary due to global changes in continental crustal composition (Taylor and McLennan 1985). A granitic source for these quartzites is suggested by the relatively low Cr/Th (1.66-15.86) and Sc/Th (0.04-1.00) ratios in many samples (Fig.3.6a). The high Cr/Th (24.32-102.6) and Sc/Th (1.27-16.40) in few samples also point towards some mafic influence. High Cr/Th in one sample unaccompanied by high Sc/Th possibly suggest enhancement of Cr in sediment sources by weathering (Condie & Wronkiewicz, 1990; Fig.3.6b). Wide variation in Y/Ni is also probable indicators of source heterogeneity (Fig.3.6c).

The quartzites also display REE patterns similar to typical average post-Archean shales. The non-matching values in Ce in different samples may be attributed to formation of Ce bearing phosphates in those samples due to secondary processes e.g. fluid infiltration. The geochemical evidence suggests that the deposition of the protolith took place in a differentiated stable cratonic environment with some inputs from granitoids and some mafic rocks.

3.11 Comparison of chemical signatures of the studied KQ with the neighbouring rocks

The textural features preserved in and the spatial distribution of the studied rocks are consistent with the view that the muscovite poor KQ and muscovite rich KQ rocks are integral parts of the SSZ. The SSZ is enclosed between the metasupracrustal rocks of the Chaibasa Formation to the north and Dhanjori group to the south (Fig. 1). Studies have shown that the REE and HFSE of rocks remain virtually unaffected by superposed weathering and hydrothermal alterations in most of the geological processes (Wronkiewicz and Condie, 1987). A comparison of the trace element compositions including HFSE and REE of the studied rocks with the enclosing lithologies can help test the possibility that the genetic link among these lithologies. To do this exercise the trace element concentrations of the muscovite-poor kyanite-quartzite with its unusual Al- and silica- rich compositions are normalized to the average compositions of the metasupracrustal rocks of the adjoining Dhanjori Gp. and Chaibasa Fm. The rock compositions used for normalization in this study are presented in Table-3.6. The compositions of the muscovite rich KQ are excluded in view of the secondary nature of muscovite (section 3.2). A flat normalized pattern with the normalization ratio close to 1 should establish a genetic link between the studied KQ and the normalized compositions. The normalized diagrams are presented in Fig.3.7 (a, b). Owing to the absence of Ta and Co concentration values in the adjoining lithologies, normalized value for these could not be measured (shown as gap in the normalized pattern). The normalized diagrams suggest the following:

1. The REE and HFSE (barring Nb) concentrations of the studied KQ resemble the average REE and HFSE concentrations of the Dhanjori phyllite and Chaibasa phyllite and schists (Fig. 3.7a).

2. The higher Nb values of the studied KQ could be related to the higher concentration of rutile, the sink for Nb of the studied rocks could be related to the higher modal proportion of rutile in the studied KQ , the sink for Nb. This argument is consistent with the higher Ta (rutile is the sink) values of the studied KQ when normalized against UCC (Fig. 3.4b,c).
3. The relatively fluid mobile elements namely U and Th show depletion when the studied KQ are normalized with the phyllite and schists from the Chaibasa Fm and phyllite from the Lower Dhanjori Fm (Fig. 3.7a). The actinides are known to be mobile when rocks interact with oxidized fluid.
4. Compared to the neighbouring rocks the KQ rocks have a higher Pb concentration. Few samples of KQ have higher Cr values as compared to Dhanjori phyllite and Chaibasa schists.

Discussion: Metasomatism played an important role during deformation in the SSZ (Roy and Matin, 2020). From the textural studies the deformed kyanite form enigmatic textures which can only be explained if the metasomatism predated the metamorphism of the rocks. Ductile deformation and dynamic recrystallization of kyanite is a rare feature which can be explained by conjunction of two factors 1) Shearing in SSZ taking place over a long period of time 2) Influx of fluids through shear zone which aided the strain softening process.

The grey box in Fig. 3.8 shows the approximate P-T conditions determined from the garnetiferous chloritoid schists (Sengupta, 2012), muscovite poor KQ bearing borosilicate veins (Sengupta et al., 2011) and kyanite quartzite having aluminophosphate rich pockets from different parts of SSZ. The temperature is corroborated by the quartz deformation textures observed in the studied rocks. Also shown in the figure are experimentally determined reactions relevant to the mineralogical assemblage of the studied rocks. Textural relations suggest that the pyrophyllite and diaspore present here

have formed later at the cost of kyanite and corundum respectively. Pyrophyllite which formed kyanite have been totally been obliterated during peak metamorphic event. Reaction line 4 represents transition of chloritoid to staurolite and the latter mineral is absent from the studied rocks which suggest that the T conditions did not cross over to the stability field of staurolite at any point in time (discussed in detail in Chapter 4). Corundum formed at the expense of kyanite and diaspore formed later from both kyanite and corundum when pressure-temperature decreased.

The chemical alteration indices, trace element signatures and oxygen isotope data point that the protolith was derived mostly from mature sedimentary rocks of Chaibasa Fm. with minor influences from mafic rocks (Dhanjori Group). It is evident that the unusual composition of the KQs of SSZ are a result of fluid interaction with protolith that led to a SiO_2-rich rock with moderate Al_2O_3 content and very low concentrations of alkali metals and alkaline earths.

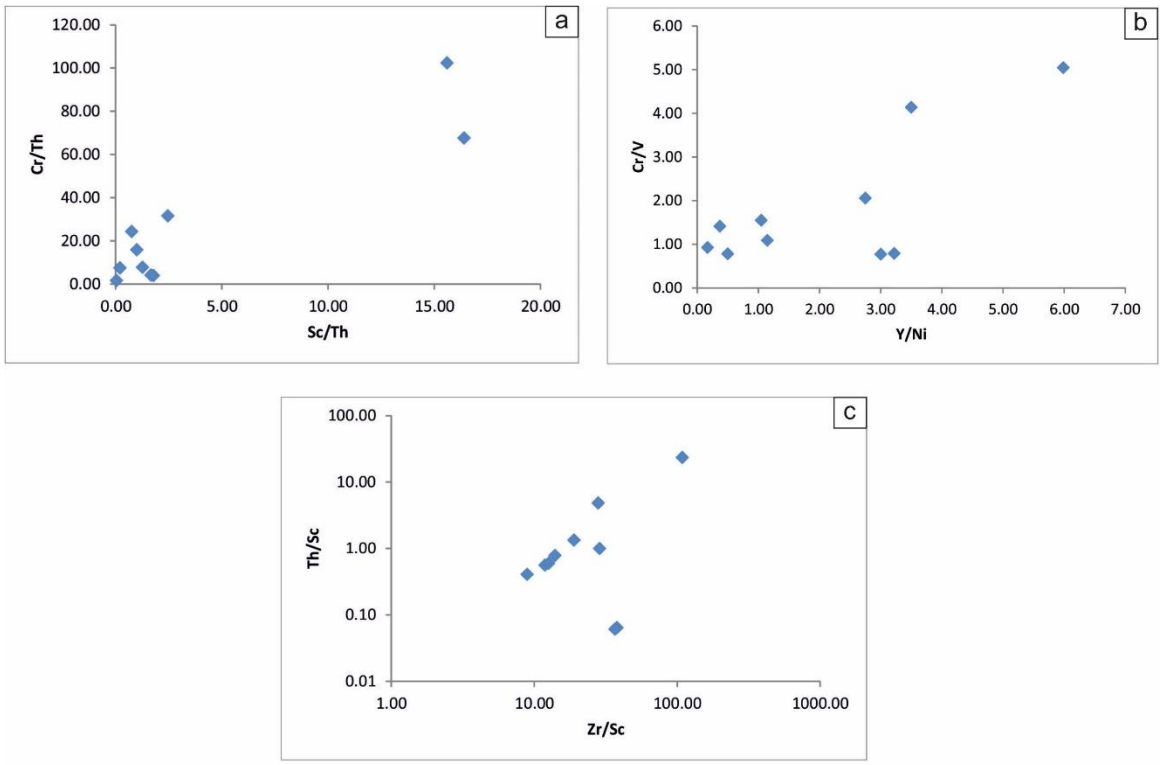

Fig. 3.6:a) Plot of Cr/Th versus Sc/Th (after Condie and Wronkiewicz 1990). Note that the quartzites samples show a wide variation in both Cr/Th (1.66-102.6) and Sc/Th (0.04-16.4) ratios b)Plot of Cr/V versus Y/Ni (after McLennan et al. 1993). A wide variation in Y/Ni (0.17-5.98) ratios is noticed as well c)Plot of Th/Sc versus Zr/Sc (after McLennan et al.1993). Note the considerable variation in Th/Sc ratios and some variation in Zr/Sc ratios

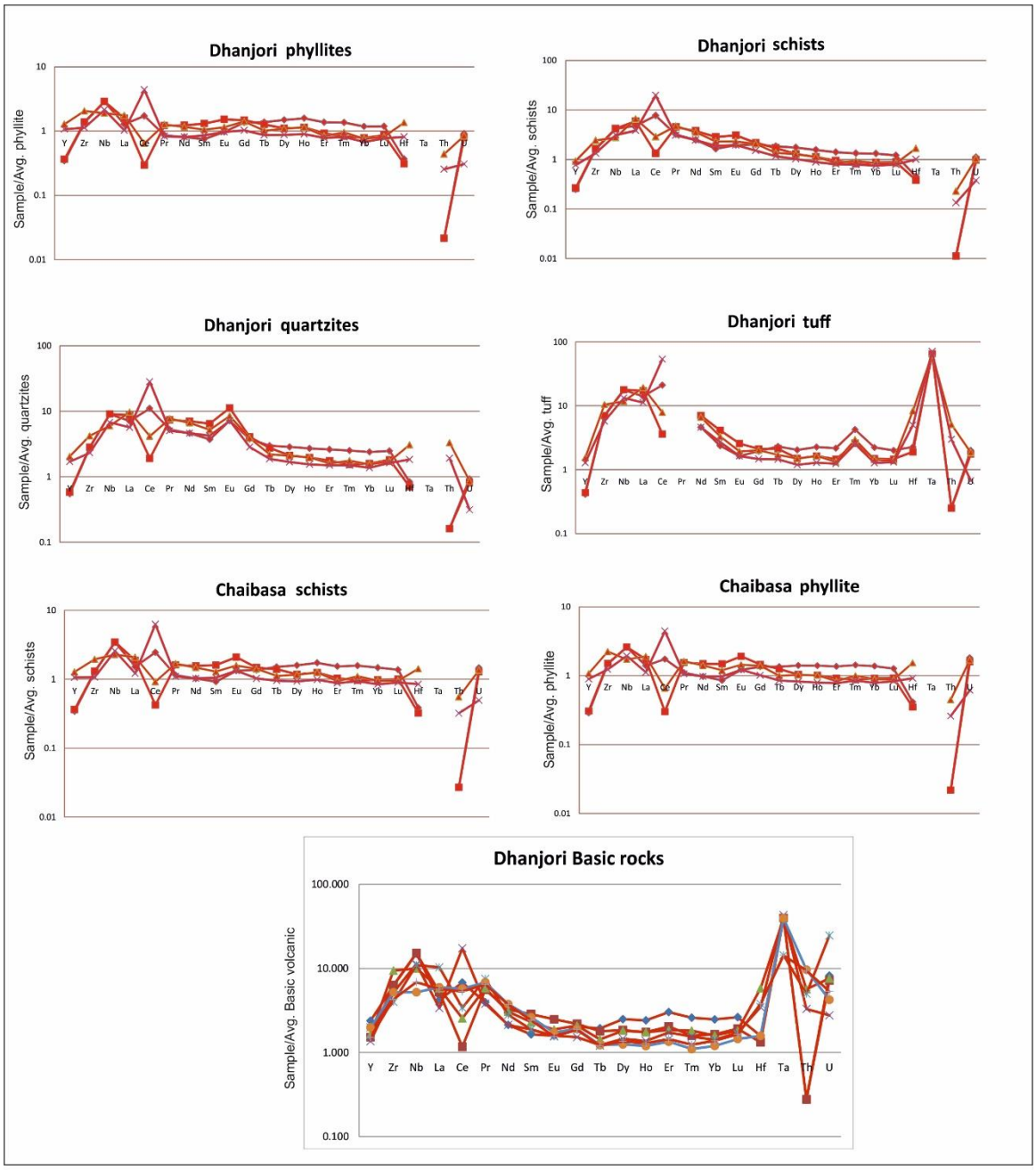

Fig 3.7a:Spider diagrams of immobile trace elements normalised to averaged concentrations in neighbouring meta-sediments and metavolcanics from the NSFB calculated from data of Roy et al. 2002, De et. al. 2015 and Singh et al. 2018

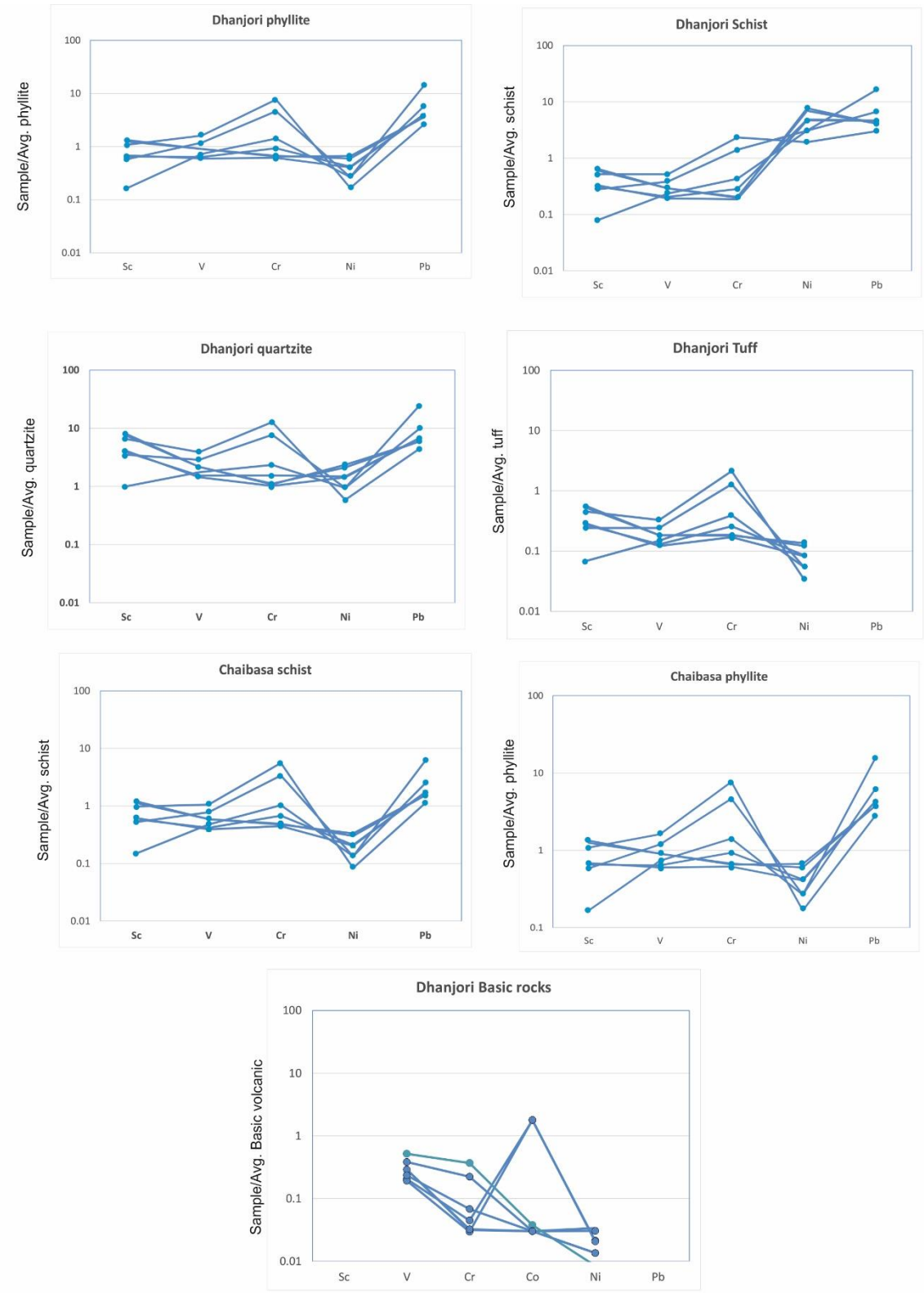

Fig 3.7 b) Spider diagram of compatible trace elements in KQ normalised to average concentrations of neighbouring metasedimentary and metavolcanic rocks of study area. Data of neighbouring rocks taken from Roy et al. 2002, Mazumder and Arima 2009, De et al. 2015, Singh et al. 2018

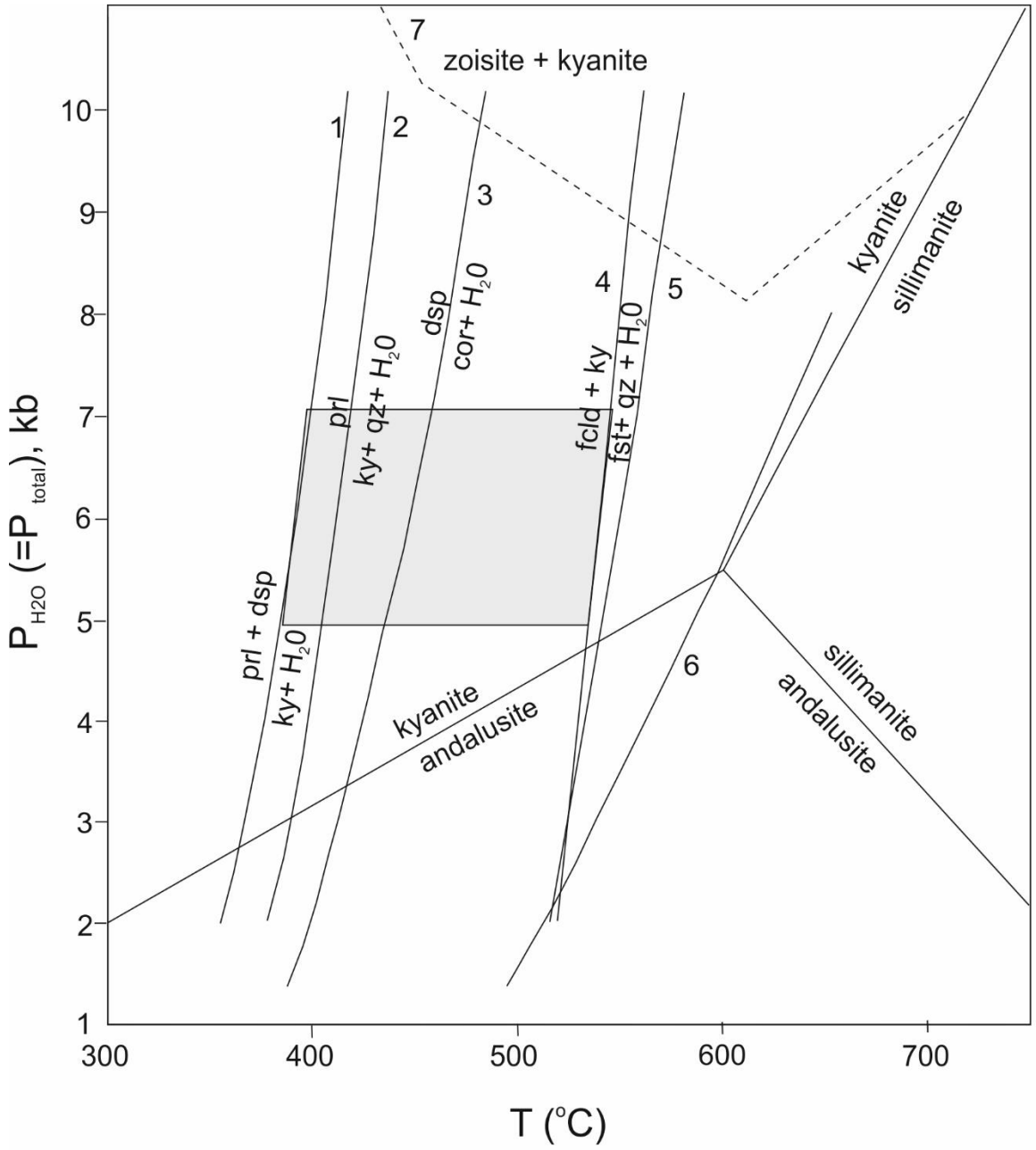

Fig. 3.8: P-T diagram showing experimentally determined equilibria pertinent to the mineralogy of aluminous rocks. Equilibrium curves are: 1. pyrophyllite + diaspore = kyanite + H_20 (Haas and Holdaway, 1973); 2. pyrophyllite = kyanite + quartz + H_20 (Haas and Holdaway, 1973); 3. diaspore = corundum + H_20 (Haas, 1972);4. Fe-chloritoid + kyanite = Fe-staurolite + quartz + H_20, QFM buffer (Hoschek, 1967; Richardson, 1968; Rao and Johannes, 1979); 5. chloritoid + 0_2 = staurolite + magnetite + quartz, MH buffer (Ganguly and Newton, 1968); 6. margarite = anorthite + corundum + H_20 (Chatterjee,1974); 7. dashed line indicates lower pressure stability of the assemblage kyanite + zoisite according to thermodynamic calculations in the system $CaO-Al_20_3$ $-Si0_2$ $-H_20$ (Perkins et al., 1980); stabilityfields of the Al-silicates are average values of Althaus (1967) and Richardson et al. (1969), see Jansen and Schuiling (1976), and Jansen et al. (1977). Prl=pyrophyllite, fcld=Fe-chloritoid, ky=kyanite, fst=Fe-staurolite, dsp=diaspore, qz=quartz. Mineral abbreviations are after Whitney and Evans (2010)

References

Allaz, J., Zurich, E., Steck, A., 2005. Formation of aluminosilicate-bearing quartz veins in the Simano nappe (Central Alps): Structural, thermobarometric and oxygen isotope constraints Electron Probe Microanalysis View project Electron microprobe analysis of REE minerals View project, Article in Swiss Journal of Geosciences Supplement.

Althaus, E., 1967. The triple point andalusite—sillimanite—kyanite. Contributions to Mineralogy and Petrology 16, 29–44.

Beane, R.J., Field, C.K., 2007. Kyanite deformation in whiteschist of the ultrahigh-pressure metamorphic Kokchetav Massif, Kazakhstan, in: Journal of Metamorphic Geology. pp. 117–128. https://doi.org/10.1111/j.1525-1314.2007.00692.x

Beitter, T., Wagner, T., Markl, G., 2008. Formation of kyanite-quartz veins of the Alpe Sponda, Central Alps, Switzerland: Implications for Al transport during regional metamorphism. Contributions to Mineralogy and Petrology 156, 689–707. https://doi.org/10.1007/s00410-008-0310-4

Bhat, M.I., Ghosh, S.K., 2001. Geochemistry of the 2.51 Ga old Rampur group pelites, western Himalayas: implications for their provenance and weathering. Precambrian Res 108, 1–16.

Carter, N.L., Tsenn, M.C., 1987. Flow properties of continental lithosphere. Tectonophysics 136, 27–63.

Chatterjee, N.D., 1976. Margarite stability and compatibility relations in the system CaO-Al2O3-SiO2-H2O as a pressure-temperature indicator. American Mineralogist 61, 699–709.

Condie, K.C., Wronkiewicz, D.J., 1990. A new look at the Archaean-Proterozoic boundary sediments and the tectonic setting constraint, in: Developments in Precambrian Geology. Elsevier, pp. 61–83.

Connolly, J.A.D., 2009. The geodynamic equation of state: what and how. Geochemistry, geophysics, geosystems 10.

Connolly, J.A.D., 2005. Computation of phase equilibria by linear programming: a tool for geodynamic modeling and its application to subduction zone decarbonation. Earth Planet Sci Lett 236, 524–541.

De, S., Mazumder, R., Ohta, T., Hegner, E., Yamada, K., Bhattacharyya, T., Chiarenzelli, J., Altermann, W., Arima, M., 2015. Geochemical and Sm–Nd isotopic characteristics of the Late Archaean-Palaeoproterozoic Dhanjori and Chaibasa metasedimentary rocks, Singhbhum craton, E. India: Implications for provenance, and contemporary basin tectonics. Precambrian Res 256, 62–78.

Fedo, C.M., Wayne Nesbitt, H., Young, G.M., 1995. Unraveling the effects of potassium metasomatism in sedimentary rocks and paleosols, with implications for paleoweathering conditions and provenance. Geology 23, 921–924.

Forshaw, J.B., Pattison, D.R.M., 2022. Major-element geochemistry of pelites. Geology. https://doi.org/10.1130/g50542.1

Ganguly, J., Newton, R.C., 1968. Thermal stability of chloritoid at high pressure and relatively high oxygen fugacity. Journal of Petrology 9, 444–466.

Ghosh, M., Mukhopadhyay, D., Sengupta, P., 2006. Pressure–temperature-deformation history for a part of the Mesoproterozoic fold belt in North Singhbhum, Eastern India. J Asian Earth Sci 26, 555–574.

Ghosh, S., Sarkar, S., 2010. Geochemistry of Permo-Triassic mudstone of the Satpura Gondwana basin, central India: Clues for provenance. Chem Geol 277, 78–100.

Gottardi, R., Teyssier, C., Mulch, A., Seaton, N., 2008. Crustal Thinning, Fluid Flow, and the Preservation of a High Transient Geotherm in the Raft River Detachment, NW Utah, in: 2008 Joint Meeting of The Geological Society of America, Soil Science Society of America, American Society of Agronomy, Crop Science Society of America, Gulf Coast Association of Geological Societies with the Gulf Coast Section of SEPM.

Haas, H., Holdaway, M.J., 1973. Equilibria in the system Al2O3-SiO2-H2O involving the stability limits of pyrophyllite, and thermodynamic data of pyrophyllite. Am J Sci 273, 449–464.

Hass, H., 1972. Diaspore-corundum equilibrium determined by epitaxis of diaspore on corundum. American Mineralogist: Journal of Earth and Planetary Materials 57, 1375–1385.

Hassan, S., Ishiga, H., Roser, B.P., Dozen, K., Naka, T., 1999. Geochemistry of Permian–Triassic shales in the Salt Range, Pakistan: implications for provenance and tectonism at the Gondwana margin. Chem Geol 158, 293–314.

Hirth, G., Tullis, J.A.N., 1992. Dislocation creep regimes in quartz aggregates. J Struct Geol 14, 145–159.

Hoschek, G., 1967. Untersuchungen zum Stabilitätsbereich von Chloritoid und Staurolith. Contributions to Mineralogy and Petrology 14, 123–162.

Jansen, J.B.H., Schuiling, R.D., 1976. American Journal of Science. ajs 276, 1225–1253.

Kisters, A.F.M., Kolb, J., Meyer, F.M., Hoernes, S., 2000. Hydrologic segmentation of high-temperature shear zones: structural, geochemical and isotopic evidence from auriferous mylonites of the Renco mine, Zimbabwe. J Struct Geol 22, 811–829.

Kolb, J., Rogers, A., Meyer, F.M., Vennemann, T.W., 2004. Development of fluid conduits in the auriferous shear zones of the Hutti Gold Mine, India: evidence for spatially and temporally heterogeneous fluid flow. Tectonophysics 378, 65–84.

Mancktelow, N.S., 2006. How ductile are ductile shear zones? Geology 34, 345–348. https://doi.org/10.1130/G22260.1

McDonough, W.F., Sun, S. -s., 1995. The composition of the Earth. Chem Geol 120, 223–253. https://doi.org/https://doi.org/10.1016/0009-2541(94)00140-4

Mclennan, S.M., 2001. Relationships between the trace element composition of sedimentary rocks and upper continental crust.

McLennan, S.M., Hemming, S., 1992. Samarium/neodymium elemental and isotopic systematics in sedimentary rocks. Geochim Cosmochim Acta 56, 887–898.

Menegon, L., Pennacchioni, G., Heilbronner, R., Pittarello, L., 2008. Evolution of quartz microstructure and c-axis crystallographic preferred orientation within ductilely deformed granitoids (Arolla unit, Western Alps). J Struct Geol 30, 1332–1347.

Nesbitt, H.W., Young, G.M., 1989. Formation and diagenesis of weathering profiles. J Geol 97, 129–147.

Nesbitt, H.W., Young, G.M., 1984. Prediction of some weathering trends of plutonic and volcanic rocks based on thermodynamic and kinetic considerations. Geochim Cosmochim Acta 48, 1523–1534.

Nesbitt, H.W., Young, G.M., 1982. Early Proterozoic climates and plate motions inferred from major element chemistry of lutites. Nature 299, 715–717.

Owens, B.E., Pasek, M.A., 2007. Kyanite Quartzites in the Piedmont Province of Virginia: Evidence for a Possible High-Sulfidation System. Economic Geology 102, 495–509. https://doi.org/0361-0128/07/3665/495-15

Passchier, C.W., Trouw, R.A.J., 2005. Microtectonics. Springer Science & Business Media.

Perkins, D.I., 1980. Application of new thermodynamic data to mineral equilibria. University of Michigan.

Rao, B.B., Johannes, W., 1979. Further data on the stability of staurolite, Neues Jahrb. Mineral. Monath 10, 437–447.

Regenauer-Lieb, K., Yuen, D.A., 2003. Modeling shear zones in geological and planetary sciences: solid-and fluid-thermal–mechanical approaches. Earth Sci Rev 63, 295–349.

Richardson, S.W., 1968. Staurolite stability in a part of the system Fe-Al-Si-OH. Journal of Petrology 9, 467–488.

Richardson, S.W., Gilbert, M.C., Bell, P.M., 1969. Experimental determination of kyanite-andalusite and andalusite-sillimanite equilibria; the aluminum silicate triple point. Am J Sci 267, 259–272.

Rollinson, H.R., 1993. Using geochemical data: Evaluation, presentation, interpretation. Longman Scientific & Technical, London.

Roy, A., Matin, A., 2020. Study of small-scale structures and their significance in unravelling the accretionary character of Singhbhum shear zone, Jharkhand, India. Journal of Earth System Science 129. https://doi.org/10.1007/s12040-020-01496-9

Ryan, N.A., 2010. Microstructures of a deformed kyanite-quartz vein of the Raft River Mountains in northwest Utah, USA. Carleton College, Northfield, Minnesota.

Sengupta, N., Mukhopadhyay, D., Sengupta, P., Hoffbauer, R., 2005. Tourmaline-bearing rocks in the Singhbhum shear zone, eastern India: Evidence of boron infi ltration during regional metamorphism. American Mineralogist 90, 1241–1255. https://doi.org/0003-004X/05/0809ñ1241$05.00/DOI: 10.2138/am.2005.1578

Sengupta, N., Sengupta, P., Sachan, H.K., 2011. Aluminous and alkali-deficient tourmaline from the Singhbhum Shear Zone, East Indian shield: Insight for polyphase boron infiltration during regional metamorphism. American Mineralogist 96, 752–767. https://doi.org/10.2138/am.2011.3560

Sharp, Z.D., Wostbrock, J.A.G., Pack, A., 2018. Mass-dependent triple oxygen isotope variations in terrestrial materials. Geochem Perspect Lett 7, 27–31. https://doi.org/10.7185/geochemlet.1815

Singh, S., Chandan, K.K., Jha, V., 2018. Geochemistry of Paleo to Mesoproterozoic Metasedimentary Units of Chandil Formation, North Singhbhum Crustal Province: Implications for Provenance and Source Area Weathering. Journal of the Geological Society of India 92, 166–172. https://doi.org/10.1007/s12594-018-0976-9

Stipp, M., Stünitz, H., Heilbronner, R., Schmid, S.M., 2002. Dynamic recrystallization of quartz: correlation between natural and experimental conditions. Geological Society, London, Special Publications 200, 171–190.

Sullivan, W.A., 2008. Significance of transport-parallel strain variations in part of the Raft River shear zone, Raft River Mountains, Utah, USA. J Struct Geol 30, 138–158.

Sun, S.-S., McDonough, W.F., 1989. Chemical and isotopic systematics of oceanic basalts: implications for mantle composition and processes. Geological Society, London, Special Publications 42, 313–345.

Taylor, S.R., McLennan, S., 2009. Planetary crusts: their composition, origin and evolution. Cambridge University Press.

Taylor, S.R., McLennan, S.M., 1995. The geochemical evolution of the continental crust. Reviews of geophysics 33, 241–265.

Taylor, S.R., McLennan, S.M., 1985. The continental crust: its composition and evolution.

Whitney, D.L., Dilek, Y., 2000. Andalusite-sillimanite-quartz veins as indicators of low-pressure-high-temperature deformation during late-stage unroofing of a metamorphic core complex, Turkey. Journal of Metamorphic Geology 18, 59–66.

Whitney, D.L., Evans, B.W., 2010. Abbreviations for names of rock-forming minerals. American Mineralogist 95, 185–187. https://doi.org/10.2138/am.2010.3371

Wronkiewicz, D.J., Condie, K.C., 1987. Geochemistry of Archean shales from the Witwatersrand Supergroup, South Africa: source-area weathering and provenance. Geochim Cosmochim Acta 51, 2401–2416.

Yadav, B.S., Wanjari, N., Ahmad, T., Chaturvedi, R., 2016. Geochemistry and petrogenesis of proterozoic granitic rocks from northern margin of the chotanagpur gneissic complex (CGC). Journal of Earth System Science 125, 1041–1060. https://doi.org/10.1007/s12040-016-0709-7

CHAPTER 4

Chloritoid bearing kyanite quartzite

The chloritoid-bearing Kyanite quartzite rock (CKQ) forms a part of the kyanite quartzite (Chapter 3) that occur all along the northern margin of the SSZ. The CKQ occur discreetly throughout the shear zone. Chloritoid associated with the KQ and kyanite muscovite schist (KMS) occur in the form of veins, patches, porphyroblasts, deformed nodules, etc. Association of chloritoid with the KQ forms is the subject of the present study.

4.1 Field study:

At Surda, the KQ appears as a white massive unit with a knotty surface due to presence of nodules of kyanite that have been more resistant to deformation than the rest of the rock (Fig. 4.1b). In narrow zones, the rock has a sheeted appearance due to the development of shear foliation (Fig. 4.1b, c). The porphyroblasts of kyanite exhibit variable impress of deformation. Consequently, the shape of the kyanite pods varies from elliptical tabular to augen shaped to sigmoidal (Fig. 4.1b, c, d). Prismatic kyanite grains are aligned along the shear foliation (Fig. 4.1e).The shear foliation swerves around the augen-shaped kyanite pods (Fig. 4.1d). The quartz veins in the KQ are torn apart and kyanite is seen developing at the interface between the quartz vein and host KQ (Fig. 4.1 f). The KQ is found to grade into kyanite-muscovite schist, which further grades into chloritoid-muscovite schist.

The chloritoid porphyroblasts associated with the KQ, occur as patchesand veins that dissect the host KQ (Fig. 4.1g). Also the patches of chloritoid containing inclusions of kyanite are found in the vicinity of deformed quartz veins (Fig. 4.1h). Chloritoid grains are also closely associated with deformed quartz veins (Fig. 4.1i) in the chloritoid-garnet-biotite schists.

At Jaduguda, the KQ is boudinaged and patchesof chloritoid along with some muscovite have developed at the boudin necks (Fig. 4.1j). The chloritoid patch appears to develop at the boudin neck replacing kyanite in the vicinity (Fig. 4.1k). Small veins of chloritoid are dispersed in the KQ.

At Kanyaluka, garnet-chloritoid-muscovite-biotiteschist is seen closely associated with KQ. Even here at some places undeformed nodular aggregates and patches of chloritoid exhibiting rosette structure is also noticed in the schists (Fig. 4.1l). Patches of chloritoid are developed in close association with deformed apatite veins (Fig. 4.1m)

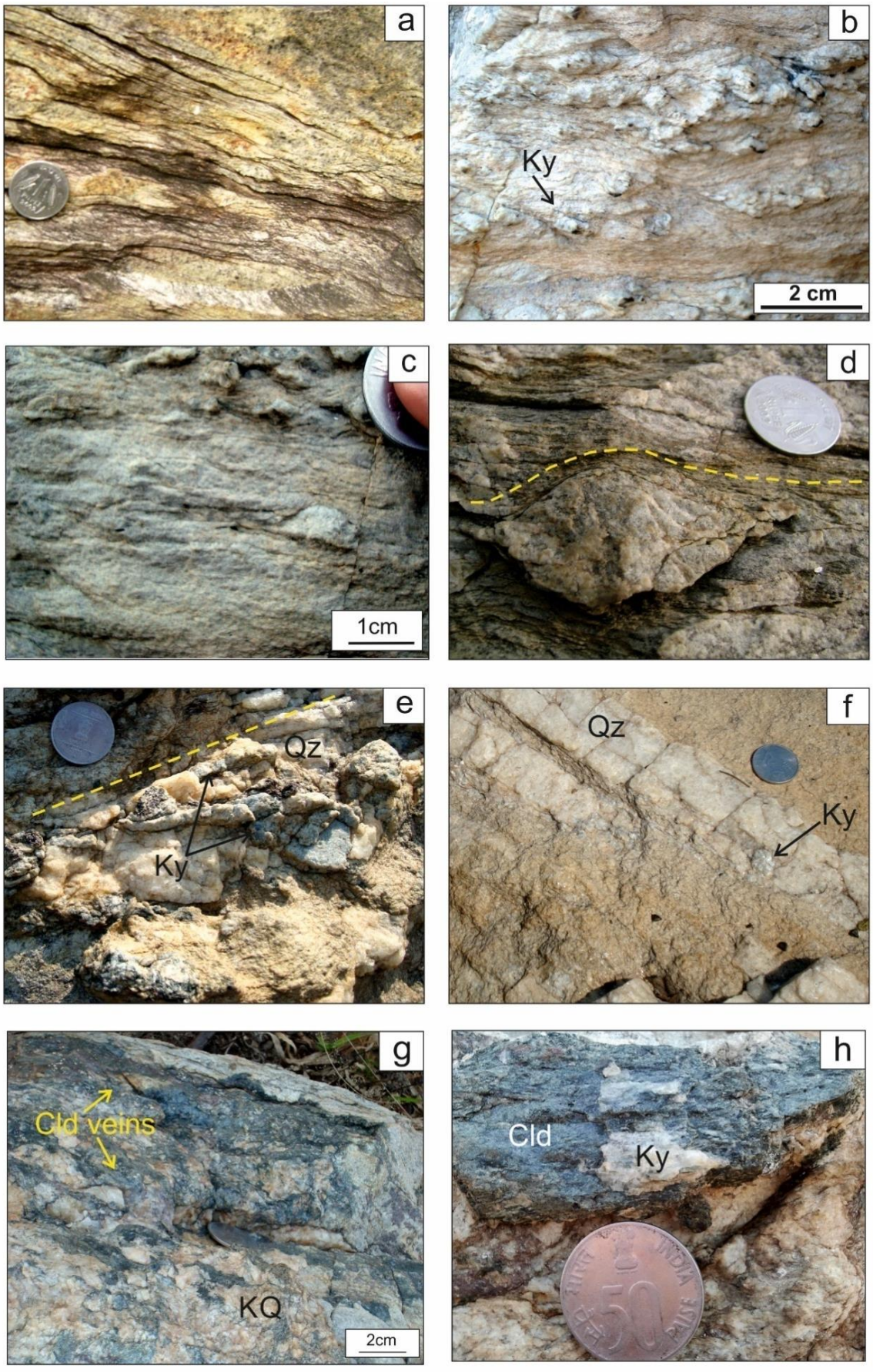
a
b
Ky
2 cm
c
1cm
d
e
Qz
Ky
f
Qz
Ky
g
Cld veins
KQ
2cm
h
Cld
Ky

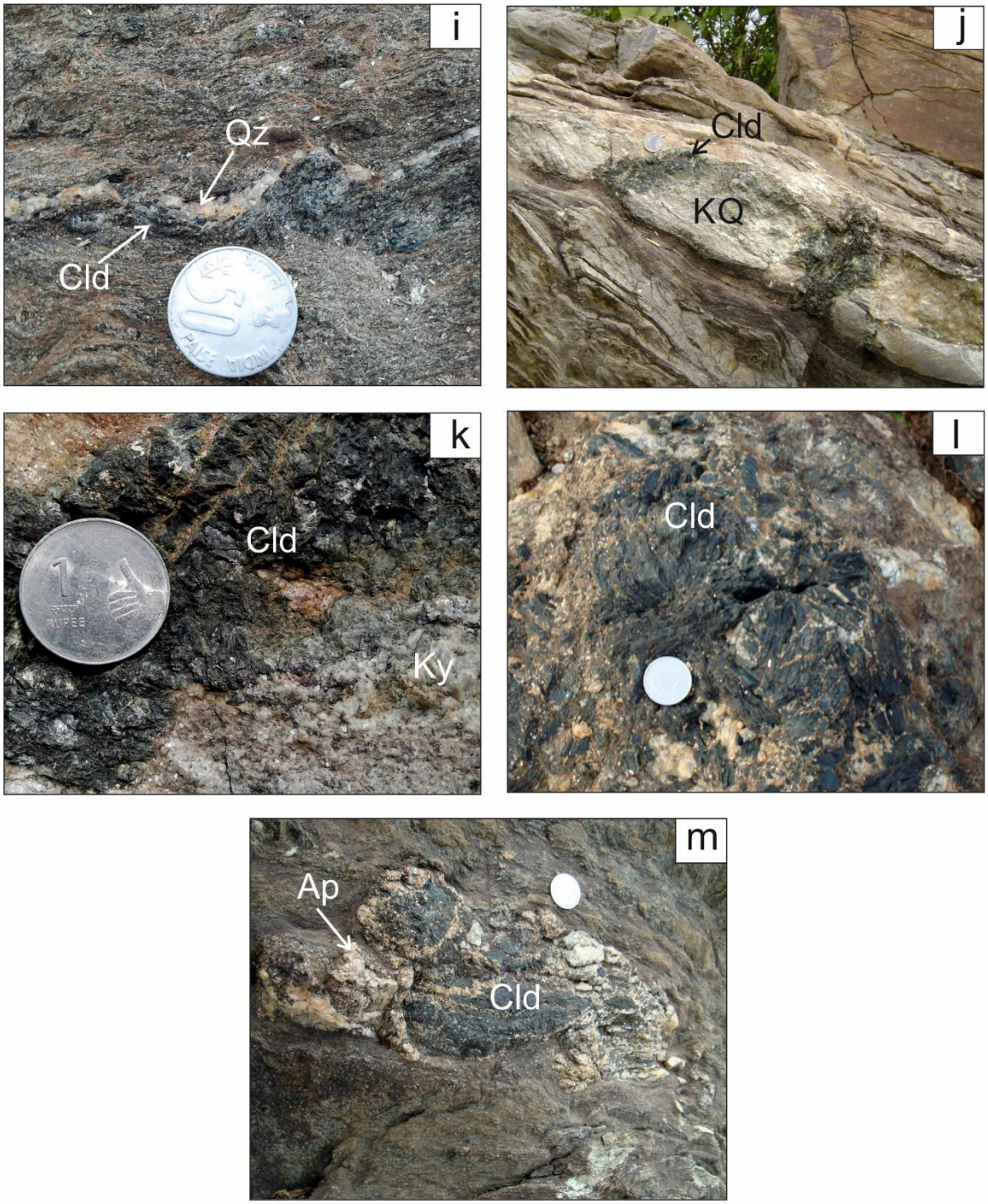

Fig. 4.1 a) Kyanite rich quartzite layers alternate with cryptocrystalline quartz rich layers b) Sheared kyanite quartzite with nodules of kyanite pods c) Sheeted appearance of KQ. Kyanite pods of different shapes are present d) Augen shaped kyanite pod in sheared kyanite quartzite e) Prismatic kyanite grains with quartz veins developing along shear foliation f) Quartz veins hosted in the torn apart and kyanite developing at the vein-host contact g) Chloritoid veins aligned along shear foliation of the KQ h) Chloritoid blade with relict kyanite grain inside i) Chloritoid associated with deformed quartz veins in garnet-chloritoid-muscovite schist j) Boudinaged KQ with chloritoid developing along with some muscovite at the boudin necks k) Chloritoid grains developing haphazardly replacing kyanite at the boudin necks of KQ l)Undeformed nodular aggregates and blades of chloritoid exhibiting rosette structure in garnet-chloritoidbearing schists m) Chloritoid associated with deformed apatite veins Cld-Chloritoid, Ky-Kyanite, Qz-Quartz, Ap-Apatite, KQ-kyanite quartzite. Abbreviations of mineral names in figures have been used after Whitney and Evans (2010).

4.2 Petrography:

The major portion (~70%) of the rock is occupied by prismatic to acicular kyanite blades. Kyanite, quartz and rutile form the earliest recognizable assemblagein the rock. Randomly oriented kyanite blades display a rosette structure (Fig 4.2a).Some kyanite blades are kinked or bent (Fig. 4.2b). Kyanite grains also show undulose extinction (Fig. 4.2b) and grain perpendicular fractures (Fig. 4.2b) as an effect of deformation. The quartz grains in interstitial spaces are recrystalized. These features suggest that at the time of formation of kyanite no significant directional stress was present. Subsequently the rock was deformed presumably at the time of shear defomation. In most samples the modal amount of chloritoid is 10-15%.

Muscovite which defines the schistosity in the rock replaces the kyanite grains (Fig. 4.2c,l) Rutile grains showing corroded grain boundaries are present in close association with muscovite indicating participation in the muscovite forming reaction (Fig. 4.2d). Chloritoid grains are present as 1) patches parallel to schistosity (Fig. 4.2e) and as 2) stubby euhedral grains which are athwart schistosity (Fig. 4.2f). Small grains of chloritoid developed parallel to schistosity are indicators that the mineral developed syntectonically (Fig. 4.2e) while the stubby grains indicate post-tectonic development (Fig. 4.2g). Chloritoid grains replace the kyanite grainspreserving the shape of the kyanite though i.e. a case of pseudomorphism (Fig. 4.2g,i). Muscovitereplaces the chloritoidgrains which have formed earlier at the expense of kyanite and magnetitein fluid rich environments (Fig. 4.2h). In the BSE images corroded grains of paragonite rich muscovite occur inside stubby chloritoid grains (Fig. 4.2i) while subhedral to anhedral magnetiteare dispersed in kyanite and chloritoid (Fig. 4.2i,j,k).Subhedral chloritoid grains replace kyanite from the boundaries. They display tounging (finger like protrusions) into kyanite grains (Fig. 4.2j). These chloritoid grains with uneven grain boundaries also have kyanite inclusions inside

them. Diaspore develops as a late phase by replacing kyanite, muscovite and chloritoid (Fig. 4.2k).

These textures indicate that the earliest assemblage of KQ formed under stress free conditions. The kyanite was then affected by subsequent deformations and it also was replaced by muscovite syntectonically. Chloritoid develops from kyanite and magnetiteand the growthis syntectonic but evidentlyoutlasted deformation. Muscovite anddiaspore replace both kyanite and chloritoid understress free conditions.

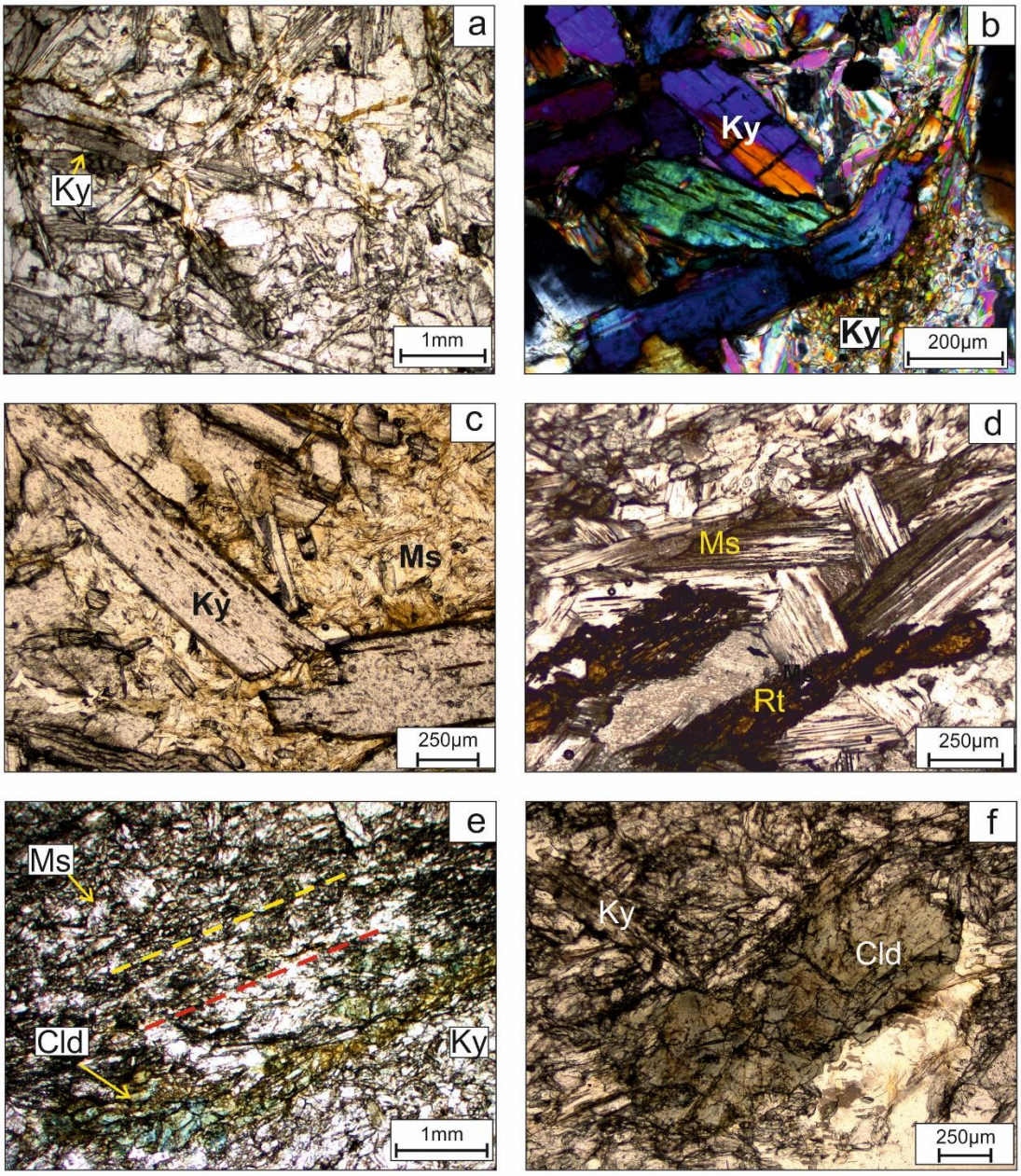

Fig. 4.2. a) Rosette kyanite growth in comparitively stress free regions of SSZ b) Kinked/Bent Kyanite grain exhibiting undulatory extinction. Recrystallized kyanite growing along the boundaries of the bent grain c) Kyanite replaced by muscovite. d) Kyanite completely replaced by muscovite and rutile with corroded grain boundaries e)Chloritoid blades developed parallel to schoistosity of kyanite quartzite f) Stubby chloritoid grain growing athwart to schistosity. Abbreviations of mineral names in figures have been used after Whitney and Evans (2010).

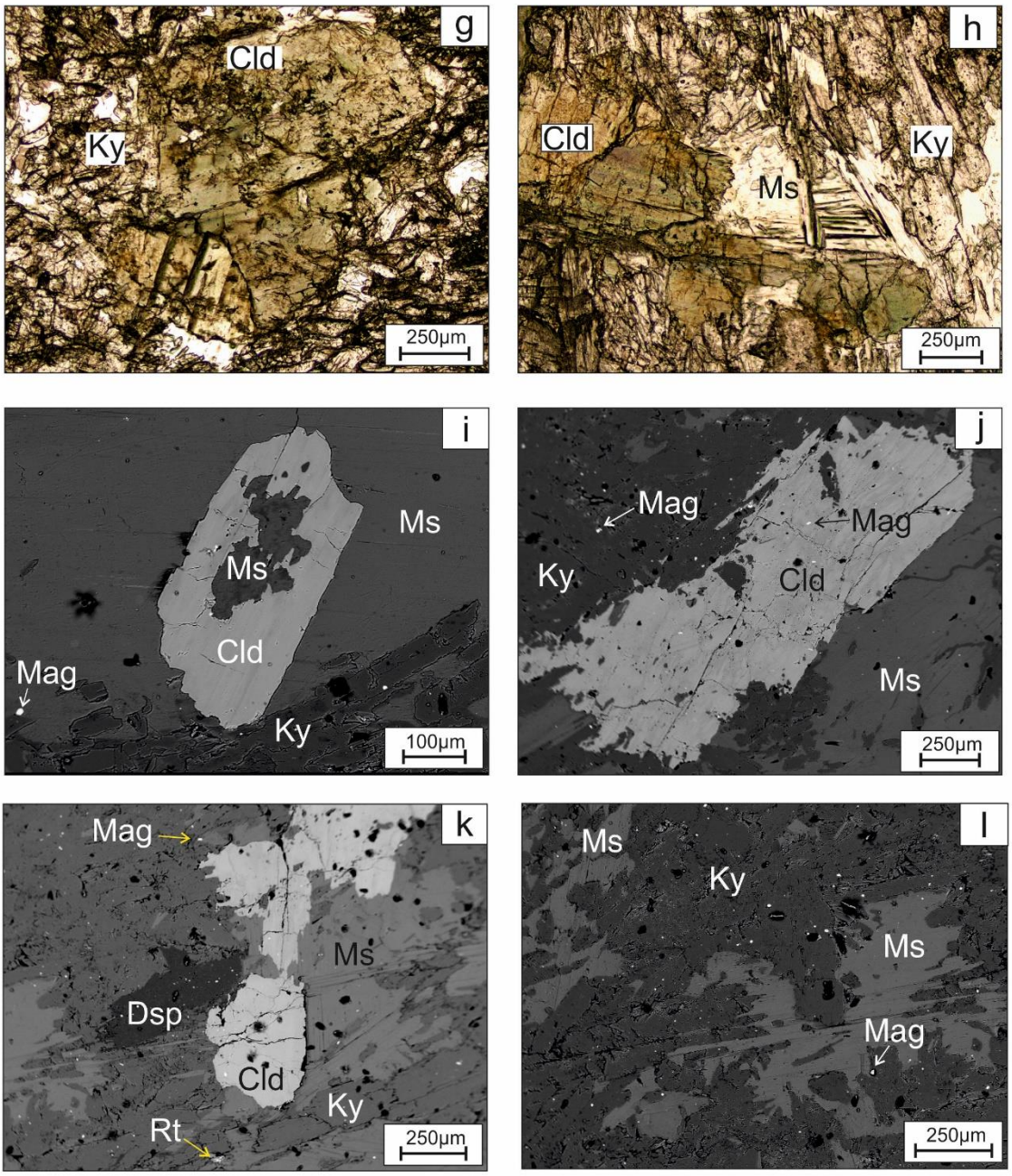

Fig 4.2 continued g) Chloritoid replacing kyanite while preserving the shape of the kyanite grain h) Muscovite replacing both kyanite and chloritoid i) Paragonite rich muscovite as inclusion in chloritoid grain j) Chloritoid replacing kyanite from the boundaries evident by the toungues of chloritoid protruding into kyanite. A relict grain is also visible inside chloritoid k) Chloritoid replacing kyanite while muscovite replacesboth kyanite and chloritoid. Diaspore is seen forming at a late stage by replacing kyanite (l) Muscovite replacing kyanite in the form of a network. Cld-Chloritoid, Mag-Magnetite, Ms-Muscovite, Ky-Kyanite, Qz-Quartz, Rt-Rutile, Dsp-Diaspore. Abbreviations of mineral names in data tables and figures have been used after Whitney and Evans (2010).

4.3 Mineral chemistry

The compositions of the minerals in the CKQ are measured with Cameca SX100Electron Probe Micro Analyzer (EPMA) Central Petrological Laboratory, Geological survey of India, Kolkata. The analytical details are presented in the Appendix III. The representative analyses of the minerals are given in the Tables 4.1-4.2. In the following section, the salient compositional characteristics of the minerals are presented:

Kyanite: Kyanite is virtually Al_2SiO_5 with trace contents of Fe (0.001-0.008 a.p.f.u.). Kyanite close to chloritoid is richer in Fe (0.008 a.p.f.u.) than the distal kyanite (0.001 a.p.f.u.).

Chloritoid: Chloritoid is essentially a solid-solution of $Fe_2Al_4Si_2O_{10}(OH)_4$ and $Mg_2Al_4Si_2O_{10}(OH)_4$ with minor MnO (upto 0.26 wt%). ZnO, NiO, CaO and alkalis are virtually always below detection limit. TiO_2 is not detectable in most analyses and only upto 0.02 wt% was measured. Compositions of chloritoid in the KQs are extremely Fe-rich (X_{Mg}=0.11-0.18) where the range of X_{Mg} for most grains of chloritoid being 0.11-0.12 with rim of a chloritoid grain showing slightly high value of 0.18.The chemical composition of chloritoid plotted in Fe-Mn-Mg classification shows that the composition does not vary much and are mostly concentrated towards the Fe apex.The levels of Fe^{3+} in the chloritoid analyses that were recalculated following the procedure of Chopin et al. (1992) are as low as 0.01-0.05 a.p.f.u. Assuming that chloritoid has the ideal structural formula $(Fe^{2+},Mg,Mn)_2$ $(Al,Fe^{3+})Al_3$ $Si_2O_{10}(OH)_4$, the $Fe^{3+}/(Fe^{3+} + Fe^{2+})$ ratio for chloritoid from this study can be estimated at 0.02-0.04.

Muscovite: Muscovite in the studied area shows a considerable amount of paragonite component varying between 16-17 mol% normally. The Al content in muscovite vary from5.538-5.642 a.p.f.u., while K and Na content varies between 1.543-1.665 a.p.f.u. and

0.311-0.342 a.p.f.u. The muscovite grains that are in close association with chloritoid are richer in paragonite component varying between 40-42% (points 3/1 amd 4/1 in Table 4.2). The paragonite grains contain Al and Na varying between 6.073-6.142 a.p.f.u. and 1.818-1.855 a.p.f.u.

Rutile, magnetite and quartz have virtually end member compositions.

In kyanites, the partial pressure of oxygen controls the substitution of Fe^{3+} for Al (Chinner et al., 1969). A slightly higher concentration of Fe in kyanites associated with chloritoid corroborate the fact that fO_2 was higher than when the chloritoids were forming. The ferrous content of the chloritoids is high compared to ferric content and sometimes it may be related to the oxidation state of the host rock during formation of the mineral. It is observed that chloritoids from the schists of SSZ show Fe+Mg+Mn slightly excess than 2.00 and a weak negative correlation between Fe+Mg+Mn and Al (Fig. 4.4). This trend indicates the presence of some ferric Fe substituting for Al, most likely in the M(1A) octahedral of the brucite-type layer (Hanscom, 1980). The $Fe^{3+}/(Fe^{3+} + Fe^{2+})$is low compared to most chloritoids found in other studies in other rock types (Halferdahl, 1961; Liou & Chen, 1978). The low Fe^{3+} content of the chloritoids in this study in spite of its coexistence with Fe-Ti oxides may be a consequence of excess Al_2O_3 of the schists which maximises Al solubility in the mineral. Calculated structural formula however doesn't suggest any entry of Al in the tetrahedral Si site. The higher paragonite content of muscovite that replaces chloritoid reflects that muscovite inherited the Al content from chloritoid.

4.4 Textural modelling: Chloritoid forming from kyanite

Formation of chloritoid after kyanite requires open system process. To understand the process of chloritoid formation in the open system textural modelling study was performed integrating the inputs from the textural analyses and measured chemical condition (REF).

The C-Space program was used for the purpose. The program uses the method of singular value decomposition technique to achieve the desired results (Lang et al. 2004). The detail of the computational procedure is given in the Appendix I.

Results

Following modelled reactions are consistent with both the textural features and the compositional characteristics of the minerals. Also included in the reactions are the solid volume change of the reactons (given in the parenthesis)

Chloritoid forming reaction

18.20 **Kyanite** + 40.46 H_2O + 1.00 Na^+ + 362.60 Fe^+ + 43.40 Mg^{2+} = 7.43 **Chloritoid**……..(1) ($\Delta V_{reaction(solid)}$ *= 231.1 cc/mol*)

Kyanite replaced by muscovite

4.24 **Kyanite** + 3.96 H_2O + 47.34 K^+ + 8.92 Na^+ + 4.13 Fe^+ = 1.00**Muscovite**……(2) ($\Delta V_{reaction(solid)}$ *= -43.75 cc/mol*)

Muscovite and diaspore replacing kyanite and chloritoid

8.6064 **Kyanite** + 27.9216 **Chloritoid**+ 1.0000 H_2O + 17.0905 K^+ + 3.0935 Na^+ = 10.2831 **Muscovite** + 36.2770 **Diaspore**+ 49.1199 Fe^{2+} +6.0481 Mg^{2+}……(3) ($\Delta V_{reaction(solid)}$ *= -63.07 cc/mol*)

Chloritoid and kyanite replaced by muscovite

3.41**Kyanite** + 1.92 **Chloritoid**+ 7.40 K^++ 1.39 Na^+= 2.00**Muscovite**+ 2.30 H_2O + 6.94 Fe^{2+}+ 1.00Mg^{2+}……(4) ($\Delta V_{reaction(solid)}$ = *-131.18 cc/mol*)

Chloritoid replacing muscovite

2.07 **Muscovite** + 4.06 H_2O + 10.12 Fe^+ + 1.39 Mg^{2+} = 3.88 **Chloritoid** + 5.30 K^+ + 1.00 Na^+ ……(5) ($\Delta V_{reaction(solid)}$ =*243.58 cc/mol*)

Owing to lower thermal stability of diaspore, the reaction (3) is likely to have formed at distinctly lower temperature and in a separate phase of alteration.

.

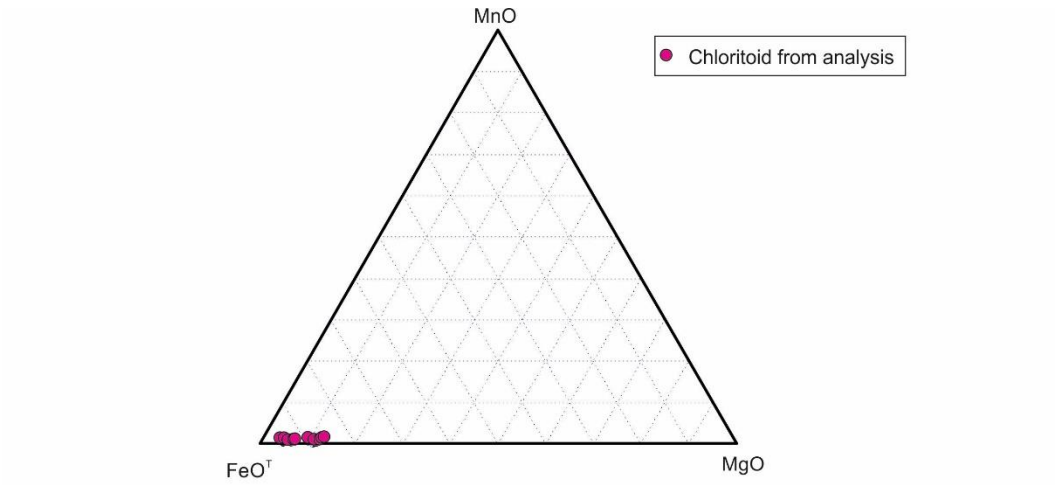

Fig 4.3: Chloritoid from kyanite quartzites near Surda plotted on Fe-Mg-Mn classification.Note that chloritoid is extremely rich in iron and plot close to Fe on the Fe-Mg arm.

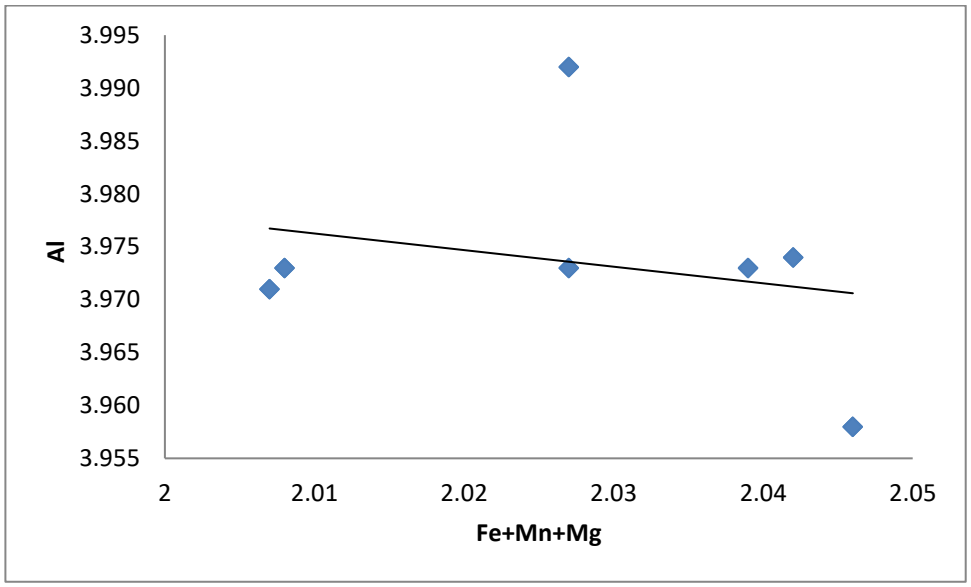

Fig 4.4: A weak negative correlation between Fe+Mg+Mn and Al is noticed in the graphs

Table 4.1: Representative oxide analyses and calculated cations of Kyanite and chloritoid

	Kyanite			Chloritoid						
	S23	S23	S23	S 23a	S 23a	S 23a	S 23a	S 23a	S 23a	S 23a
DataSet/ Point	5 / 1 .	15 / 1 .	9 / 1 .	1 / 1 .	2 / 1 .	7 / 1 .	8 / 1 .	11 / 1 .	12 / 1 .	13 / 1 .
SiO_2	36.89	36.97	36.89	24.13	24.07	24.06	23.97	23.91	24.28	23.90
TiO_2	0.00	0.00	0.00	0.00	0.00	0.00	0.03	0.00	0.07	0.00
Al_2O_3	63.80	62.93	63.35	40.53	40.98	40.27	40.50	40.34	40.69	39.99
Cr_2O_3	0.01	0.07	0.12	0.00	0.08	0.00	0.01	0.00	0.00	0.10
FeO	0.00	0.03	0.37	25.96	25.69	25.60	26.05	25.48	23.67	25.33
MnO	0.03	0.04	0.00	0.13	0.26	0.14	0.17	0.13	0.03	0.10
MgO	0.01	0.01	0.00	1.72	1.90	2.02	1.75	2.01	2.97	1.72
CaO	0.00	0.04	0.01	0.00	0.00	0.04	0.01	0.02	0.00	0.00
Na_2O	0.05	0.02	0.01	0.00	0.00	0.03	0.03	0.03	0.00	0.00
K_2O	0.02	0.00	0.03	0.00	0.00	0.00	0.00	0.01	0.04	0.00
Total	100.81	100.11	100.78	92.470	92.980	92.160	92.520	91.930	91.750	91.140
Si	0.988	0.997	0.990	2.006	1.989	2.006	1.995	1.998	2.011	2.013
Ti	0.000	0.000	0.000	0.000	0.000	0.000	0.002	0.000	0.004	0.000
Al	2.014	2.000	2.004	3.973	3.992	3.958	3.974	3.973	3.973	3.971
Cr	0.000	0.001	0.003	0.000	0.005	0.000	0.001	0.000	0.000	0.007
Fe	0.000	0.001	0.008	1.805	1.775	1.785	1.813	1.780	1.639	1.784
Mn	0.001	0.001	0.000	0.009	0.018	0.010	0.012	0.009	0.002	0.007
Mg	0.000	0.000	0.000	0.213	0.234	0.251	0.217	0.250	0.367	0.216
Ca	0.000	0.001	0.000	0.000	0.000	0.004	0.001	0.002	0.000	0.000
Na	0.003	0.001	0.001	0.000	0.000	0.005	0.005	0.005	0.000	0.000
K	0.001	0.000	0.001	0.000	0.000	0.000	0.000	0.001	0.004	0.000
Σcation	3.007	3.003	3.007	8.007	8.013	8.018	8.019	8.019	8.000	7.998
X_{Mg}				0.11	0.12	0.12	0.11	0.12	0.18	0.11
Fe^{3+}				0.03	0.03	0.05	0.04	0.04	0.01	0.01
Fe^{2+}				1.78	1.75	1.74	1.77	1.74	1.63	1.78

*Note: *Fe^{3+} recalculation after Chopin et al. (1992), X_{Mg} =Mg/(Mg + Fe^{2+}); cation recalculation on 12(O).*

Table 4.2: Representative oxide analyses and calculated cations of Muscovite and paragonite

Sample #	Muscovite (paragonite rich)		Muscovite					Paragonite		
Point #	3 / 1 .	4 / 1 .	6 / 1 .	10 / 1 .	14 / 1 .	20 / 1 .	21 / 1 .	2 / 1 .	25 / 1 .	26 / 1 .
Al_2O_3	38.33	37.32	35.23	35.00	35.19	35.21	35.22	40.61	40.23	40.77
FeO	1.70	0.58	1.14	1.29	0.87	1.00	1.13	0.56	0.45	0.34
TiO_2	0.00	0.15	0.18	0.28	0.13	0.25	0.36	0.06	0.11	0.03
ZnO	0.00	0.00	0.00	0.00	0.00	0.00	0.00	0	0	0
SiO_2	46.10	46.89	46.29	45.95	45.43	45.65	45.18	46.52	45.89	45.95
K_2O	5.87	6.52	9.79	9.70	9.34	9.68	8.90	0.66	0.51	0.43
CaO	0.03	0.06	0.00	0.00	0.00	0.01	0.02	0.21	0.27	0.25
Na_2O	3.33	3.17	1.24	1.20	1.29	1.31	1.18	7.39	7.46	7.36
Cr_2O_3	0.10	0.00	0.19	0.03	0.05	0.00	0.00	0	0.00	0
MnO	0.15	0.09	0.00	0.00	0.01	0.05	0.00	0.01	0.00	0.00
MgO	0.38	0.21	0.81	0.75	0.56	0.66	0.63	0.13	0.16	0.11
NiO	0	0	0	0	0	0	0	0	0	0
Total	95.99	94.99	94.87	94.2	92.87	93.82	92.62	96.15	95.08	95.24
Al	5.875	5.756	5.538	5.542	5.630	5.594	5.642	6.073	6.082	6.142
Fe	0.185	0.063	0.127	0.145	0.099	0.113	0.128	0.059	0.048	0.036
Ti	0.000	0.015	0.018	0.028	0.013	0.025	0.037	0.0057	0.0106	0.0029
Zn	0.000	0.000	0.000	0.000	0.000	0.000	0.000	0.000	0.000	0.000
Si	5.993	6.134	6.173	6.172	6.165	6.152	6.139	5.901	5.885	5.872
K	0.974	1.088	1.665	1.662	1.617	1.664	1.543	0.107	0.083	0.070
Ca	0.004	0.008	0.000	0.000	0.000	0.001	0.003	0.029	0.037	0.034
Na	0.839	0.804	0.321	0.313	0.339	0.342	0.311	1.818	1.855	1.824
Cr	0.010	0.000	0.020	0.003	0.005	0.000	0.000	0.000	0.000	0.000
Mn	0.017	0.010	0.000	0.000	0.001	0.006	0.000	0.001	0.000	0.000
Mg	0.074	0.041	0.161	0.150	0.113	0.133	0.128	0.025	0.031	0.021
Ni	0.000	0.000	0.000	0.000	0.000	0.000	0.000	0.000	0.000	0.000
Σcation	13.971	13.919	14.023	14.015	13.983	14.029	13.930	14.019	14.032	14.001
End members(mol)										
Ti-muscovite	0.00	0.01	0.01	0.01	0.01	0.01	0.02	0.00	0.01	0.00
phlogopite-annite	0.06	0.00	0.01	0.02	0.01	0.01	0.04	0.03	0.03	0.04
celadonite	0.00	0.03	0.11	0.08	0.07	0.09	0.00	0.00	0.00	0.00
pyrophyllite	0.05	0.04	0.00	0.01	0.02	0.00	0.07	0.02	0.02	0.03
paragonite	0.42	0.40	0.16	0.16	0.17	0.17	0.16	0.91	0.93	0.91
margarite	0.00	0.00	0.00	0.00	0.00	0.00	0.00	0.01	0.02	0.02
muscovite	0.47	0.51	0.71	0.72	0.73	0.72	0.72	0.02	0.00	0.01

**End-member recalculation after Holdaway et al. (1988); cation recalculation on 22(O).*

4.5 Physical conditions of metamorphism

The mineral assemblage of the CKQ is not suitable for application of most of the conventional geothermobarometers, nevertheless P-T conditions of metamorphism has been constrained from (1) muscovite –paragonite thermometer and (2) P-T pseudosection for the appropriate bulk compositions.

4.5.1 Muscovite – paragonite geothermometer

Natural paragonite-muscovite pairs define a solvus similar to solvus defined by co-existing alkali feldspars (Eugster and Yoder, 1955). Compositions of such co-existing paragonite-muscovite pairs serve as a monitor of formation or final equilibration temperature (Rosenfeld et al., 1958). This quasibinary pair was used to develop parametric equations for calculating an average, pressure dependant (2-8 kbar) binary Pg-Ms solvus (Blencoe et al., 1994, (Guidotti et al., 1994). Equation E1 below gives the relation between T, $X_{ms}^{Ms(Pg)}$ and $X_{ms}^{Pg(Ms)}$. The temperature T derived from this equation depends on the difference between $X_{ms}^{Ms(Pg)}$ and $X_{ms}^{Pg(Ms)}$, which is a measure of solvus closure for a given temperature (Blencoe et al., 1994).

$$T = 796.5 + 415.47 \ln (1 - (X_{ms}^{Ms(Pg)} - X_{ms}^{Pg(Ms)})^2) \quad \text{……..(E1)}$$

Where T= temperature in °C

$X_{ms}^{Ms(Pg)}$ = mole fraction of muscovite in a Ms coexisting with Pg

$X_{ms}^{Pg(Ms)}$ = mole fraction of muscovite in a Pg coexisting with Ms

Muscovite-paragonite compositions from the CKQ rock used to calculate temperature through this relation give a range of 532°C to 598°C the average being 557°C (Tab. 4.3).

4.5.2 Geothermobarometry using the phase equilibria modelling(pseudosection)

In this section, an attempt has been made through pseudosection modelling to constrain the P-T conditions prevailing during formation of the kyanite + chloritoid assemblage. In view of heterogeneous distribution of the minerals and coarse grain size in the studied rock, reaction volume has been computed from the modal volume in a chloritoid –bearing domain and the measured phase compositions. The detail of the process is given in Appendix IV. The whole rock composition that could be measured from XRF would give erroneous result.The computer program PERPLE_X version 6.9 (Connolly, 2005, 2009) with the thermodynamic dataset of Holland and Powell (1998) and the following solution models were used: Holland and Powell (1998) for garnet, staurolite, chloritoid and biotite and White et al. (White et al., 2014) for mica and chlorite. H_2O was considered as a saturated component, a likely situation in low grade rocks (below granulite facies condition). In view of the mineral compositions **MnTiNKFMASH** (MnO-TiO_2-Na_2O-K_2O-FeO-MgO-Al_2O_3-SiO_2-H_2O) system has been chosen**.** CaO was excluded from the system as it is present only in negligible proportions in the minerals and it was checked that its absence does not have any major impact on the relative phase relations. Fig 4.5.1 represents the P-T pseudosection calculated using bulk 1. The kyanite+ chloritoid+ rutile+ quartz+ muscovite assemblage determines the peak metamorphic field (marked in blue) in P-T space. The studied rock lacks pyrophyllite and staurolite that constrain the temperature between 400°C-540°C at pressure below 8 kbar. Pyrophyllite, however is present in several neighbouring rocks and in other kyanite quartzites of the region isformed after kyanite during retrogression or during a separate phase of low temperature metamorphism.Absence of sillimanite and andalusite suggest that the pressure was above 4 kbar (above the Al_2SiO_5 triple point, Fig. 4.5.1-green dotted line, Phillpot and Ague, 2009). Absence of suitable marker does not allow precise determination of the

metamorphic pressure. Notwithstanding the uncertainties that are associated with the muscovite paragonite thermometry and the P-T pseudosection, temperature close to 500°C seems to be reasonable at which the chloritoid was formed.

Table 4.3: Representative oxide analyses and calculated cations of Muscovite-paragonite pairs

	Muscovite			Paragonite		
Sample #	Ms1	Ms2	Ms3	Pg1	Pg2	Pg3
Al_2O_3	37.73	37.78	37.53	40.61	40.23	40.77
FeO	1.06	0.62	0.85	0.56	0.45	0.34
TiO_2	0.00	0.12	0.01	0.06	0.11	0.03
ZnO	0.00	0.00	0.00	0.00	0.00	0.00
SiO_2	46.30	46.72	46.63	46.52	45.89	45.95
K_2O	7.42	7.23	7.35	0.66	0.51	0.43
CaO	0.03	0.06	0.02	0.21	0.27	0.25
Na_2O	1.78	2.46	1.85	7.39	7.46	7.36
Cr_2O_3	0.00	0.00	0.00	0.00	0.00	0.00
MnO	0.13	0.08	0.11	0.01	0.00	0.00
MgO	0.25	0.29	0.25	0.13	0.16	0.11
NiO	0.00	0.00	0.00	0.00	0.00	0.00
Total	95.99	94.99	94.23	96.15	95.08	95.24
Al	5.89	5.76	5.81	6.07	6.08	6.14
Fe	0.19	0.06	0.09	0.06	0.05	0.04
Ti	0.00	0.01	0.00	0.01	0.01	0.00
Zn	0.00	0.00	0.00	0.00	0.00	0.00
Si	6.01	6.14	6.14	5.90	5.89	5.87
K	1.23	1.21	1.24	0.11	0.08	0.07
Ca	0.00	0.01	0.00	0.03	0.04	0.03
Na	0.45	0.62	0.47	1.82	1.85	1.82
Cr	0.01	0.00	0.00	0.00	0.00	0.00
Mn	0.02	0.01	0.01	0.00	0.00	0.00
Mg	0.07	0.04	0.05	0.02	0.03	0.02
Ni	0.00	0.00	0.00	0.00	0.00	0.00
Σcation	13.88	13.88	13.81	14.02	14.03	14.00
End members(mol)						
paragonite	0.23	0.31	0.24	0.91	0.93	0.91
muscovite	0.61	0.58	0.61	0.02	0.00	0.01
$X_{ms}^{Ms(Pg)}$	0.73	0.66	0.72			
$X_{ms}^{Pg(Ms)}$				0.06	0.04	0.04
Mineral Pair	**Ms1-Pg1**	**Ms2-Pg2**	**Ms3-Pg3**			
T (°C)	541.44	598.17	531.95			

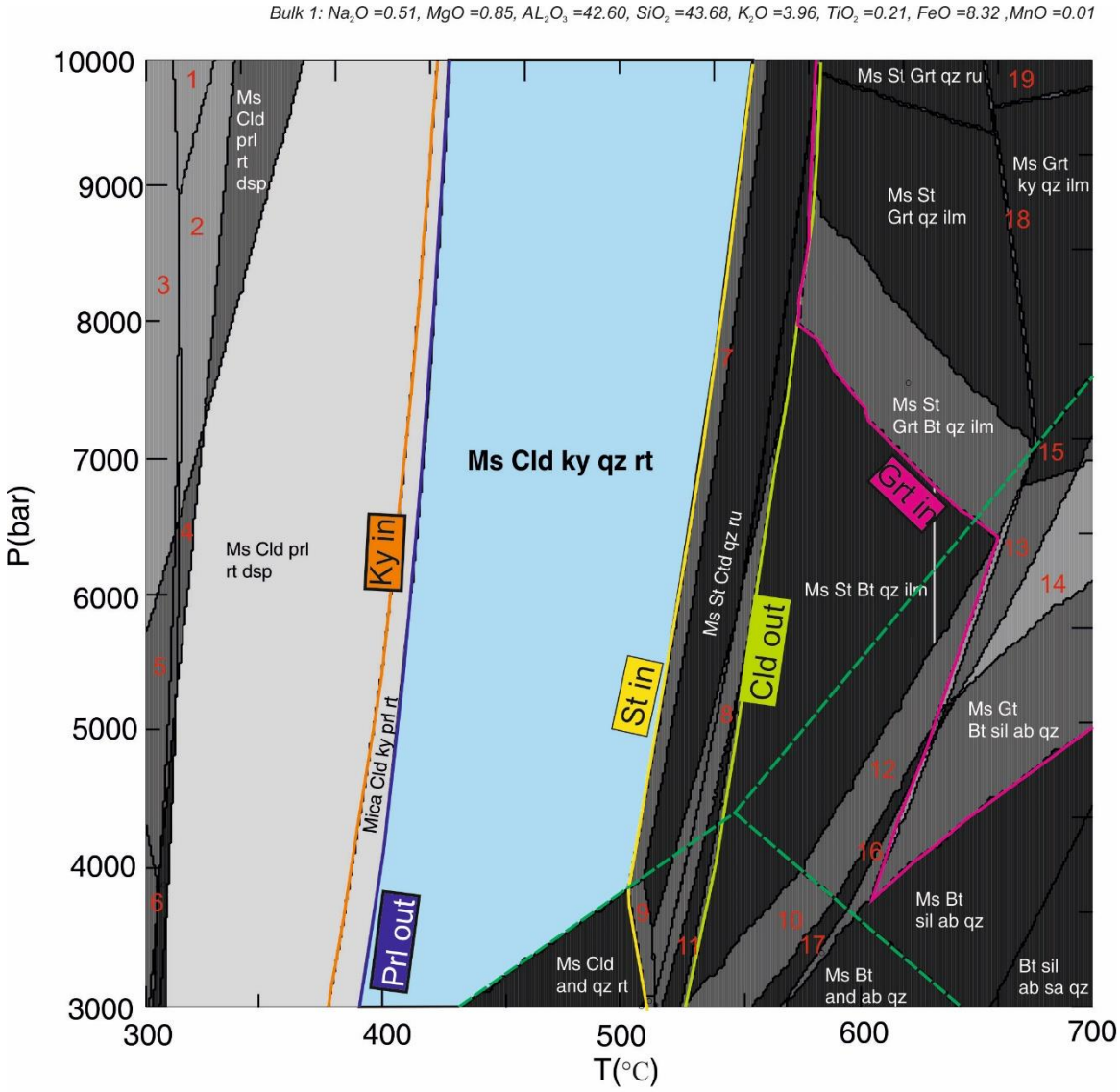

Fig 4.5.1. a)P-T pseudosection calculated for Chloritoid bearing kynaite quartzites of Jaduguda in MnTiNKFMASH model system with bulk 1. The bulk composition is given as wt% of the oxides. Field marked in blue colour in the diagram represents the peak assemblage of the rock. Cld-Chloritoid, Prl-Pyrophyllite, St-Staurolite, Dsp-Diaspore, Ms-Muscovite, Ky-Kyanite. All mineral abbreviations are after Whitney and Evans (2010).

The phases stable in fields numbered in red are given below

1.Ms Cld mcar qz rt dsp
2.Ms Cld mcar prl rt dsp
3.Ms Cld mcar kln qz rt
4.Ms Cld mcar prl rt dsp
5.Ms Cld mcar kln qz rt
6. Chl Ms Cld kln qz rt
7. Ms St Cld ky qz rt
8. Chl Ms St Cld qz ilm
9. Ms St Cld and qz rt
10. Ms St Bt and qz ilm
11. Chl Ms St q ilm
12. Ms St Bt sil qz ilm
13. Ms Grt Bt sil qz ilm
14. Ms Grt Bt sil ab qz ilm
15. Ms Grt sil qz ilm
16. Ms St Bt sil qz
17. Ms St Bt and qz
18. Ms St Grt ky qz ilm
19. Ms Grt ky qz rt

4.5.3 Stability of different mineral assemblages calculated through chemical potential diagrams (μ-μ)

The KQ in which the CKQ occurs as veins and pods does not contain any source of Fe and Mg from which large volume of chloritoid (upto 40 vol% at places) could form. The C-space reaction modelling shows that H_2O and a number of elements including Fe, Mg were introduced from an external source during chloritoidization of kyanite. (Reaction 1). The phases, corundum, quartz, chloritoid, garnet and kyanite are chosen. Within the P-T range of the calculation only kyanite is stable. To understand the process of chloritoidization of kyanite two sets of μSiO_2-μFeO diagrams were constructed in the FeO-Al_2O_3-SiO_2-H_2O (FASH) system. In one set pressure was held constant at 6kb and temperature varied from 450°C to 600°C. (Fig. 4.5.2). In the other set temperature was held constant at 500°C at different pressures (5, 6, 7 and 8kb; Fig. 4.5.3). The computer program PERPLEX (Version 6.8.9) is used with the thermodynamic data from Holland and Powell (1998). The influence of activities of the minerals on the chemical potential diagrams are also shown. The activity of chloritoid is computed with the AX program of Holland and Powell (1998) from the measured compositions. Since the studied rock does not develop staurolite and garnet, the chemical potential diagrams are calculated over a range of activities of these phases (Fig. 4.5.5, 4.5.6). The activity of H_2O is considered as 1, an assumption that is considered reasonable for low grade metamorphic rocks (REF). Also included in the chemical potential diagram is the minimum silica activity at which quartz is stable (the Qz sat line).

Results

I. Chemical potential diagrams FASH system

In the isobaric sections (at 6kbar) and in the temperature range of 450°C-600°C, the chemical potential diagram shows that stability field of chloritoid is dramatically reduced and eventually disappeared beyond 550°C. Stability of kyanite (with quartz) is restricted to higher μSiO_2 and μFeO with increase in temperature. Stability of corundum also increased with increasing temperature with stability field of quartz + corundum. In presence of quartz, the stability field of chloritoid is separated from kyanite by staurolite at temperature between 550°C to 600°C. At temperature between 450°C-500°C, the boundary between chloritoid and kyanite is insensitive to μSiO_2. This then follows that an increase in μFeO in the metasomatic fluid can transform kyanite to chloritoid. This observation is consistent with the field features showing the chloritoidization of kyanite in the quartz bearing rock (Fig. 4.2g,i). To prevent staurolite, the temperature should be 500°C or below. It is also evident that the geothermal gradient should not be hotter than 83°C/kbar for metasomatic chloritoid formation after kyanite. The probable range of μSiO_2 and μFeO for the assemblage kyanite-chloritoid-quartz is marked with red bold line as μSiO_2 cannot be greater than 1.

The isothermal section (500°C), shows that with increasing pressure (5-8kbar) the kyanite-chloritoid phase boundary remains intact in the pressure range above 5kbar. Staurolite does not appear above 5kbar. The field of chloritoid shrinks in favour of the stability field of garnet (Fig. 4.5.3d). The stability fields of kyanite and corundum remain virtually constant. Although not documented in this study, the isothermal-isobaric chemical potential diagrams raise that possibility that silica metamomatism of corundum could also form kyanite rich rock in nature. It is also possible that desilication of kyanite can form metasomatic corundum that is reported in some

kyanite-rich quartz-free rock in the SSZ (marked by thin red arrow in Fig 4.5.3) (Sarkar and Gupta, 2012).

Fig. 4.5.4 shows that reduction in the activity of H_2O has a dramatic effect on the stability of chloritoid. While, a reduced activity of H_2O reduces the stability field of chloritoid at the expenses of garnet and staurolite, the enlargement of garnet is more conspicuous than the stability field of staurolite (Fig. 4.5.4b,c). However, in presence of quartz, change of activity of H_2O has no effect on chloritoid-kyanite relation.

In order understand the effects of mineral compositions on the FASH μ-μ topology a series of diagrams are computed for constant pressure and temperature (6 kbar, 500°C). The activity of iron endmember of chloritoid (a_{fCtd}) has been computed from the measured compositions of chloritoid using the A-X program of Holland and Powell (1998). The CKQ does not contain garnet or staurolite. Fig 4.5.5 shows that for the calculated activity of chloritoid, garnet only appears in the almandine activity at 0.6 or less. Above this range, chloritoid is prevalent in the area at the higher μFeO and μSiO_2. Further reduction of the activity of almandine would lead to a marked reduction of the chloritoid activity. Staurolite appears only if activity of Fe-staurolite drops down to 0.4 or less (Fig.4.5.6). However, staurolite never appears in quartz bearing rock at activity greater than 0.4 (Fig.4.5.6).

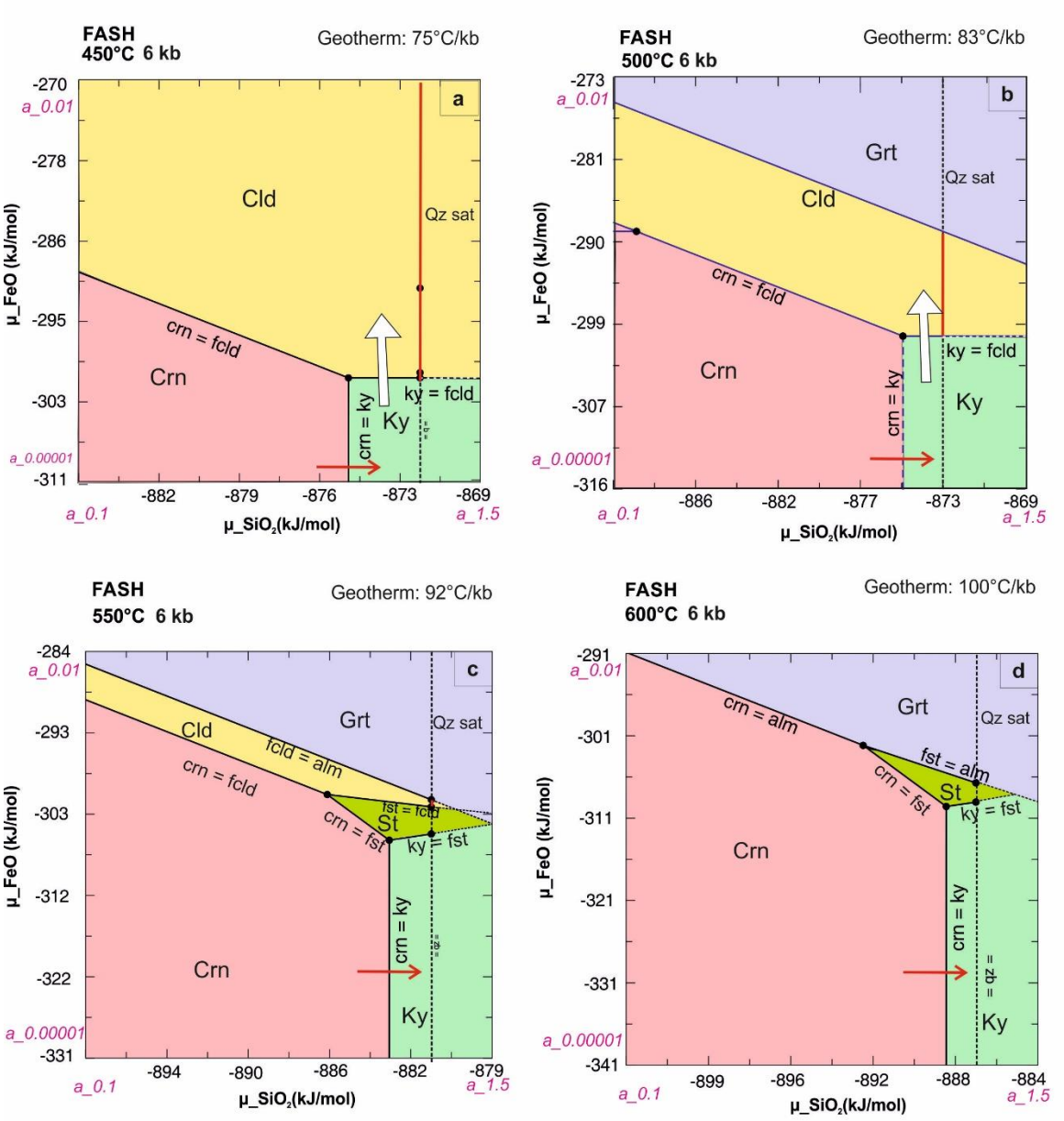

Fig 4.5.2 μSiO_2-μFeO diagram computed at 6kb and a) 450°C, b)500°C, c)550°C and d)600°C in a FASH (FeO-Al_2O_3-SiO_2-H_2O) system showing that chloritoid forms both from corundum and kyanite. Above 550°C chloritoid cannot form from kyanite at 6kb pressure. The thick white arrow indicates formation of chloritoid from kyanite. The red bold line marks the region of chloritoid +quartz stability just on the quartz saturation line. Mineral abbreviations: Crn=corundum, Cld=chloritoid, Fcld=Fe-chloritoid, Grt-garnet, Alm= almandine, Ky=kyanite, Qz=quartz. Mineral abbreviations are after Whitney and Evans (2010).

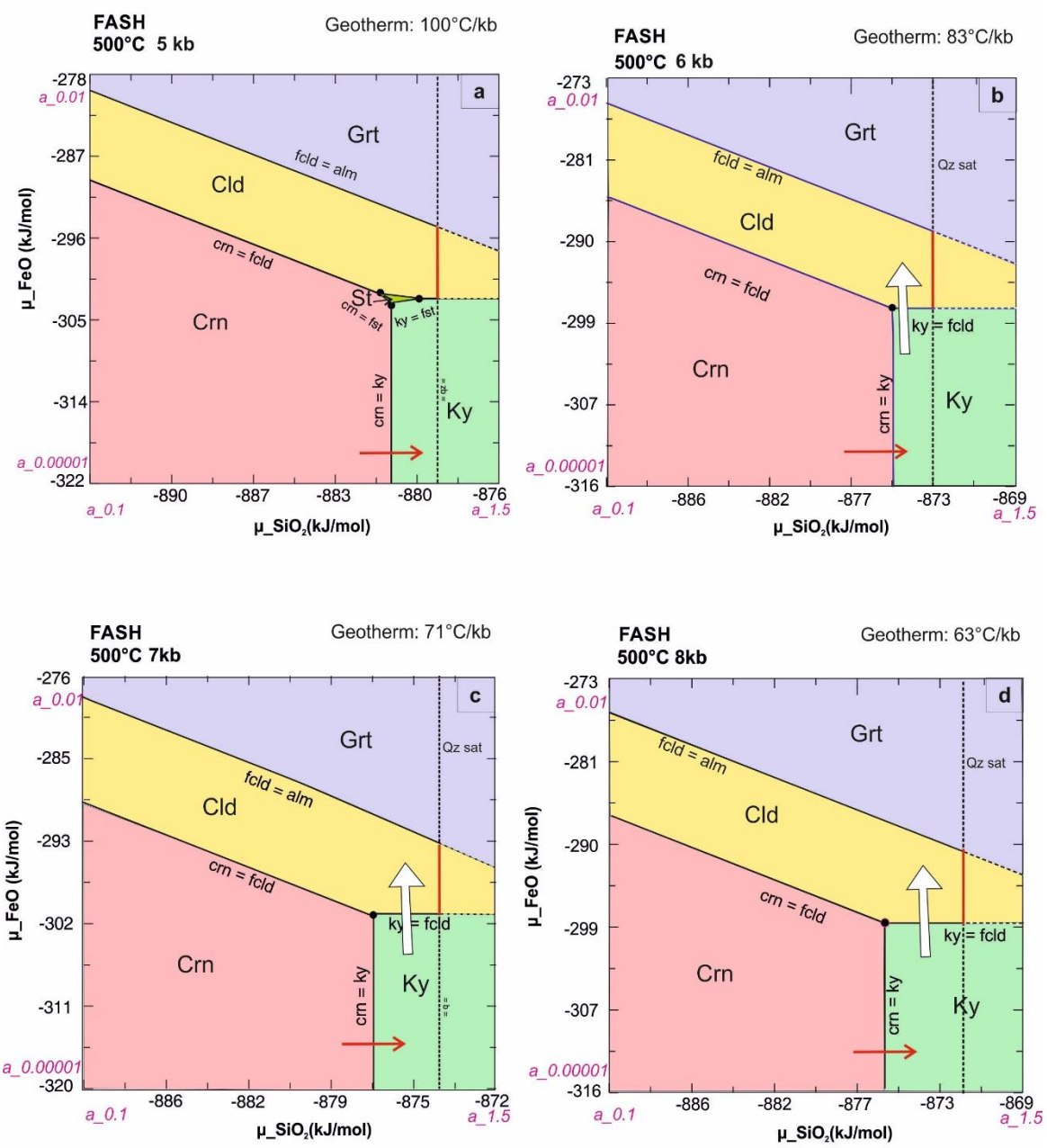

Fig 4.5.3 μSiO_2-μFeO diagram computed at 500°C and a) 5kb, b)6kb, c)7kb and d)8kb in a FASH (FeO-Al_2O_3-SiO_2-H_2O) system. The red bold line marks the region of chloritoid +quartz stability just on the quartz saturation line. Mineral abbreviations: Crn=corundum, Cld=chloritoid, Fcld=Fe-chloritoid, Grt-garnet, Alm=almandine, Ky=kyanite, Qz=quartz.

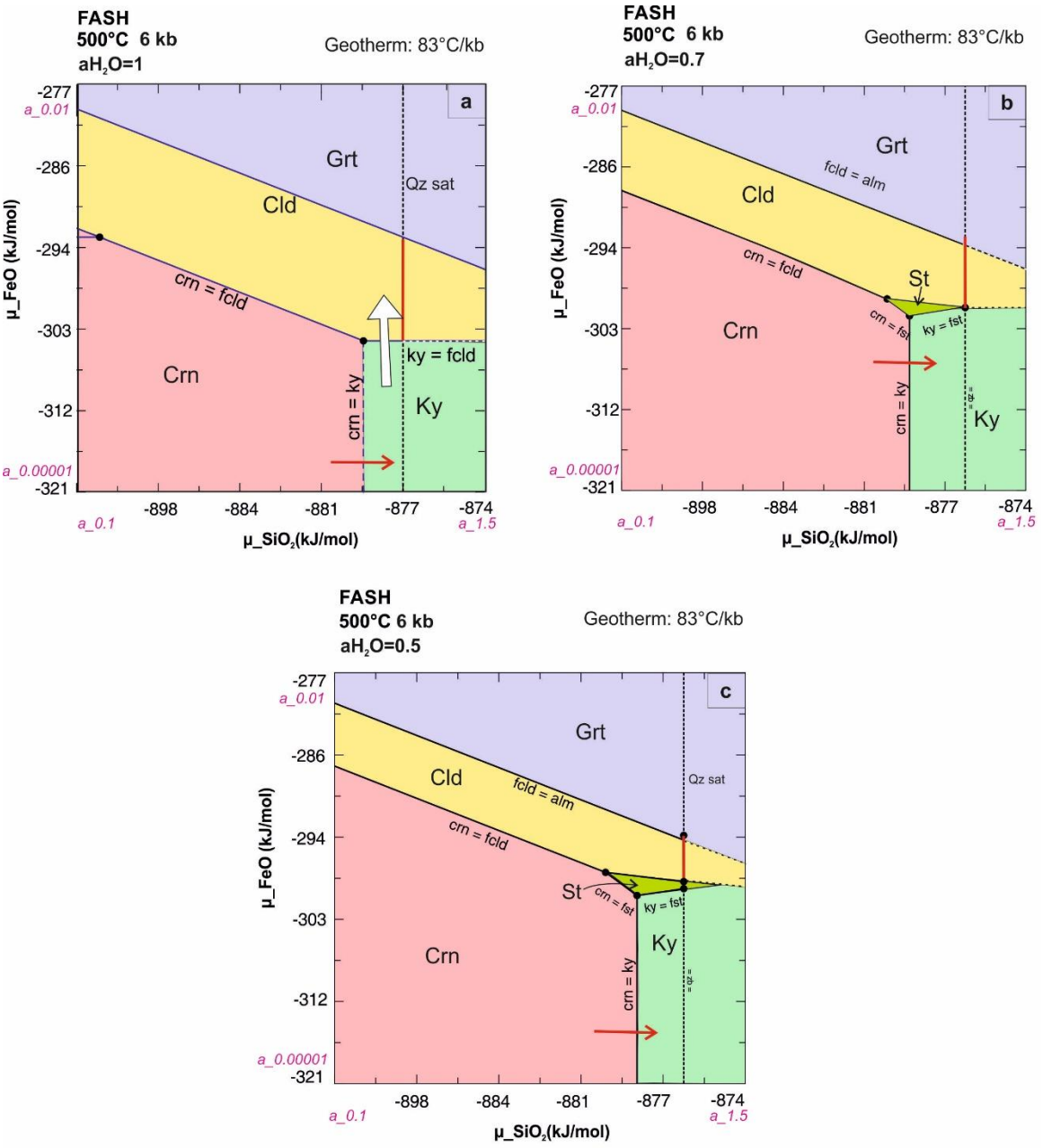

Fig 4.5.4 μSiO_2-μFeO diagram computed at 6kb and 500°C a)aH_2O=1 b)aH_2O=0.7 and c) aH_2O=0.5 in a FASH (FeO-Al_2O_3-SiO_2-H_2O) system showing that staurolite instead of chloritoid develops at from kyanite if aH_2O=0.7 or below is taken instead of aH_2O=1; The red bold line marks the region of chloritoid + quartz stability just on the quartz saturation line. Mineral abbreviations: Crn=corundum, Cld=chloritoid, Fcld=Fe-chloritoid, Grt-garnet, Alm=almandine, Ky=kyanite, Qz=quartz. Mineral abbreviations are after Whitney and Evans (2010)

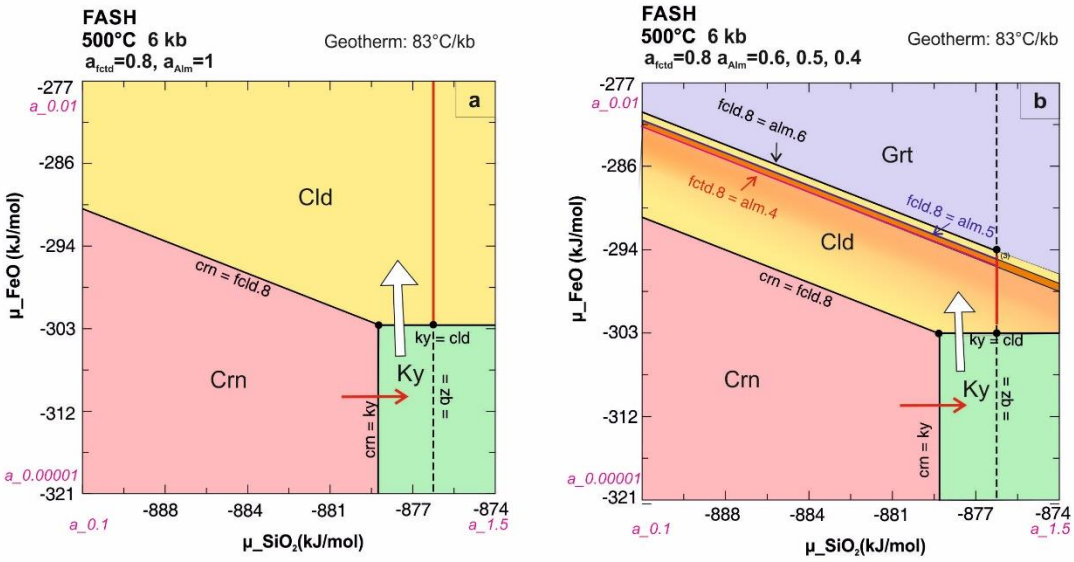

Fig 4.5.5 μSiO_2-μFeO diagram computed at 6kb and 500°C with different activities of almandine and a_{Fctd}=0.8 a) a_{Alm}=0.6 where no garnet field is present b) a_{Alm} is varied through 0.5 to 0.3.The garnet field appears and shifts to lower μFeO in a FASH (FeO-Al_2O_3-SiO_2-H_2O) system with decreasing a_{Alm}; The red bold line marks the region of chloritoid +quartz stability just on the quartz saturation line. Mineral abbreviations: Crn=corundum, Cld=chloritoid, Fcld=Fe-chloritoid, Grt-garnet, Alm=almandine, Ky=kyanite, Qz=quartz. Mineral abbreviations are after Whitney and Evans (2010). fcld.8= Fe-chloritoid activity 0.8; alm.6= almandine activity 0.6, alm.5=almandine activity 0.5, alm.4=almandine activity 0.4

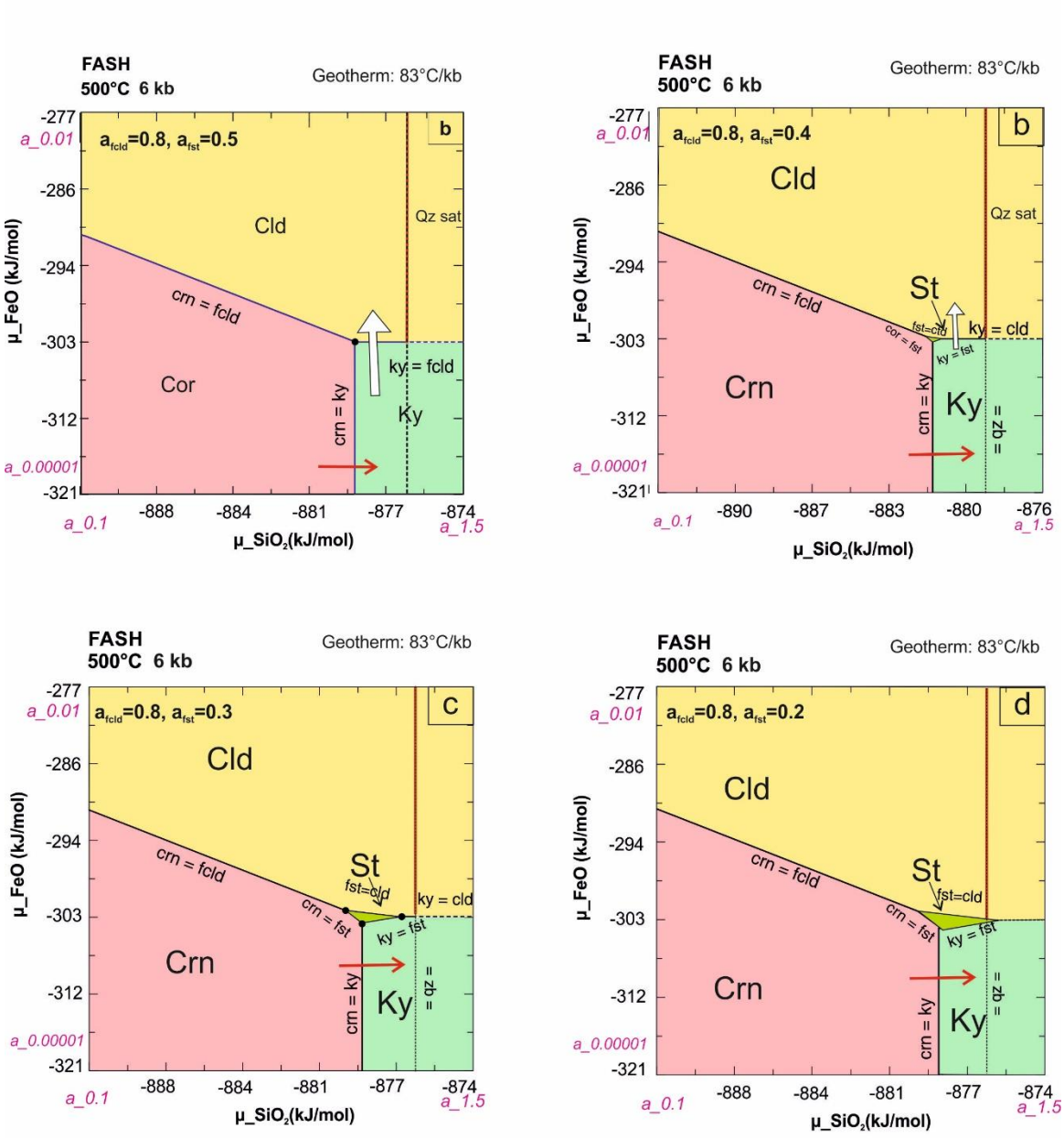

Fig 4.5.6 μSiO_2-μFeO diagram computed at 6kb and 500°C with different activities of staurolite and a_{Fctd}=0.8 in a FASH (FeO-Al_2O_3-SiO_2-H_2O) system c) a_{Fst}=0.6 where no staurolite field is present b) Staurolite appears at a_{Fst}=0.5 c)Staurolite shifts to higher μFeO at a_{Fst}=0.4 d) Staurolite field is larger and shifts to higher μFeO at a_{Fst}=0.3 The garnet field appears here ; The red bold line marks the region of chloritoid +quartz stability just on the quartz saturation line. Mineral abbreviations: Crn=corundum, Cld=chloritoid, Fcld=Fe-chloritoid, Grt-garnet, Alm=almandine, Ky=kyanite, Qz=quartz, St=staurolite, Fst=Fe-staurolite. Mineral abbreviations are after Whitney and Evans (2010)

4.6 Summary

The foregoing analyses suggest that the rocks of the studied area witnessed metamorphism in low temperature and moderate pressure conditions. Chloritoid formed at such low P-T conditions are not common. Usually, chloritoid bearing metapelitic rocks are reported from several regional metamorphic terrains (Atkinson, 1956; Chinner, 1967; Baltatzis & Wood, 1977; Holdaway, 1978; Liou and Chen, 1978; Lal & Ackermand, 1979; Labotka, 1981; Ashworth & Evirgen, 1984; (Javkhlan et al., 2013). It has been reported rarely from contact metamorphic zones (Atherton, 1980; Kaneko & Miyano, 1990; Okuyama-Kusunose, 1994; Flinn et al., 1996; Likhanov et al., 2001) and hydrothermal environments (Ochoa et al., 2007). In hydrothermal environments and contact aureoles chloritoid rarely develops due to constraints in bulk composition and narrow temperature intervals. In this study the field disposition (formation of chloritoid at boudin heads) and textural evidences point towards its hydrothermal nature. Chloritoids of Singhbhum shear zone are found primarily associated with i) Quartz-chlorite-muscovite-biotite-magnetite rock ii) Garnet-muscovite-biotite-magnetite-quartz rock and iii) Kyanite-quartz-muscovite-magnetite rocks. The associations are found at short distances from one another indicating that varying bulk chemistry of rocks played a more important role than thermo-barometric factors in the development of these assemblages.

Stability of chlotitoid: Experimental studies on oxide mixtures, to determine the stability of chloritoid in fluid rich environments, with oxygen fugacities defined by Ni-NiO buffer, revealed that at pressures between 1 to 5kb, chloritoid was not stable above 850K and decomposed partially to Fe-cordierite and hercynite (Reaction 1) (Grieve and Fawcett, 1974).

Chloritoid = Fe-cordierite + Hercynite spinel + H_2O ……(1)

Chloritoid = Al-Ferroanthophyllite + Staurolite + Hercynite spinel + H_2O ……..(2)

57 Chloritoid+ 4 O_2 = 12 Staurolite+ 3 Almandine + 8 Magnetite+ 51 H_2O…….(3)

At pressure greater than 5.5 kb, aluminous ferro-anthophyllite, staurolite appeared as products along with hercynite (Reaction 2). Aluminous ferro-anthophyllite was replaced by almandine at higher temperature. The breakdown of chloritoid at lower oxygen fugacities of QFM buffer gives the same products only at slightly higher temperatures (Grieve and Fawcett, 1974). The breakdown of chlorioitd to hercynite-rich spinel (i.e. Fe^{2+} to Fe^{3+} phase) is an oxidation reaction. The lower oxygen fugacities favour the thermal stability of chloritoid and reduces the stability field for aluminous ferro-anthophyllite assemblage. The experimental data of Halferdhal (1961b) was based on the unreversed breakdown of natural chloritoid and chloritoid synthesis experiment where the equilibrium phases are stabilized at higher temperature and also makes almandine a stable product. Ganguly (1969) opined that at higher oxygen fugacities magnetite becomes more stable than hercynite (Reaction 3). Presence of additional components like MgO may also lower the thermal stability of chloritoid. In natural systems K_2O component is reflected by the presence of muscovite and biotite, while phases like muscovite, aluminosilicates and quartz become part of chloritoid producing reactions. Richardson (1968) determined chloritoid stability limits in the presence of aluminosilicates and quartz (Reaction 4). Reactions 5 (Tilley, 1925), 6 (Harker, 1932) and 7 are dependent on oxygen fugacities and determine chloritoid stabilities in the absence of aluminosilicates.

Chloritoid + Aluminosilicate = Staurolite + Quartz + H_2O …….(4)

Chloritoid + Muscovite + Quartz = Staurolite + Biotite + H_2O ……(5)

Chloritoid + Quartz = Almandine + Staurolite + H_2O …….(6)

Chloritoid + Quartz = Al-Ferroanthophyllite + Staurolite + H_2O ……..(7)

These findings are consistent with disapperence of chloritoid at the boundary of Greenschist-Amphibolite facies and appearance of staurolite + almandine + anthophyllite in regional metamorphism (823K, 4-8 kb). Ferro-anthophyllite and cordierite appear at the albite-epidote and hornblende hornfels boundary (773-823K, 0.5-3 kb) (Winkler, 1967).

In the present study kyanite+rutile+quartz form the earliest assemblage. The low ferric composition of chloritoid indicates lower oxygen fugacities which stabilize chloritoid. The presence of chloritoid + kyanite + quartz + muscovite and absence of pyrophyllite, staurolite indicate that P-T conditions can be restricted based of the stability of these phases only. The muscovite-paragonite pair constrains the temperature range down to 532°C to 598°C. In order to reconstruct the metamorphic P-T conditions, the textural relations have been interpreted in the numerically computed phase diagrams in the MnTiNKFMASH system (Fig 4.6.7). Only the temperature range of 400°C-520°C for stabilization of the peak metamorphic aseemblage could be achieved through it. The chemical potential diagrams map the formation of chloritoid at prograde peak through breakdown of kyanite and also the breakdown of chloritoid during retrograde phase to diaspore which are consistent with the textural observations. The chemical potential diagrams constrain the P-T range down to ~ 6kb and ~500°C. Petrological studies on metapelitic rocks i.e. chloritoid-garnet-biotite-chlorite schists near Surda were carried out by Sengupta (2012) and established through quantitative geothermobarometry and pseudosections that prograde metamorphism culminated at 6.3±1 kbar and 490±40 °C which corroborates the P-T range established through this study.

References

Albee, A.L., 1972. Metamorphism of pelitic schists: reaction relations of chloritoid and staurolite. Geol Soc Am Bull 83, 3249–3268.

Ashworth, J.R., Evirgen, M.M., 1984. Mineral chemistry of regional chloritoid assemblages in the Chlorite Zone, Lycian Nappes, South-west Turkey. Mineral Mag 48, 159–165. https://doi.org/DOI: 10.1180/minmag.1984.048.347.01

Atherton, M.P., 1980. The occurrence and implications of chloritoid in a contact aureole andalusite schist from Ardara, County Donegal. Journal of Earth Sciences 101–110.

Atkinson, D.J., 1956. The Occurrence of chloritoid in the Hecla Hoek Formation of prince charles foreland, Spitsbergen. Geol Mag 93, 63–71.

Baltatzis, E., Wood, B.J., 1977. The occurrence of paragonite in chloritoid schists from Stonehaven, Scotland. Mineral Mag 41, 211–216.

Blencoe, J.G., Guidotti, C. v, Sassi, F.P., 1994. The paragonite-muscovite solvus: II. Numerical geothermometers for natural, quasibinary paragonite-muscovite pairs. Geochim Cosmochim Acta 58, 2277–2288.

Chinner, G.A., 1967. Chloritoid, and the isochemical character of Barrow's zones. Journal of Petrology 8, 268–282.

Chinner, G.A., Smith, J. v, Knowles, C.R., 1969. Transition-metal contents of Al2SiO5 polymorphs. Am J Sci 267, 96–113.

Chopin, C., Seidel, E., Theye, T., Ferraris, G., Ivaldi, G., Catti, M., 1992. Magnesiochloritoid, and the Fe-Mg series in the chloritoid group. European Journal of Mineralogy 67–76.

Eugster, H.P., Yoder, H.S., 1955. The join muscovite-paragonite. Carnegie Institute of Washington Yearbook 54, 124–126.

Flinn, D., Key, R.M., Khoo, T.T., 1996. The chloritoid schists of Shetland and their thermal metamorphism. Scottish Journal of Geology 32, 67–82.

Ganguly, J., 1969. Chloritoid stability and related paragenesis; theory, experiments, and applications. Am J Sci 267, 910–944.

Grambling, J.A., 1983. Reversals in Fe-Mg partitioning between chloritoid and staurolite. American Mineralogist 68, 373–388.

Grieve, R.A.F., Fawcett, J.J., 1974. The stability of chloritoid below 10 kb PH2O. Journal of Petrology 15, 113–139.

Guidotti, C. v, Sassi, F.P., Blencoe, J.G., Selverstone, J., 1994. The paragonite-muscovite solvus: I. PTX limits derived from the Na-K compositions of natural, quasibinary paragonite-muscovite pairs. Geochim Cosmochim Acta 58, 2269–2275.

Halferdahl, L.B., 1961a. Chloritoid: its composition, X-ray and optical properties, stability, and occurrence. Journal of Petrology 2, 49–135.

Halferdahl, L.B., 1961b. Chloritoid: its composition, X-ray and optical properties, stability, and occurrence. Journal of Petrology 2, 49–135.

Hanscom, R., 1980. The structure of triclinic chloritoid and chloritoid polymorphism. American Mineralogist 65, 534–539.

Harker, A., 1932. Metamorphism, Methuen & Co. Ltd., London 280.

Holdaway, M.J., 1978. Significance of chloritoid-bearing and staurolite-bearing rocks in the Picuris Range, New Mexico. Geol Soc Am Bull 89, 1404–1414.

Holland, T.J.B., Powell, R., 1998. An internally consistent thermodynamic data set for phases of petrological interest. Journal of metamorphic Geology 16, 309–343.

Javkhlan, O., Takasu, A., Bat-Ulzii, D., Kabir, M.F., 2013. Metamorphic pressure-temperature evolution of garnet-chloritoid schists from the Lake Zone, SW Mongolia. Journal of Mineralogical and Petrological Sciences 108, 255–266.

Kaneko, Y., Miyano, T., 1990. Contact metamorphism by the Bushveld Complex in the northeastern Transvaal, South Africa. Journal of Mineralogy, Petrology and Economic Geology 85, 66–81.

Labotka, T.C., 1981. Petrology of an andalusite-type regional metamorphic terrane, Panamint Mountains, California. Journal of Petrology 22, 261–296.

Lal, R.K., Ackermand, D., 1979. Coexisting chloritoid-staurolite from the Sillimanite (fibrolite) zone, Sini, district Singhbhum, India. Lithos 12, 133–142.

Likhanov, I.I., Reverdatto, V. v, Sheplev, V.S., Verschinin, A.E., Kozlov, P.S., 2001. Contact metamorphism of Fe-and Al-rich graphitic metapelites in the Transangarian region of the Yenisei Ridge, eastern Siberia, Russia. Lithos 58, 55–80.

Liou, J.G., Chen, P.-Y., 1978. Chemistry and origin of chloritoid rocks from eastern Taiwan. Lithos 11, 175–187.

Ochoa, M., Arribas, J., Mas, R., Goldstein, R.H., 2007. Destruction of a fluvial reservoir by hydrothermal activity (Cameros Basin, Spain). Sediment Geol 202, 158–173.

Okuyama-Kusunose, Y., 1994. Phase relations in andalusite-sillimanite type Fe-rich metapelites: Tono contact metamorphic aureole, northeast Japan. Journal of Metamorphic Geology 12, 153–168.

Richardson, S.W., 1968. Staurolite stability in a part of the system Fe-Al-Si-OH. Journal of Petrology 9, 467–488.

Rosenfeld, J.L., Thompson, J.B., Zen, E., 1958. Data on coexistent muscovite and paragonite. Geol Soc Am Bull 69, 1637.

Sengupta, N., 2012. Stability of chloritoid 1 biotite-bearing assemblages in some metapelites from the Palaeoproterozoic Singhbhum Shear Zone, Eastern India and their implications. Geol Soc Spec Publ 365, 91–116. https://doi.org/10.1144/SP365.6

Tilley, C.E., 1925. Petrographical notes on some chloritoid rocks. Geol Mag 62, 309–319.

White, R.W., Powell, R., Holland, T.J.B., Johnson, T.E., Green, E.C.R., 2014. New mineral activity–composition relations for thermodynamic calculations in metapelitic systems. Journal of Metamorphic Geology 32, 261–286.

Winkler, H.G.F., 1967. The Abukuma-Type Facies Series, in: Petrogenesis of Metamorphic Rocks. Springer, pp. 116–124.

Whitney, D.L., Evans, B.W., 2010. Abbreviations for names of rock-forming minerals. Am. Mineral. 95, 185–187. https://doi.org/10.2138/am.2010.3371

CHAPTER 5

Lazulite and augelite bearing kyanite quartzite

In this chapter petrology of the Mg bearing aluminophosphate (AP), lazulite and hydrated aluminophosphate augelite reported from muscovite poor KQ exposed near Kanyaluka, Jharkhand, are discussed. The minerals are found as disseminated sea-green colour pockets or patches in the kyanite quartzite rocks (KQ). In the vicinity of this KQ, chloritoid -garnet -biotite schists, garnet-muscovite-biotite schists and tourmalinite rocks are exposed. Association of exotic AP minerals with KQ forms the subject of this present study.

5.1 Field features

The studied KQ rocks bearing AP minerals occur as milky white detached outcrops along the north-eastern fringe of the SSZ, and close to its boundary with the NSFB (Fig.5.1). The general trend of the SSZ swings from E-W to NNE-SSW just north of Kanyaluka (Fig 1.1). Here the KQ forms detached layers that occur on the hanging-wall side of the SSZ (Fig 5.1). The KQ studied near Kanyaluka shows millimeter to decimeter thick layers rich in kyanite (~50-70 vol%) within quartzite unit (Fig. 5.2a). This compositional banding is roughly parallel with the regularly N-S trending regional mylonitic foliation. Laterally continuous kyanite-rich bands show variation in thickness both along and across the strike (Fig.5.2a, b and c). The boundary between the kyanite-rich layers and the host quartzite is generally planar but locally the boundary of the two compositional bands simulates sedimentary structures like load cast (Fig.5.2b) and ripple marks (Fig. 5.2b). The rhythmic intercalations of kyanite and quartz-rich layers are cut by veins rich in kyanite (~70 vol%) with little quartz (Fig.5.2c). Sea-green coloured lazulite-rich lensoid pods, a few centimeters to several decimeters across, are restricted within the kyanite-rich bands and rarely in the kyanite-quartz veins (Fig.5.2d and e). Tropical

weathering preferentially leached out the AP mineral rich pods and left vugs in the kyanite-rich bands (Fig.5.2f). Field features thus suggest that formation of lazulite occured after the formation of the kyanite-quartz veins. The KQ rocks are intimately associated with highly iron-rich chloritoid (X_{Mg}=0.08-0.14)-garnet (X_{alm}= Fe/(Fe+Mg+Mn+Ca) = 0.90-0.93)-biotite (X_{Mg}=0.34-0.41) schists, garnet-muscovite-biotite schists and tourmalinite (Fig.5.1; Sengupta 2012). In places network of magnetite-apatite segregations occur in the associated chloritoid-mica schists (Sengupta 2012). All these rocks including the KQ rocks are deformed with the development of a prominent NNE-SSW mylonitic foliation dipping to the east.

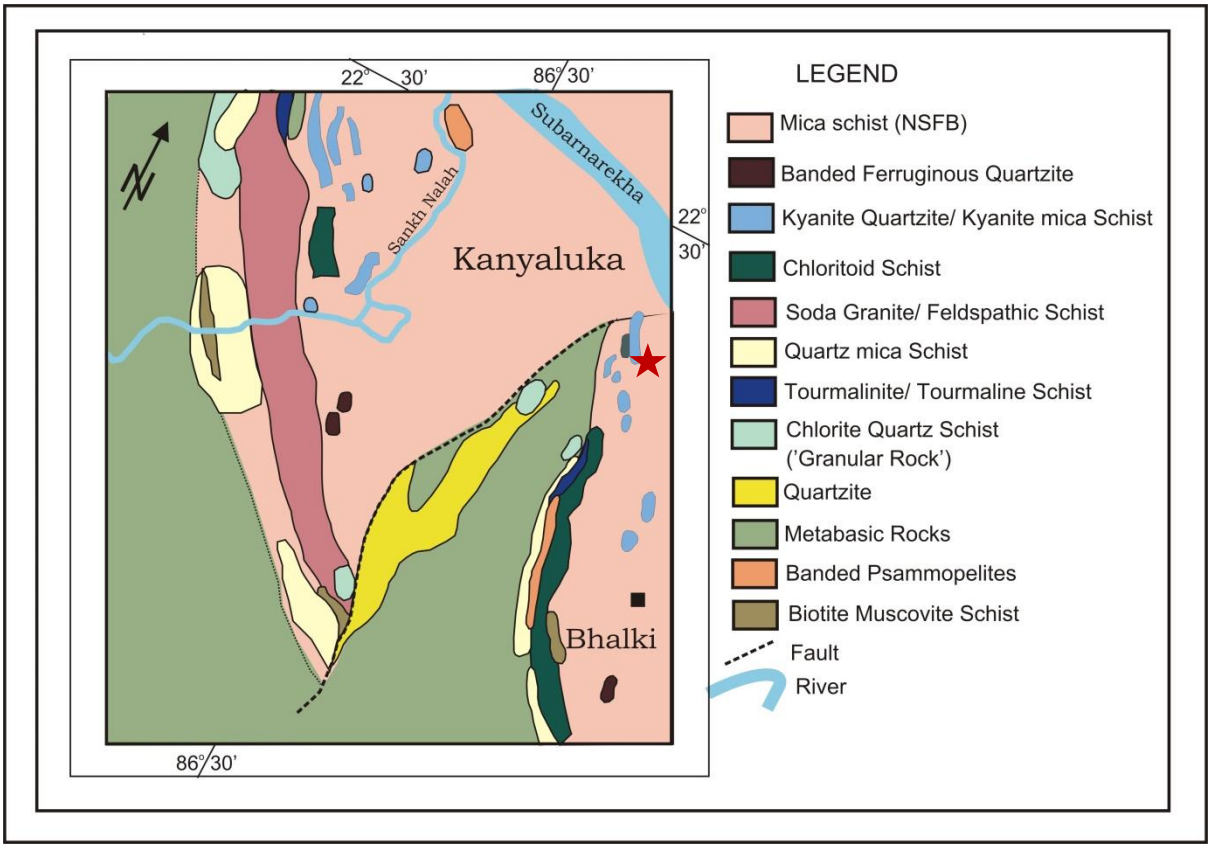

Fig. 5.1: Lithological map of the southern part of the Singhbhum Shear Zone near Kanyaluka. The red star indicates the area where the studied rock is exposed.

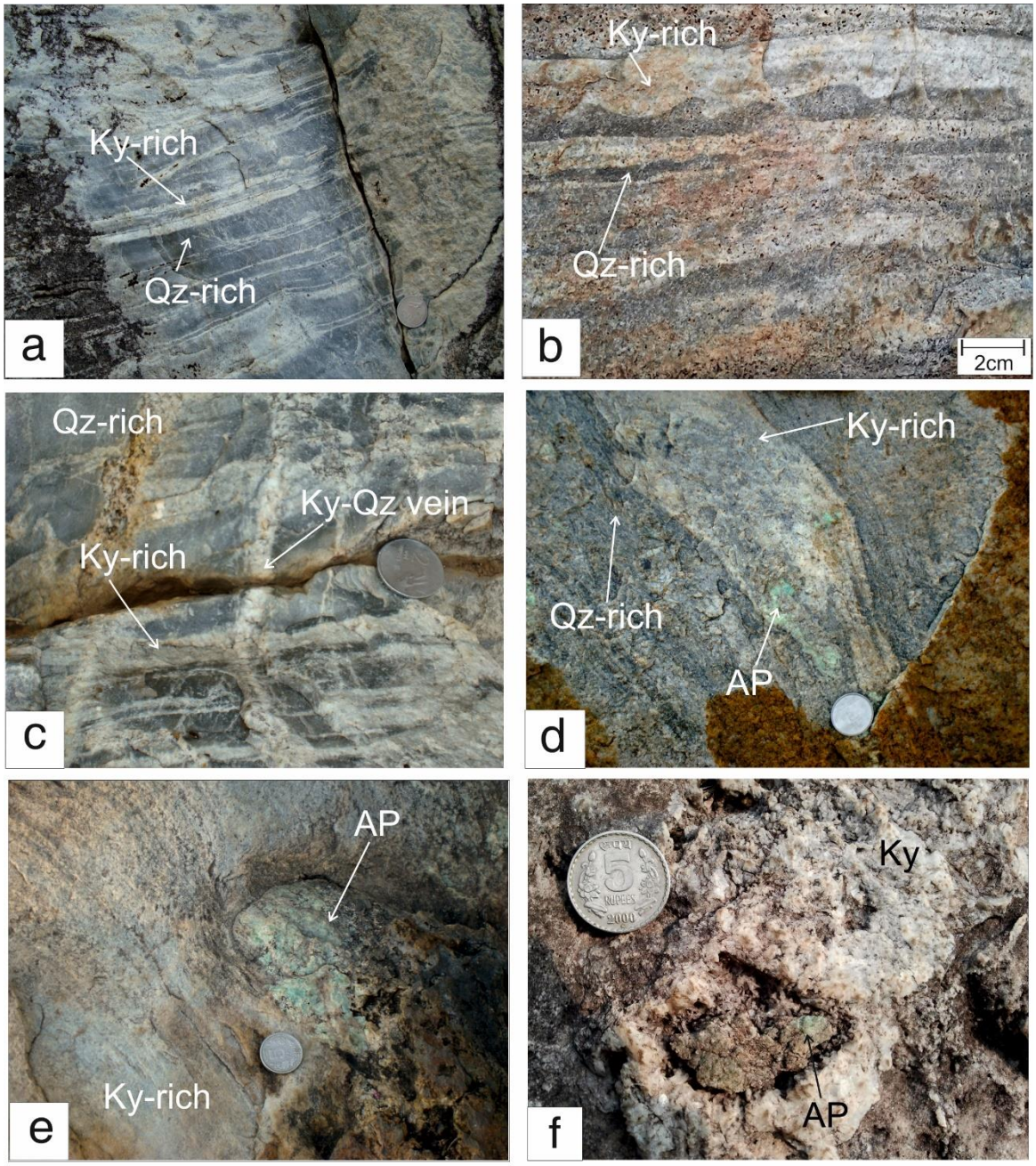

Fig. 5.2 a) Compositional banding exhibited by kyanite and quartz rich layers in KQ b) Primary sedimentary features observed in KQ c) Kyanite-quartz veins cutting across at a high angle to the compositional banding in KQ d) Sea-green colour pods of aluminophosphate (AP) minerals in kyanite-rich layers e) Large patches of AP minerals in KQ f) Vugs produced due to dissolution of AP minerals in tropical weathering. All sample locations are near Kanyaluka, Jharkhand. KQ= Kyanite quartzite AP=Aluminophosphate minerals including lazulite, augelite and florencite.All other mineral abbreviations are after Whitney and Evans (2010)

5.2 Petrography

Kyanite occupies more than 70 vol% of the kyanite–rich band. In the domains of least deformation, random orientation of prismatic grains of kyanite shows a rosette structure with quartz and rutiles occupying the interstitial spaces (Fig.5.3a). Commonly, the kyanite blades and the interstitial quartz grains show impress of intense deformation which are manifested by folding of kyanite grains (Fig.5.3b), development of kink bands and undulatory extinction in kyanite grains (Fig.5.3c), recrystallization of kyanite blades (Fig. 5.3d) and formation of core-and-mantle structures due to marginal recrystallization (Fig.5.3e) and recrystallization of quartz grains occurring in the interstitial spaces formed by kyanite blades (Fig. 5.3b). Kyanite is volumetrically minor (<15 vol%) in the quartzite layer (Fig. 5.3f). A prominent mylonitic foliation with distinct S-C fabric is defined by ovoid to elliptical grains of quartz in the quartzite layer (Fig. 5.3f). Individual quartz grain shows distinct subgrains (Fig.5.3f). Degree of recrystallization of the deformed quartz grains varies upto 30%. The recrystallized grains show polygonal outline and form Y-shaped triple-point junction (Fig.5.3f).

Though the individual kyanite grains are strongly deformed (manifested by banding and kinking of grains), their overall distribution attests to the view that the kyanite prisms were haphazardly oriented prior to shearing. Florencite is seen replacing kyanite blades in a few domains.

Augelite and lazulite developed only in kyanite rich bands and veins (only lazulite). The aluminophosphate rich pods are dominated by lazulite (60-90 vol%). Commonly, kyanite grains are torn out and extensively replaced by lazulite (Fig.5.3g). At an advanced stage of replacement, island of kyanite is present in the matrix of lazulite (Fig.5.3g,h). Florencite that appears as small bright grains which form by replacing

kyanite (discussed in chapter 6) is present stranded in lazulite that replaces kyanite (Fig.5.3i). This feature suggests that florencite was also stable during the formation of lazulite and did not participate in formation of lazulite. Augelite occurs as corroded grains in lazulite (Fig.5.3h). Augelite replaces kyanite and islands of kyanite are seen floating in augelite (Fig. 5.3j). These textures support that both augelite and kyanite participated in the formation of lazulite. Quartz grains are embayed by lazulite and as well as by augelite (Fig. 5.3k) suggesting that quartz was dissolved during the growth of these minerals. Augelite is absent in kyanite-quartz veins. Undulose extinction was noted in a few grains of lazulite, but most of the grains are devoid of any impress of deformation. It suggests that lazulite developed at the terminal phase of and outlasted shear deformation. Sporadically in kyanite-quartz veins, lazulite replaces both kyanite.

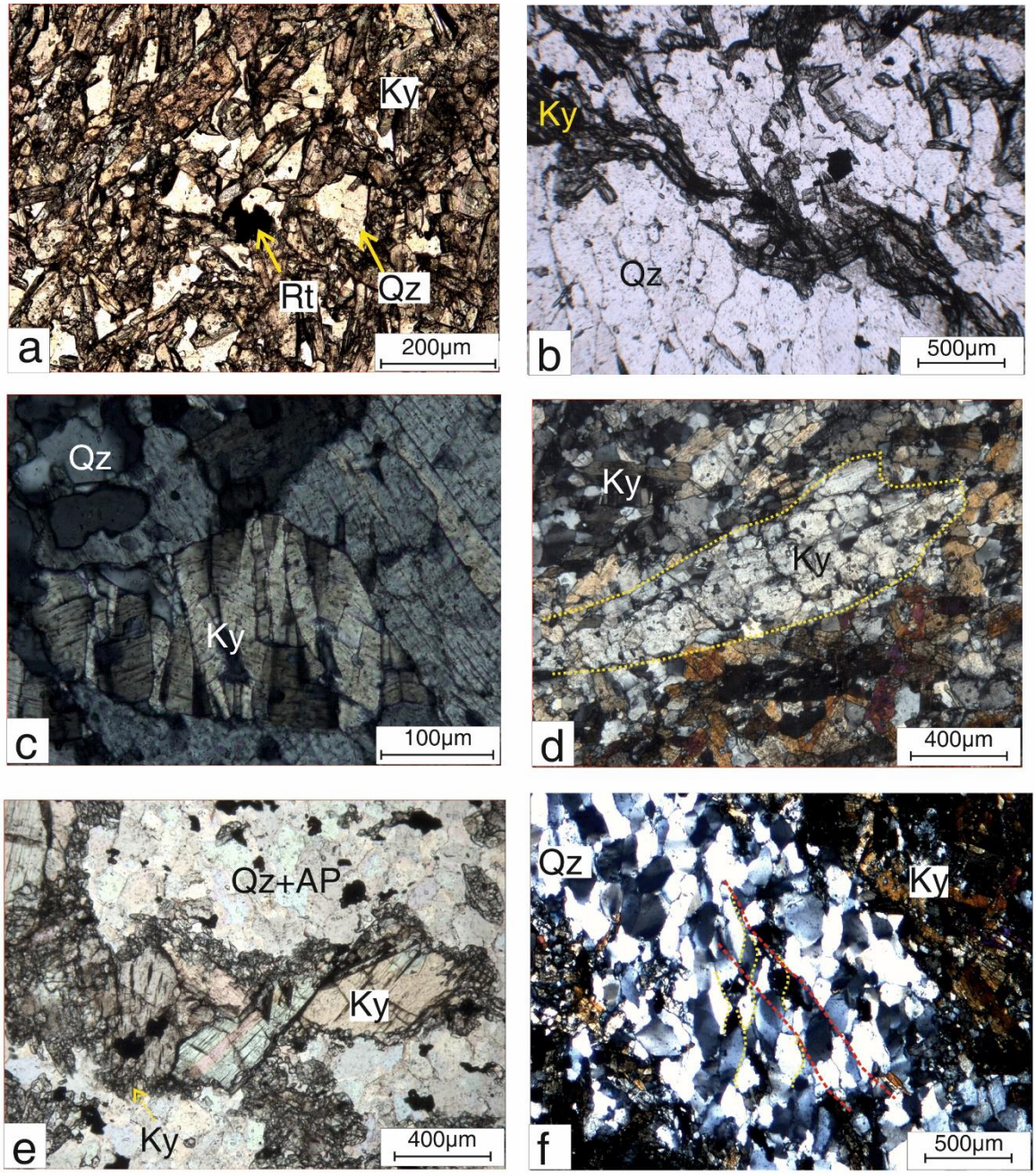

Fig 5.3:(a)Kyanite grains show random orientation in KQ (b) Folded kyanite grain in intensely deformed KQ Quartz grains are also intensely deformed (c) Kink bands and undulatory extinction in kyanite (d) Kyanite grain entirely recrystallized (e) Core mantle features in kyanite due to recrystallization of kyanite at grain boundary (f) Mylonitised quartz-rich layer in KQ with assymmetric quartz veins defining the S-C fabric All samples are from Kanyaluka, Jharkhand. KQ= kyanite quartzite, AP= aluminophosphate minerals lazulite (laz),augelite (aug) and florencite (fl). Other mineral abbreviations after Whitney and Evans (2010)

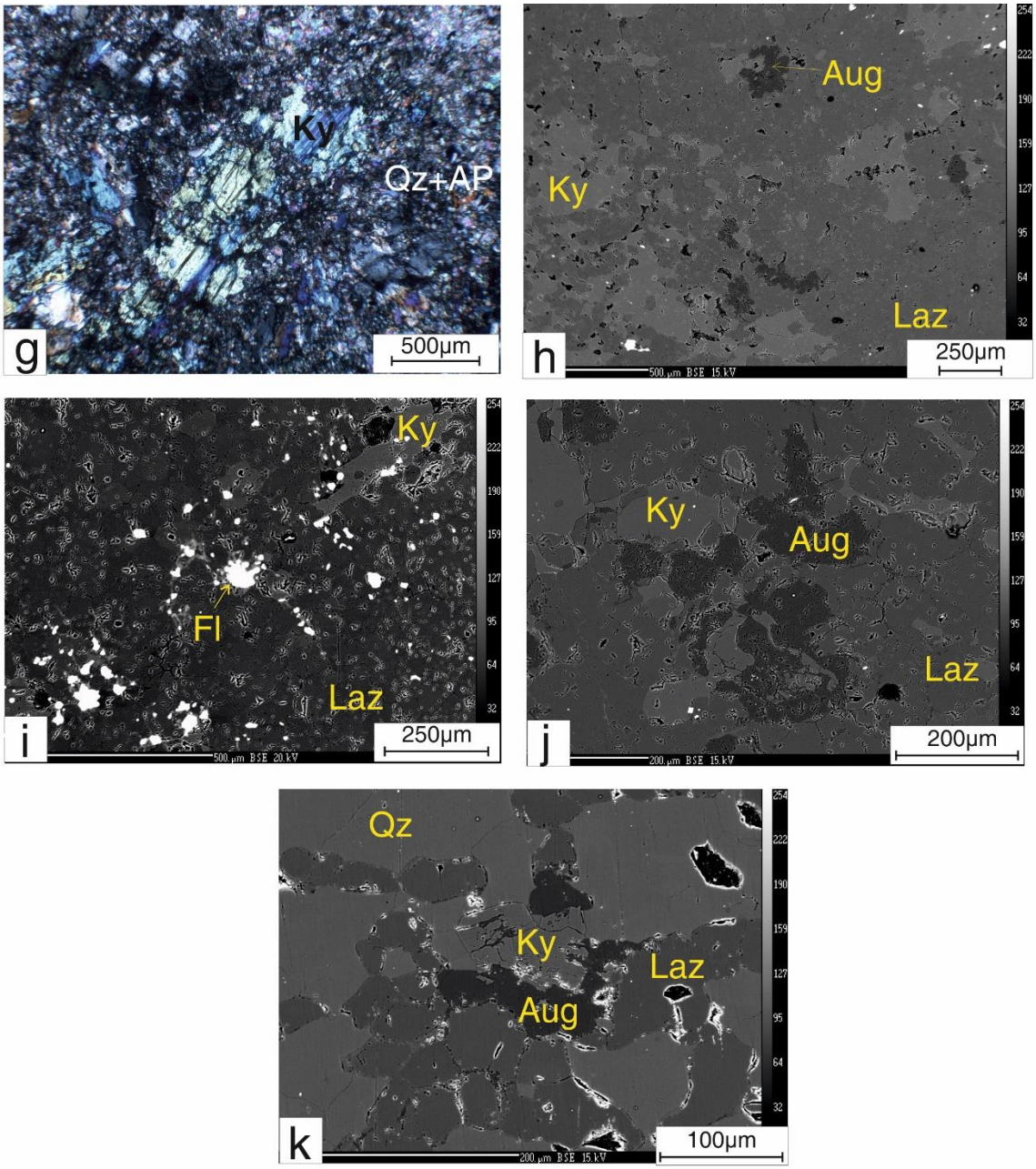

Fig 5.3:(g) Aluminophosphate minerals replacing kyanite. Kyanite grains display corroded grain margins andextensive replacement (h) General view of aluminophosphate rich pods where lazulite is the dominating mineral. Islands of kyanite and augelite are seen in lazulite (i) Florencite grains formed by replacing kyaniteare left stranded in lazulite (j) Kyanite grains seen as inclusions in augelite (k) Kyanite being replaced by augelite which is further replaced by lazulite. All samples are from Kanyaluka, Jharkhand. AP= aluminophosphate minerals lazulite (laz), augelite (aug) and florencite (fl). Mineral abbreviations after Whitney and Evans (2010)

5.3 Mineral Chemistry

Chemical compositions of the minerals in the studied rock are measured with Cameca SX100 Electron Probe Micro Analyzer (EPMA) Central Petrological Laboratory, Geological survey of India, Kolkata. The analytical details are presented in the Appendix III. The representative analyses of the minerals are given in the Tables 5.1. In the following section, the salient compositional characteristics of the minerals are presented:

Lazulite: The lazulite is compositionally homogeneous with very high Mg# (Mg/Mg+Fe~ 0.98±0.1). Compared to lazulite from many other localities of the world (e.g. Uher et al., 2009, Morteani et al., 2001), the measured compositions of lazulite show unusually low scorzalite. Trace amounts of Ti (0.002-0.005 apfu) and Mn (upto 0.005 apfu) are also present.

Augelite: Compositions of augelite is close to the end-member composition of $Al_2(PO_4)(OH)_3$ with small amount of SiO_2 (upto 1.2 wt%) and MgO (upto 0.65 wt%).

Florencite: Composition of florencite in the studied rock is described in details in chapter 6 and Table-5.1 shows the compositional range of florencite. Florencite is a solid solution of Ce-, La- and Nd-endmembers with small amount of CaO (up to 0.64 wt%) and ThO_2 (up to 1.2 wt%).

Kyanite, rutile and quartz have virtually end-member compositions.

Table 5.1 : Representative oxide analyses and calculated cations of Lazulite and Augelite mineral from studied area and Lazulite from other published data

Elements	Lazulite (this study)						Lazulite from Slovakia (Uher et al. 2009)	Lazulite from Brazil (Morteani et al. 2001)	Augelite (this study)			
SiO_2	0.03	0.00	0.10	0.09	0.10	0.03**	n.a.	0.04-0.66	1.22	0.11	0.11	0.16**
TiO_2	0.00	0.03	0.03	0.05	0.05	0.00	n.a.	0.03-1.00	0.00	0.08	0.03	0.13
Al_2O_3	33.57	33.48	33.37	33.82	33.42	33.92	30.86-33.16	31.09-33.15	47.99	48.55	49.93	49.31
Cr_2O_3	0.00	0.00	0.00	0.00	0.00	0.00	n.a.	n.a.	0.00	0.00	0.08	0.00
Fe_2O_3*	0.00	0.00	0.00	0.00	0.00	0.00	0.00	_	0.07	0.63	0.31	0.01
FeO*	0.51	0.56	0.60	0.32	0.44	0.30	1.79-3.60	0.47-7.97	0.00	0.00	0.00	0.00
MnO	0.00	0.00	0.01	0.14	0.03	0.00	0.00-0.01	n.a.	0.03	0.10	0.00	0.00
MgO	13.34	13.19	13.39	13.84	13.28	13.27	11.26-12.21	9.22-13.94	0.65	0.03	0.02	0.01
CaO	0.01	0.02	0.04	0.00	0.00	0.00	0.00-0.03	0.00-0.02	0.05	0.00	0.01	0.04
Na_2O	0.05	0.00	0.00	0.00	0.00	0.00	0.00-0.05	0.00-0.02	0.01	0.02	0.00	0.04
K_2O	0.00	0.00	0.00	0.02	0.01	0.03	0.00-0.03	0.00-0.02	0.00	0.00	0.00	0.00
P_2O_5	47.53	47.49	47.46	46.44	44.89	45.18	42.32-46.89	45.91-49.59	36.49	32.04	33.36	34.45
Total	**95.04**	**94.77**	**95.00**	**94.81**	**92.32**	**92.77**	**87.13-94.92**	**95.26-97.96**	**86.51**	**81.49**	**83.84**	**84.18**
Oxygen basis	9	9	9	9	9	9	9	18	11	11	11	11
	a.p.f.u.	*a.p.f.u.*	*a.p.f.u.*	*a.p.f.u.*	*a.p.f.u.*	*a.p.f.u.*	*a.p.f.u.*	*a.p.f.u.*	*a.p.f.u.*	*a.p.f.u.*	*a.p.f.u.*	*a.p.f.u.*
Si	0.001	0.000	0.005	0.005	0.005	0.002	n.a.	0.000-0.020	0.081	0.008	0.008	0.011
Ti	0.000	0.001	0.001	0.002	0.002	0.000	n.a.	0.000-0.010	0.000	0.004	0.002	0.007
Al	1.974	1.974	1.964	2.000	2.031	2.048	1.873-2.047	3.680-3.900	3.756	4.065	4.055	3.978
Cr	0.000	0.000	0.000	0.000	0.000	0.000	n.a.	n.a.	0.000	0.000	0.004	0.000
Fe^{3+}	0.000	0.000	0.000	0.000	0.000	0.000	0.000	_	0.003	0.034	0.016	0.001
Fe^{2+}	0.021	0.023	0.025	0.013	0.019	0.013	0.075-0.152	0.040-0.670	0.000	0.000	0.000	0.000
Mn	0.000	0.000	0.000	0.006	0.001	0.000	0.000-0.005	n.a.	0.002	0.006	0.000	0.000
Mg	0.992	0.983	0.997	1.035	1.020	1.013	0.863-0.934	1.390-1.990	0.064	0.003	0.002	0.001
Ca	0.001	0.001	0.002	0.000	0.000	0.000	0.000-0.002	b.d.l.	0.004	0.000	0.001	0.003
Na	0.005	0.000	0.000	0.000	0.000	0.000	0.000-0.005	b.d.l.	0.001	0.003	0.000	0.005
K	0.000	0.000	0.000	0.001	0.001	0.002	0.000-0.002	0.000-0.010	0.000	0.000	0.000	0.000
P	2.008	2.011	2.007	1.973	1.959	1.959	1.994-2.000	4.000	2.052	1.927	1.946	1.996
Total	**5.002**	**4.995**	**5.001**	**5.035**	**5.039**	**5.036**	**4.876-5.081**	**9.710-10.810**	**5.963**	**6.050**	**6.034**	**6.001**
X_{Mg}=Mg/(Fe+Mg)	0.98	0.98	0.98	0.99	0.98	0.99	0.85-0.92	0.67-0.98				
Lazulite (mol)	0.98	0.98	0.98	0.99	0.98	0.99	0.85-0.92	0.67-0.99				
Scorzalite (mol)	0.02	0.02	0.02	0.01	0.02	0.01	0.08-0.15	0.01-0.33				

*Fe calculated as FeO or Fe_2O_3 ; oxides are in wt%, cations in a.p.f.u.;n.a. = not avaliable, b.d.l. = below detection limit

.....continued

* *data used for C-space analysis

Table 5.1 Representative oxide analyses and calculated cations of Florencite, Kyanite and Rutile mineral from studied area.

Elements	Florencite	Kyanite	Rutile
SiO_2	0.00-0.06	37.42**	0.02
TiO_2	0.00-0.07	0	100.9
Al_2O_3	27.28-28.47	63.48	0.06
Cr_2O_3	0.00	0	0.06
$Fe_2O_3^*$	0.00	0	0
FeO	0.00-0.01	0.05	0
MnO	0.00	0	0.1
CaO	0.42-0.64	0	0.02
MgO	0.01-0.10	0.02	0
Na_2O	0.09-0.11	0.03	0.02
K_2O	0.00-0.01	0.01	0.03
P_2O_5	30.72-30.84	0	0
ZrO_2	0.00	-	-
Nb_2O_5	0.00-0.04	-	-
La_2O_3	6.83-7.69	-	-
Ce_2O_3	10.93-12.15	-	-
PbO	0	-	-
ThO_2	0.49-1.18	-	-
U_2O_3	0.02-0.04	-	-
BaO	0	-	-
SrO	0.10-0.15	-	-
Nd_2O_3	2.61-2.70	-	-
Sm_2O_3	1.06-1.10	-	-
SO_3	0.00	-	-
Total	**82.08-83.81**	**101.02**	**101.02**
Oxygen basis	11	5	2
	a.p.f.u.	*a.p.f.u.*	*a.p.f.u.*
Si	0.00	1.000	0.000
Ti	0.00	0	0.998
Al	2.89-2.99	1.9987	0.001
Cr	0.00	0	0.001
Fe^{3+}	0.00	0.000	0.000
Fe^{2+}	0.00	0.0011	0.001
Mn	0.00	0.000	0.000
Ca	0.04-0.06	0	0.000
Mg	0.00-0.01	0.0008	0.000
Na	0.02-0.03	0.0016	0.001
K	0.00	0.0003	0.000
P	2.33-2.35	0	0.000
Zr	0	-	-
Nb	0	-	-
La	0.11-0.13	-	-
Ce	0.18-0.20	-	-
Pb	0	-	-
Th	0.01-0.02	-	-
U	0	-	-
Ba	0	-	-
Sr	0.00-0.01	-	-
Nd	0.08-0.09	-	-
Sm	0.03-0.04	-	-
S	b.d.l.	-	-
Total cation	**5.79-5.80**	**3.002**	**1.002**
ΣREE	0.42-0.45		
Florencite(mol%)	86.69-89.94		
Goyazite(mol%)	1.03-1.47		
Crandallite(mol%)	8.70-11.84		

*Fe calculated as FeO or Fe_2O_3 ;oxides are in wt%, cations are in a.p.f.u.; n.a. = not avaliable, b.d.l. = below detection limit

* *data used for C-space analysis

5.4 Textural modeling and element mobility

Paragenetic relations among minerals in the lazulite-augelite bearing assemblage suggest that kyanite and quartz were replaced successively by augelite and lazulite. Formation of the aluminophosphate minerals from kyanite requires open system process. Detail of chemical processes that led to stabilization of augelite and lazulite can be best understood if balanced chemical reactions are written combining observed textural relations and compositions of the participating phases.

The C-Space program was used for the purpose. The program uses the method of singular value decomposition technique to achieve the desired results (Lang et al., 2004). The detail of the computational procedure is given in the Appendix I.

Results

The following chemically balanced reactions are obtained for one mole of augelite and lazulite respectively:

Augelite forming reaction

1. 1.829 Ky + 0.998 P+ 1.5 H_2O + 0.001 Ca = 1 Aug + 1.666 Al + 0.001 Mg + 1.822 SiO_2 + 0.002 Fe + 0.0002 Na

   ΔV_{solid} =-6.14cc, Fluid / rock ratio=0.38, ~46% loss of Al

Lazulite forming reaction

2. 1.778 Ky + 0.667 Aug + 1.294 P + 1.011 Mg + 0.011 Fe + 0.0001 Na = 1 Laz + 2.833 Al + 1.78 SiO_2 + 0.001 Ca

   ΔV_{solid}=-29.18cc, ~58% loss of Al

Reactions 1 and 2 explain the observed sequential development of minerals (kyanite to augelite to lazulite) in the lazulite-rich pods. The modelled chemical reactions suggest that several chemical species including Al, P, Mg, SiO_2 and H_2O were mobile during formation of augelite and lazulite. Reaction 1 is the first metasomatic event in formation of the AP mineral rich pods (metasomatism 1) which represents addition of P and H_2O to the rock to form augelite from kyanite. Reaction 2 is the second (or later) metasomatic event (metasomatism 2) which introduces Mg into the rock to form lazulite from augelite and kyanite. Table 5.2 shows the amount of different chemical species that were added to or subtracted from the KQ rocks during formation of aluminophosphate minerals for a hypothetical 1000 cc of rock with only augelite and lazulite respectively.

The mineralogical composition of the AP rich pods is significantly different from the KQ rocks and this mineralogical heterogeneity makes it difficult to estimate the initial bulk compositions. Further presence of kyanite veins in the rock makes it further difficult. Mineralogical heterogeneity gives rise to large variation in SiO_2 and Al_2O_3 in bulk compositions (Table 5.3). The difference of bulk compositions AP-rich pods and three compositions of the KQ rock are carried out to predict the initial composition of the rock. The comparison corroborates the textural modelling that significant MgO and P_2O_5 are added while SiO_2 and Al_2O_3 are lost during transformation of KQ rocks to AP rich pods (Table 5.3).

Table 5.2: Change of masses (+ = gain, - = loss) of different mobile species calculated reaction 1 X 2 for 1000 c.c. rock

Species (in moles)	P	Al	Mg	SiO_2	Ca	H_2O	Na	Fe	Fluid/Rock
Augelite	13.55	-22.62	-0.013	-24.74	0.01	20.37	-0.002	-0.027	0.38
Lazulite	13.27	-29.06	10.37	-18.26	-0.01	0	0.001	0.11	-

Table 5.3. Representative bulk compositions of a phosphate-rich pod (AP) and their immediate host rock

Sample no.	NSKQR1	NSKQR2	NSKQR3	AP	L-G1	L-G2	L-G3
SiO_2	54.58	47.71	62.98	27.14	−27	−21	−36
TiO_2	0.41	0.5	0.73	0.27	0	0	0
Al_2O_3	43.14	49.99	34.18	38.78	−4	−11	5
Cr_2O_3	0	0	0	0	0	0	0
Fe_2O_3	0.03	0.05	0.12	0.26	0	0	0
FeO	0	0	0	0	0	0	0
MnO	0	0	0	0	0	0	0
MgO	0.16	0.15	0.03	5.46	5	5	5
CaO	0.26	0.38	0.27	0.23	0	0	0
Na_2O	0.15	0.18	0.02	0.2	0	0	0
K_2O	0.01	0.04	1.36	0.24	0	0	−1
P_2O_5	0.75	0.78	0.174	22.94	22	22	23
Total	99.5	99.78	99.86	95.53$^{\$}$			

Notes: $^{\$}$LOI = 3.96 wt.%, L-G: loss (–) or gain (+) of components (L-G1 = AP-NSKQR1, L-G2 = AP-NSKQR2, L-G3 = AP-NSKQR3). Losses and gains

5.5 Physical conditions of formation of lazulite and augelite

The aluminophosphate minerals that developed in the KQ rocks are not suitable for quantitative geothermobarometry. Nevertheless, extant experimental data on the stability of lazulite, augelite and the other aluminophosphate minerals put some constraint to P-T condition of formation of the aluminophosphate minerals in the KQ rocks. Fig.5.4 represents experimentally constrained reactions in the system MgO-FeO-Al_2O_3-P_2O_5-SiO_2-H_2O involving kyanite, augelite and lazulite. The temperature for the stability of the assemblage augelite-kyanite-quartz-Mg-lazulite is constrained within 410-490^oC by reactions in the P-T space (Fig.5.4). The inferred temperature range is in good agreement with the temperature estimated from the adjoining metasedimentary rock (490^o ± 40^oC, Sengupta, 2012) and also with the microstructures of kyanite and quartz (Vernon 2004). The assemblage kyanite-augelite-lazulite-quartz is, however, a weak pressure sensor and suggests pressure above 2-3 kbar (Fig.5.4). Sengupta (2012) showed that the rocks in and around Kanyaluka underwent Barrovian metamorphism along a clock-wise P-T trajectory that culminated at ~6 ±1kbar and 490° ± 40°C. It is therefore expected that the aluminophosphate bearing KQ rocks too experienced the same P-T condition. This then follows that the KQ rocks were buried to the depth of ~20-22 km (corresponding to lithostatic pressure of ~6 ±1 kbar) during the time of formation of aluminophosphate minerals.

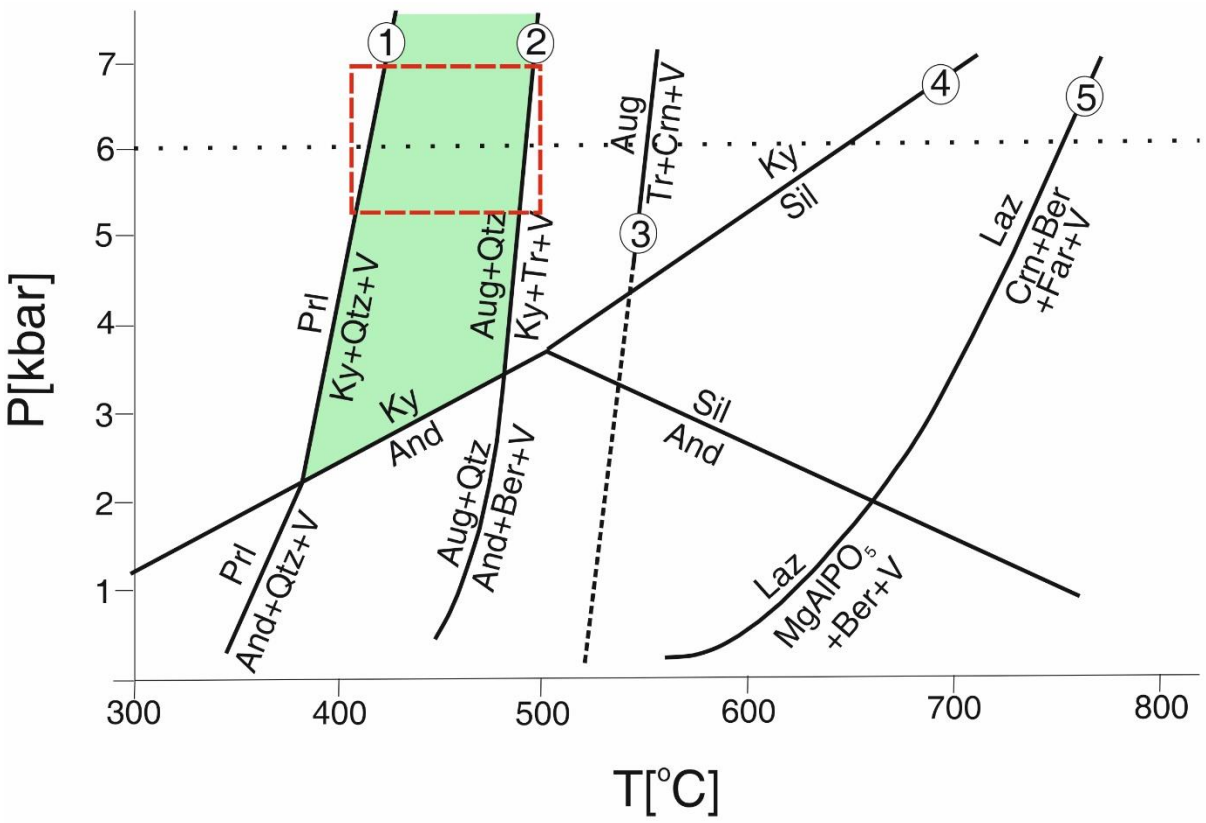

Figure 5.4: Pressure–temperature diagram illustrating the invariant points and univariant curves in the system Al_2O_3-SiO_2-MgO-P_2O_5-H_2O and stability of aluminium silicates, augelite, and lazulite (after Chakraborty et al. 2014). The green-coloured area marks the temperature range, where the assemblage kyanite + augelite + quartz + lazulite is stable. The redrectangle marks the P-T range where the studied phosphate bearing assemblage was likely to have stabilized. The inferred P-T conditions are in good agreement with the P-T conditions inferred from the adjoining lithology (Sengupta 2012). See text for more details. Curves 1 and 4 are taken from Morteani et al. (2001); curves 2 and 3 are taken from Wise and Loh (1976); and curve 5 is taken from Schmid-Beurmann et al. (1995). And= andalusite; Ky= kyanite; Prl= pyrophyllite; Qtz= quartz; Sil= sillimanite; Laz= lazulite; Ber= berlinite; Crn= crandallite; Aug= augelite; Tr= troleiite.

5.6 Summary

Lazulite and augelite formed in the KQ are rare aluminophosphate minerals that are reported from a few localities of the world (see Uher et al., 2009; Morteani et al., 2001; Dill et al., 2008). Though lazulite and augelite are reported from rocks formed over a wide range of P-T-fluid compositions, physicochemical condition of formation of these two minerals are studied from a few localities (~400^{o}C, 3.4 kbar, Morteani et al., 2001; 300°-500°C, <3 kbar, Bernhard, 2001; <100°C, < 2kbar, Marfil et al., 2013, 300°-700°C, 3-30 kbar, Uher et al., 2009). Experimental studies have established lazulite stability upto 660°C and 1-12 kbar (Wise and Loh 1976; Schmid-Beurmann et al., 2000). Experimental study in the Al-P-O-H system and the observations from natural rocks show that the assemblage augelite + kyanite is stable at conditions 380–475°C and pressure >2 kbar (Wise and Loh, 1976; Visser et al. 1997). The assemblage kyanite + lazulite has a wide thermal and baric stability (>400°C and >2 kbar, Schmid-Beurmann et al., 1999 and Morteani et al., 2001). Thus, the assemblage kyanite + augelite + lazulite is stable at temperature >400°C and pressure >4kbar which is consistent with the estimated temperature (410-490^{o}C) of formation in the study area.

The foregoing analyses suggest that lazulite and augelite in the study area were formed in an open system with P and Mg being transported into the rock by metasomatic fluids through two successive metasomatic events with different fluid compositions. The shear planes in the Singhbhum Shear Zone acted as conduits for P and Mg-rich fluids. Metamorphic and hydrothermal (*sensu lato*) fluids are commonly out of equilibrium with the rocks these fluids interact with (reviewed in Harlov & Austrheim, 2013). Consequently, many exotic minerals including AP, APS (alumino-phosphate-sulphate minerals) and borosilicates are formed in zones of intense fluid-rock interactions

(Bernhard 2001; Morteani et al., 2001; Harlov and Austrheim 2013; Uher et al., 2009; Sengupta et al., 2005, 2011; Pal et al., 2011; Marfill et al., 2013).

References

Bernhard, F., 2001. Replacement of monazite by florencite during hydrothermal alteration, in: EUG XI Congress Abstracts. p. 678.

Bucholz, C.E., Ague, J.J., 2010. Fluid flow and Al transport during quartz-kyanite vein formation, Unst, Shetland Islands, Scotland. Journal of Metamorphic Geology 28, 19–39. https://doi.org/10.1111/j.1525-1314.2009.00851.x

Dill, H.G., Melcher, F., Gerdes, A., Weber, B., 2008. The origin and zoning of hypogene and supergene Fe-Mn-Mg-Sc-U-REE phosphate mineralization from the newly discovered Trutzhofmühle aplite, Hagendorf Pegmatite Province, Germany. Can Mineral 46, 1131–1157. https://doi.org/10.3749/canmin.46.5.1131

Harlov, D.E., Austrheim, H., 2013. Metasomatism and the chemical transformation of rock: rock-mineral-fluid interaction in terrestrial and extraterrestrial environments, in: Metasomatism and the Chemical Transformation of Rock. Springer, pp. 1–16.

Lang, H.M., Wachter, A.J., Peterson, V.L., Ryan, J.G., 2004. Coexisting clinopyroxene/spinel and amphibole/spinel symplectites in metatroctolites from the Buck Creek ultramafic body, North Carolina Blue Ridge. American Mineralogist 89, 20–30.

Manning, C.E., 2007. Solubility of corundum + kyanite in H2O at 700°C and 10 kbar: Evidence for Al-Si complexing at high pressure and temperature. Geofluids 7, 258–269. https://doi.org/10.1111/j.1468-8123.2007.00179.x

Marfil, R., la Iglesia, A., Estupiñán Letamendi, J., 2013. Origin and nature of the aluminium phosphate-sulfate minerals (APS) associated with uranium mineralization in triassic red-beds (Iberian Range, Spain). Estudios Geológicos 10, 39–89.

Morteani, G., Ackermand, D., Heinrich Horn, A., Rio Paraun, P., 2001. Aluminium-phosphates and borosilicates in muscovite-kyanite metaquartzites near Diamantina (Minas Gerais, Brazil): Petrogenetic implications. Periodico di Mineralogia 70, 111–129.

Pal, D.C., Chaudhuri, T., McFarlane, C., Mukherjee, A., Sarangi, A.K., 2011. Mineral chemistry and in situ dating of allanite, and geochemistry of its host rocks in the Bagjata Uranium Mine, Singhbhum Shear Zone, India—implications for the chemical evolution of REE mineralization and mobilization. Economic Geology 106, 1155–1171.

Schmid-Beurmann, P., Morteani, G., Cemič, L., 1997. Experimental determination of the upper stability of scorzalite, FeAl2 [OH/PO4] 2, and the occurrence of minerals with a composition intermediate between scorzalite and lazulite (ss) up to the conditions of the amphibolite facies. Mineral Petrol 61, 211–222.

Sengupta, N., 2012. Stability of chloritoid 1 biotite-bearing assemblages in some metapelites from the Palaeoproterozoic Singhbhum Shear Zone, Eastern India and their implications. Geol Soc Spec Publ 365, 91–116. https://doi.org/10.1144/SP365.6

Sengupta, N., Mukhopadhyay, D., Sengupta, P., Hoffbauer, R., 2005. Tourmaline-bearing rocks in the Singhbhum shear zone, eastern India: Evidence of boron infi ltration during regional metamorphism. American Mineralogist 90, 1241–1255. https://doi.org/0003-004X/05/0809ñ1241$05.00/DOI: 10.2138/am.2005.1578

Sengupta, N., Sengupta, P., Sachan, H.K., 2011. Aluminous and alkali-deficient tourmaline from the Singhbhum Shear Zone, East Indian shield: Insight for polyphase boron infiltration during regional metamorphism. American Mineralogist 96, 752–767. https://doi.org/10.2138/am.2011.3560

Uher, P., Mikuš, T., Milovský, R., Biroň, A., Spišiak, J., Lipka, J., Jahn, J., 2009. Lazulite and Ba, Sr, Ca, K-rich phosphates-sulphates in quartz veins from metaquartzites of Tribeč Mountains, Western Carpathians, Slovakia: Compositional variations and evolution. Lithos 112, 447–460. https://doi.org/10.1016/j.lithos.2009.03.046

Wagner, T., Beitter, T., Markl, G., 2009. Geochemical modeling of the formation of kyanite-quartz veins, Alpe Sponda, Central Alps. Geochimica et Cosmochimica Acta Supplement 73, A1400.

Whitney, D.L., Evans, B.W., 2010. Abbreviations for names of rock-forming minerals. American Mineralogist 95, 185–187. https://doi.org/10.2138/am.2010.3371

Wise, W.S., Loh, S.E., 1976. Equilibria and origin of minerals in the system Al2O3-AlPO4-H2O. American Mineralogist 61, 409–413.

CHAPTER 6

Florencite bearing kyanite quartzite

In this chapter petrology of the exotic REE (Rare Earth Elements) bearing aluminophosphate (florencite) that is being reported for the first time from the Precambrian Shield of India is discussed. Florencite is found disseminated in muscovite poor KQ near Kanyaluka and is found in the sea-green patches along with other lazulite and augelite (discussed in Chapter 5). The KQ rock is associated with chloritoid -garnet -biotite schists, garnet-muscovite-biotite schists and tourmalinite. Before presenting the field relations and chemistry of the florencite and the associated minerals of this study, a general description of the mineral is given below.

6.1 General information about florencite

The mineral florencite belongs to the Alunite group of minerals. The alunite supergroup with general formula $AB_3(XO_4)_2(OH)_6$ comprises of three groups which, combined, contain more than 40 mineral species. A site has a 12 fold coordination and occupied by a large monovalent, bivalent, trivalent or rarely tetravalent cation (K^+, Na^+, NH^{4+}, Ag^+, Pb^{2+}, Hg^{2+}, Ca^{2+}, Ba^{2+}, Sr^{2+}, Rb^+, Ti^{2+}, Bi^{3+}, REE^{3+}, Th^{4+}). B site has 6-fold coordination and is occupied by Al^{3+}, Fe^{3+}, Cu^{2+}, Zn^{2+}, Sn^{2+}, V^{3+}, Cr^{3+}, Ga^{3+}, Mg^{2+}. X site has 4-fold coordination and occupied by P^{5+}, S^{6+} and As^{5+} and rarely by Cr^{6+}, Sb^{5+} and Si^{4+}(Dill, 2001; Bayliss et al., 2010, Georgieva and Velinova, 2012). Owing to their open structures the minerals can accommodate a large number of cations and anions viz. variable amounts of Ca^{2+}, Pb^{2+}, Hg^{2+}, K^+, Ba^{2+}, Sr^{2+}, Rb^+ (in A-site), Fe^{3+}, Cu^{2+}, Zn^{2+}, Sn^{2+}, V^{3+}, Cr^{3+}, and Ga^{3+} (in B-site). Thus the mineral can provide a wealth of information about the source and composition of metamorphic and hydrothermal fluids (Visser, 1997, Nagy et al., 2002, Dill, 2001, Gaboreau et al., 2005, Hikov et al., 2010, Izbrodin et al., 2011, Repina, 2011, and Janots et al., 2006). Aluminophosphates (APS) of the alunite supergroup can be deposited in a variety of

sedimentary, igneous and metamorphic environments (Table 6.1). They are observed in sedimentary environments like marine sediments, calcareous, phosphorite-bearing, argillaceous–carbonaceous, aranaceous, coal-bearing environments, in soils and paleosols, and in saprolite (bauxites, laterites). Peraluminous parent rocks enriched in S and/or P are a prerequisite for the formation of APS minerals (Dill 2001). They can also occur in igneous rocks in acidic to intermediate pyroclastic, volcanic or subvolcanic rocks especially near porphyry-type intrusions with epithermal Au-Ag deposits (Arribas et al., 1995; Hikov et al., 2010; Repina 2011). Peraluminous rocks enriched in S and/or P of volcanic and sedimentary origin or low grade metamorphosed rocks from sedimentary or volcanic protoliths can give rise to APS mineralization (Georgiva et al., 2012; Hikov, 2019; Höfig et al., 2021). Even in higher grade metamorphic terrains APS minerals can form through fluid assisted mineralization (Ek and Nysten, 1990). Both supergene and hypogene processes can give rise to complex solid solutions which precipitate APS minerals (Strunz and Tennyson, 1983; Scott, 1987; Valeton et al., 1997; Jambor, 1999; Dill et al., 2008).In nature, however, only some minerals out of the broad spectrum of APS minerals play a major part in rock- and ore-forming processes (Dill, 2001). The reported occurrences of florencite and its chemistry are presented in Table-6.3.

Chemical substitutions in florencite

APS minerals demonstrate a large variety of chemical compositions owing to the chemical substitutions that take place. Coupled substitutions involving Ca,Sr ↔ LREE at A site and S ↔ P at X site cause solid solutions to form between goyazite ($SrAl_3[PO_3(O_{0.5}(OH)_{0.5})]2(OH)_6$), crandallite($CaAl_3[PO_3(O_{0.5}(OH)_{0.5})]2(OH)_6$) and florencite ($LREEAl_3(PO_4)_2(OH)_6$) (Gaboreau et al., 2005). Often brabantitic replacement $2REE^{3+} \leftrightarrow Th^{4+} + Ca^{2+}$ takes place in the A-site for florencite to form solid solutions between florencite- svanbergite- ThAl phosphate (Nagy et al., 2002). Ce, La and Nd are the main

LREE that occupy the A site in florencite and causes solid solutions between florencite-(Ce, La, Nd) (Georgieva and Velinova, 2012).

Chemical environment for florencite

Florencite, like other APS minerals, is formed in a range of near surface geological environments (like sedimentary and diagenetic) and also through metamorphic and hydrothermal processes (Nagy et al., 2002, Hikov et al., 2010, Schmandt et al., 2019).Florencite was first reported in France in heavy mineral concentrates from Cambro-Ordovician mudstone/sandstone sediments from the northern Armorican Massif (Devismes et al., 1968). It is typical in advanced argillic alteration zones from high-sulphidation hydrothermal systems related to Cu-Au deposits (Kunov, 1999, Georgieva and Velinova, 2012). It is also associated with unconformity type uranium deposits (Gaboreau et al., 2005). In western Peru kaolin deposit florencite forms from supergene alteration of rhyolitic rocks (Dill et al. 1997). Florencite is also commonly cited as a detrital mineral in various placer deposits (e.g. Gabon; Janeczek and Ewing, 1996). APS minerals may be authigenic in shales and sandstones (e.g. early diagenetic REE) as Al phosphate minerals in marine sandstones are a major sink for oceanic biogenic phosphorus (Pouliot and Hofmann, 1981; Rasmussen, 1996). They may be a weathering product in argillized igneous rocks, resulting from pervasive chemical alteration of primary phosphates (Brown, 1986; Schwab et al., 1989). Banfield and Eggleton (1989) described the extensive supergene replacement of apatite by florencite-(La) and florencite-(Ce), along with euhedral hydrous Ce phosphate (rhabdophane) in Bemboka granodiorite (southern New South Wales, Australia).Once formed, however florencite is very difficult to be destroyed even in weathering profiles and controls the mobility of LREE over a wide range of geological conditions (Gaboreau et al., 2005, Izbrodin et al., 2011, Repina, 2011). Florencite forms solid solutions with other APS minerals like

goyazite- svanbergite- woodhouseite (Dill 2001; Nagy et al., 2002; Bayliss et al. 2010) which can be used to monitor the physico-chemical conditions of formation (Gaboreau et al., 2005).

Table 6.1: Global incidences of florencite reported from various rock types and varying natural environment

Sl.no.	Host rock	Age of host rock	Associated minerals	Locality	Florencite type	Florencite formation process	Authors
1	Andesite and vuggy silica	Paleogene and Neogene	Alunite-woodhousite-crandalite-quartz-pyrite-kaolinite	Velence mountains Hungary and Klokoc Podpolom, Slovakia		Advanced argillic alteration-extensive leaching of apatite by strongly acidic SO4 bearing magmatic hydrothemal fluids	Bajnoczi et al 2004
2	Granite	Early Devonian	Florencite and rhabdophane	New South Wales, Australia	Florencite (Ce) Florencite (La)	Dissolution of apatite and exchange of Ca and REE- May have formed both from REE introduced into rock and REE present in granite-Ce is strongly concentrated in clay-size (< 2 #m) materials-weathering caused enrichment	Banfield et al 1989
3	Lazulite-quartz veins in polymetamorphic metapelites and metapsammites	Carboniferous to Permian	Qz, Ms, Chl and minor kyanite and chloritoid, apatite, zircon, rutile, xenotime, mona/florencite	Styria, Austria	Florencite (Ce)	Hydrothermal alteration of monazite by vein forming fluids in proximal parts of alteration zones-addition of Al, P and H2O	Bernhard 2001
4	Brecciated veins in Archean and Paleoproterozoic metasedimentary rocks close to regional unconformities	Archean and Paleoproterozoic	Xenotime, quartz and muscovite-sericite-illite assemblages	Tanami and Hall Creek regions of W. Australia	Florencite (Ce)	syn-ore hydrothermal mineral assemblage	Dehkordi and Spandler 2019
5	Quartz veins and aplites in host granitic rock	Late Carboniferous	gorceixite – florencite – plumbogummite – crandallite series	Hagendorf Pegmatite province, Germany		Supergene enrichment	Dill et al., 2008

Sl.no.	Host rock	Age of host rock	Associated minerals	Locality	Florencite type	Florencite formation process	Authors
6	Carbonatites	64.7 ± 0.5 Ma to 65.5 ± 0.8 Ma	quartz, florencite, strontianite, barite, sparse bastnasite-parisite-synchysite	Amba Dongar, Gujarat	Florencite (Ce)	Hydrothermal alteration of primary minerals in carbpnatite	Doroshkevich et al., 2009
7	Sandstones and basement (metasedimentary) rocks	Paleo- to Mesoproterozoic basement	Chlorite, illite, monazite, pyrite, sudoite, apatite, APS minerals	East Alligator river Uranium Field, Australia		Hydrothermal alteration	Gabroreau et al., 2005
8	Mica schist lenses in gneisses	Permian	Mg-chlorite, talc, chloritoid, minor phengite, florencite, monazite, allanite	Gran Paradiso Massif, Western Alps	Florencite (Ce) and Florencite (La)	Metasomatic alteration	Radulescu et al., 2009
9	Carbonaceous schists	Ordovician	Quartz, muscovite, chlorite, kaolinite, pyrophyllite, dickite, jarosite, rutile, iron oxyhydroxides, zircon, xenotime, monazite, ilmenite, barite	Armorican Massif, France	Florencite (Ce)	Authigenic, diagenetic, or of a detrital origin in mudstone host rock	Gaudin et al., 2020
10	Volcanic and volcano-sedimentary complex (Dacite-andesitic lavas, volcanogenic breccias and tuffs)	Upper Cretaceous	quartz, dickite, kaolinite, nacrite, pyrite, aluminium phosphate-sulphate (APS) minerals, diaspore, pyrophyllite, alunite and zunyite	Bulgaria	Florencite (Ce)	Hydrothermal alteration (advanced argillic alteration)	Georgiva et al., 2012
11	Carbonatite, laterite and clays	Palaeoproterozoic	florencite, cerianite, haematite, goethite, hollandite, pyrolusite, rutile, kaolinite, illite	Morro dos Seis Lagos deposit, Amazonas, Brazil	Florencite (Ce) Florencite (La)	Primary in carbonatite Authigenic in clays	Giovannini et al., 2021

Sl.no.	Host rock	Age of host rock	Associated minerals	Locality	Florencite type	Florencite formation process	Authors
12	Carbonatite		florencite, goyazite, gorceixite	Kangankunde carbonatite, Nyasaland	Florencite (Ce)	Late-stage replacement processes or under supergene conditions	Mckie 1962
13	Volcano-plutonic edifice emplaced in Paleozoic metamorphic and plutonic (granitoids) basement	Late Cretaceous	Alunite,woodhouseite-svanbergite s.s., pyrophyllite, dickite, kaolinite, diaspore, zunyite.	Asarel porphyry copper deposit, Central Srednogorie, Bulgaria	Florencite (Ce)	Hydrothermal alteration(advanced argillic alteration)	Hikov et al., 2010; Hikov 2019
14	Caldera volcaniclastics and lower cone lavas	Present day caldera floor volcaniclastics and lavas	Florencite, fluorapatite, clinopyroxene, plagioclase, quartz, illite, chlorite, pyrophyllite, rutile	Brothers volcano, Kermadec arc	NA	Hydrothermal alteration in submarine arc-hosted hydrothermal systems	Hofig et al., 2021
15	Quartzitic garnet–kyanite schist	Mesozoic	Garnet, chloritoid, kyanite, muscovite, quartz, florencite, allanite, Ce-epidote, monazite	Eclogite Zone, Tauern Window, Austria	Florencite (Ce)	Part of peak assemblage of medium T and high P metamorphism assisted by fluids	Hoschek 2016
16	Kyanite schists as xenoliths in granitoids	Neoproterozoic to end—Palaeozoic	kyanite, quartz, muscovite, paragonite, topaz, rutile, magnetite, hematite,Lazulite-scorzalite, trolleite,svanbergite, woodhouseite, goyazite, crandallite, florencite-(Ce) and natroalunite	Ichetuyskoye area, West Transbaikalia, Russia	Florencite (Ce)	Retrograde metamorphism later assisted by fluid influx	Izbrodin et al., 2011

Sl.no.	Host rock	Age of host rock	Associated minerals	Locality	Florencite type	Florencite formation process	Authors
17	Metapelites (schists) and associated veins	Oligocene to lower Miocene	Chlorite–phengite–chloritoid-zircon-florencite	Sebtide Complex, Internal Rif, Morocco	Florencite (Ce)	Metamorphic origin	Janots et al., 2006
18	Siltstone	Late Precambrian	Quartz, dolomite, hematite, apatite, rutile, zircon, some clay minerals, florencite	Shituru deposit of Shaba in the Zairian copperbelt	Florencite (Ce)	Hydrothermal events that altered the siltstone	Lefebre and Gasparrini, 1980
19	Mica schists	Hercynian	Kyanite, muscovite, quartz, apatite, monazite, florencite	Sopron Hills, Eastern Alps	Florencite (Ce)	Metasomatism	Nagy et al., 2002
20	Biotite schists, chlorite schists, kyanite-quartz-sericite schists	Proterozoic	Allanite, epidote, monazite, florencite,titanite	Jaduguda uranium deposit, Singhbhum Shear Zone, eastern India	Florencite (Ce)	Hydrothermal origin	Pal et al., 2021
21	Quartz veins of Au–REE mineral occurrences in rhyolites and mafic rocks	Late Riphean	Quartz–hematite–sericite–chloritoid–pyrophyllite schists with diasporite lenses, hematite–manganese nodules, and REE phases like florencite, xenotime, chernovite, La bearing apatite, allanite, kainosite, gasparite, cerianite, bastnaesite, yttrocrasite, and Th and HREE bearing polycrase	Maldynyrd Range, Nether Polar Urals	Florencite (Ce), (Nd), (Sm)	Hydrothermal origin	Repina 2011

6.2 Field occurrence of florencite bearing kyanite quartzite (FKQ)

The area under investigation falls in the eastern part of the Singhbhum shear zone, where it takes a bend towards south near Kanyaluka. The kyanite quartzites are present as string of isolated outcrops in this region (Fig 5.1 from Chapter 5). The kyanite-quartzite is laminated in nature with alternate kyanite and quartz rich layers. The kyanite rich layers often contain >60 vol% kyanite appear brighter white in colour, while the quartz rich layers contain >80-90 vol% quartz and have a grey colour appearance (Fig 5.2a,b from Chapter 5). The thickness of these layers varies from few millimetres to few decimetres. The kyanite-rich rock develops centimetre to decimetre thick bands of intense shearing. The kyanite rich layers contain pockets of sea-green colour aluminophosphate minerals (mostly lazulite) which are dispersed in haphazard manner (Fig. 5.2 d,e). Small veins of aluminophosphate minerals are also found in the kyanite quartzite. However, the aluminophosphate veins and pockets are restricted to the kyanite rich layers only (Fig. 5.2d). The rock is spatially associated with chloritoid-bearing schist, psammopelites, mica schists and bands of toumalinite.

6.3 Petrography

The host rock comprises of kyanite, quartz and rutile as the earliest mineral assemblage. In the less deformed parts randomly oriented kyanite grains form a mesh which occupies 80 vol% of the rock (Fig 6.1a). The interstitial spaces are occupied by quartz and rutile (Fig 6.1a). In the intensely deformed regions, the kyanite blades are kinked, bent or fractured while the quartz grains show undulose extinction (Fig. 6.1b). Petrographic examination of the sea-green pockets reveals an association of lazulite, augelite, florencite, kyanite, quartz and rutile with lazulite being the major mineral (Fig. 6.1d). Deformed recrystallised kyanite grains resembling core-mantle texture are replaced by aluminoposphates (AP) viz. augelite and lazulite (Fig 6.1c). The lazulite and augelite grains are usually colourless, white or pale shades of yellow (Fig 6.1c). The kyanite grains have a corrugated boundary owing to replacement by AP minerals (Fig. 6.1c,e). Corroded grains of rutile are also observed. Florencite grains occur as disseminations and appear as bright spots in a dull backdrop of lazulite, kyanite and augelite (Fig 6.1d). The size of the subhedral crystals ranges between 10-20 microns and few crystals of ~50 microns are observed. The grains are disseminated in the rock and appear as idioblastic, subhedral to anhedral crystals. Florencite crystals with finger-like protrusions are seen replacing kyanite (Fig 6.1g). Textural features in the less deformed parts attest to the view that most florencite crystals are left stranded within lazulite when the latter mineral replaced kyanite (Fig 6.1h). This feature suggests equilibrium coexistence of florencite and lazulite. Some grains of florencite in lazulite show small amount of corrosion at their rim indicating very minor participation in the formation of lazulite (Fig 6.1d). Zircon grains in the kyanite quartzite also display a phosphate rich rim (Fig. 6.1i). Florencite, lazulite and augelite show no signatures of deformation i.e. they are essentially undeformed. Muscovite though ubiquitously present in other kyanite quartzites, is absent in this.

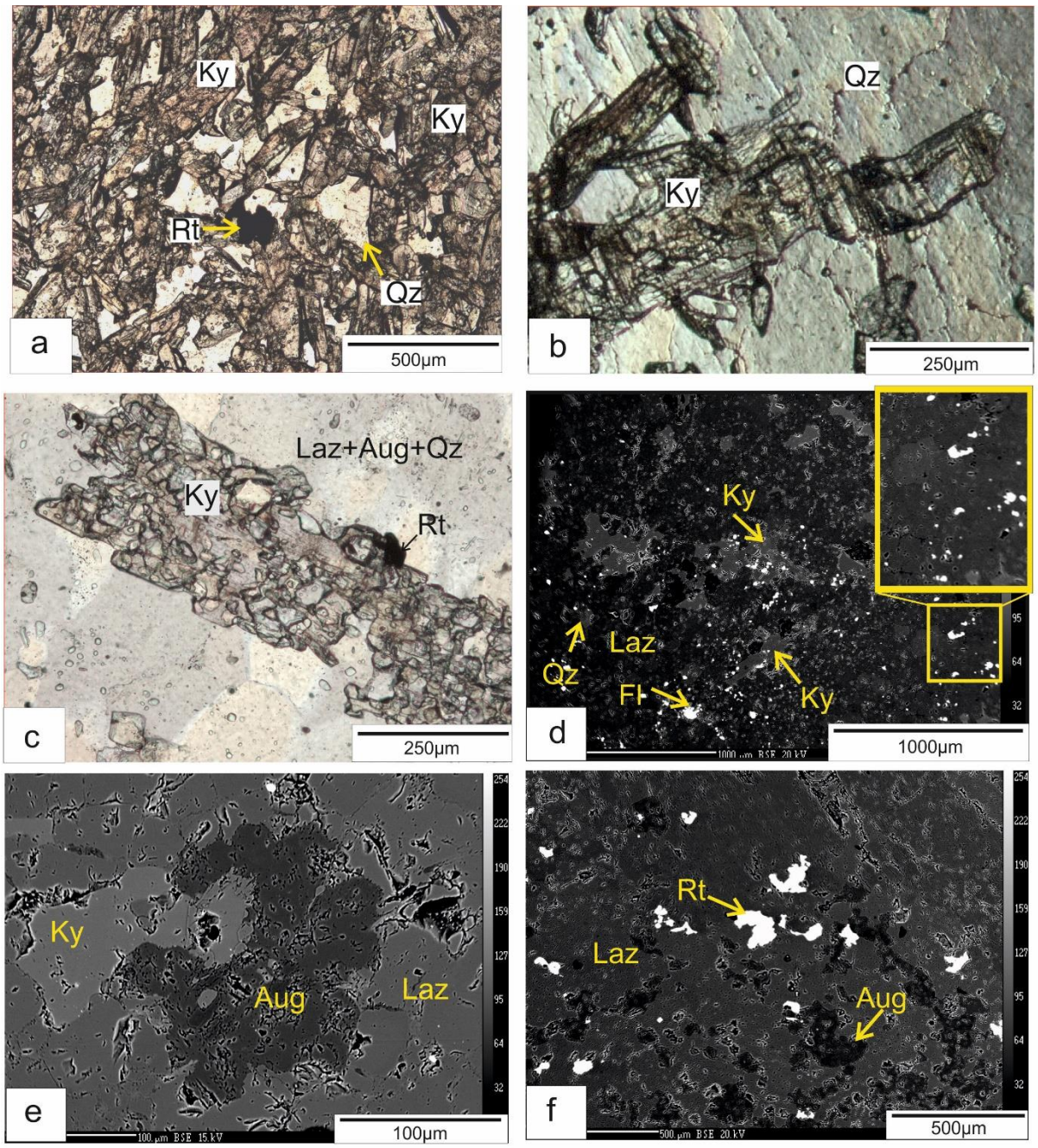

Fig 6.1(a) Randomly oriented kyanite grains forming a mesh-like appearance. Some corroded rutile grains and quartz are also seen in the interstitial spaces (b) Kyanite poor zone in the host rock showing the presence of deformed (kinked) kyanite (c) Kyanite grains replaced by lazulite, quartz and augelite. Recrystallised kyanite developing over kyanite (d) Overall view of the lazulite rich zone: relicts of kyanite showing corroded boundary are sparsely distributed here. The small bright spots seen here are florencite. The inset box blows up a part of the photo showing rare corroded florencite grain in lazulite (e) Kyanite replaced by augelite exhibiting corrugated boundary and inclusions of kyanite are found inside augelite. Augelite replaced by lazulite also exhibits corrugated boundary (f) Corroded grains of rutile andaugelite observed in lazulite. Laz=Lazulite, Aug=Augelite, Fl=Florencite. All other mineral abbreviations are after Whitney and Evans (2010).

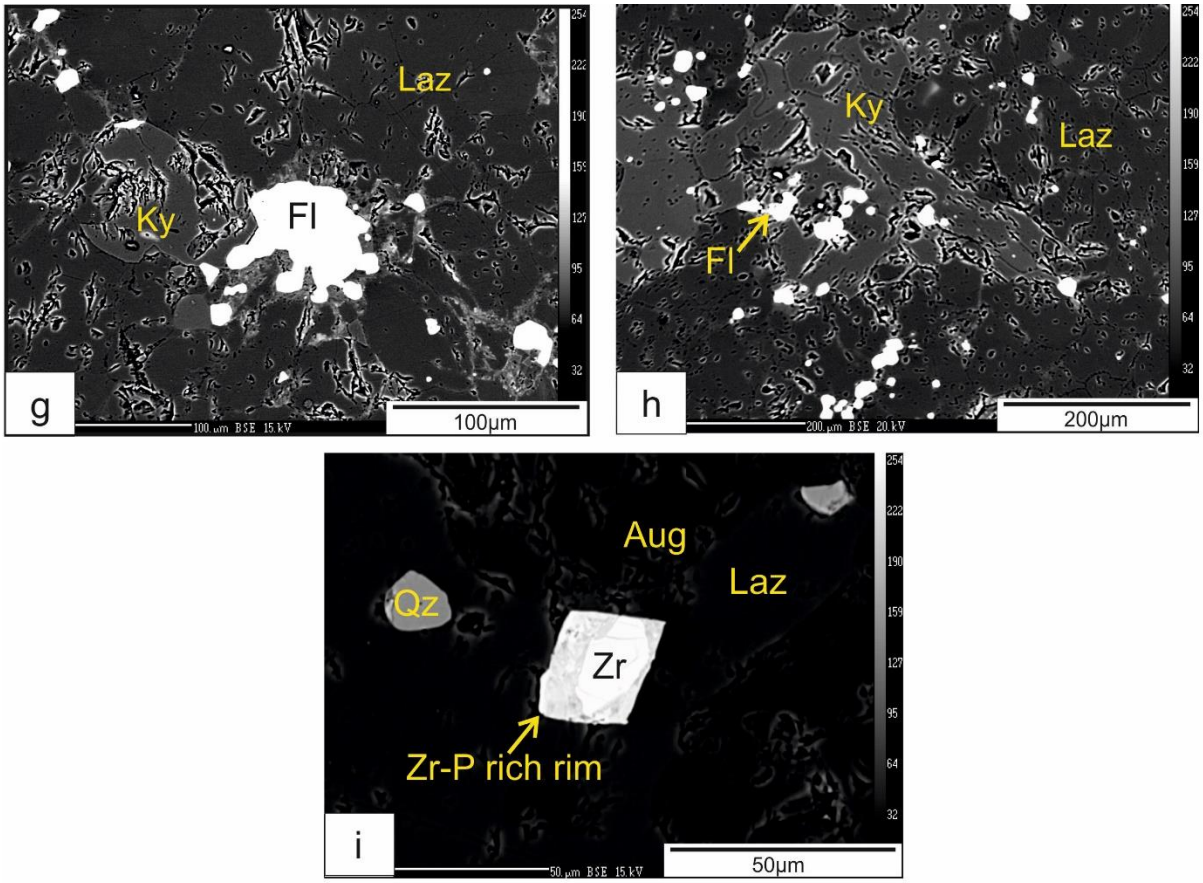

(g) Florencite grain with protruding grain boundary replaces kyanite (h) Florencite inclusions in kyanite while similar idioblastic florencite grains are stranded within lazulite (i) Detrital zircon grains in lazulite with a phosphate rich rim. Laz=Lazulite, Aug=Augelite, Fl=Florencite. All other mineral abbreviations are after Whitney and Evans (2010).

6.4 Mineral Chemistry

The chemical compositions of florencite and adjacent minerals are measured carbon-with electron microprobe analysis (EMPA) The detail of the analytical procedure is discussed in Appendix-III. The composition of florencite is recalculated on 11 oxygen basis and the nomenclature of the different species is according to Bayliss et al. (2010). Representative analyses of florencite and the associated minerals are presented in Table 6.1. The WDS spectrum of florencite shows that La and Ce are the main REE elements in the mineral (Fig 6.3).

The mineral florencite has a trigonal symmetry with a space group R_3m and is present as pseudocubic rhombohedra (Gaboreau et al., 2005). In florencite the A site is occupied mostly by Ce, La, Sm or Nd, the B site by Al and X site by P (Dill, 2001; Gaboreau et al., 2005; Repina et al., 2011). Compositionally florencite is essentially a solid solution of the species Florencite-(Ce) (48.7mol%), Florencite-(La) (29.9mol%), and Florencite- (Nd) (21.3mol%) (Table 6.1). The A-site in the florencite in this study is occupied by Ce, La, Nd, Sr, Ca and Al. The structural formula for the florencite grains from the study area is $La_{0.12}Nd_{0.09}Ce_{0.19}Sr_{0.01}Ca_{0.05}Al_{2.93}(P_{2.34}O_8)(OH)_6$. Similar to other natural florencite compositions, concentrations of LREE outweigh the concentrations of HREE (Gaboreau et al., 2005; Table 6.3). The concentrations of HREE, S, and As are below the detection limit of electron microprobe. Ce_2O_3 and La_2O_3 vary between 10.93-12.15 and 6.83-7.69 wt%. Concentrations of Sr (0.002 to 0.008 apfu), Ba (~0.00003 apfu), Ca (0.040 to 0.062 apfu), and K (0.001 to 0.012 apfu) are low. Concentration of ThO_2 varies between ~0.5 and 1.2wt% (0.01–0.024 apfu). The WDS spectrum suggests that the elements that are not measured do not have any significant concentrations (Fig 6.2a). Lazulite is dominated by Mg (98.06 mol% lazulite) with a small amount of scorzalite (1.94mol% Fe-Lazulite, Table 6.2).

The small amount Sr and Ca in the structure enters the structure of the florencite due to the substitution $3(Sr^{2+}, Ca^{2+}) = 2LREE^{3+}$ which represents a compositional spectrum from the florencite end member $[LREEAl_3(PO_4)_2(OH)_6]$ to the svanbergite/ woodhouseite $[(Sr,Ca)Al_3(SO_4)(PO_4)(OH)_6]$ end members. Entry of small amount of Th and Ca in the structure of florencite can also be explained by a cheralite-type substitution $REE^{3+} \longleftrightarrow Th + Ca$ (Nagy et al. 2002, Georgieva and Velinova 2012, Gaboreau et al. 2005).

6.5 Comparison of the chemistry of florencite of the studied rocks with other reported occurrences

Usually the published chemical data of APS minerals shows a wide variation in composition (Morteani and Ackermand, 2005, 2004,Deyell et al., 2005, Dill 2001) which are controlled by the chemical compositions of the mineralizing fluids (Izbrodin et al., 2006) and also by the composition of the protolith. Presence of Sr, Cs, Ns (What is this?) and SO_3 in considerable amount in florencite-(Ce) indicate solid solutions with goyazite, crandallite and natroalunite (Dill, 2003). P-bearing alunite and APS minerals of the svanbergite-woodhouseite group with subordinate amounts of gorceixite, florencite and goyazite were described in La Vanguardia kaolinite deposit near Illapel, Chile (Dill et al., 1995) and in dacite, andesite, rhyolite, trachite lavas and tuffs of Red Mountain, USA, Socosmayo, EI Sol 3, La Providencia, El Guitarrero, Peru (Dill, 2001). In the Ichetuyskoye occurrence, Russia, extensive solid solution exists between svanbergite-goyazite and woodhouseite-crandallite series (Izbrodin et al., 2011) where lazulite+scorzalite+trolleite give way to florencite+monazite+augelite+woodhouseite+svanbergite+alunite and later to natroalunite. However such extensive solid solutions are not present in the studied rocks and florencite-(Ce) occurs as end member composition with very less content of goyazite and crandallite (Fig 6.3b,d).

In Table 6.3 and Fig. (6.2.b,c) the florencite compositions from published data are compared with its counterpart from other metamorphic and igneous rock in other the world it is observed that these grains have higher concentrations of Ce and P (Fig 6.2b,c) Fig 6.2c. shows that the APS minerals in high-sulphidation epithermal Cu-Au and carbonatite ores evolve towards woodhouseite (S rich) and goyazite (Sr rich) compositions respectively (Dehkordi and Spandler 2019). Near unconformity related uranium ores the whole spectrum of florencite to svanbergite compositions are usually found (Moralev et al. 2005; Dehkordi and Spandler 2019; Fig 6.2d). Florencite developing near unconformity related U deposits are reported to have higher Sr content (McArthur Basin =2.3 wt%, Gaboreau et al. 2005; Athabasca Basin = 5.0 wt%, Gaboreau et al. 2007; Dehkordi and Spandler 2019). However, it was observed end member florencite compositions are found proximal to the U-mineralized zones and compositions towards the svanbergite end member represent syn-ore alteration zones distal to the U mineralization (Dehkordi and Spandler 2019). Diagenetic sedimentary hosted U fields however plot very close to svanbergite compositions. Hydrothermal Au-REE quartz veins of the sub-polar Urals also fall close to florencite end member compositions (Dehkordi and Spandler 2019). These are said to be derived from sedimentary host rocks(Moralev et al., 2005). Florencite related to IOCG deposits are richer in LREE compared to other settings (Schmandtet al. 2019). Thus, APS minerals which are genetically linked to sedimentary rocks cover the extent from florencite to svanbergite end-members. The Ce content of florencite from this study is however similar to a) some of the florencite observed in the unconformity related deposits in Tanami and Hall Creek regions of W. Australia (Dehkordi and Spandler 2019) b)Metasomatic florencite in kyanite schists of Sopron Hills, Eastern Alps (Nagy et al., 2002) c) Metamorphic florencite in quartzites and kyanite schists of eclogite zone, Tauern, Australia (Hoschek, 2016) d) Retrograde florencite formed kyanite schists in Ichetuyskoye area, Russia (Izbrodin et al., 2011). Higher Ce values

than the studied florencite are observed only in metasomatic florencite in mica schist lenses in Gran Paradiso, Western Alps (Giovannini et al., 2021).

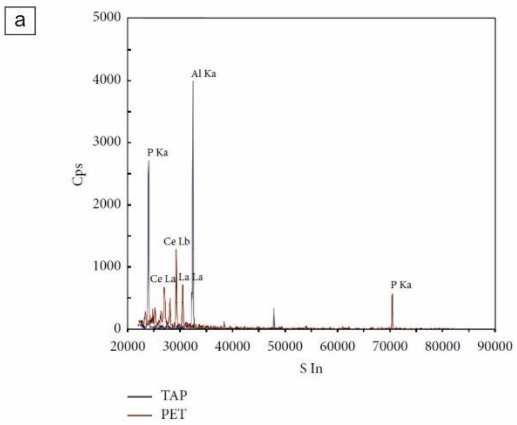

Fig 6.2a: WDS of florencite showing Al, P, Ce, and La. TAP and PET are crystals of the electron microprobe machine.

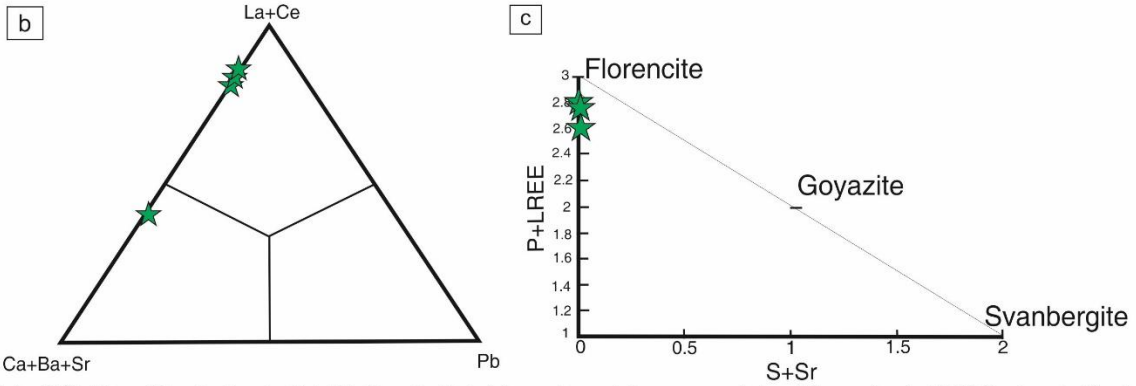

Fig.6.2b:The (Ca + Ba + Sr)-Pb-(La + Ce) triangular plot proposed by Storr et al. (1991). La + Ce is representative of florencite (=$CeAl_3(OH)_6/(PO_4)_2$), Ca+ Ba+Sr stands for svanbergite (=$Sr\ Al_3(OH)_6/\ (PO_4)(SO_4)$), gorceixite (= $BaAl_3(OH)_6/(PO_4)_2.H_20$), woodhouseite (=$Ca\ Al_3(OH)_6/\ (PO_4)(SO_4)$). Pb represents hinsdalite (=$PbAl_3(OH)_6/(PO_4)(SO_4)$).The green star mark the data points of our study whichclearly indicate florencite composition. Fig.6.2c: Cross plot diagram of P+LREE versus S+Sr(Gaboreau et al. 2005) The green star points mark position of the data from the studied rocks.

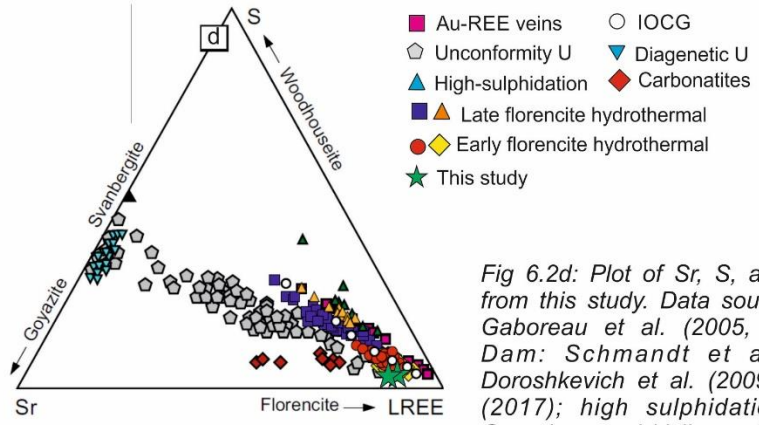

Fig 6.2d: Plot of Sr, S, and LREE, for florencite-(Ce) from this study. Data sources: unconformity-related U: Gaboreau et al. (2005, 2007); IOCG-type Olympic Dam: Schmandt et al. (2019); carbonatites: Doroshkevich et al. (2009) and Broom-Fendley et al. (2017); high sulphidation epithermal Cu-Au ore: Georgieva and Velinova (2014); Au-REE-quartz veins: Repina et al. (2014); and diagenetic sedimentary-hosted U: Marfil et al. (2013); hydrothermal (Dehkordi and Spandler 2019)

Table 6.2 :Representative analyses of florencite,lazulite,augelite,kyanite and rutile mineral from studied area. Florencite mineral composition has been compared with compositions from different localities. Note n.a. = not avaliable, b.d.l. = below detection limit

Location / Elements	Florencite (calculated on 11 oxygen basis. Values in wt%)			Lazulite (values in wt%)	Augelite (values in wt%)	Kyanite (values in wt%)				Rutile (values in wt%)
	Singhbhum Shear Zone (SSZ)					Singhbhum Shear Zone (SSZ)				
SiO_2	0.00	0.06	0.01	0.01	0.23	34.92	36.23	34.73	36.69	0.00
TiO_2	0.07	0.00	0.04	0.03	0.06	0	0	0.01	0.02	100.90
Al_2O_3	28.47	27.37	27.28	33.49	49.30	63.02	62.83	62.74	62.45	0.06
Cr_2O_3	0.00	0.00	0.00	0.00	0.08	0.1	0	0.04	0.04	0.13
FeO	0.00	0.01	0.00	0.00	0.00	0.02	0	0.01	0.03	0.10
MnO	0.00	0.00	0.00	0.43	0.04	0	0.04	0.01	0.02	0.00
CaO	0.42	0.64	0.54	0.01	0.00	0.02	0.05	0	0.00	0.01
MgO	0.01	0.05	0.10	13.32	0.03	0	0.01	0.01	0.01	0.00
Na_2O	0.09	0.09	0.11	0.03	0.00	0	0	0	0.06	0.00
K_2O	0.00	0.00	0.01	0.00	0.00	0	0	0.02	0.02	0.01
P_2O_5	30.81	30.72	30.84	48.44	37.09	0.07	0.09	0.03	0.00	0.00
ZrO_2	0.00	0.00	0.00							
Nb_2O_5	0.00	0.00	0.04							
La_2O_3	6.83	7.69	7.12							
Ce_2O_3	10.93	12.15	11.78							
Pr_2O_3	n.a.	n.a.	n.a.							
PbO	0.00	0.00	0.00							
ThO_2	0.49	1.18	1.18							
U_2O_3	0.04	0.02	0.02							
BaO	0.00	0.00	0.00							
SrO	0.12	0.15	0.10							
Nd_2O_3	2.70	2.61	2.69							
Sm_2O_3	1.10	1.06	1.09							
SO_3	0.00	0.00	0.00							
Total	82.08	83.81	82.95	95.76	86.83	98.15	99.25	97.6	99.40	101.25
	a.p.f.u.	*a.p.f.u.*	*a.p.f.u.*	*a.p.f.u.*	*a.p.f.u.*	*a.p.f.u.*	*a.p.f.u.*	*a.p.f.u.*	*a.p.f.u.*	*a.p.f.u.*
Si	0.00	0.01	0.00	0.00	0.02	0.961	0.985	0.962	1.00	0.00
Ti	0.00	0.00	0.00	0.00	0.00	0.000	0.000	0.000	0.00	1.00
Al	2.99	2.90	2.89	1.95	3.84	2.045	2.013	2.048	2.00	0.00
Cr	0.00	0.00	0.00	0.01	0.00	0.002	0.000	0.001	0.00	0.00
Fe	0.00	0.00	0.00	0.02	0.00	0.000	0.000	0.000	0.00	0.00
Mn	0.00	0.00	0.00	0.00	0.00	0.000	0.001	0.000	0.00	0.00
Ca	0.04	0.06	0.05	0.00	0.00	0.001	0.002	0.000	0.00	0.00
Mg	0.00	0.01	0.01	0.98	0.00	0.000	0.000	0.000	0.00	0.00
Na	0.02	0.02	0.02	0.00	0.00	0.000	0.000	0.000	0.00	0.00
K	0.00	0.00	0.00	0.00	0.00	0.000	0.000	0.001	0.00	0.00
P	2.33	2.34	2.35	2.03	2.08	0.012	0.015	0.005	0.00	0.00
Zr	0.00	0.00	0.00							
Nb	0.00	0.00	0.00							
La	0.11	0.13	0.12							
Ce	0.18	0.20	0.19							
Pr										
Pb	0.00	0.00	0.00							
Th	0.01	0.02	0.02							
U	0.00	0.00	0.00							
Ba	0.00	0.00	0.00							
Sr	0.01	0.01	0.01							
Nd	0.09	0.08	0.09							
Sm	0.03	0.03	0.03							
S	b.d.l.	b.d.l.	b.d.l.							
Total cation	5.80	5.80	5.79	4.98	5.95	3.02	3.02	3.02	3.00	1.00
ΣREE	0.42	0.45	0.44							
Florencite(mol%)	89.94	86.69	88.45							
Goyazite(mol%)	1.36	1.47	1.03							
Crandallite(mol%)	8.70	11.84	10.52							

Table 6.3 :Representative analyses of florencite from studied area compared with compositions from different localities. Note n.a. = not avaliable, b.d.l. = below detection limit

Location / Elements	Florencite from this study (calculated on 11 oxygen basis. Values in wt%)	Florencite data by Nagy *et al* 2002 (values in wt%)	Florencite data by Janots *et al* 2005 (values in wt%)	Florencite data by Doroshkevich *et al* 2009 (values in wt%)	Florencite (La) Banfield 1989	Florencite (Ce) Banfield 1989	Dehkordi and Spandler 2019	Radulescu et al., 2009	Giovannini et al., 2021	Hikov 2010	Hoschek 2016	Izbrodin et al., 2011
	Singhbhum Shear Zone (SSZ)	Sopron Hills, Eastern Alps, Hungary.	Sebtide complex, Rif,Morocco.	Amba-Dongar, Gujarat,India.	New South Wales, Australia	New South Wales, Australia	Tanami and Hall Creek, Australia	Gran Paradiso Massif, Western Alps	Morro dos Seis Lagos deposit, Amazonas, Brazil	Central Srednogorie, Bulgaria	Eclogite Zone, Tauern Window, Austria	
SiO_2	0.00-0.06	n.a.	0.24-4.2	>0.75	n.a.	n.a.	0.07-2.07	n.a.	n.a.	n.a.	0.12	n.a.
Al_2O_3	27.28-28.47	28.66-31.89	27.10-31.92	27.86-30.67	22.8-45	25-45.4	29.2-31.7	29.95-29.98	14.96-18.65	34.43	30.41-31.31	28.46-29.64
FeO	0.00-0.01	n.a.	0.17-1.4	n.a.	1.7-4.6	1.3-12.5	0.09-1.80	n.a.	1.12-1.48	n.a.	0.03-0.62	n.a.
CaO	0.42-0.64	0.72-1.44	0.42-0.69	0.23-0.81	0.7-3.5	0.7-3.2	0.86-1.49	n.a.	0.44-1.09	1.21	0.23-0.64	0.37-0.75
MgO	0.01-0.10	n.a.	0.02-0.70	n.a.	n.a.	n.a.	n.a.	n.a.	n.a.	n.a.	0-0.01	n.a.
Na_2O	0.09-0.11	n.a.	0.01-0.06	n.a.	n.a.	n.a.	n.a.	n.a.	n.a.	n.a.	0-0.01	0.04-0.21
P_2O_5	30.72-30.84	26.97-28.93	22.4-26.4	26.08-28.56	8.1-26.8	8-28.9	21.2-26	28.31-28.33	19.77-21.14	21.42	26.94-27.77	24.97-26.50
La_2O_3	6.83-7.69	6.46-8.66	4.22-4.25	3.91-12.64	11.4-18.0	3.2-6.1	3.27-4.81	12.62-14.12	1.93-4.43	3.01	4.28-8.80	8.93-9.55
Ce_2O_3	10.93-12.15	10.91-14.33	8.37-9.26	4.94-12.32	0.7-2.6	4.6-8.3	7.66-12.5	16.56-18.19	11.84-16.85	6.82	11.86-16.51	11.76-14.89
Pr_2O_3	n.a.				n.a.	n.a.	1.14-1.91	n.a.	0.07-0.59	n.a.	1.05-1.70	0.93-1.34
ThO_2	0.49-1.18	0.55-9.94	0.59-1.09	n.a.	n.a.	n.a.	0-0.39	n.a.	3.32-3.84	n.a.	0.32-2.85	0.38-0.87
U_2O_3	0.02-0.04	n.a.	0.07-0.17	n.a.	n.a.	n.a.	n.a.	n.a.	n.a.	n.a.	0.01-0.07	n.a.
BaO	0	n.a.	n.a.	n.a.	0-2.2	0.3-7.2	n.a.	n.a.	5.27-7.64	n.a.	n.a.	n.a.
SrO	0.10-0.15	0.16-0.67	1.32-5.91	4.47-13.36	n.a.	n.a.	0.89-6.02	n.a.	0.77-1.07	9.63	0.04-0.17	1.67-4.27
Nd_2O_3	2.61-2.70	1.65-5.00	3.96-4.80	1.02-2.91	3.2-5.0	1-4.9	3.02-8.37	1.60-2.51	2.48-3.62	n.a.	3.80-7.48	1.73-3.08
Sm_2O_3	1.06-1.10	0.10-0.92	0.55-0.60	n.a.	0.5-0.9	0.6-1.6	0.24-1.11	n.a.	0.59-0.81	n.a.	0.11-1.12	0.24
SO_3	0.00	n.a.	0.21-0.59	1.08-4.71	n.a.	n.a.	0.71-5.14	n.a.	n.a.	11.70	0.28-0.61	n.a.
Total	82.08-83.81	87.69-90.36	78.21-86.35	71.40-78.98	62-98	57-93	81.3-86	89-93.13	85.23-93.65	88.26	89.42-91.14	88.10-89.08

6.6 Textural modelling:

Formation of florencite, a REE phosphate, after kyanite requires open system process. To understand the process of florencite formation in the open system textural modelling study I performed integrating the inputs from the textural analyses and measured chemical condition.The C-Space program was used for the purpose. The program uses the method of singular value decomposition technique to achieve the desired results (Lang et al. 2004). The details of the computational procedure is given in the Appendix I.

Results

Following modelled reactions are consistent with both the textural features and the compositional characteristics of the minerals.

Florencite and other Aluminophosphate minerals from Kyanite

5.4 **Kyanite** + 7.33 P + 1.59 Mg + 13.29 H_2O + 0.023 Na + 0.061 Ca + 0.007 Fe + 0.15 La+ 0.11 Nd + 0.25 Ce + 0.01 Sr = 1**Florencite +** 1 **Lazulite**+ 1 **Augelite** + 1.79 SiO_2 …….(R1)

The modeled reaction suggest that several elements were mobile during the formation of florencite and the associated aliminophosphate minerals in which the REE and P were transported by aqueous fluids.

6.7 Summary

The Singhbhum Shear Zone has encountered several hydrothermal REE mineralization and mobilization over a period of ~900 Ma. REE is transported through fluids in the form of complexes with several anions (Seward et al., 2014). For REE to form a complex with P temperature >400°C, acidic pH and 10 wt% salinity is required (Pourtier et al. 2010). As reported by Pal et al. (2021) the Singhbhum Shear Zone has seen three major events of LREE-metasomatism dated at i) c.a. 1.88& 1.80 Ga (Development of extension related faults between Dhanjori Group and Chaibasa Formation on the southern boundary of Singhbhum craton. U mineralization) ii) c.a. 1.66-1.64 Ga (Probable re-activation of faults due extension or part-closing of basin south of Dalma Volcanic Belt) iii) c.a. 950±50 Ma (Last pervasive hydrothermal event related to final closing of NSMB). The rocks of the SSZ have undergone multiple episodes of deformation/metamorphism between ca. 1.60 and ca. 1.0 Ga (Mahato et al., 2008; Chatterjee et al., 2010). The APS and AP minerals have not suffered any deformation but replace deformed kyanite which leads us to presume that the last phase of LREE mobilization in the SSZ dated c.a. 950±50 Ma may have supplied the required elements for formation of florencite.

References

Arribas, A., 1995. Geology, geochronology, fluid inclusions, and isotope geochemistry of the Rodalquilar gold alunite deposit, Spain. Econ. Geol. 90, 795–822. https://doi.org/10.2113/gsecongeo.90.4.795

Bajnóczi, B., Seres-Hartai, E., Nagy, G., 2004. Phosphate-bearing minerals in the advanced argillic alteration zones of high-sulphidation type ore deposits in the Carpatho-Pannonian region. Acta Mineral. Szeged 45, 81–92.

Banfield, J.F., Eggleton, R.A., 1989. Apatite replacement and rare earth mobilization, fractionation, and fixation during weathering. Clays Clay Miner. 37, 113–127. https://doi.org/10.1346/CCMN.1989.0370202

Bayliss, P., Kolitsch, U., Nickel, E.H., Pring, A., 2010. Alunite supergroup: recommended nomenclature. Mineral. Mag. 74, 919–927. https://doi.org/10.1180/minmag.2010.074.5.919

Bernhard, F., 2001. Scandium mineralization associated with hydrothermal lazulite-quartz veins in the Lower Austroalpine Grobgneis complex, Eastern Alps, Austria, in: Mineral Deposits at the Beginning of the 21st Century. CRC Press, pp. 935–938.

Broom-Fendley, S., Brady, A.E., Wall, F., Gunn, G., Dawes, W., 2017. REE minerals at the Songwe Hill carbonatite, Malawi: HREE-enrichment in late-stage apatite. Ore Geol. Rev. 81, 23–41.

Brown, W.L., 1986. Book Review: Phosphate minerals. edited by JO Nriagu and PB Moore, Springer-Verlag, Berlin, 1984, 442 pp., cloth, $57.50. Geochim. Cosmochim. Acta 50, 1833.

Chatterjee, N., Banerjee, M., Bhattacharya, A., Maji, A.K., 2010. Monazite chronology, metamorphism-anatexis and tectonic relevance of the mid-Neoproterozoic Eastern Indian Tectonic Zone. Precambrian Res. 179, 99–120. https://doi.org/10.1016/j.precamres.2010.02.013

Devismes, P., Guigues, J., Laurent, Y., Parfenoff, A., 1968. Première découverte de florencite en France. Bull. Minéralogie 91, 500–502.

Deyell, C.L., Rye, R.O., Landis, G.P., Bissig, T., 2005. Alunite and the role of magmatic fluids in the Tambo high-sulfidation deposit, El Indio-Pascua belt, Chile. Chem. Geol. 215, 185–218. https://doi.org/10.1016/j.chemgeo.2004.06.038

Dill, H.G., 2003. A comparative study of APS minerals of the Pacific Rim fold belts with special reference to south American argillaceous deposits. J. South Am. Earth Sci. 16,

301–320. https://doi.org/10.1016/S0895-9811(03)00099-3

Dill, H.G., 2001. The geology of aluminum phosphate and sulphates of the alunite group minerals: A review. Earth Sci. Rev. 53, 35–93. https://doi.org/10.1016/S0012-8252(00)00035-0

Dill, H.G., Bosse, H.R., Henning, K.H., Fricke, A., Ahrendt, H., 1997. Mineralogical and chemical variations in hypogene and supergene kaolin deposits in a mobile fold belt the Central Andes of northwestern Peru. Miner. Depos. 32, 149–163. https://doi.org/10.1007/s001260050081

Dill, H.G., Fricke, A., Henning, K.H., Gebert, H., 1995. An APS mineralization in the kaolin deposit Desa Toraget from northern Sulawesi, Indonesia. J. Southeast Asian Earth Sci. 11, 289–293. https://doi.org/10.1016/0743-9547(94)00037-F

Dill, H.G., Melcher, F., Gerdes, A., Weber, B., 2008. The origin and zoning of hypogene and supergene Fe-Mn-Mg-Sc-U-REE phosphate mineralization from the newly discovered Trutzhofmühle aplite, Hagendorf Pegmatite Province, Germany. Can. Mineral. 46, 1131–1157. https://doi.org/10.3749/canmin.46.5.1131

Doroshkevich, A.G., Viladkar, S.G., Ripp, G.S., Burtseva, M. V., 2009. Hydrothermal REE mineralization in the Amba Dongar carbonatite complex, Gujarat, India. Can. Mineral. 47, 1105–1116. https://doi.org/10.3749/canmin.47.5.1105

Ek, R., Nysten, P., 1990. Phosphate mineralogy of the Hålsjöberg and Hökensås kyanite deposits. GFF 112, 9–18. https://doi.org/10.1080/11035899009453156

Gaboreau, S., Cuney, M., Quirt, D., Beaufort, D., Patrier, P., Mathieu, R., 2007. Significance of aluminum phosphate-sulfate minerals associated with U unconformity-type deposits: The Athabasca basin, Canada. Am. Mineral. 92, 267–280.

Gaboreau, S.T., Beaufort, D.A., Vieillard, P.H., Patrier, P.A., 2005. Alumunium phosphate – sulfate minerals associated with Proterozoic unconformity-type uranium deposits in th East Alligator River Uranium field, Northern territorie , Australia 43, 813–827.

Gaudin, A., Ansan, V., Lorand, J.P., Pont, S., 2020. Genesis of a florencite-bearing kaolin deposit on ordovician schists at Saint-Aubin-des-Châteaux, Armorican Massif, France. Ore Geol. Rev. 120. https://doi.org/10.1016/j.oregeorev.2020.103445

Georgieva, S., Velinova, N., 2012. Florencite- (Ce, La, Nd) from the advanced argillic alterations in the Chelopech high-sulphidation epithermal Cu-Au deposit , Bulgaria. Bulg. Geol. Soc. 23–24.

Giovannini, A.L., Bastos Neto, A.C., Porto, C.G., Takehara, L., Pereira, V.P., Bidone, M.H., 2021. REE mineralization (primary, supergene and sedimentary) associated to the Morro

dos Seis Lagos Nb (REE, Ti) deposit (Amazonas, Brazil). Ore Geol. Rev. 137. https://doi.org/10.1016/j.oregeorev.2021.104308

Hikov, A., 2019. First find of florencite- (Ce , La , Nd) in advanced argillic altered rocks from the Asarel porphyry copper deposit , Central Srednogorie. Rev. Bulg. Geol. Soc. 80, 33–35.

Hikov, A., Lerouge, C., Velinova, N., 2010. Geochemistry of alunite group minerals in advanced argillic altered rocks from the Asarel porphyry copper deposit, Central Srednogorie. Rev. Bulg. Geol. Soc. 71, 133–148.

Höfig, T., Mott, A., Miller, B., Horkley, L., Zhang, C., Peate, D., 2021. Tracking the evolution of a submarine arc-hosted hydrothermal system through the deportment of phosphorous and rare-earth elements. Abstr. Present. Goldschmidt virtual 3. https://doi.org/10.7185/gold2021.8098

Hoschek, G., 2016. Phase relations of the REE minerals florencite, allanite and monazite in quartzitic garnet–kyanite schist of the Eclogite Zone, Tauern Window, Austria. Eur. J. Mineral. 28, 735–750. https://doi.org/10.1127/ejm/2016/0028-2549

Izbrodin, I.A., Ripp, G.S., Doroshkevich, A.G., 2011. Aluminium phosphate and phosphate-sulphate minerals in kyanite schists of the Ichetuyskoye area, West Transbaikalia, Russia: Crystal chemistry and evolution. Mineral. Petrol. 101, 81–96. https://doi.org/10.1007/s00710-010-0135-5

Izbrodin, I.A., Ripp, G.S., Karmanov, N.S., 2006. Sulfate-Bearing Apatite of the Kyakhta Sillimanite Deposit (Western Baikal Region). Zap. Ross. Miner. O-va 135, 71–82.

Jambor, J.L., 1999. Nomenclature of the alunite supergroup. Can. Mineral. 37, 1323–1341.

Janeczek, J., Ewing, R.C., 1996. Florencite-(La) with fissiogenic REEs from a natural fission reactor at Bangombe, Gabon. Am. Mineral. 81, 1263–1269. https://doi.org/10.2138/am-1996-9-1024

Janots, E., Negro, F., Brunet, F., Goffé, B., Engi, M., Bouybaouène, M.L., 2006. Evolution of the REE mineralogy in HP-LT metapelites of the Sebtide complex, Rif, Morocco: Monazite stability and geochronology. Lithos 87, 214–234. https://doi.org/10.1016/j.lithos.2005.06.008

Kunov, A., 1999. Convergence of minerals with alunite-type structure (phosphates , phosphates-sulfates and sulfates), some cases from Bulgaria. Geol. Balc. 29, 71–79.

Lefebvre, J.J., Gasparrini, C., 1980. Florencite, an occurrence in the Zairian copperbelt. Can. Mineral. 18, 301–311.

Mahato, S., Goon, S., Bhattacharya, A., Mishra, B., Bernhardt, H.J., 2008. Thermo-tectonic

evolution of the North Singhbhum Mobile Belt (eastern India): A view from the western part of the belt. Precambrian Res. 162, 102–127. https://doi.org/10.1016/j.precamres.2007.07.015

McKie, D., 1962. Goyazite and florencite from two African carbonatites. Mineral. Mag. J. Mineral. Soc. 33, 281–297. https://doi.org/10.1180/minmag.1962.033.259.03

Moralev, G. V., Borisov, A. V., Surenkov, S. V., Nagaeva, S.P., Tarbaev, M.B., Kuznetsov, S.K., Onishchenko, S.A., Efanova, L.I., Soboleva, A.A., 2005. Distribution and modes of occurrence of REE at the Chudnoe and Nesterovskoe occurrences of Au-Pd-REE ore mineralization in the Maldynyrd Range, Nether-Polar Urals. Geokhimiya 43, 1175–1195.

Morteani, G., Ackermand, D., 2005. Mineralogy, geochemistry and petrology of an amphibolite-facies aluminum-phosphate and borosilicate (APB)-bearing quartzite from the Mesoproterozoic Itremo Group (Central Madagascar). Neues Jahrb. fur Mineral. Abhandlungen 182, 123–148. https://doi.org/10.1127/0077-7757/2006/0036

Morteani, G., Ackermand, D., 2004. Mineralogy and geochemistry of Al-phosphate and Al-borosilicate-bearing metaquartzites of the northern Serra do Espinhaço (State of Bahia, Brazil). Mineral. Petrol. 80, 59–81. https://doi.org/10.1007/s00710-003-0019-z

Nagy, G., Draganits, E., Demény, A., Pantó, G., Árkai, P., 2002. Genesis and transformations of monazite, florencite and rhabdophane during medium grade metamorphism: Examples from the Sopron Hills, Eastern Alps. Chem. Geol. 191, 25–46. https://doi.org/10.1016/S0009-2541(02)00147-X

Nazari-Dehkordi, T., Spandler, C., 2019. Paragenesis and composition of xenotime-(Y) and florencite-(Ce) from unconformity-related heavy rare earth element mineralization of northern Western Australia. Mineral. Petrol. 113, 563–581. https://doi.org/10.1007/s00710-019-00676-w

Pal, D.C., Basak, S., McFarlane, C., Sarangi, A.K., 2021. EPMA geochemistry and LA-ICPMS dating of allanite, epidote, monazite, florencite and titanite from the Jaduguda uranium deposit, Singhbhum Shear Zone, eastern India: Implications for REE mineralization vis-à-vis tectonothermal events in the Proterozoic Mo. Precambrian Res. 359, 106208.

Pouliot, G., Hofmann, H.J., 1981. Florencite; a first occurrence in Canada. Can. Mineral. 19, 535–540.

Radulescu, I.G., Rubatto, D., Gregory, C., Compagnoni, R., 2009. The age of HP metamorphism in the Gran Paradiso Massif, Western Alps: a petrological and

geochronological study of “silvery micaschists.” Lithos 110, 95–108.

Rasmussen, B., 1996. Early-diagenetic REE-phosphate minerals (florencite, gorceixite, crandallite, and xenotime) in marine sandstones: A major sink for oceanic phosphorus. Am. J. Sci. 296, 601–632. https://doi.org/10.2475/ajs.296.6.601

Repina, S. A., 2011. Fractionation of REE in the xenotime and florencite paragenetic association from Au-REE mineral occurrences of the Nether-Polar Urals. Geochemistry Int. 49, 868–887. https://doi.org/10.1134/S0016702911090060

Repina, S.A., Khiller, V. V, Makagonov, E.P., 2014. Microheterogeneity of crystal growth zones as a result of REE fractionation. Geochemistry Int. 52, 1057–1071.

Schmandt, D.S., Cook, N.J., Ciobanu, C.L., 2019. Rare earth element phosphate minerals from the Olympic Dam Cu-U-Au- Ag deposit , South Australia : Recognizing temporal-spatial controls on REE mineralogy in an evolved IOCG system. Can. Mineral. Vol. 57, 3–24. https://doi.org/10.3749/canmin.1800043

Schwab, R.G., Herold, H., Costa, M.L. da, Oliveira, N.P., 1989. The formation of aluminous phosphates through lateritic weathering of rocks, in: Weathering: Its Products and Deposits. pp. 369–386.

Scott, K.M., 1987. Solid solution in, and classification of, gossan-derived members of the alunite-jarosite family, northwest Queensland, Australia. Am. Mineral. 72, 178–187.

Seward, T.M., Williams-Jones, A.E., Migdisov, A.A., 2014. The chemistry of metal transport and deposition by ore-forming hydrothermal fluids. Treatise on geochemistry 29–57.

Strunz, H., Tennyson, C., 1983. Mineralogische Tabellen. Eine Klassifizierung der Mineralien auf kristallchemischer Grundlage. Mit einer Einführung in die Kristallchemie. Akademische Verlagsgesellschaft Geest & Portig K.-G. Leipzig 1982 621 Seiten, 101 Abbildungen, 8 Tabellen, 1 Übersic, Crystal Research and Technology. John Wiley & Sons, Ltd. https://doi.org/https://doi.org/10.1002/crat.2170180509

Valenton, I., Schumann, A., Vinx, R., Wieneke, M., 1997. Supergene alteration since the upper cretaceous on alkaline igneous and metasomatic rocks of the Pocos de Caldas ring complex, Minas Gerais, Brazil. Appl. Geochemistry 12, 133–154. https://doi.org/10.1016/S0883-2927(96)00060-1

Visser, D., 1997. Augelite and cerian crandallite in dumortierite quartzites , Vaca Morta quarry , Vereda range , Macatibas , Bahia , Brazil 61, 607–609.

Whitney, D.L., Evans, B.W., 2010. Abbreviations for names of rock-forming minerals. Am. Mineral. 95, 185–187. https://doi.org/10.2138/am.2010.3371

CHAPTER 7

Discussion

In the preceding sections field relations and petro-mineralogical attributes of the kyanite quartzite and formation of muscovite (Chapter-3), chloritoid (Chapter-4), florencite (Chapter-6) and lazulite-augelite (Chapter-5) are presented. The information provides clues regarding the likely origin and metasomatic alteration of the enigmatic kyanite-quartzite rock. The stability of the metasomatic mineral assemblages in the studied kyanite quartzite put constraints on the tectonics of the SSZ that facilitated the fluid ingress and provide suitable physical conditions for the stability of the metasomatic assemblages in the studied rocks. These are presented in the following sections:

7.1 Origin of Kyanite quartzite and development of muscovite

The foregoing analyses suggest that the studied kyanite quartzite, like similar rocks elsewhere in the world, has unusual bulk compositions that are exceptionally rich in Al_2O_3 and SiO_2 and depleted in FeO, MgO, CaO and Na_2O relative to the known metasedimentary and metaigneous rocks in the continental crust (Morteani and Ackermand, 2004; Müller et al., 2007; Owens and Pasek, 2007; Bijnaar et al., 2016). Before discussing the origin of this enigmatic kyanite- quartzite, certain characteristic features of the rock are summarised below:

1. Exposures of the kyanite-quartzite (KQ) can be traced all along the hanging wall side of the SSZ though patches of the rocks are reported from the heart of metasedimentary rocks of the adjoining Chaibasa Fm (Sengupta et al., 2005). Field and petrographic features of the KQ are consistent with the view that the rock is an integral part of the SSZ.
2. The KQ is variably deformed with ductile shear deformation and is metasomatised to form muscovite rich KQ. In places the infiltration driven process produced

assemblages with chloritoid (Chapter 4), florencite (Chapter 6) and alumina phosphates (Chapter 5).

3. In places the KQ show centimetre to decimetre thick compositional banding that are alternatively rich in kyanite and quartz (Chapter 3,5,6). Some field features in the banded KQ resembles sedimentary structures (Chapter-3,5).
4. Large blades of kyanite in the KQ form rosette texture in places (Chapter 3,4).
5. In many places kyanite bearing veins that cut the regional planar fabric show wall-controlled growth of kyanite (Fig. 3.1o). The veins are also deformed.
6. In the Al_2O_3-SiO_2 diagram, the compositions of the studied KQ are plotted close to a line joining kaolinite, pyrophyllite and quartz (Fig. 3.4a)
7. The studied muscovite poor KQ have high values for alteration index (average CIA~98, CIW~99, PIA~99. AAAI~95) relative to the shale and unaltered igneous rocks
8. The compatible elements, REE and most of the HFSE of the studied muscovite poor and muscovite rich KQ show 1:1 correlation with the average composition of the upper continental crust (Fig. 3.4b-h, Chapter 3).

   Relative to the Primitive Mantle compositions, the compositions of the studied KQ have elevated LILE, HFSE and LREE with a prominent Nb and Pb anomaly. The KQ shows exceptional Al_2O_3 contents and low FeO, MgO, CaO and Na_2O relative to the average sedimentary (and its metamorphic equivalent) and granite (and its metamorphic equivalent) compositions (Table 3.5, chapter 3).
9. In terms of the REE and most of the HFSE concentrations, the studied muscovite poor and rich KQ show remarkable resemblance with the adjoining schist and phyllite of the Chaibasa Fm and phyllites of the Lower Dhanjori Fm.

10. $\delta^{18}O$ values of kyanite in the KQ have restricted values (7.042-7.672) and overlap with the $\delta^{18}O$ values of kyanite reported from the hydrothermally deposited kyanite-quartz veins (section 3.6, Chapter 3). These observations together with the bulk rock compositions suggest that the protoliths of the KQ was sourced from the upper continental crust that were intensely altered by fluids.

The published information suggest that three major processes can produce the kyanite-quartz bearing rocks. These are:

A. Hydrothermally precipitated kyanite and quartz rich veins

In this scenario, Al-Si are transported by oxyhydroxide complexes are deposited in the veins upon cooling and interaction with the host rock of the veins (Allaz et al., 2005; Beitter et al., 2008; Bucholz and Ague, 2010). The $\delta^{18}O$ values of kyanite in the hydrothermally precipitated kyanite-quartzite overlap with the studied rock. However, a number of features described in point (3), (4) and (8) mentioned above, speak against transport of Al-and Si- by fluid and deposition of the same in the vein. Rather, the textural and chemical features of the studied KQ are consistent with residual enrichment of Al_2O_3 and SiO_2. However, the cross cutting kyanite (±quartz) veins (point 5), certainly supports direct precipitation of kyanite from aqueous fluid. The vein mineralogy is consistent with enhanced solubility of Al in the aqueous fluid, presumably in the form of Al-Si complexes, and precipitation of the same in the veins during change in physicochemical condition (Ague, 1995; Tagirov et al., 2004, 2002; Manning, 2007, 2006; Beitter et al., 2008). Since the veins are deformed, formation and deformation of the kyanite veins (±quartz) seem to be coeval with the protracted shear deformation in the SSZ.

If the possibility of hydrothermal transportation of Al_2O_3 and SiO_2 for the main kyanite quartzite bodies (barring the kyanite veins) are discarded, only the processes of residual enrichment of Al_2O_3 and SiO_2 can explain the enigmatic compositions of the KQ. Two different processes of residual enrichment of Al_2O_3 and SiO_2 are proposed. These are:

B. Residual enrichment of Al and Si during weathering

Studies have shown that extensive tropical weathering can leach out alkali and Fe-Mg-Ca from the silicate rocks and can produce bauxitic deposit at the top followed by saprolitic clay zone with kaoline below (Bijnaar et al., 2016). Metamorphism of this clay horizon can convert kaoline to pyrophyllite to kyanite-quartz rock (Bijnaar et al., 2016). The high alteration index (point 7), variable quartz-kyanite ratio, and the structure of the of the studied KQ (point 3,4) are consistent with in-situ formation of the kyanite quart rock from a residual clay deposit. Similar REE and HFSE (barring Nb) concentrations of the studied rocks with the adjoining lithologies (point 9) are also consistent with formation of the kyanite-quartz rock. This contention is also consistent with the observation from the Al_2O_3-SiO_2 diagram (Fig.3.4a, Chapter 3) where the studied KQ samples are plotted along the line joining kaolinite, pyrophyllite and quartz. Formation of the studied KQ by metamorphism of a weathering profile has its limitations. There is no pyrophyllite inclusion present within kyanite. The pyrophyllite and diaspore that are present in the studied area are secondary in origin. Furthermore, decomposition of pyrophyllite produces kyanite: quartz in the volume ratio of 1:1.6. In many places, massive kyanite with very little or no quartz is preserved. Moreover, field and petrographic features also do not suggest leaching of quartz in the rock. Clustering of $\delta^{18}O$ values in the range of (7.042-7.672) are inconsistent with residual

enrichment by rock- meteoric fluid interaction where distinctly lower $\delta^{18}O$ values of kyanite is expected (<4 per mil, Zakharov et al., 2017; Sharp et al., 2018).

C. *Residual enrichment of Al and Si through advanced argillic alteration*

A number of studies have documented that interaction of hot sulphidic aqueous hydrothermal fluid can completely leach out alkalies and Fe-Mg-Ca from rocks, leaving a Al-Si rich residue (reviewed in Bijnaar et al. 2016). Depending upon the physical condition of argillic alteration the end product could be pyrophyllite-quartz or Al_2SiO_5-quartz deposits. The geochemistry and the $\delta^{18}O$ values of kyanite (7.042-7.672) from the KQ and its close proximity with Cu-Fe sulphide deposits are consistent with formation of kyanite-quartz due to interaction of hot fluids, presumably derived from a magmatic source (Xiaoye et al., 2017; Sengupta and Pack, 2018) with the schists and phyllite of the adjoining Dhanjori (only the phyllite) and Chaibasa Fm. Pal et al. (2021) demonstrated that the Cu-Fe sulphide deposits in the SSZ (~1.8-1.9 Ga) predate that ductile deformation in the SSZ and accompanying metamorphism/metasomatism (at ~1.6 Ga and 1.0 Ga). The study of Pal et al. (2021) strengthens the possibility of advanced argillic alteration in the SSZ. Studies have also shown that the precursor of the Cu-Fe sulphide ores were extensively remobilized during tectonothermal processes associated with SSZ (Reviewed in Sarkar and Gupta, 2012; Pal et al., 2009; Pal et al., 2021). Ca. 1.8 Ga old monazite has been reported from the muscovite bearing kyanite quartzite (Pal et al.2021). This then follows that the advanced argillic alteration of the schist and phyllite and formation of kyanite quartzite (or its Al-rich protolith) could also occur during the period (~1.9-1.8 Ga). The kyanite-quartz veins, that are synkinematic to shearing in the SSZ, are part of a younger event that affected the ~1.8 Ga kyanite bearing host rock. Studies from many other areas where advanced argillic alteration

has been documented, kyanite was interpreted to have formed after andalusite, pyrophyllite or quartz-kaolin assemblage (developed at low pressure <2 kbar) during overprinting regional greenschist-amphibolite facies metamorphism (reviewed in Bijnaar et al. 2016 and references therein; Larsson 2001). Unlike these studies, the studied kyanite quartzite do not preserve any such low pressure-temperature minerals. The present database cannot rule out the possibility of complete obliteration of these minerals during the regional greenschist-amphibolite facies metamorphism as demonstrated in other areas of the world (reviewed in Bijnaar et al. 2016). If this possibility is validated in future, the unusually Al_2O_3 rich protolith of the kyanite quartzite would be linked to the ~1.9-1.8 Ga ore forming process that preceded the regional metamorphism at ~1.6 Ga. The SSZ show repeated shearing that are accompanied by mobilization of the Cu-Fe-sulphide ores which are deformed (reviewed in Sarkar and Gupta, 2010). Based on field and petrographic evidence, it is proposed that the local mobility of Al and Si and the formation of kyanite-quartz veins occurred during the regional metamorphism and shear deformation at ~1.6 Ga. This study demonstrates contrasting behaviour of Al. The main kyanite quartzite bodies in the studied area show residual enrichment of Al, presumably due to argillic alteration of schist and pelite at ~1.8 Ga (Pal et al.2021). The kyanite veins, on the other hand, show mobility of Al (and Si) in crustal fluids that deposited kyanite quartz veins, synkinematic to 1.6 Ga tectonothermal event (reviewed in Pal et al. 2021)

7.1.1 Al-solubility and its transportation in hydrothermal fluids

Aluminium (Al) is considered immobile compared to other elements during fluid-rock interaction (Verdes et al., 1992). Some workers proposed that Al must have higher solubility at *higher P-T conditions* and can be transported in large amounts in aqueous

crustal fluids (Yardley, 1977; Yardley and Shmulovich, 1995). Studies by Manning (2006,2007) and Tagirov et al. (2002,2004) suggest that solubility of Al in fluids under upper to mid-crustal conditions is much higher than by formation of stable Al complexes with inorganic ligands. Also Al transport on a local scale can take place due to Al diffusion along strong chemical potential gradient (Widmer and Thompson, 2001). In contrast some workers propose that the solubility of majority of minerals is controlled by *fluid acidity* rather than by P-T conditions (Azimov and Bushmin, 2007). For any acidic solution, Si, K and Na have the highest mobility while Ca and Mg are mobile in acidic solutions and inert in neutral or alkaline solutions. Al is mobile in alkaline and ultra-acidic solutions but inert in neutral and slightly acidic solutions. There are many evidences for incongruous dissolution of aluminium silicates with preferential transfer of silica into the solution and precipitation of aluminium which is due to considerably different solubilities of SiO_2 and Al_2O_3 in aqueous solutions. A comparative study of solubility of different mineral groups like feldspars, micas, chlorites, amphiboles, etc. suggest that it is independent of their structure and mostly controlled by composition. The low mobility of Al is indicated by the solubility of corundum. For a fluid in equilibrium with corundum the content of Al varies from $1.5x10^{-5}$mol/kg H_2O ($400^{O}C$, 1 kbar, and 10^{-3} M HCL solution) to 0.9 mol/kg H_2O ($800^{O}C$, 5 kbar and 1M NaOH solution) thus proving that the solubility of Al increases with increasing alkalinity (Azimov and Bushkin, 2007). However, in alkaline fluids the increase in pH causes increase in solubility of both Al and silica due to formation of $HSiO_3^-$ and ion pairs with Na, K, Mg and Ca.

Beitter et al. (2008) studied the kyanite-quartz veins of Alpe Sponda, Central Alps, Switzerland, and the kyanite veins contain substantial amount of kyanite, similar to the present case of study, which could have been formed only through mobilisation of a significant amount of Al. Such high solubility of Al required *high concentration of unusual*

ligands e.g. fluorine or boron that would result in the formation of Al fluoride and borate complexes which are stable at higher temperatures but even such aqueous Al speciation is not significant under geologically reasonable conditions (Mysen, 2022). Al-Si complexing in amphibolite grade metamorphic fluids is also an essential factor that controls transport of Al. Aqueous fluids derived from regional devolatilization are close to quartz concentration (Manning and Boettcher, 1994) and the Al concentrations are controlled by temperature dependant silica solubility (Xie and Walther, 1993). Mysen (2022) confirms that decrease in pH through reactions with rocks buffering the fluid pH to a lower value has an important control on the reaction:

$$Al_2SiO_5\ (Ky) + SiO_2\ (Qz) + 7H_2O = 2AlSi(OH)_6O^- + 2H^+ \quad \ldots\ldots\ldots\ldots\ldots\ (1)$$

At higher temperatures a neutral species of Al –Si complex would be predominant over $AlSi(OH)_6O^-$ making the solubility of quartz+kyanite independent of pH.

$$Al_2SiO_5\ (Ky) + SiO_2\ (Qz) + 5H_2O = 2AlSi(OH)_5O \quad \ldots\ldots\ldots\ldots\ldots\ldots\ldots\ldots(2)$$

For fluids with moderate to high salinity Na-Al-Si complexing may play a major role.

$$Al_2SiO_5\ (Ky) + SiO_2\ (Qz) + 7H_2O + 2Na^+ = 2NaAlSi(OH)_6O + 2H^+ \ldots\ldots\ldots\ldots\ldots\ldots(3)$$

To ensure high precipitation of Al in the veins, very high Al solubility coupled with constant low silica solubility must be attained which is at very low pH values about 2.5 (Beitter et al. 2008). In the study area absence of mica in the phosphate bearing KQs supports the view that the infiltrating fluids were acidic with low concentrations of alkali.

The veins of kyanite-quartz truncating the schistosity of the rocks compel us to consider theories of mobilization of Al and this study supports the recent observations of that significant amount of Al can be mobile in infiltration-driven metamorphism or hydrothermal process.

7.2 The stratigraphic status of the kyanite quartzite

The SSZ is sandwiched between the meta-volcano sedimentary succession of the Dhanjori Gp. to the south and metapelite-quartzite dominated Chaibasa Fm. to the north (Fig.1). Owing to intense deformation and fluid-rock interactions, it is difficult to decipher the genetic affinity of the shear zone rocks particularly the kyanite quartzite. In the preceding sections, it has been demonstrated that geochemistry of the kyanite quartzite is akin to both the metapelite of the Chaibasa Fm. as well as the phyllites of the Lower Dhanjori Fm. The outcrops, though not continuous, the segmented kyanite quartzite units appear to form at immediate contact between the SSZ and the Chaibasa Fm. The kyanite quartzite is conspicuously absent near the southern margin of the SSZ where the rocks of Dhanjori Gp. are exposed. This observation and the presence of kyanite-quartzite (with variable amount of muscovite) well within the heart of the Chaibasa Fm. (Sengupta et al.2005) are consistent with the view that the kyanite-quartzite could be a part of the Chaibasa Fm. This inference alone, however, does not guarantee that all rocks of the SSZ are metasomatized Chaibasa Fm. More studies are warranted to establish the genetic relation of the exotic rocks of the SSZ with the bounding wall rocks.

7.3 Origin of chloritoid in the kyanite quartzite

The study reports metasomatic chloritoid forming after kyanite. Fe (with variable Mg) metasomatism is consistent with the field observations. Although chloritoid has been reported from the hydrothermally altered rock and veins (Gustafson, 1946; Osterberg, 1985), pseudomorphic replacement of kyanite by chloritoid is reported possibly first time from nature. Geothermal gradient plays a crucial role in the stability of chloritoid in the suitable bulk compositions. The geothermal gradient hotter than 83°C/kbar does not allow metasomatic chloritoid after kyanite in the FASH system. For hotter geothermal gradient (>83°C/kbar), Fe-metasomatism would follow the path Kyanite→ staurolite→ garnet (Fig. 4.5.2). A reduction of H_2O activity destabilizes chloritoid by enlarging the stability fields of garnet and staurolite (Fig. 4.5.4, chapter 4). Effects of non - FASH components in the chloritoid, garnet and staurolite effectively increases the stability field of chloritoid unless the reduction of activities in staurolite and garnet are too large (Fig. 4.5.5, 4.5.6). This is consistent with the view that Fe number (Fe/Fe+Mg) of chloritoid is close to the coexisting staurolite (Albee, 1962, 1970).

The textural modelling establishes that for chloritoid to form from kyanite a large amount of Fe was transported via fluids. In crustal hydrothermal fluids, Fe solubility is higher in oxide-silicate assemblages rather than sulphides, as sulphur reduces the solubility of Fe in fluids (Bodnar et al., 2014). Fe^{2+} ion becomes soluble in tetrahedral co-ordination ($FeCl_4^{2-}$or $FeCl_3(H_2O)^-$) in high Cl bearing fluids/brine up to the haematite-magnetite buffer (Scholten et al., 2019). If fO_2 exceeds the haematite-magnetite buffer Fe^{3+} becomes the prevalent ion transported as $FeCl_4^-$ up to 600°C. The fluid affecting the kyanite quartzite is estimated to be highly acidic brine solutions (from this study and Sengupta et al. 2011). Presence of magnetite establishes that the fO_2 was ~~within~~ close to the haematite-magnetite

buffer, while P-T estimates temperatures of ~500°C and hence it can be said that Fe was transported as $FeCl_4^{2-}$ or $FeCl_3(H_2O)^-$ complexes (Scholten et al., 2019).

7.3.1 Chloritoidization of kyanite-quartzite (KQ): The role of permeability

It is mentioned in chapter 4 that chloritoidization of kyanite and muscovite in the studied rock is likely to have occurred at ~6 ±1 kbar and ~ 500°C. The pressure of 6 kbar corresponds to a crustal depth of ~20 km. At such depth, the rocks cannot have intrinsic porosity. This poses a problem for large scale (more than several centimetres) metasomatic reactions in open system, for example muscovitization and chloritoidization in the studied rocks. This then follows that the metasomatic reactions must accompany certain process that create and maintain fluid path (Putnis and Austrheim, 2010). Textural modelling study has identified that kyanite and muscovite were replaced with chloritoid. Though chloritoid formed in the sequence Kyanite→ muscovite→ chloritoid, direct transformation of kyanite to chloritoid is more prevalent in the studied rocks. Considering the fact that the chloritoid was formed by infiltration driven processes, solution of kyanite (or muscovite) and precipitation of chloritoid seem to be the likely mechanism (Putnis and Austrheim, 2010). The solution reprecipitation mechanism can explain the structure and texture of the chloritoid bearing pods and veins in the studied rock. The mass balanced reactions that explain the formation of chloritoid have large positive volume change (reactions 1&5, Chapter 4). Similar positive solid volume change of the metasomatic reactions including serpentinization of olivine in troctolite is reported from many places (Bach and Klein, 2009). Several studies have demonstrated that positive solid volume change generates deviatoric stress at the point of the reaction that eventually leads to hydrofracturing (Shervais et al., 2005; Janssen et al., 2008; Jamtveit et al., 2009). Operation of this process is well documented in the serpentinization of olivine (Shervais et al., 2005). It is therefore,

likely that continuous hydrofracturing along the fluid path made the deep seated kyanite-quartzite permeable to fluid. Formation of network and veins of chloritoid in kyanite quartzite is consistent with the feed-back mechanism involving chloritoidization of kyanite and creation of secondary porosity (hydrofractures) and fluid flow. On the other hand, muscovitzation of kyanite (reaction 2, Chapter 4) involve a reduction of solid-volume change. This means that progress of this reaction will generate porosity (reaction enhanced porosity, Jamtveit et al., 2008). This secondary porosity will create space for the percolating fluid and the reaction continues along the fluid path. Textural features suggest that muscovitization, at least in some parts of the rock, preceded the chloritoidization (Fig. 4.2e). All these features suggest that mechanism of permeation of the metasomatic fluid in the kyanite-quartzite was complex and included both hydrofracturing as well as reaction enhanced porosity generation.

7.3.2 The composition of the metasomatic fluid

Reaction modelling and the observation from the chemical potential diagrams (Chapter-4) suggest that the metasomatic fluids that formed chloritoid in the studied rock was rich in Fe and K with small and variable amount of Mg and Na. Studies have shown that the mixing of CO_2-H_2O and H_2O-(Na-K)Cl become immiscible at high temperature (≥800°C, Duan et al., 1995). The reason being CO_2-H_2O and H_2O-Na(K)Cl show positive and negative deviation from the ideal mixing (Manning and Aranovich, 2014). Considering the P-T condition of formation of chloritoids, it is expected that the metasomatic fluid had both CO_2-H_2O and H_2O-Na(K)Cl(brine) components. A number of experimental studies have demonstrated that brine has distinctly lower wetting properties with silicate grains relative to CO_2-H_2O fluid (Gibert et al., 1998; Trommsdorff and Skippen, 1986; Newton and Manning, 2010). Consequently, the brine moves faster through the silicate network relative to CO_2-H_2O mixture (Newton and Manning 2010). Studies have shown that a large

quantities of Fe can be dissolved in brine in the form of Fe-Cl complexes over a range of fO_2 and temperature (Scholten et al., 2019). The solubility of Fe reaches maxima at fO_2 near QFM (quartz-fayalite-magnetite) buffer. The chloritoid bearing assemblage in the studied rock has the assemblage magnetite – quartz-rutile. This suggests that fO_2 was above but close to the QFM buffer (Spear, 1993). Dominant Fe^{2+} in the chloritoid structure also suggest this view. The brine rich fluids are also rich in alkalis (Aranovich, 2017). Taken together all the information, it seems likely that the metasomatic fluid was brine that was charged with alkali ions and Fe (+Mg). Owing to low dihedral angle of the brine molecule and the reaction induced porosity, the metasomatic fluid moved through the silicate network of the studied rock, interacted with kyanite and produced chloritoid at the abeyant physical condition.

7.4 Origin of florencite in the Kyanite quartzite

The textural evidence and the modelled reaction (R1, Chapter 6) suggest that florencite (+ lazulite, augelite) was formed in the studied area in an open system with REE, P and Sr being transported into the rock by metasomatic fluid. The euhedral and subhedral form of the florencite and the random orientation of the associated APS minerals suggest that formation of the assemblage outlasted the shear deformation.

7.4.1 REE and P transportation in hydrothermal fluid

REEs belong to High Field strength Elements (HFSE). The HFSE are less likely to be transported in most of the geological environment. However, significant transportation of REE and P in fluids and efficient precipitation of both ions are required for formation of REE-phosphates in hydrothermal systems. REE form stable complexes with OH^-, F^-, CO_3^{2-}, Cl^- and PO_4^{3-} (Seward et al., 2014). A primary transportation occurs as REE-Cl complexes at acidic conditions in Cl-F bearing fluids (Migdisov et al., 2016). Phosphate in comparison contributes very less in transportation of REE at lower temperatures upto 300°C in acidic conditions as monazite and xenotime become the dominant REE phosphates (Migdisov et al., 2016). However, monazite formation under prograde conditions (300-800°C) at near neutral pH suggest REE-phosphate complex stability at higher temperatures (Pourtier et al., 2010). Recent experimental studies of granitic hydrothermal systems have established that at temperature >400°C and salinity ~10 wt% NaCl, P solubility exceeds that of F in F and P bearing fluids. P mostly occurs as $H_3PO_4°$ or $H_4P_2O_7°$ at slightly acidic pH and high P concentrations (Pourtier et al. 2010). Under highly acidic conditions, the ions dissociate to form $H_2PO_4^-$ ions. As REE solubility also increases at lower pH, the REE-P complexing can form very easily under these conditions. Destabilization of other REE-transporting complexes by precipitation of minerals like sulphides (for SO_4 complexes), fluorapatite (for

F-complexes) can increase REE-P complexing in remaining fluids (Migdisov et al., 2016). Interaction with phosphate enriched rocks introduces phosphate ligands into hydrothermal fluids which also help REE-P complexes reach saturation (Chakhmouradian et al., 2017).

The foregoing analyses is consistent with the view that florencite in the studied rock was formed by advective transport of LREE and P presumably as REE-Phosphate complex. Singhbhum shear zone is characterized by repeated infiltrations of aqueous fluids that resulted in mineralization of Cu-Fe-U-P and tourmalinization (reviewed in Sengupta et al., 2011; Sarkar and Gupta 2012;Pal et al., 2021). Deposition of hydrothermal REE-bearing minerals in SSZ have been reported previously (Pal et al., 2021). Several studies have demonstrated that florencite develops in hydrothermally altered (sensulato) rock in which the metasomatic fluids are oxidized and slightly acidic in pH (Visser et al., 1997,Nagy et al., 2002, Gaboreau et al., 2005,Hikov et al., 2010 and Georgieva and Velinova, 2012). In view of this we envisage that infiltration of acidic fluid from an extraneous source during final stage of metamorphism forming the kyanite quartzite rock to be responsible for the development of florencite in the studied rock Absence of muscovitization of kyanite in kyanite quartz rock of this particular studied area and extensive tourmalinization of the adjoining rocks (Sengupta et al. 2011) supports the view that acidic metasomatic fluids infiltrated the rocks of the area. As described earlier acidic fluids with high salinity at >400°C can dissolve a large amount of PO_4^{-3} and LREE as these chemical species form the ligand (REE (PO_4)°aq) (Ayers and Watson, 1991, c.f. Jones and Wall, 1996). This fluid upon interacting with peraluminous host rock stabilized florencite (Nagy et al. 2002). However, the source of REE and PO_4 that infiltrated into the studied rock is not clear.

Studies have shown that hydrothermal REE deposits are formed when REE minerals are precipitated from hydrothermal fluids associated with alkaline to peralkaline granite, syenite magmatism (Gysi and Williams-Jones, 2013; Vasyukova et al., 2016) or

carbonatite (Wall et al., 2008; Bodeving et al., 2017) or peralkaline agpaitic rocks (Möller and Williams-Jones, 2016, Williams-Jones, 2017). They are sometimes associated with subalkaline granitic rocks (Djenchuraeva et al., 2008) and IOCG deposits (Schmandt et al., 2017). The most common minerals in hydrothermal systems are monazite (REE-phosphate), xenotime (REE-phosphate) and bastnaesite (REE-flurocarbonate). However, the present study area doesn't have the presence of carbonatites or alkaline rocks in the vicinity (nearest being in SPSZ) and hence they are not considered for source prospects. The peraluminous granite that occurs closest to the studied area is soda granite (Fig.1). However, the soda granite is highly deformed by shear deformation and hence cannot be the source of REE and P as florencite and the associated minerals outlast shear deformation. Pal et al. (2021) reported three major events of REE metasomatism in the SSZ i.e. 1.88 and 1.80 Ga, 1.66-1.64 Ga and 0.95±0.5 Ga. These may be linked to major tectonic events of the SSZ and NSFB i.e. development of extension related faults at margin of Dhanjori Group and Chaibasa formation, reactivation of those faults in later extension or part-closure of basin south of Dalma Volcanic Belt and final closure of NSFB. More studies on the issue could reveal the potential source of the REE-P bearing hydrothermal fluid.

There are several instances to show that apatite is one of the most resistant minerals during weathering, sedimentary transport and metamorphism. However intense weathering of apatite in the presence of clay minerals may produce crandallite, augelite and other Al-rich phosphates (Visser et al. 1997). Phosphate for aluminophosphate-sulphide (APS) minerals in the sandstones of the Chaswood Formation (Pe-Piper and Dolansky, 2005), of the Athabasca basin (Gaboreau et al., 2007) and in quartzites of Serra do Espinhaco (Morteani and Ackermand, 2004) were provided by dissolution or replacement of apatite. Replacement of apatite in the Summitville gold-copper deposit (Stoffregen and Alpers, 1987) and in the weathering crusts on phosphorites (Egorevskoe, Kimovskoe deposit) of

the Russian Platform (Zanin, 1975) gave rise to APS minerals. Apatite dissolution during metamorphism has formed lazulite in other kyanite quartzites (Morteani and Ackermand, 1996). Florencite-(Ce) crystallized on the surfaces of apatite or monazite-(Ce) grains in kyanite quartzites of the Sopron Hills from REE-containing hydrous fluids (Nagy et al., 2002). Florencite has also formed by replacement of monazite in Jaduguda, Singhbhum shear zone (Pal et al., 2021). There is no primary apatite or other phosphate minerals in this studied kyanite quartzite. However, apatite is present as a common accessory phase in nearby garnet-biotite schists and soda granites, which cannot be the source of P as discussed earlier. It is not clear in this case if the P required for the formation of florencite is sourced from the adjoining rocks or from an extraneous fluid. However apatite-magnetite rocks of SSZ could have acted as a source for P. To stabilize florencite and other aluminophosphate (AP) phases high activity of PO_4^{3-} and broad interval of pH (3-8) are important for APS minerals to crystallize (Stoffregen and Alpers, 1987; Ripp et al., 1998; Schwab et al., 2005; Chakraborty et al., 2014). Some studies have shown that particularly more activity of PO_4^{3-} and higher pH (7-7.5) is needed for florencite compared to svanbergite (Ripp et al., 1998).

Monazite-(Ce) from neighbouring rocks is presumably the main source of REE for florencite-(Ce) as it is the only Ce bearing mineral present in abundance in the neighbouring rocks. Apatite can also incorporate REE and it may also have acted as a source for Ce. Replacement of monazite-(Ce) by florencite is also reported by Pal et al (2021) from shear zone rocks nearby. As mentioned earlier that the Ce content of the florencite reported from this study is quite high and enough LREE had to be transported in the fluids for its formation.

7.5 Origin of lazulite-augelite assemblage: The Mg-P metasomatism

It is evident from the foregoing discussion that kyanite, quartz with minor rutile constitute the earliest stabilized minerals in the banded KQ rocks. Subsequent to formation of kyanite and quartz grains, the banded KQ rock was intensively sheared and later subjected to Mg-P metasomatism to form AP minerals. Figure 7.1 gives the schematic representation of formation of AP minerals from KQ rocks. Augelite is the first aluminophosphate mineral to form from kyanite due to infiltration of P-rich fluids. In the next stage lazulite formed due to Mg metasomatism of kyanite and augelite. Reactions 1 and 2 (Chapter 5) that explain formation of augelite and lazulite respectively have large negative change of volume of solid minerals. This then follows that progress of these reactions will create porosity in the host rock (reaction enhanced porosity) and which in turn will further facilitate the ingress of fluid. Table 5.2 (Chapter 5) shows the change of mass in the banded KQ rocks during metasomatism for 1000cc of rocks made up of augelite and lazulite respectively. Reaction 1 and 2 (Chapter 5) were used to calculate the change of mass (in moles) of different chemical species including H_2O. It is evident from Table 5.2 that a fluid–rock ratio of only 0.38 is sufficient to completely convert kyanite-quartz assemblage to augelite. Preservation of kyanite together with sporadic occurrence of lazulite-augelite bearing pods is consistent with limited fluid infiltration into the KQ rocks. Restriction of augelite and lazulite in kyanite-rich bands suggest control of aluminous protolith on the formation of these two aluminophosphate minerals (Morteani et al., 2001). It is evident from the reactions 1 and 2 (Chapter 5) that large amount of Al and silica was released during the formation of lazulite and augelite. These released Al and silica are presumed to have moved out from the reaction site as no new Al-Si bearing minerals were formed in the vicinity of augelite and lazulite. It seems reasonable that the infiltrating fluid that produced aluminophosphate minerals in the kyanite-rich bands transported the released

Al and Si in the form of Al-Si complexes (reactions 1 and 2, Chapter 5) as determined by Manning (2007) from experiments in Al-Si-O-H system. This fluid percolated the fractures in the banded KQ rocks and may have deposited some of the kyanite-quartz rich veins at the terminal phase of shearing. The undeformed grains of AP minerals and replacement of kyanite quartz vein by lazulite suggests that the metasomatic process continued at the terminal stage i.e. subsequent to shear deformation. Textural features demonstrate that florencite did not break down during the formation of augelite and lazulite. This together with lack of any phosphate or Mg-bearing mineral in the primary assemblage suggest that significant Mg and P were added to the KQ rocks by infiltrating fluid to produce augelite and lazulite (X_{Mg}=0.98) rich pods (see Table 5.2,5.3; Chapter 5). Field feature, microstructures and the estimated temperature and pressure from the lazulite- augelite bearing assemblage suggest that infiltration driven metamorphism of the KQ rocks accompanied by ductile shearing occurred at the culmination of regional metamorphism (490±40°C) at ~6 ±1kbar.

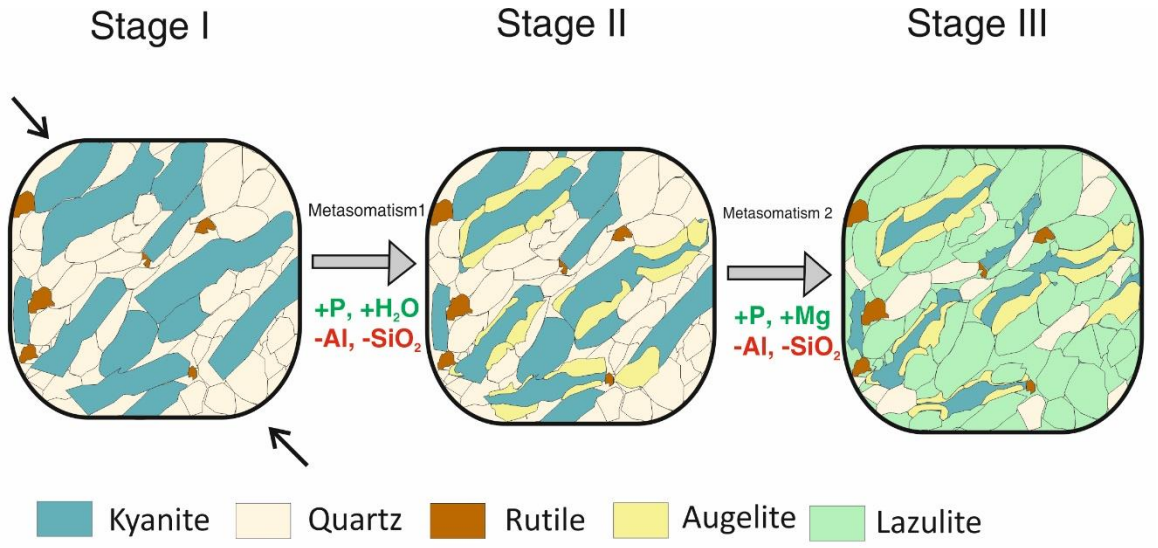

Figure 7.1: Schematic representation of phosphate metasomatism of the kyanite-rich rock (KQR) during Palaeoproterozoic orogenesis.'+' and '–' signs represent chemical species that are added to and subtracted from the host KQR, respectively (after Chakraborty et al., 2014). Stage I: deformation and dimensional orientation of quartz and kyanite grains during tectonism. Stage II: infiltration of aqueous fluid rich in P and conversion ofkyanite to augelite. During this metasomatic process (metasomatism 1), Al and SiO_2 were removed from the KQR. Stage III: infiltration of aqueous fluids rich in P and Mg and formation of lazulite at the expanse of augelite and kyanite. This metasomatism (metasomatism 2) also released Al and SiO_2 .

7.5.1 Mg-P metasomatism and formation of lazulite

Genesis of lazulite and augelite is commonly linked to metamorphism of P and Mg rich sediments (such as sabkha-type sedimentary package, e.g. Morteani et al., 2001; Morteani and Ackermand, 2004; Morteani and Ackermand, 2006; Marfil et al., 2013). The model proposed for genesis of lazulite in this study is strikingly different from genesis of lazulite in a closed system. Some studies describe lazulite from hydrothermal or metasomatic deposits (Duggan and Jones, 1990; Bernhard, 2001; Izbrodin et al., 2011, 2009; Uher et al., 2009) and our study is similar to them in many aspects. Studies show that P can be transported in large amounts by acidic fluids (discussed earlier in section 7.3). The associated apatite-magnetite rocks of the SSZ may have acted as the source of phosphates and led to Al-P complexing in the acidic hydrothermal fluids (as discussed earlier also). However, they could not have been source for Mg. There are no reported evaporitic

deposits in the SSZ (reviewed in Sarkar and Gupta 2012). Hence Mg derived from evaporate is not an option. This raises two possibilities:

1. The hydrothermal fluid became rich in Mg after deposition of Cu-Fe ores and later leached out P from adjoining apatite-rich rocks which later interacted with KQ to deposit lazulite
2. Mg was derived from the infiltrating fluids that are unrelated to the hydrothermal fluids that deposited the Cu-Fe sulphide ores in the adjoining areas.

The composition of chloritoid in the chloritoid bearing KQ suggest that the infiltrated fluid that metasomatized kyanite and formed chloritoid was rich in Fe. It is therefore likely that the KQ was infiltrated by fluids of different Fe/Mg ratio and REE contents spatially during the evolution of the SSZ. Present information cannot suggest if these fluids are genetically linked or not. More studies are required to trace the source(s) of the different metasomatic fluids that interacted with the KQ and the other parts of the SSZ.

7.6 Tectonic implication: The Al-P bearing mineral proxy

The foregoing analyses can be interpreted in the light of tectonism that affected the SSZ and NSFB. Topological constraints in the MFAPSH system, observed microstructures, and quantitative barometry in the adjoining metapelites suggest that the AP minerals were formed within a restricted P-T window (440 ± 40°C, ~6.3 ± 1 kbar). Similar P-T conditions are also inferred for the stability of chloritoid in the KQ (6±1 kbar, ~500°C, Chapter-4). The supracrustal rocks from parts of NSFB and adjoining SSZ evolved along a clockwise P-T trajectory that culminated at 6.3 ± 1 kbar and 490 ± 40°C (Sengupta, 2012).This is in

good agreement with the P-T conditions deduced in the chloritoid- and lazulite augelite bearing KQ. The geothermal gradient inferred from the stability of chloritoid (83°C/kbar) is also consistent with a clock wise P-T trajectory (Brown, 2014). The main deformation and metamorphism event for SSZ took place at ~1.6 Ga (reviewed in Sengupta 2012; Pal and Rhede, 2013; Table 2.3). Extant studies on rocks from NSFB and SSZ show that these share a common tectonothermal event at ~1.6 Ga. The pressure (~6± 1 kbar) inferred from schists adjoining the lazulite-augelite bearing KQ indicates that the protolith was buried under 18-22 km thick continental crust. The P-T values estimated for the AP-bearing assemblage plots well above the steady state geotherm for Proterozoic cratons (Ganguly et al., 1995; Fig. 7.2). The diagram (Fig. 7.2) also shows two transient geotherm that are likely to develop in fold-thrust belts due to decay of radionuclides in the continental thrust sheets of different thicknesses (25 and 35 km). The estimated P-T of the AP bearing assemblage plots on the geotherm of 25 km thick continental thrust sheet (Fig. 7.2). Hence it can be presumed that an ~19-24 km thick slab of NSFB was responsible for metamorphism of the studied rock.

A generalised tectonic model for the NSFB can be proposed from the foregoing analyses (Fig. 7.3). In the initial stages the sediments of NSFB were deposited on the Mesoarchaean Singhbhum Granite during Palaeoproterozoic extensional event (cf. Sarkar and Gupta 2012). Huge amount of basic magmatism (represented by Dhanjori and Dalma formations) occurred during the extensional event (Fig. 7.3, Stage I). The volcano-sedimentary protolith was then deformed and metamorphosed during late Palaeoproterozoic orogenesis (Fig. 7.3; Stage II and III). At the culmination of N-S compression the SSZ was formed. The NSFB was thrust upon the Singhbhum Granite along SSZ (Fig. 7.3, Stage III). Thus, it can be inferred that metasomatic rocks provide a valuable insight about the P-T fluid evolution in orogenic belts (cf. Harlov and Austrheim 2013)

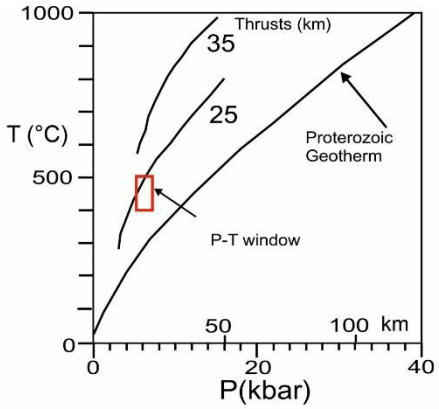

Fig 7.2:Perturbation of Proterozoic steady-state geotherm due to overthrusting of blocks having thicknesses of 35 and 25 km at constant basal heat flux (21.3 mW/m^2) and constant uplift rate of 0.1 mm/year (Ganguly et al. 1995). Note that the P-T box estimated in this study falls on the transient geothermal gradient calculated for a 25 km-thick thrust slice.

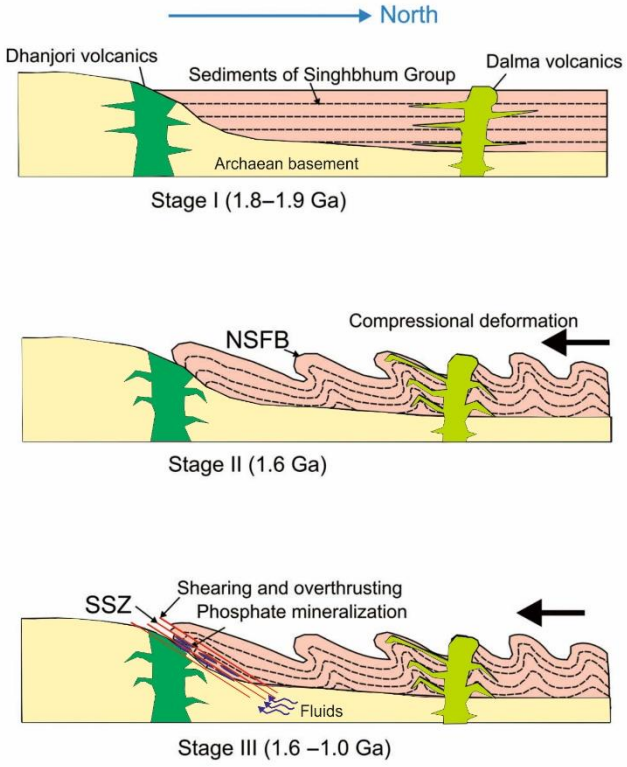

Fig. 7.3: Schematic evolution of the NSFB and SSZ (modified after Sarkar and Gupta 2012). Stage I: Formation of sedimentary basin on the basement of Singhbhum Granite. Puncture of the sedimentary sequences and the basement rocks by Palaeoproterozoic basic magmas (Dhanjori and Dalma volcanics). Stage II: Compression of volcano-sedimentary sequences of the NSFB. Stage III: Formation of the SSZ at the culmination of the deformation and metamorphism followed by fluid ingress and phosphate metasomatism in parts of the SSZ. Schematic diagram after Chakraborty et al., 2014. Chronologies of the different stages given are from Pal and Rhede (2013).

References

Ague, J.J., 1995. Mass transfer during Barrovian metamorphism of pelites, south-central Connecticut; II, Channelized fluid flow and the growth of staurolite and kyanite. Am. J. Sci. 294, 1061–1134.

Albee, A.L., 1970. Metamorphic zones in northern Vermont, in: Studies of Appalachian Geology, Northern and Maritime. Interscience publishers, New York, pp. 329–341. https://doi.org/117690

Albee, A.L., 1962. Relationships between the mineral association, chemical composition and physical properties of the chlorite series. Am. Mineral. J. Earth Planet. Mater. 47, 851–870.

Allaz, J., Maeder, X., Vannay, J.-C.J., Steck, A., 2005. Formation of aluminosilicate-bearing quartz veins in the Simano nappe (Central Alps): structural, thermobarometric and oxygen isotope constraints. Schweizerische Mineral. Und Petrogr. Mitteilungen 85, 191–214.

Aranovich, L.Y., 2017. The role of brines in high-temperature metamorphism and granitization. Petrology 25, 486–497.

Ayers, J.C., Watson, E.B., 1991. Solubility of apatite, monazite, zircon, and rutile in supercritical aqueous fluids with implications for subduction zone geochemistry. Philos. Trans. R. Soc. London. Ser. A Phys. Eng. Sci. 335, 365–375.

Azimov, P.Y., Bushmin, S.A., 2007. Solubility of minerals of metamorphic and metasomatic rocks in hydrothermal solutions of varying acidity: Thermodynamic modeling at 400-800°C and 1-5 kbar. Geochemistry Int. 45, 1210–1234. https://doi.org/10.1134/S0016702907120038

Bach, W., Klein, F., 2009. The petrology of seafloor rodingites: insights from geochemical reaction path modeling. Lithos 112, 103–117.

Beitter, T., Wagner, T., Markl, G., 2008. Formation of kyanite-quartz veins of the Alpe Sponda, Central Alps, Switzerland: Implications for Al transport during regional metamorphism. Contrib. to Mineral. Petrol. 156, 689–707. https://doi.org/10.1007/s00410-008-0310-4

Bernhard, F., 2001. Scandium mineralization associated with hydrothermal lazulite-quartz veins in the Lower Austroalpine Grobgneis complex, Eastern Alps, Austria, in: Mineral Deposits at the Beginning of the 21st Century. CRC Press, pp. 935–938.

Bijnaar, G., Bergen, M.J. Van, Wong, T.E., 2016. The kyanite quartzite of Bosland (Suriname): evidence for a Precambrian metamorphosed alteration system 2016, 447–465. https://doi.org/10.1017/njg.2016.38

Bodeving, S., Williams-Jones, A.E., Swinden, S., 2017. Carbonate–silicate melt immiscibility, REE mineralising fluids, and the evolution of the Lofdal Intrusive Suite, Namibia. Lithos 268, 383–398.

Bodnar, R.J., Lecumberri-Sanchez, P., Moncada, D., Steele-MacInnis, M., 2014. 13.5–Fluid inclusions in hydrothermal ore deposits. Treatise geochemistry. 2nd edn. Elsevier, Oxford 119, 142.

Brown, M., 2014. The contribution of metamorphic petrology to understanding lithosphere evolution and geodynamics. Geosci. Front. 5, 553–569.

Bucholz, C.E., Ague, J.J., 2010. Fluid flow and Al transport during quartz-kyanite vein formation, Unst, Shetland Islands, Scotland. J. Metamorph. Geol. 28, 19–39. https://doi.org/10.1111/j.1525-1314.2009.00851.x

Chakhmouradian, A.R., Reguir, E.P., Zaitsev, A.N., Couëslan, C., Xu, C., Kynický, J., Mumin, A.H., Yang, P., 2017. Apatite in carbonatitic rocks: Compositional variation, zoning, element partitioning and petrogenetic significance. Lithos 274, 188–213.

Chakraborty, M., Sengupta, N., Biswas, S., Sengupta, P., 2014. Phosphate minerals as a recorder of P-T-fluid regimes of metamorphic belts: example from the Palaeoproterozoic Singhbhum Shear Zone of the East Indian shield. Int. Geol. Rev. 57, 1619–1632. https://doi.org/10.1080/00206814.2014.982216

Djenchuraeva, R.D., Borisov, F.I., Pak, N.T., Malyukova, N.N., 2008. Metallogeny and geodynamics of the Aktiuz–Boordu mining district, northern Tien Shan, Kyrgyzstan. J. Asian Earth Sci. 32, 280–299.

Duan, Z., Møller, N., Weare, J.H., 1995. Equation of state for the NaCl-H2O-CO2 system: prediction of phase equilibria and volumetric properties. Geochim. Cosmochim. Acta 59, 2869–2882.

Duggan, M., Jones, M., 1990. Phosphate minerals in altered andesite from Mount Perry, Queensland, Australia. Can. Mineral. 28, 125–131.

Gaboreau, S., Cuney, M., Quirt, D., Beaufort, D., Patrier, P., Mathieu, R., 2007. Significance of aluminum phosphate-sulfate minerals associated with U unconformity-type deposits: The Athabasca basin, Canada. Am. Mineral. 92, 267–280.

Gaboreau, S.T., Beaufort, D.A., Vieillard, P.H., Patrier, P.A., 2005. Alumunium phosphate – sulfate minerals associated with Proterozoic unconformity-type uranium deposits in th East Alligator River Uranium field, Northern territorie , Australia 43, 813–827.

Ganguly, J., Singh, R.N., Ramana, D. V, 1995. Thermal perturbation during charnockitization and granulite facies metamorphism in southern India. J. Metamorph. Geol. 13, 419–430.

Georgieva, S., Velinova, N., 2012. Florencite- (Ce, La, Nd) from the advanced argillic alterations in the Chelopech high-sulphidation epithermal Cu-Au deposit , Bulgaria. Bulg. Geol. Soc. 23–24.

Gibert, F., Guillaume, D., Laporte, D., 1998. Importance of fluid immiscibility in the H 2 O-NaCl-CO 2 system and selective CO 2 entrapment in granulites; experimental phase diagram at 5-7 kbar, 900 degrees C and wetting textures. Eur. J. Mineral. 10, 1109–1123.

Gustafson, J.K., 1946. Two occurrences of chloritoid as a hydrothermal mineral in igneous rocks. Am. Mineral. J. Earth Planet. Mater. 31, 313–316.

Gysi, A.P., Williams-Jones, A.E., 2013. Hydrothermal mobilization of pegmatite-hosted REE and Zr at Strange Lake, Canada: A reaction path model. Geochim. Cosmochim.

Acta 122, 324–352.

Hikov, A., Lerouge, C., Velinova, N., 2010. Geochemistry of alunite group minerals in advanced argillic altered rocks from the Asarel porphyry copper deposit, Central Srednogorie. Rev. Bulg. Geol. Soc. 71, 133–148.

Izbrodin, I.A., Ripp, G.S., Doroshkevich, A.G., 2011. Aluminium phosphate and phosphate-sulphate minerals in kyanite schists of the Ichetuyskoye area, West Transbaikalia, Russia: Crystal chemistry and evolution. Mineral. Petrol. 101, 81–96. https://doi.org/10.1007/s00710-010-0135-5

Izbrodin, I.A., Ripp, G.S., Karmanov, N.S., 2009. Phosphate and sulfate-phosphate mineralization in sillimanite-bearing rocks at the Kyakhta deposit, western Transbaikal region. Geol. Ore Depos. 51, 617–626. https://doi.org/10.1134/S1075701509070101

Jamtveit, B., Malthe-Sørenssen, A., Kostenko, O., 2008. Reaction enhanced permeability during retrogressive metamorphism. Earth Planet. Sci. Lett. 267, 620–627.

Jamtveit, B., Putnis, C. V, Malthe-Sørenssen, A., 2009. Reaction induced fracturing during replacement processes. Contrib. to Mineral. Petrol. 157, 127–133.

Janssen, A., Putnis, A., Geisler, T., Putnis, C. V, 2008. The mechanism of experimental oxidation and leaching of ilmenite in acid solution, in: 9th International Congress for Applied Mineralogy, ICAM 2008. pp. 503–506.

Jones, A.P., Wall, F., 1996. Williams CT (1996) Rare earth minerals: chemistry, origin and ore deposits.

Manning, C.E., 2007. Solubility of corundum + kyanite in H2O at 700°C and 10 kbar: Evidence for Al-Si complexing at high pressure and temperature. Geofluids 7, 258–269. https://doi.org/10.1111/j.1468-8123.2007.00179.x

Manning, C.E., 2006. Mobilizing aluminum in crustal and mantle fluids. J. Geochemical Explor. 89, 251–253. https://doi.org/10.1016/j.gexplo.2005.12.019

Manning, C.E., Aranovich, L.Y., 2014. Brines at high pressure and temperature: thermodynamic, petrologic and geochemical effects. Precambrian Res. 253, 6–16.

Manning, C.E., Boettcher, S.L., 1994. Rapid-quench hydrothermal experiments at mantle pressures and temperatures. Am. Mineral. 79, 1153–1158.

Marfil, R., La Iglesia, A., Estupiñan, J., 2013. Origin and nature of the aluminium phosphate-sulfate minerals (APS) associated with uranium mineralization in triassic red-beds (Iberian Range, Spain). Estud. Geol. 69, 21–34. https://doi.org/10.3989/egeol.40879.176

Migdisov, A., Williams-Jones, A.E., Brugger, J., Caporuscio, F.A., 2016. Hydrothermal transport, deposition, and fractionation of the REE: Experimental data and thermodynamic calculations. Chem. Geol. 439, 13–42.

Möller, V., Williams-Jones, A.E., 2017. Magmatic and hydrothermal controls on the mineralogy of the basal zone, Nechalacho REE-Nb-Zr deposit, Canada. Econ. Geol. 112, 1823–1856.

Möller, V., Williams-Jones, A.E., 2016. Petrogenesis of the Nechalacho Layered Suite, Canada: magmatic evolution of a REE–Nb-rich nepheline syenite intrusion. J. Petrol. 57, 229–276.

Morteani, G., Ackermand, D., 2006. Mineralogy, geochemistry and petrology of an amphibolite-facies aluminum-phosphate and borosilicate (APB)-bearing quartzite from the Mesoproterozoic Itremo Group (Central Madagascar). Neues Jahrb. fur Mineral. 182, 123–148.

Morteani, G., Ackermand, D., 2004. Mineralogy and geochemistry of Al-phosphate and Al-borosilicate-bearing metaquartzites of the northern Serra do Espinhaço (State of Bahia, Brazil). Mineral. Petrol. 80, 59–81. https://doi.org/10.1007/s00710-003-0019-z

Morteani, G., Ackermand, D., 1996. Aluminium phosphates in muscovite-kyanite metaquartzites from Passo di Vizze (Alto Adige, NE Italy). Eur. J. Mineral. 853–870.

Morteani, G., Ackermand, D., Horn, A.H., 2001. Aluminium-phosphates and borosilicates in muscovite-kyanite metaquartzites near Diamantina (Minas Gerais , Brazil): Petrogenetic implications The rocks studied in this paper are examples of the rather rare cases of sedimentary phosphate-rich rocks of Mi 111–129.

Müller, A., Ihlen, P.M., Wanvik, J.E., Flem, B., 2007. High-purity quartz mineralisation in kyanite quartzites, Norway. Miner. Depos. 42, 523–535. https://doi.org/10.1007/s00126-007-0124-8

Mysen, B., 2022. Fluids and physicochemical properties and processes in the Earth. Prog. Earth Planet. Sci. 9, 54. https://doi.org/10.1186/s40645-022-00516-0

Nagy, G., Draganits, E., Demény, A., Pantó, G., Árkai, P., 2002. Genesis and transformations of monazite, florencite and rhabdophane during medium grade metamorphism: Examples from the Sopron Hills, Eastern Alps. Chem. Geol. 191, 25–46. https://doi.org/10.1016/S0009-2541(02)00147-X

Newton, R.C., Manning, C.E., 2010. Role of saline fluids in deep-crustal and upper-mantle metasomatism: insights from experimental studies. Geofluids 10, 58–72.

Osterberg, S.A., 1985. Stratigraphy and Hydrothermal Alteration of Archean Volcanic Rocks at the Headway-Coulee Massive Sulfide Prospect, Northern Onaman Lake Area, Northwestern Ontario.

Owens, B.E., Pasek, M.A., 2007. Kyanite quartzites in the Piedmont Province of Virginia: Evidence for a possible high-sulfidation system. Econ. Geol. 102, 495–509. https://doi.org/10.2113/gsecongeo.102.3.495

Pal, D.C., Barton, M.D., Sarangi, A.K., 2009. Deciphering a multistage history affecting U–Cu (–Fe) mineralization in the Singhbhum Shear Zone, eastern India, using pyrite textures and compositions in the Turamdih U–Cu (–Fe) deposit. Miner. Depos. 44, 61–80.

Pal, D.C., Basak, S., McFarlane, C., Sarangi, A.K., 2021. EPMA geochemistry and LA-ICPMS dating of allanite, epidote, monazite, florencite and titanite from the Jaduguda uranium deposit, Singhbhum Shear Zone, eastern India: Implications for REE

mineralization vis-à-vis tectonothermal events in the Proterozoic Mo. Precambrian Res. 359, 106208.

Pal, D.C., Rhede, D., 2013. Geochemistry and chemical dating of uraninite in the Jaduguda Uranium Deposit, Singhbhum Shear Zone, India—Implications for uranium mineralization and geochemical evolution of uraninite. Econ. Geol. 108, 1499–1515.

Pe-Piper, G., Dolansky, L.M., 2005. Early diagenetic origin of Al phosphate-sulfate minerals (woodhouseite and crandallite series) in terrestrial sandstones, Nova Scotia, Canada. Am. Mineral. 90, 1434–1441.

Pourtier, E., Devidal, J.-L., Gibert, F., 2010. Solubility measurements of synthetic neodymium monazite as a function of temperature at 2 kbars, and aqueous neodymium speciation in equilibrium with monazite. Geochim. Cosmochim. Acta 74, 1872–1891.

Putnis, A., Austrheim, H., 2010. Fluid-induced processes: metasomatism and metamorphism. Geofluids 10, 254–269.

Ripp, G.S., Kanakin, S. V, Shcherbakova, M.N., 1998. Phosphate mineralization in metamorphosed high-alumina rocks of the Ichetuyskoye ore occurrence. Zap. Vseross Miner. Obs. 127, 98–108.

Sarkar, S.C., Gupta, A., 2012. Crustal evolution and metallogeny in India, Crustal Evolution and Metallogeny in India. Cambridge University Press, New York. https://doi.org/10.1017/CBO9781139196123

Schmandt, D.S., Cook, N.J., Ciobanu, C.L., Ehrig, K., Wade, B.P., Gilbert, S., Kamenetsky, V.S., 2017. Rare earth element fluorocarbonate minerals from the olympic dam Cu-U-Au-Ag deposit, South Australia. Minerals 7, 202.

Scholten, L., Schmidt, C., Lecumberri-Sanchez, P., Newville, M., Lanzirotti, A., Sirbescu, M.-L.C., Steele-MacInnis, M., 2019. Solubility and speciation of iron in hydrothermal fluids. Geochim. Cosmochim. Acta 252, 126–143. https://doi.org/https://doi.org/10.1016/j.gca.2019.03.001

Schwab, R.G., Pimpl, T., Schukow, H., Stolle, A., Breitinger, D.K., 2005. Compounds of the crandallite-type: Synthesis, properties and thermodynamic data of Ca-Sr-Ba-Pb-(arseno)-woodhouseites. Neues Jahrb. für Mineral. 207–218.

Sengupta, N., 2012. Stability of chloritoid + biotite-bearing assemblages in some metapelites from the Palaeoproterozoic Singhbhum Shear Zone , eastern India and their implications Stability of chloritoid 1 biotite-bearing assemblages in some metapelites from the Palaeoprote. https://doi.org/10.1144/SP365.6

Sengupta, N., Mukhopadhyay, D., Sengupta, P., Hoffbauer, R., 2005. Tourmaline-bearing rocks in the Singhbhum shear zone, eastern India: Evidence of boron infiltration during regional metamorphism. Am. Mineral. 90, 1241–1255.

Sengupta, S., Pack, A., 2018. Triple oxygen isotope mass balance for the Earth's oceans with application to Archean cherts. Chem. Geol. 495, 18–26. https://doi.org/10.1016/j.chemgeo.2018.07.012

Seward, T.M., Williams-Jones, A.E., Migdisov, A.A., 2014. The chemistry of metal transport and deposition by ore-forming hydrothermal fluids. Treatise on

geochemistry 29–57.

Sharp, Z.D., Wostbrock, J.A.G., Pack, A., 2018. Mass-dependent triple oxygen isotope variations in terrestrial materials. Geochemical Perspect. Lett. 7, 27–31. https://doi.org/10.7185/geochemlet.1815

Shervais, J.W., Kolesar, P., Andreasen, K., 2005. A field and chemical study of serpentinization—Stonyford, California: chemical flux and mass balance. Int. Geol. Rev. 47, 1–23.

Spear, F.S., 1993. Metamorphic phase equilibria and pressure-temperature-time paths. Mineral. Soc. Am. Monogr. 352–356.

Stoffregen, R.E., Alpers, C.N., 1987. Woodhouseite and svanbergite in hydrothermal ore deposits; products of apatite destruction during advanced argillic alteration. Can. Mineral. 25, 201–211.

Tagirov, B., Schott, J., Harrichoury, J.-C., 2002. Experimental study of aluminum–fluoride complexation in near-neutral and alkaline solutions to 300 C. Chem. Geol. 184, 301–310.

Tagirov, B., Schott, J., Harrichoury, J.-C., Escalier, J., 2004. Experimental study of the stability of aluminate-borate complexes in hydrothermal solutions. Geochim. Cosmochim. Acta 68, 1333–1345.

Trommsdorff, V., Skippen, G., 1986. Vapour loss ("boiling") as a mechanism for fluid evolution in metamorphic rocks. Contrib. to Mineral. Petrol. 94, 317–322.

Uher, P., Mikuš, T., Milovský, R., Biroň, A., Spišiak, J., Lipka, J., Jahn, J., 2009. Lazulite and Ba, Sr, Ca, K-rich phosphates-sulphates in quartz veins from metaquartzites of Tribeč Mountains, Western Carpathians, Slovakia: Compositional variations and evolution. Lithos 112, 447–460. https://doi.org/10.1016/j.lithos.2009.03.046

Vasyukova, O. V, Williams-Jones, A.E., Blamey, N.J.F., 2016. Fluid evolution in the Strange Lake granitic pluton, Canada: Implications for HFSE mobilisation. Chem. Geol. 444, 83–100.

Verdes, G., Gout, R., Castet, S., 1992. Thermodynamic properties of the aluminate ion and of bayerite, boehmite, diaspore and gibbsite. Eur. J. Mineral. 767–792.

Visser, D., Felius, R.O., Moree, M., 1997. Augelite and cerian crandallite in dumortierite quartzites, Vaca Morta quarry, Vereda range, Macaúbas, Bahia, Brazil. Mineral. Mag. 61, 607–609. https://doi.org/10.1180/minmag.1997.061.407.11

Wagner, T., Beitter, T., Markl, G., 2009. Geochemical modeling of the formation of kyanite-quartz veins, Alpe Sponda, Central Alps. Geochim. Cosmochim. Acta Suppl. 73, A1400.

Wall, F., Niku-Paavola, V.N., Storey, C., Müller, A., Jeffries, T., 2008. Xenotime-(Y) from carbonatite dykes at Lofdal, Namibia: unusually low LREE: HREE ratio in carbonatite, and the first dating of xenotime overgrowths on zircon. Can. Mineral. 46, 861–877.

Widmer, T., Thompson, A.B., 2001. Local origin of high pressure vein material in eclogite

facies rocks of the Zermatt-Saas Zone, Switzerland. Am. J. Sci. 301, 627–656.

Xiaoye, J., Li, J., Hofstra, A., Sui, J., 2017. Magmatic-hydrothermal origin of the early Triassic Laodou lode gold deposit in the Xiahe-Hezuo district, West Qinling orogen, China: implications for gold metallogeny. Miner. Depos. 52, 1–20. https://doi.org/10.1007/s00126-016-0710-8

Xie, Z., Walther, J. V, 1993. Quartz solubilities in NaCl solutions with and without wollastonite at elevated temperatures and pressures. Geochim. Cosmochim. Acta 57, 1947–1955.

Yardley, B.W.D., 1977. The nature and significance of the mechanism of sillimanite growth in the Connemara Schists, Ireland. Contrib. to Mineral. Petrol. 65, 53–58.

Yardley, Bruce W D, Shmulovich, Kirill I, 1995. An introduction to crustal fluids BT - Fluids in the Crust: Equilibrium and transport properties, in: Shmulovich, K I, Yardley, B W D, Gonchar, G.G. (Eds.), . Springer Netherlands, Dordrecht, pp. 1–12. https://doi.org/10.1007/978-94-011-1226-0_1

Zakharov, D.O., Bindeman, I.N., Slabunov, A.I., Ovtcharova, M., Coble, M.A., Serebryakov, N.S., Schaltegger, U., 2017. Dating the Paleoproterozoic snowball Earth glaciations using contemporaneous subglacial hydrothermal systems. Geology 45, 667–670.

Zanin, I., 1975. Material composition of phosphate crust weathering and deposit of phosphates, Nauka Publ. Nauka, Sibirskoe otd-nie, Novosibirsk.

APPENDIX

APPENDIX-I

Singular Value Decomposition technique used by C-Space for deducing mineral reactions

The computer program "C-Space" published by Torres-Roldan et. al. (2000) is based on the algorithm published by Fisher (1989, 1993). It applies the method of SVD described below to generate all possible balanced chemical reactions involving a given set of mineral compositions or chemical species. Singular value decomposition (SVD) is a simple but robust matrix technique that is widely used by the geoscientist for modelling metamorphic textures (Lang et al., 2004). This technique calculates linear dependencies and suggests possible reactions from a compositional matrix M of m minerals in terms of n components (Lang et al. 2004). In this study, the computer program CSpace (Torres-Roldan et al., 2000) was used to perform the matrix operation required for SVD.

Theoretical Background:

If "m" and "n" represent the rows and columns of a given matrix, then a set of linearly

independent relations exist as follows :

$a_{11}X_1 + a_{12}X_2 + a_{13}X_3 + \ldots\ldots + a_{1}nXn = Y_1$

$a_{21}X_1 + a_{22}X_2 + a_{23}X_3 + \ldots\ldots + a_{2}nXn = Y_2$

$a_{31}X_1 + a_{32}X_2 + a_{33}X_3 + \ldots\ldots + a_{3}nXn = Y_3$

……...

$am_1X_1 + am_2Xm_2 + am_3X_3 + \ldots + amnXn = Ym$

These equations can be expressed in the following matrix form :

A.X=Y …….. (1)

where, A,X and Y are as follows:

$$\begin{bmatrix} a_{11} & a_{12} & a_{13} \ldots\ldots\ldots & a_{1n} \\ a_{21} & a_{22} & a_{23} \ldots\ldots\ldots & a_{2n} \\ a_{21} & a_{22} & a_{23} \ldots\ldots\ldots & a_{2n} \\ \ldots & \ldots & \ldots \ldots & \\ a_{m1} & a_{m2} & a_{m3} \ldots\ldots\ldots & a_{mn} \end{bmatrix} = A \begin{bmatrix} X_1 \\ X_2 \\ X_3 \\ \ldots \\ X_m \end{bmatrix} = X \begin{bmatrix} Y_1 \\ Y_2 \\ Y_3 \\ \ldots \\ Y_m \end{bmatrix}$$

Various techniques like the Gauss-Jordan elimination, the SVD etc. maybe used to solve equation 1 (Press et al., 2007). Of these, the SVD is a powerful method as it not only minimizes numerical errors but also provides solutions in cases where other methods fail to give satisfactory results (Press et al., 2007). According to the SVD, an m x n matrix A (m=number of rows, n=number of coloumns), where $m \geq n$, maybe expressed as

A=U.W.V …….(2)

where,

U = m x n column orthogonal matrix,

W = n x n diagonal matrix with positive or zero elements,

V = transpose of an n x n orthogonal matrix.

Thus, from (1) and (2) we may write :

U.V.W.X = Y .....(3)

The above equation can be re-written in the form :

W.z = d …..(4)

where,

$z = VT \cdot X$,

$d = UT \cdot Y$

Equation (4) may be solved to get the values of the unknowns X_1 to Xn .

In geological problems, “m” signifies the number of minerals and/or chemical phases and “n” is the number of system components in terms of which composition of these minerals or phases may be expressed. These are used to generate an m x n matrix as in A of equation (1). As described above, the SVD technique is applied to solve this matrix using equation (4).

The computer program C-Space (Torres-Roldan et al., 2000) has been used to perform the matrix operation. The program calculates several balanced reactions in terms of molar coefficients. From these calculated reactions, only those reactions have been chosen that are at par with our textural observations. Thereafter, the volume change of each reaction (ΔV_{SOLID}) is calculated by multiplying the molar coefficients of the phases with their molar volumes obtained using the computer program PERPLEX_6.8.0 (Connolly, 2005, 2009) with the updated thermodynamic data of Holland and Powell (1998).

APPENDIX-II

Chemical alteration indices used in calculations

Chemical Index of Alteration (CIA): Nesbitt and Young (1982) introduced the relatively simple chemical index of alteration (CIA), which monitors the progressive alteration of plagioclase and potassium feldspar to clay minerals. The index is calculated using molecular proportions in the equation

$CIA = [Al_2O_3/ (Al_2O_3+ CaO^*+Na_2O+K_2O)] \times 100$

In the equation CaO* is the amount of CaO incorporated in the silicate fraction of rock (corrected for calcium residing in carbonates and phosphates).

A-CN-K ternary diagram: The use of Al_2O_3 –(CaO* + Na_2O) - K_2O ternary plot is favoured in evaluation of chemical weathering trends than simple comparison of numerical value (Nesbitt & Young, 1984, 1989; Roddaz et al., 2006; Raza et al., 2010, 2012) as geological systems are complex and a single calculated value may not adequately reflect their complexities. The A-CN-K diagram displays the molar proportions of Al_2O_3 (A apex), CaO*+Na_2O (CN apex) and K_2O (K apex), where CaO* represents CaO incorporated into silicate minerals (Nesbitt and Young, 1984, 1989). Plagioclase and K-feldspar plot at 50% Al_2O_3 on the left and right boundaries, respectively to form the 'feldspar join'. Biotite plots with K-feldspar, augite and amphiboles plot near the CN apex and calcite plots at the Ca ape. Illite and smectites plot on the diagram at 70% and 85% Al_2O_3. The clay mineral groups, kaolin, chlorites and gibbsite plot at the A apex (100% Al_2O_3). The initial weathering trends of igneous rocks are sub-parallel to CN-A join as Ca and Na rom plagioclase are leached from the profile in preference to Al_2O_3, thus the residues are enriched in Al_2O_3. As weathering progresses, clay minerals are produced at the expense of feldspars and bulk composition of soil/sediments samples evolve up the diagram towards A apex, along the weathering trend. The most intensely weathered samples will therefore, plot highest on the

diagram, reflecting the preponderance of aluminous clay minerals. The weathering trend intersects then A-K boundary once all plagioclase is weathered and then is redirected towards the A apex because K is extracted from the residues in preference to Al. The A-CN-K plot is useful for evaluating fresh rock composition and examining their weathering trends since unweathered primary igneous rocks have CIA values close to 50 (Fedo et al., 1995) i.e. close to the feldspar join on A-CN-K diagram, backward projection of the weathered samples should lead to a point on the feldspar join which approximates plagioclase/K-feldspar ratios of their source rock. Also the amount of K enrichment and the palaeoweathering index prior to such enrichment can be ascertained from A-CN-K plot (Fedo et al., 1995) as this type of K-enrichment involves addition of K_2O to aluminous clays, which follows a path towards the K_2O apex of the triangle. K metasomatism of sediments can take two different paths representing either conversion of aluminous clay minerals to illite and/or conversion of plagioclase to K-feldspar. Both these processes result in the samples being enriched in K_2O and therefore offset from the weathering trend.

A-CNK-FM ternary diagram: A second diagram was introduced by Nesbitt and Young (1989), to illustrate the relationship between leucocratic and melanocratic constituents in weathering profiles. CaO*, Na_2O and K_2O (CNK) are plotted at the lower apex, Al_2O_3 (A apex) at the top and FeO (total iron as FeO) and MgO are summed to form the third variable. All variables are taken in molecular proportions. The diagram is referred to as the A-CNK-FM diagram. It is similar to the ACF diagram used in metamorphic petrology. Plagioclase plus K-feldspar plot of the left hand boundary at 50% Al_2O_3. Illite plots on the left boundary, at approximately 75% and greater Al_2O_3, meanwhile kaolin and gibbsite plot at the A apex. Biotite plots three quarters of the way along the line between feldspars and FM apex. Chlorite plots on the right hand boundary, as a solid solution, with Al_2O_3 ranging from approximately 15 to 25%. Smectite plots within the triangle somewhat above 50% Al_2O_3. Weathering trends

cannot be calculated from this diagram because the requisite kinetic data are not available and therefore, trends are derived from weathering profile alone.

Chemical Index of Weathering (CIW): The two major elements indices proposed to monitor chemical weathering: CIA (Nesbitt and Young, 1982) and CIW (Harnois, 1988). CIW is the best measure of intensity of chemical weathering as CIA calculations involve K_2O, which is a mobile oxide (Condie, 1993). This limits its application to sediments in which potassium has been actually leached.

CIW- $[Al_2O_3 / Al_2O_3 + (CaO+Na_2O)] \times 100$

Here, Al_2O_3, CaO, Na_2O are in molecular proportions. CaO and Na2O are mobile components while Al_2O_3 is considered immobile. The difference between CIW index for source rock and sediments reflects the amounts of chemical weathering experienced by the weathered material. The CIW index can be applied to silicate rocks of felsic to mafic composition and is superior to other weathering indices, in that it involves a restricted number of components which have simple well known and consistent behaviour during weathering.

ACN ternary diagram or Plagioclase Index of Alteration (PIA): The chemical weathering can also be indicated by PIA i.e. Plagioclase Index of Alteration. (Fedo et al., 1995), especially when plagioclase weathering needs to be monitored. The values are calculated using the formula

PIA= $(Al_2O_3-K_2O)/(Al_2O_3-K_2O + CaO^* + Na_2O-K_2O) \times 100$

where all variable are in molar proportions and CaO* is the CaO content of silicate fraction only.

Advanced argillic alteration index: This index helps in quantifying the intensity of alteration.

AAAI=$100 \times SiO_2/[SiO_2 + (10 \times MgO) + (10 \times CaO) + (10 \times Na_2O)]$.

APPENDIX-III

Analytical techniques

Microprobe analysis for silicates and phosphates including REE bearing phases

Most mineral analyses were performed at the Central Petrological Laboratory, Geological survey of India, Kolkata, using Cameca electron probe. Anhydrous silicate, oxide and metal standards were used appropriate to the mineral analysed, and full ZAF corrections were made. Dwell time for all the measured elements were set as 10 sec at peak and 5 sec at background. The standards (and emission lines) used are: jadeite (Na-Kα), albite (Si-Kα), diopside (Mg-Kα), apatite (Ca-Kα, PKα), CaF_2 (F-Kα), corundum (Al-Kα), orthoclase (K-Kα), Cr_2O_3 (Cr-Kα), NaCl (Cl-Kα), Fe_2O_3 (Fe-Kα), synthetic MnTi (Mn-Kα, Ti-Kα). TAP crystal was used to analyze F, Na, Al, Si and Mg; PET for Ca, Ti, K and Cl; LPET for P; LIF for Mn and Fe. For elements other than Sr, Ba, and the REE, the accelerating voltage used was 15 kV with a 12 nA current.

For the analysis of florencite, containing REE, 20 kV accelerating voltage and 20 nA current were used. The standards are used for REE is REE glass, Sr is celestite, and Ba is barite. The raw data were processed using the PAP procedure (Pouchou and Pichoir, 1984). At least three spot analyses were done at every spot to check the consistency of analyses.

Bulk data analysis for rocks: Rocks were collected from fresh outcrops. After crushing in a metal crusher, all samples were analysed in XRF (for major oxides) and ICPMS (for trace elements) installed at the Mineralogisch-Petrologisches Institut, University of Bonn.

Oxygen isotope analysis

Oxygen isotope analysis of kyanite grains was carried out at Stable Isotope Laboratory, University of Gottingen, Germany. In situ spot analysis of kyanite grains were made from

kyanite quartzite thin sections <300µm in diameter. The samples are placed in a nickel sample holder in a 304-stainless steel chamber and heated with 20W CO_2 laser. Infrared laser radiation is admitted through a BaF_2 window. BrF5 is used as an oxidation agent for laser fluorination of samples. The released oxygen is passed through a cold trap and then through a hot mercury fluorine getter. The gas is then converted to CO_2 by reaction with hot carbon in the presence of platinum catalyst. The CO_2 is passed through a mass spectrometer. Reaction times for each sample is <2 minutes. Analyses were made from <1-4µmoles of CO2 gave the expected $\delta^{18}O$ values. The precision and accuracy is equivalent to conventional fluorination method. The $\delta^{17}O$ and $\delta^{18}O$ values are reported relative to VSMOW scale. Reproducibility was tested on San Carlos olivine (laser fluorination) and Dorentrup quartz (Ni tubes) to ± 0.5‰ for $\delta^{18}O$ and ± 0.01‰ for $\Delta'^{17}O$ (1σ, SD).

APPENDIX-IV

Bulk calculation for chloritoid bearing KQ (CKQ)

The CKQ has heterogeneous distribution of the minerals and coarse grain size in the studied rock, reaction volume has been computed from the modal volume in a chloritoid –bearing domain and the measured phase compositions. The modal volume of minerals calculated from chloritoid rich portions of KQ are visually estimated. The following table provides us with the calculations for bulk of CKQ.

Table 7: Calculation of bulk from modal volume of minerals in CKQ

Minerals	Modal vol%	Molar Vol (cc/mol)	Moles of each mineral phase	Oxides	Total weight of oxides from mineral phases	Estimated Bulk data (wt%)
Kyanite	40.00	44.17	17.67	SiO_2	3020.60	43.68
Muscovite	19.50	143.6	28.00	TiO_2	5.04	0.07
Chloritoid	15.00	139.39	20.91	Al_2O_3	2945.78	42.60
Quartz	25.00	22.69	5.67	FeO	575.24	8.32
Rutile	0.50	18.91	0.09	MnO	0.71	0.01
				MgO	58.82	0.85
				Na_2O	35.08	0.51
				K_2O	274.14	3.96
				Total		100.00

References

Condie, K.C., 1993. Chemical composition and evolution of the upper continental crust: contrasting results from surface samples and shales. Chem Geol 104, 1–37.

Connolly, J.A.D., 2009. The geodynamic equation of state: what and how. Geochemistry, geophysics, geosystems 10.

Connolly, J.A.D., 2005. Computation of phase equilibria by linear programming: a tool for geodynamic modeling and its application to subduction zone decarbonation. Earth Planet Sci Lett 236, 524–541.

Fedo, C.M., Wayne Nesbitt, H., Young, G.M., 1995. Unraveling the effects of potassium metasomatism in sedimentary rocks and paleosols, with implications for paleoweathering conditions and provenance. Geology 23, 921–924.

Fisher, G.W., 1993. An improved method for algebraic analysis of metamorphic mineral assemblages. American Mineralogist 78, 1257–1261.

Fisher, G.W., 1989. Matrix analysis of metamorphic mineral assemblages and reactions. Contributions to Mineralogy and Petrology 102, 69–77.

Harnois, L., 1988. The CIW index: a new chemical index of weathering. Sediment Geol 55, 319–322.

Holland, T.J.B., Powell, R., 1998. An internally consistent thermodynamic data set for phases of petrological interest. Journal of metamorphic Geology 16, 309–343.

Lang, H.M., Wachter, A.J., Peterson, V.L., Ryan, J.G., 2004. Coexisting clinopyroxene/spinel and amphibole/spinel symplectites in metatroctolites from the Buck Creek ultramafic body, North Carolina Blue Ridge. American Mineralogist 89, 20–30.

Nesbitt, H.W., Young, G.M., 1989. Formation and diagenesis of weathering profiles. J Geol 97, 129–147.

Nesbitt, H.W., Young, G.M., 1984. Prediction of some weathering trends of plutonic and volcanic rocks based on thermodynamic and kinetic considerations. Geochim Cosmochim Acta 48, 1523–1534.

Nesbitt, H.W., Young, G.M., 1982. Early Proterozoic climates and plate motions inferred from major element chemistry of lutites. Nature 299, 715–717.

Pouchou, J.L., Pichoir, F., 1984. A new model for quantitative analyses. I. Application to the analysis of homogeneous samples. Rech. Aerospat. 3, 13–38.

Press, W.H., Teukolsky, S.A., Vetterling, W.T., Flannery, B.P., 2007. Numerical recipes 3rd edition: The art of scientific computing. Cambridge university press.

Raza, M., Ahmad, A.H.M., Shamim Khan, M., Khan, F., 2012. Geochemistry and detrital modes of Proterozoic sedimentary rocks, Bayana Basin, north Delhi fold belt: implications for provenance and source-area weathering. Int Geol Rev 54, 111–129.

Raza, M., Dayal, A.M., Khan, A., Bhardwaj, V.R., Rais, S., 2010. Geochemistry of lower Vindhyan clastic sedimentary rocks of Northwestern Indian shield: Implications for composition and weathering history of Proterozoic continental crust. J Asian Earth Sci 39, 51–61.

Roddaz, M., Brusset, S., Baby, P., Hérail, G., 2006. Miocene tidal-influenced sedimentation to continental Pliocene sedimentation in the forebulge–backbulge depozones of the Beni–Mamore foreland Basin (northern Bolivia). J South Am Earth Sci 20, 351–368.

Torres-Roldan, R.L., Garcia-Casco, A., Garcia-Sanchez, P.A., 2000. CSpace: An integrated workplace for the graphical and algebraic analysis of phase assemblages on 32-bit Wintel platforms. Comput Geosci 26, 779–793.

PAPERS & ABSTRACTS

PUBLISHED PAPERS

Chakraborty, M., Biswas, S., Sengupta, N., Sengupta, P., 2014a. First report of florencite from the Singhbhum shear zone of the East Indian Craton. Int. J. Mineral. 1–8. https://doi.org/10.1155/2014/978793

Chakraborty, M., Sengupta, N., Biswas, S., Sengupta, P., 2014b. Phosphate minerals as a recorder of P-T-fluid regimes of metamorphic belts: example from the Palaeoproterozoic Singhbhum Shear Zone of the East Indian shield. Int. Geol. Rev. 57, 1619–1632. https://doi.org/10.1080/00206814.2014.982216

PUBLISHED ABSTRACTS

Chakraborty, M., Biswas, S., 2020. Origin of dumortierite deposits in Kyanite rich quartzite from parts of the Singhbhum Shear Zone , India : Evidence for large scale boron metasomatism along ductile shear zone, in: 36th International Geological Congress Abstract Volume. pp. 2605–2606.

Chattopadhyay, N., Chakraborty, M., Ray, S., Sanyal, S., 2016. Origin of atypical Fe-Mn-deposits along the South Purulia Shear Zone: Evidence of low temperature hydrothermal activity at near surface condition, in: Developments in Geosciences in the Past Decade - Emerging Trends for the Future & Impact on Society & Annual General Meeting of the Geological Society of India, Seminar Abstract Volume. pp. 119–122.

Biswas, S., Sengupta, N., Ray, S., Chakraborty, M., Sanyal, S., Sengupta, P., 2013. Repeated

boron infiltration and ductile shearing at continental suture zone : An example from the South Purulia Shear Zone, West Bengal, India, in: 3rd Precambrian Continental Growth and Tectonism; Abstract Volume, IAGR Conference Series. pp. 36–37.

Chakraborty, M., Sengupta, N., Biswas, S., Sengupta, P., 2013. Deep crustal ductile shearing, infiltration driven metamorphism and formation of alumino-phosphate minerals: An example from the Palaeoproterozoic Singhbhum Shear Zone, East Indian shield, in: 3rd Precambrian Continental Growth and Tectonism, Abstract Volume, IAGR Conference Series. pp. 38–39.

Ray, S., Biswas, S., Chakraborty, M., Sanyal, S., Sengupta, P., 2012. Mass transport during fennitization of granite at the contact of carbonatite at Beldihi, Purulia, West Bengal, in: National Seminar on Recent Advances and Future Challenges in Geochemistry & Geophysics the Indian Scenario, BHU. p. 114.